Spectroscopic Studies of Near Stable Cadmium and Indium Nuclei

S. D. Langdown

Submitted for the Degree of Doctor of Philosophy
Department of Physics
School of Electronics and Physical Sciences
University of Surrey

January 2004

Abstract

A fusion-evaporation reaction between a thick self-supporting ^{110}Pd target and a ^{7}Li beam has been used to populate and study indium and cadmium nuclei with A=112−114 using the YRAST Ball γ-ray spectrometer array. Previously unreported states in ^{112}In and ^{114}In have been observed by use of γ−γ and γ^3 coincidences, and tentative spin and parity assignments using γ-ray angular correlation and distribution analysis have identified several bands consisting of stretched dipole transitions. Experimental $B(M1)/B(E2)$ values extracted from these dipole bands are consistent with values indicative of a shears mechanism. The experimental $B(M1)/B(E2)$ values have been compared with theoretical values calculated using the semi-classical Dönau formalism and are consistent with a single $g_{9/2}$ proton coupled to various rotationally aligned neutron configurations. Calculations of $\mathcal{I}^{(2)}/B(E2)$ result in values in excess of those usually obtained from rotational bands based on collective rotation and further add to the evidence of angular momentum generation by the shears mechanism. Two previously unreported states in ^{112}Cd have been observed which allow the observation of the vibrational to rotational evolution by use of E-GOS curves.

The commissioning of SASSYER, a recoil separator situated at the Wright Nuclear Structure Laboratory, Yale University, is documented in Appendix A. The use of an array of solar cells as a recoil detector is reported and the initial performance of SASSYER is investigated.

Acknowledgements

First and foremost, I'd like to thank my supervisor Dr. Paddy Regan for overseeing my research for the past three years. Guidance and support has been almost entirely been provided by Paddy and I'd like to thank him for his words of encouragement and for reading numerous drafts of this thesis and pointing out the errors therein. I would also like to take this opportunity to acknowledge the EPSRC for the financial support they have reliably provided during this time.

There are numerous people who have helped and encouraged me during the years I have been studying physics, the first being my physics teacher at school, Mr Buck. I'd like to thank him for allowing us to have a relatively 'free hand' when it came to exploring the laws and limitations of physics in those unforgettable practical lessons. Equations always became more meaningful after watching the item in question explode.....

I was fortunate enough to spend a year at Yale University and I'd like to thank Prof. Casten for his kind invitation and Mary-Anne Schultz for her advice and assistance in moving to America. I'd also like to acknowledge the staff of Clark's restaurant in New Haven for providing one of the most memorable moments of my PhD, when I finally managed to eat an entire Clark's pizza unaided.

I'd like to thank everybody within the physics community who has assisted me during the past three years of study: the staff, students and postdocs at

Surrey, Yale and all the other universities and facilities I have been to; my co-inhabitants of the office at Surrey who have allowed me to immerse myself deep in thought in relative peace; Dr. Duncan Appelbe for his prompt expertise in all things Radware; Dr. Arata Yamamoto for entertaining discussions ranging from Japanese socio-economic policies to the merits of various donuts; and to all the boys and girls outside of physics who kept me in touch with the rest of the world and who never asked me "why?"

Finally, to my parents, who I think know that I am eternally grateful to them for what they have provided me with over the past 26 years, but just in case they don't know, I'd like to dedicate this thesis to them. May you always think of me and my nuclei when you dust it.

Contents

List of Figures

List of Tables

Introduction

The study of the γ-ray decay properties of the atomic nucleus has provided an enormous quantity of information on the behaviour of such a system when under physical stress. The behaviour of the nucleus when stressed by rapid rotation (i.e. at high spins) allows us to observe the interplay between single-particle factors and collective (rotational or vibrational) states. At one limit, the nucleons within a nucleus act coherently and collective bands develop that follow the $I(I+1)$ rotational pattern, whilst at the other limit, a few individual nucleons may carry all the angular momentum of a high-spin state. Between these limits we sometimes find a complex behaviour and other times a coexistence of these simpler limiting behaviours. The study of nuclei at high angular momenta can be cast into the form of first understanding these two limits themselves, and then the interplay between them as the spin increases.

The decay of nuclei to their ground states is characterized by the emission of cascades of γ-ray transitions. The information about how the nuclear structure changes during the decay as it loses energy and angular momentum is obtained by measuring the properties of the γ rays in these cascades, such as energy, decay rates and angular distributions. This in turn provides insight into the nuclear force and how nucleons interact.

Physics of the $A\sim110$ Region

Nuclei in the $A\sim110$ region have been studied in recent years in search of bands exhibiting properties characteristic of the shears mechanism [1, 2], a prediction of tilted axis cranking [3]. In such sequences, angular momentum is generated in a manner that appears similar to collective rotation in well deformed nuclei, despite the small quadrupole deformations of these nuclei due to the proximity of the Z=50 spherical shell gap. Evidence of this phenomenon has been reported in neutron deficient $_{48}$Cd [4, 5, 6], $_{50}$Sn [7, 8, 9], and $_{51}$Sb nuclei [10, 11], which all have ΔI=1 cascades based on high-Ω $g_{9/2}$ proton holes coupled to low-Ω $g_{7/2}/d_{5/2}$ and $h_{11/2}$ neutrons. Similar bands have been reported in the odd-A In isotopes ^{109}In [12], ^{111}In [13] and ^{113}In [14] and the even-A In isotopes ^{108}In and ^{110}In [15]. Figure 1 shows the known magnetic dipole rotational bands in the region of $A\sim110$. The interpretation of these ΔI=1 bands suggests that further exploration in this mass region is worthwhile in order to extend the experimental information for odd-odd nuclei which have configurations of valence nucleons that are favourable for the shears mechanism.

Experimental data on the levels of even-even In nuclei are plentiful but similar data for odd-odd In nuclei in the mass region around $A\sim110$ are quite scarce. This is due to lack of suitable stable beam-target combinations prohibiting the study of heavier isotopes as evaporation residues in heavy-ion fusion-evaporation reactions. Figure 2 shows the level schemes of the previously reported transitions in ^{112}In and ^{114}In [16] before the current work was undertaken. The main aim of this work is to further investigate this region, by population of high-spin states in ^{112}In and ^{114}In with the intention of extending the experimental information on the shears mechanism.

The secondary aim of this work is to probe the vibrational to rotational evolution of $^{112-114}$Cd through the use of E—Gamma-Over Spin (E-GOS) curves [17].

This simple prescription for discerning the evolution from vibrational to rotational structure has recently been proposed and allows the distinction between rotational and vibrational ranges of spin to be vividly highlighted without the need for any structural preconceptions. The cadmium isotopes demonstrate this trend dramatically, specifically ^{108}Cd and ^{110}Cd [17]. By populating $^{112-114}$Cd to higher spins, it will be possible to extend our knowledge of vibrational to rotational evolution in the nuclei.

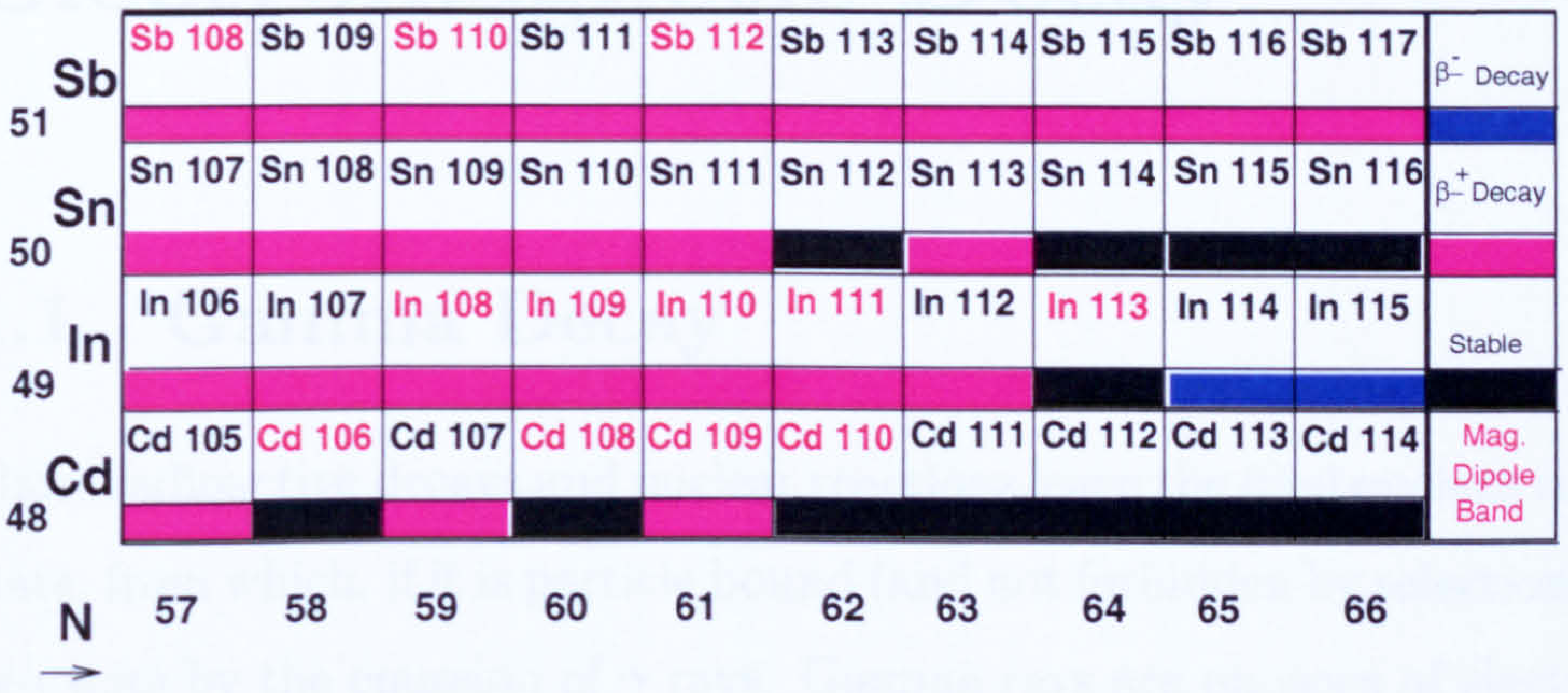

Figure 1: Isotope chart of Z versus N for the A ~110 mass region. Nuclei with previously reported magnetic dipole rotational bands are shown in red.

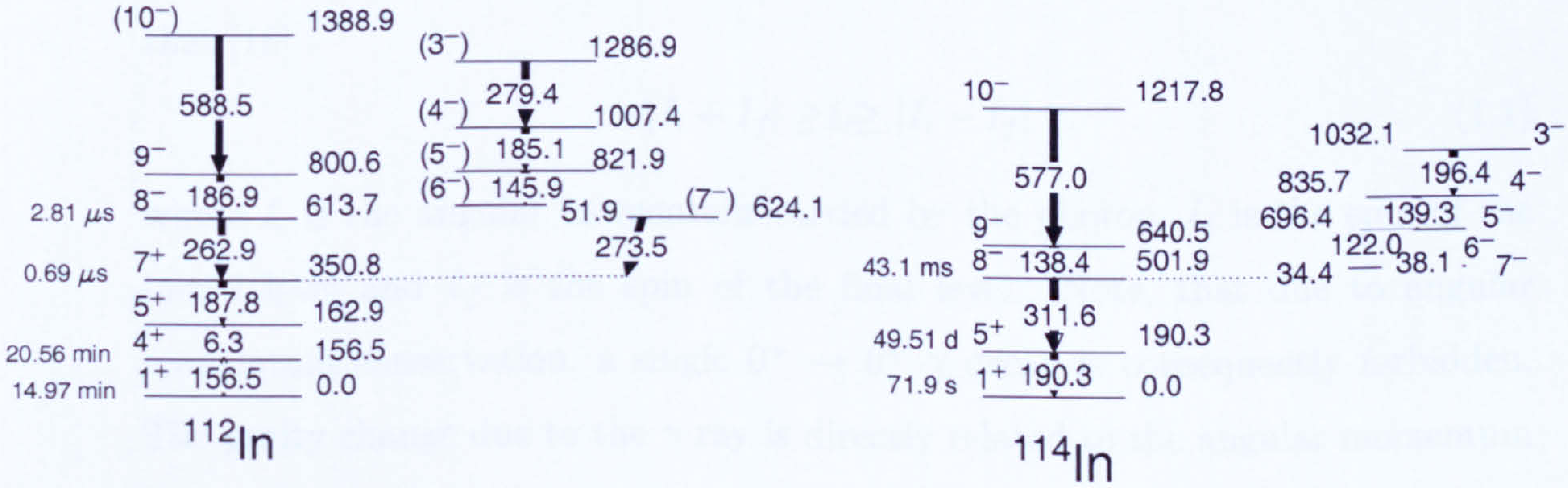

Figure 2: Level scheme of transitions previously reported in ^{112}In and ^{114}In [16].

Chapter 1

Electromagnetic Decay

1.1 Gamma Decay

Many radioactive decays and nuclear reactions leave the final nucleus in an excited state, from which, if it is particle bound (and not forbidden by selection rules), can de-excite by the emission of γ rays. Gamma rays are photons of electromagnetic radiation and as such, can be described classically in terms of multipole moments of charged distributions, namely dipoles, quadrupoles, octupoles etc. Gamma rays have an intrinsic spin of $1\hbar$ and must conserve angular momentum, such that [18]

$$|I_i + I_f| \geq L \geq |I_i - I_f| \tag{1.1}$$

where L is the angular momentum carried by the photon, I_i is the spin of the initial level and I_f is the spin of the final level. Note, that due to angular momentum conservation, a single $0^+ \rightarrow 0^+$ γ decay is consequently forbidden. The parity change due to the γ ray is directly related to the angular momentum L by the relations [18]

$$\Delta\pi = (-1)^L \tag{1.2}$$

for electric multipole radiation and

$$\Delta\pi = (-1)^{L+1} \tag{1.3}$$

for magnetic multipole radiation. Thus for a transition from a 3^+ level to a 2^- level, the multipoles $E1$, $M2$, $E3$, $M4$ and $E5$ are possible. In fact all of them will occur with competing probabilities and partial transition rates.

1.1.1 Mixed Multipolarity Transitions

The transition probability for a mixed multipolarity decay can be calculated in terms of the multipole mixing ratio, δ. The mixing ratio for ΔI=1, non-changing parity transitions is given by the ratio of the reduced matrix elements for the $E2$ and $M1$ components. This is related to their *partial transition probabilities* T, (see section 1.2) by the following expression [19]

$$\delta^2_{E2/M1} = \frac{T(E2 : J \rightarrow J-1)}{T(M1 : J \rightarrow J-1)} \tag{1.4}$$

Similarly, the branching ratio of competing ΔI=1 and ΔI=2 transitions is related to the transition probabilities through the relation [19]

$$\lambda_{E2/M1} = \frac{T(E2 : J \rightarrow J-2)}{T(M1 : J \rightarrow J-1)} \tag{1.5}$$

1.2 Electromagnetic Transition Rates

The motion of the protons in a nucleus gives rise to charge and current distributions. Charge distributions can be described by electric multipole moments and current distributions by magnetic multipole moments. The electromagnetic field produced when a nucleus emits radiation in the form of γ-rays can be described in terms of a multipole expansion [20, 21]. The total transition probability for a

γ ray of multipolarity λ and angular momentum L, from an initial state I_i to a final state I_f can be determined by [20]

$$\lambda_{fi} = \frac{8\pi(L+1)}{\hbar L((2L+1)!!)^2} \left(\frac{E_\gamma}{\hbar c}\right)^{2L+1} B(\sigma L; I_i \rightarrow I_f) \tag{1.6}$$

where the values of $B(\sigma L)$ are known as the *reduced transition probabilities* and are given by [21]

$$B(EL; I_i \rightarrow I_f) = \frac{1}{2I_i+1} \mid < f \| \hat{Q} \| i > \mid^2 \tag{1.7}$$

for an electric transition and

$$B(ML; I_i \rightarrow I_f) = \frac{1}{2I_i+1} \mid < f \| \hat{M} \| i > \mid^2 \tag{1.8}$$

for a magnetic transition, where $\hat{Q}$ and $\hat{M}$ are the electric and magnetic multipole operators respectively. It is assumed that the wavelength of the emitted radiation is long when compared to the dimensions of the nucleus. In order to account for the different possible orientations of the angular momentum L, an average over the initial m-state values and a sum over the final m-state values are performed.

Table 1.1 shows the electromagnetic transition rate estimates given in terms of the reduced transition probabilities for the lowest multipole orders. The estimates are obtained by multiplying out the constant terms in equation 1.6.

1.2.1 Weisskopf Estimates

Electromagnetic transition rates, under the assumption that the transition is due to a single proton moving from one spherical shell model state to another, can be estimated using the Weisskopf expressions [21]. For an electric transition

$T(E1)=1.59\times10^{15}B(E1)E^3$	$T(M1)=1.76\times10^{13}B(M1)E^3$
$T(E2)=1.22\times10^{9}B(E2)E^5$	$T(M2)=1.350\times10^{7}B(M2)E^5$
$T(E3)=5.76\times10^{2}B(E3)E^7$	$T(M3)=6.28\times10^{0}B(M3)E^7$
$T(E4)=1.69\times10^{-4}B(E4)E^9$	$T(M4)=1.87\times10^{-6}B(M4)E^9$

Table 1.1: Electromagnetic transition rates, T (sec^{-1}) expressed by $B(EL)$ in e$^2fm^{2L}$ and $B(ML)$ in $\mu_N^2 fm^{2L}$ and where E is the γ-ray energy measured in MeV. Taken from [22].

$$\lambda_{EL} = \frac{8\pi(L+1)}{\hbar L((2L+1)!!)^2}\left(\frac{e^2}{4\pi\epsilon_0\hbar c}\right)\left(\frac{E_\gamma}{\hbar c}\right)^{2L+1}\left(\frac{3}{L+3}\right)^2 cR^{2L} \tag{1.9}$$

and for a magnetic transition

$$\lambda_{ML} = \frac{8\pi(L+1)}{\hbar L((2L+1)!!)^2}\frac{e^2}{4\pi\epsilon_0\hbar c}\left(\mu_p - \frac{1}{L+1}\right)^2\left(\frac{\hbar}{m_p c}\right)^2\left(\frac{E_\gamma}{\hbar c}\right)^{2L+1}\left(\frac{3}{L+2}\right)^2 cR^{2L-2} \tag{1.10}$$

where μ_p is the magnetic moment of the proton and m_p is the proton mass. The wavefunctions of the states are those obtained using a square well potential. By taking $R = R_0A^{\frac{1}{3}}$ and by setting the $\left(\mu_p - \frac{1}{L+1}\right)^2$ term in equation 1.10 to be equal to 10 [21], estimates can be made for the lower multipole orders. These calculations are known as Weisskopf estimates and are not realistic calculations of the transition rates, but provide values that can be compared to those measured experimentally. If the measured transition probability is much greater than the Weisskopf estimates, then the nuclear structure is favourable for such a transition, indicating similar wavefunctions for the initial and final states, and a possible collective motion involving many nucleons.

Typical numbers of Weisskopf units for transitions of different multipolarity in different mass regions can be found in a number of summary tables [23], those for a nucleus of A=112 are plotted in figure 1.1. These estimates can be compared with experimentally determined values, possibly indicating a favourable multipolarity assignment for a previously unknown transition.

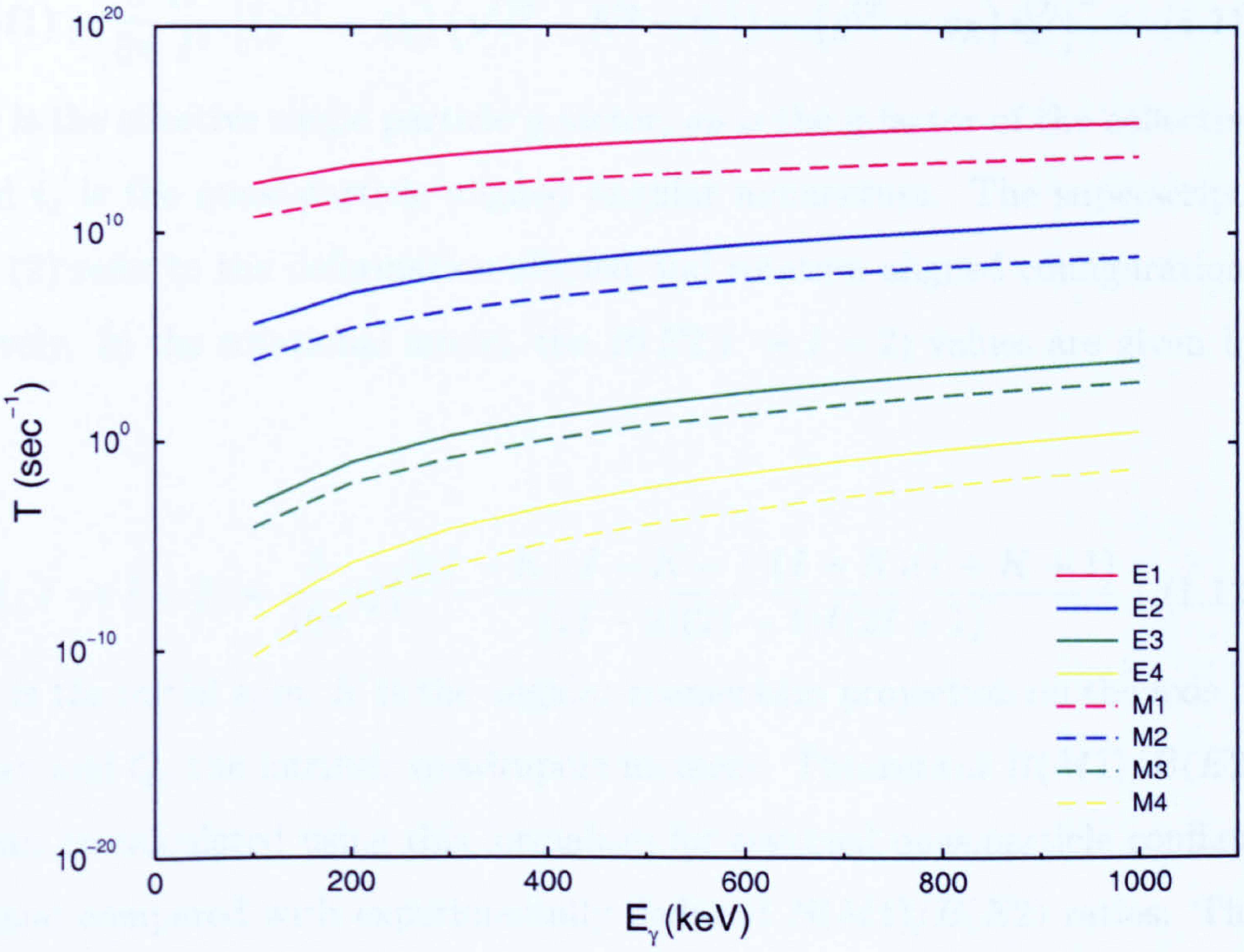

Figure 1.1: Single particle or Weisskopf estimates for A=112, as a function of γ-ray energy and differing transition multipolarity.

1.2.2 Collective Transition Rates

The collective transition probabilities for rotational nuclei have been deduced by Bohr and Mottelson [24]. In this work, it is the $M1$ and $E2$ transition probabilities that are of importance. These can be obtained by analysis with the Dönau formalism [25], a simplified geometrical model that can be used to estimate the $B(M1)$ values for a multi-quasiparticle band. For bands with no signature splitting, the $B(M1)$ values can be estimated (in units of μ_N^2) by [25]

$$B(M1) = \frac{3}{8\pi}\frac{K^2}{I^2}\left[\left(g^{(1)} - g_R\right)\left(\sqrt{I^2 - K^2} - i_x^{(1)}\right) - \left(g^{(2)} - g_R\right) i_x^{(2)}\right]^2 \qquad (1.11)$$

where g is the effective single particle g-factor, g_R is the g-factor of the collective core and i_x is the quasi-particle aligned angular momentum. The superscripts (1) and (2) refer to the deformation-aligned and rotation-aligned configurations respectively. In the rotational model, the $B(E2{:}I \rightarrow I-2)$ values are given by [25]

$$B(E2 : I \rightarrow I-2) = \frac{5}{16\pi}Q_0^2\frac{3(I-K)(I-K-1)(I+K)(I+K+1)}{(2I-2)(2I-1)I(2I+1)} \qquad (1.12)$$

where I is the initial spin, K is the angular-momentum projection on the axis of symmetry and Q_0 the intrinsic quadrupole moment. Theoretical $B(M1)/B(E2)$ values can be calculated using this formalism for assumed quasiparticle configurations and compared with experimentally deduced $B(M1)/B(E2)$ ratios. The ratio of the intrinsic magnetic dipole to electric quadrupole moment can be extracted from experimental data using the ratio of reduced transition probabilities B($M1$)/B($E2$) given by [18]

$$\frac{B(M1)}{B(E2)} = 0.697\,\frac{E_2^5}{E_1^3}\,\frac{1}{1+\delta_{E2/M1}^2}\,\frac{I_{\gamma 1}}{I_{\gamma 2}} \qquad (1.13)$$

where $E_{\gamma 1}$ and $E_{\gamma 2}$ are the respective γ-ray energies in MeV corresponding to the $M1$ (ΔI=1) and $E2$ (ΔI=2) transitions, $I_{\gamma 1}$ and $I_{\gamma 2}$ are the experimentally measured gamma-ray intensities for the respective transitions and δ is the $M1/E2$ mixing ratio for the ΔI=1 transition.

1.3 Internal Conversion

Internal conversion is an electromagnetic process that competes with γ emission [26]. In this process, the electromagnetic field of the nucleus interacts with an atomic electron and the energy released by the nuclear decay is transferred to the electron causing it to be ejected from the atom. The electron is released with a kinetic energy equal to the energy difference between the nuclear states minus the atomic binding energy for the electron shell from which it was emitted. Thus the kinetic energy of the conversion electron is given by

$$E_{e^-} = E_\gamma - B.E. \tag{1.14}$$

where E_γ is the energy of the competing γ decay and B.E. is the electron binding energy.

Following the conversion process, the atom is left with a vacancy in one of the electronic shells. This vacancy is filled very rapidly by electrons from higher energy shells, and thus we observe either characteristic X-ray emission or Auger electron emission accompanying the conversion electrons.

The internal conversion coefficient, α, gives the probability of electron emission relative to γ emission

$$\alpha = \frac{\lambda_{e^-}}{\lambda_\gamma} \tag{1.15}$$

where λ_{e^-} is the decay probability due to electron conversion and λ_γ due to γ emission. The total internal conversion coefficient, α_T, is given by the sum of the individual coefficients for each atomic shell

$$\alpha_T = \alpha_K + \alpha_L + \alpha_M + ... \tag{1.16}$$

The total decay probability, λ_T, becomes

$$\lambda_T = \lambda_\gamma(1 + \alpha_T) \tag{1.17}$$

The internal conversion coefficients for electric (E) and magnetic (M) multipoles may be calculated using the following expressions [27]

$$\alpha_{EL} \approx \frac{Z^3}{n^3}\left(\frac{L}{L+1}\right)\left(\frac{e^2}{4\pi\epsilon_0\hbar c}\right)^4\left(\frac{2m_ec^2}{E_\gamma}\right)^{L+\frac{5}{2}} \tag{1.18}$$

$$\alpha_{ML} \approx \frac{Z^3}{n^3}\left(\frac{e^2}{4\pi\epsilon_0\hbar c}\right)^4\left(\frac{2m_ec^2}{E_\gamma}\right)^{L+\frac{3}{2}} \tag{1.19}$$

where Z is the atomic number, n is the principal quantum number of the electron shell, L is the multipolarity of the transition and E_γ is the transition energy.

It can be seen from inspection of equations 2.10 and 2.11 that internal conversion depends on E_γ, Z and λL (multipolarity). This dependence is shown in figure 1.2 where α_T is plotted for $_{49}$In isotopes as a function of transition energy and multipolarity.

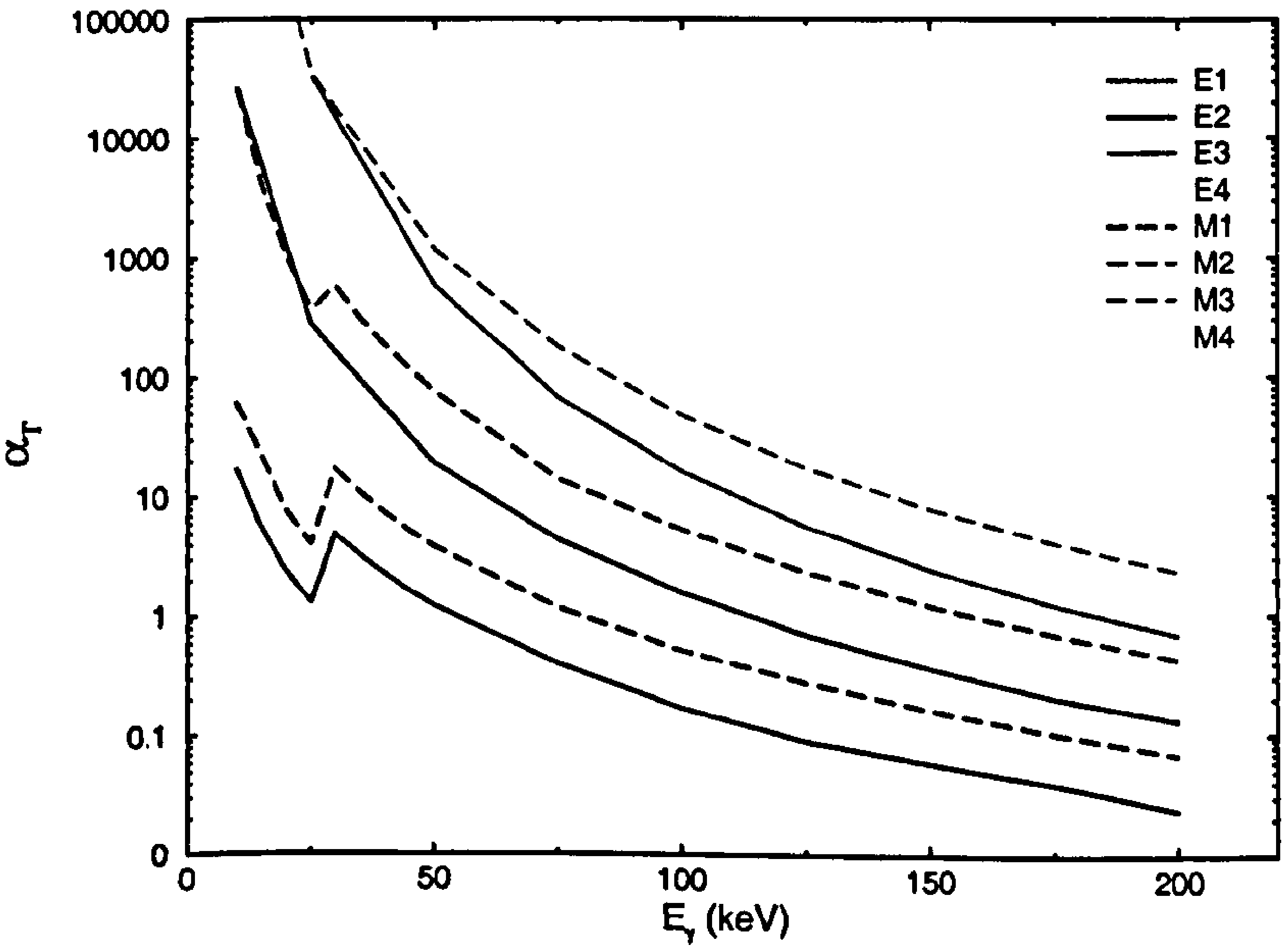

Figure 1.2: Theoretical internal conversion coefficients for K-shell electrons as a function of transition energy and for Z=49 isotopes.

1.4 Characteristic X-Rays

If orbital electrons are excited to higher energy states, after a short time (~10^{-9} s) the atomic electrons will rearrange themselves to the atomic ground state. As the electrons drop from one shell to a more bound orbital, energy is released in the form of X-rays which are characteristic of the atomic number of the material. If a vacancy is created in the K shell of an atom (the most bound or 1s orbital), then when this is filled by an electron from a higher shell, a K X-ray will be emitted. If the electron drops from the L shell to the K shell, a K_α X-ray will be emitted with an energy E(K_α) given by

$$E(K_\alpha) = E_L - E_K \tag{1.20}$$

If the filling electron originated in the M shell, then a K_β X-ray is emitted with an energy given by

$$E(K_\beta) = E_M - E_K \tag{1.21}$$

If the K shell is filled by a free or unbound electron, the maximum photon energy will be equal to the binding energy of the K shell orbital. Vacancies created in the outer shell caused by electrons dropping down and filling the K shell are subsequently filled by electrons from even higher levels. In this way, characteristic L, M etc. X-rays are also emitted.

Since they have the highest energy and the highest yield, the K-series X-rays are the most important. The energy of the characteristic K shell X-rays varies rapidly with atomic number (~Z^2).

The yield of X-ray photons is reduced by the Auger effect, an effect that occurs when the energy liberated by an electron filling a lower shell causes the ejection of another outer-shell electron. The fluorescence yield (ω) is the ratio of X-ray photons emitted from a given shell to the number of vacancies created in that shell. Since production of Auger electrons is the only other competing process, the fluorescence yield for the K shell can be defined as [26]

$$\omega_K = \frac{X_K}{(X_K + A_K)} \tag{1.22}$$

where X_K is the number of emitted X-ray photons of the K series, and A_K is the number of emitted K Auger electrons.

1.5 Magnetic Moments and g–factors

The magnetic dipole moment μ, is defined classically as

$$\mu = \frac{e}{2m} l \tag{1.23}$$

where l is the classical angular moment mvr. Quantum mechanically, l can be replaced by the expectation value relative to the axis where it has a maximum projection, which is $m_l \hbar$ with m_l=+l. Thus

$$\mu = \frac{e\hbar}{2m} l \tag{1.24}$$

where l is the angular momentum quantum number of the orbit.

The quantity $e\hbar/2m$ is called a *magneton.* Putting in the proton mass defines the *nuclear magneton,* μ_N. Equation 1.24 can be rewritten as

$$\mu = g_L l \mu_N \tag{1.25}$$

where g_L is the *g-factor* associated with the orbital angular momentum l and allows for cases when charge and mass distributions do not coincide.

To account for the intrinsic spin of protons and neutrons, the following equation can also be defined

$$\mu = g_s s \mu_N \tag{1.26}$$

where $s=\frac{1}{2}$ for protons and neutrons, and the quantity g_s is known as the spin g-factor. For a spin$-\frac{1}{2}$ point particle such as the electron, g_s=2. The proton and neutrons have measured intrinsic magnetic moments of μ=+2.79 μ_N and μ=−1.91 μ_N respectively, resulting in spin g-factors of g_s=+5.58 for a proton and g_s=−3.82 for a neutron. These values are far from the expected value of 2 for a point particle, and are evidence that protons and neutron are not elementary particles, but have an internal structure of quarks, the motion of which generate the observed spin magnetic moments.

In nuclei, the pairing force favours the coupling of nucleons so that their orbital angular momentum and spin angular each add to zero. Thus the paired nucleons do not contribute to the magnetic moment, and only the valence nucleons need be considered. In the case of odd-A nuclei, the Schmidt model [28] gives an estimate of the values of g-factors for pure, single nucleon states moving in shell model orbits, independent of the nuclear core. For a single, independent nucleon, the single particle magnetic dipole moment μ, can be calculated using the expression [29]

$$\mu = \frac{g_L\left[l(l+1) + j(j+1) - s(s+1)\right] + g_s\left[s(s+1) + j(j+1) - l(l+1)\right]}{2(j+1)} \tag{1.27}$$

Substituting $j = l \pm s$ and $s = \frac{1}{2}$, the Schmidt values for g-factors for pure protons and neutrons can be calculated [30]. For spherical shell model orbitals where $j = l + \frac{1}{2}$

$$\mu\left(j = l + \frac{1}{2}\right) = \left[\left(j - \frac{1}{2}\right) g_L + \frac{1}{2} g_s\right] \mu_N \tag{1.28}$$

and for orbitals with $j = l - \frac{1}{2}$

$$\mu\left(j = l - \frac{1}{2}\right) = \frac{j}{j+1} \left[\left(j + \frac{3}{2}\right) g_L - \frac{1}{2} g_s\right] \mu_N \tag{1.29}$$

where g_L and g_s are the free-nucleon g–factors for the orbital and spin parts respectively.

It is noticeable that many measured magnetic moments have values that fall within the Schmidt limits. As the intrinsic component of the magnetic moment depends on the charge and current distributions within the nucleon, then in the presence of other nucleons, the charge distribution of the interacting nucleons is affected, thus changing the intrinsic moment when the nucleon is bound to other nucleons to form a nucleus. The empirical data suggest that the g_s-factor needs to be attenuated by a factor of approximately 0.7 to account for the fact that the odd nucleon is not free, but is included in the nuclear medium.

In reality, most nuclear states are not pure single particle states but superpositions of a number of different configurations which are mixed together. A measurement of the magnetic dipole moment can be used to infer the underlying single particle structure and purity of such a state on account of the great difference between the g-factors associated with the various components of the total nuclear angular momentum.

Chapter 2

Nuclear Structure

2.1 The Nuclear Shell Model

In atomic physics, the shell model proved successful in providing an explanation for the details of atomic structure. Atomic shells were filled with electrons in order of increasing energy subject to the Pauli exclusion principle. As a result of the success of the atomic shell model, this model was extended to the realm of nuclei [31]. The shell model, also known as the independent particle model, treats the nucleons individually as opposed to treating the nucleus as a whole, such as in the liquid drop model. The long range repulsive Coulomb force and the short range strong attractive nuclear force interactions between nucleons are replaced by an average force, or mean-field. The shell model describes the nucleons in terms of groups of orbitals or shells, with the excitation energy of a nucleon dependent upon its quantum numbers.

In atomic structure the potential is provided by the Coulomb field of the nucleus, whereas in the nuclear case the motion of a single nucleon is governed by an average potential generated by all the other nucleons. If two nucleons collided, the energy required to excite one of them to a higher-lying orbit would be more than the nucleons are likely to transfer. Therefore, in the nuclear case it is assumed that there are no nucleon-nucleon collisions and each nucleon moves in an unperturbed single particle orbit within the nucleus. The spherical independent particle shell model Hamiltonian can be represented by

$$H = \sum_{i=1}^{A} \left[-\frac{\hbar^2}{2m} \nabla_i^2 + V(r_i) \right] \tag{2.1}$$

where the first term represents the kinetic energy of the individual nucleons and the second term represents the potential.

In order to determine the potential correctly, the differences between the nucleons at the centre and those at the surface must be taken into account. Nucleons at the centre of the nucleus experience the nuclear forces uniformly, where as nucleons at the surface experience a large force towards the centre. There are several potentials available to model the nuclear potential, these include the square well, the harmonic oscillator and the Woods-Saxon [32] potentials. The square well potential is an oversimplification as it does not approximate the shape of nuclear matter, which requires a charge distribution varying smoothly to zero. With the addition of the spin-orbit interaction (see section 2.1.1), the Woods-Saxon potential produces the correct magic numbers.

2.1.1 The Spin-Orbit Interaction

The spin-orbit term [31] arises from a coupling between the intrinsic angular momentum s, and orbital angular momentum l, of the individual nucleons, such that $j{=}l{+}s$. The energy levels of each j-shell are $2j{+}1$ degenerate, labelled by m_j. A single nucleon has $s{=}\pm\frac{1}{2}$, therefore a spin-orbit splitting of the levels occurs with values $j{=}l{\pm}\frac{1}{2}$.

The nature of the spin-orbit coupling causes high-j orbitals to be lowered in energy, resulting in the correct magic numbers being obtained. When one of these orbitals appears in a shell lower than it would have been without the spin-orbit term, it is called an "intruder" or unique parity orbital since its parity differs from the other orbitals in that shell. This model can explain many features of spherical nuclei but needs modifying to describe nuclei with many nucleons outside closed shells. The residual interactions between these many valence nucleons may be more simply described in terms of deformed potentials.

2.2 Deformation

For nuclei to rotate they must be non-spherical so that they have a preferred axis of rotation. For deformed nuclei, assuming a constant nuclear volume (i.e. incompressibility), the nuclear radius can be parameterised by [27]

$$R(\theta,\phi) = R_{av}\left[1 + \sum_{\lambda=2}^{\infty}\sum_{\mu=-\lambda}^{\lambda} \alpha_{\lambda\mu} Y_{\lambda\mu}(\theta,\phi)\right] \tag{2.2}$$

where $\alpha_{\lambda,\mu}$ are the coefficients of the spherical harmonics $Y_{\lambda\mu}(\theta,\phi)$. The λ=1 terms are normally excluded from the sum as these correspond to a translation of the centre-of-mass. The parameters λ and μ determine the surface coordinates as functions of θ and ϕ respectively. For instance, for spheroidal nuclei

$$R(\theta,\phi) = R_{av}\left[1 + \beta_2 Y_{20}(\theta,\phi)\right] \tag{2.3}$$

which is independent of ϕ. This means that such nuclei are axially symmetric, either oblate or prolate. The deformation parameter β_2 (=α_{20}), can be related to the axes of the spheroid by [27]

$$\beta_2 = \frac{4}{3}\sqrt{\frac{\pi}{5}}\frac{\Delta R}{R_{av}} \tag{2.4}$$

in which the average radius is given by $R_{av} \simeq R_0 A^{1/3}$, and ΔR is the difference between the semi-major and semi-minor axes. The larger the value of β_2 the more deformed the nucleus. Positive and negative values of β_2 correspond to prolate ("rugby ball") and oblate ("frisbee") shapes respectively. Higher order axially symmetric effects have also been observed in nuclei, such as hexadecupole deformations quantified by β_4.

Quadrupole deformations can give rise to asymmetric shapes. These triaxial distortions are governed by the γ shape degree of freedom, and this describes a stretching or squashing effect at right angles to the major nuclear axis. The γ deformation parameter is related to the $\alpha_{\lambda\mu}$ coefficients as follows [33]

$$\alpha_{20} = \beta_2 \cos\gamma \tag{2.5}$$

$$\alpha_{22} = \alpha_{2-2} = \frac{1}{\sqrt{2}}\beta_2 \sin\alpha \tag{2.6}$$

The γ deformation parameter ranges between 0° to 60° corresponding to prolate and oblate shapes respectively. A completely triaxial nucleus has γ=30°.

2.2.1 Nilsson Model

The model that describes axially symmetric nuclei is called the Deformed Shell Model [34]. In this model the Schrödinger equation is solved using a deformed anisotropic harmonic oscillator potential that is parameterised with the deformation parameter β_2. The calculated states (called Nilsson orbitals) are defined with the following quantum numbers Ω^π $[Nn_z\Lambda]$, where Ω^π is the projection of the angular momentum onto the symmetry axis, N is the total oscillator shell quantum number and determines the parity as $(-1)^N$, Λ is the projection of the particle orbital angular momentum l on the symmetry axis and n_z is the number of oscillator shell quanta along the direction of the symmetry axis.

A result of the deformation is that the orbital angular momentum l, and intrinsic spin s, are no longer good quantum numbers and thus states with different l values (but the same parity) can mix. The energy of the state now depends on the component of the angular momentum along the symmetry axis, Ω. For each orbital with angular momentum j, there are $2j+1$ values of Ω ($=m_j$ in the absence of other couplings). However, levels with $+\Omega$ and $-\Omega$ have the same energy due to the reflection symmetry of axially symmetric nuclei, so each state is now doubly degenerate, i.e. 2 particles can be placed in each state. For example the $i_{13/2}$ orbital can have $|\Omega|$ equal to 13/2, 11/2, 9/2, 7/2, 5/2, 3/2 and 1/2. The ordering of these Ω levels depends on the particular shape of the nucleus, since the lowest in energy is the orbital which interacts (or overlaps) the most with the nuclear core. For prolate nuclei the states with the lowest Ω values are the most tightly bound whereas for oblate nuclei, the highest Ω orbitals occur lowest in energy.

2.2.2 Pairing

The pairing interaction is an attractive force that occurs between identical nucleons in the same orbit. The interaction is such that the energy of the configuration for the two nucleons is much lower in energy than any other. The existence of pairing correlations in the nucleus is well supported by experimental evidence. Some examples are given below:

- The ground-state spin of all even-even nuclei is $0\hbar$, which suggests that there is a force that acts to couple nucleons pairwise such that their the angular momenta cancel out.

- The energy of the first excited non-collective state is much higher (above 1 MeV) in even-even nuclei than in odd-mass nuclei.
- The ground-state spin of odd-mass nuclei is determined by the spin of the last nucleon, which is unpaired.
- The measured moments of inertia of nuclei are much less than rigid-body values, suggesting that the nucleus may behave like a "superfluid".
- The masses of even-even nuclei, when compared to their odd-mass neighbours, are much lower. This suggests that the gain in binding energy is much larger when a nucleon is added to an odd-mass nucleus than when a nucleon is added to an even mass nucleus.

Thus, in the ground state of an even-even nucleus, all the nucleons are coupled pairwise, such that total angular momentum is $0\hbar$. The strength of the pairing interaction G, is larger for high-j orbits and is dependent upon the spatial overlap of the two nucleons. The strength therefore decreases with mass, since in heavier nuclei the outer nucleons are further apart. The strength is also lower for protons than for neutrons, due to the effect of Coulomb repulsion. The strength can be estimated from the following equations [35].

$$G_p = \frac{17}{A} MeV \qquad G_n = \frac{23}{A} MeV \tag{2.7}$$

Pairing and the Fermi Surface

The pairing interaction not only couples pairs of nucleons in state j to J^π=0^+, but also to J^π=0^+ states composed from two nucleons in a different j state, j'. The effect of this is that pairs of nucleons in an orbit j, coupled to J^π=0^+, can be "scattered" into another orbit, j', as a pair, still with $J^{\pi}=0^{+}$. Far below the Fermi surface the Pauli principle forbids such scattering to occur since the orbits above j are filled. This is how it is possible to consider independent particle motion in an object as dense as the nucleus. However, near to the Fermi surface where there is some probability that orbits are not occupied, this scattering can occur. The scattering results in a "smearing" of the Fermi surface. In the absence of pairing, orbits would simply be filled sequentially in accordance with the Pauli principle until all A nucleons has been placed in the lowest orbits, giving a sharply defined Fermi surface. The smearing of the Fermi surface leads to the concept of *quasiparticles* which can be considered as a linear combination of particle and hole wavefunctions.

2.3 Angular Momentum Generation

A nucleus can generate angular momentum in two different ways, either via collective excitations such as rotations and vibrations, or by few-nucleon excitations in which a small number of unpaired nucleons couple together to generate the angular momentum [36]. In practice most states are a combination of these two extreme modes.

2.3.1 Nuclear Rotation

An important consequence of deformation is the fact that rotational motion is a possible mode of excitation. This is due to the fact that a perfect sphere has no preferred direction in space against which a change in orientation can be measured, so quantum mechanically it cannot rotate. For a quantum system to rotate, the spherical symmetry in space must be broken. In the case of an axially-symmetric nucleus, there is a set of axes of rotation, perpendicular to the symmetry axis. The rotational angular momentum **R** is generated by the collective motion of many nucleons about this axis. Additional angular momentum can be generated by the intrinsic angular momentum of any valence nucleons **j**. Classically, the energy of a rotor is given by

$$E = \frac{1}{2}\mathcal{J}\omega^2 \tag{2.8}$$

where $\mathcal{J}$ is the moment of inertia of the system and

$$\omega = \frac{I\hbar}{\mathcal{J}} \tag{2.9}$$

where ω is the angular frequency and I is the angular momentum. Combining these two equations implies for the quantum mechanical case (when K=0)

$$E = \frac{\hbar^2}{2\mathcal{J}^{(0)}}[I(I+1)] \tag{2.10}$$

Here $\mathcal{J}^{(0)}$ represents the static moment of inertia. It should be noted that the nucleus, however, is not a rigid body, and measured moments of inertia are somewhat less (30 to 50%) than rigid body values at low spin [37]. This is due to the effects of the pairing interaction, which make the nucleus behave like a superfluid. Experimental moments of inertia are also larger than those calculated for the rotation of a superfluid, showing that the nucleus is somewhere between these two extremes.

By increasing I, the following expected excitation energies of an even-even nucleus can be achieved:

- $E(2^+)=6\frac{\hbar^2}{2I}$
- $E(4^+)=20\frac{\hbar^2}{2I}$

From these values it can be seen that the limit of the ratio of the 4^+ to 2^+ energy levels for rotational nuclei is 3.33. Therefore a comparison of the ratio of the 4^+ to 2^+ energy levels can give an indication as to the nature of the nucleus in question. In the nuclear realm nuclei tend to vary smoothly from rotational motion at mid shell to vibrational near the closed shell.

For nuclei with an unpaired valence nucleon, the intrinsic angular momentum of the valence nucleon is non-zero and two extreme limits of the nucleon-core coupling may be defined depending on the relative effects of core deformation and the strength of the Coriolis interaction. The valence nucleon is either (strongly) coupled to the deformation axis (deformed aligned limit - DAL) or (weakly) coupled to the rotation axis (rotation aligned limit -RAL).

Ground State $j-j$ Coupling in Odd-Odd Nuclei

The Gallagher–Moszkowski coupling rules [38] point out that the ground-state spins of a variety of odd-odd nuclei can be accounted for on the basis of a $j-j$ coupling model plus some simple controlling rules for coupling the angular momentum of the last proton and neutron. These rules are

$$I = j_p + j_n \quad if \quad j_p = l_p \pm \frac{1}{2} \quad and \quad j_n = l_n \pm \frac{1}{2} \tag{2.11}$$

$$I = |j_p - j_n| \quad if \quad j_p = l_p \pm \frac{1}{2} \quad and \quad j_n = l_n \mp \frac{1}{2} \tag{2.12}$$

where j_p and l_p (or j_n and l_n) represent the total and orbital angular momentum of the odd proton (or neutron).

2.3.2 The Cranked Shell Model

The cranked shell model was introduced by Inglis [39] and was further developed by Bengtsson and Franendorf [40]. The model gives a microscopic description of the influence of rotation on single-particle motion. A rotation is externally imposed on a nuclear potential, around an axis perpendicular to the symmetry axis, at a fixed rotational frequency and is treated classically. The nucleons can then be described as independent particles moving in a rotating potential.

Using a simple rotational model, the rotational frequency ω, for a transition between states of I+1 and I−1, with projections along the symmetry and rotation axes of K and I_x respectively, is given by [40]

$$\omega = \frac{dE(I)}{dI_x(I)} \approx \frac{E(I+1) - E(I-1)}{I_x(I+1) - I_x(I-1)} \tag{2.13}$$

The value of K is taken as the spin of the bandhead and the difference in the excitation energies $E(I+1) - E(I-1)$ is simply E_γ. The value of I_x can be calculated using Pythagoras theorem, such that

$$I_x(I) = \sqrt{I(I+1) - K^2} \approx \sqrt{\left(I + \frac{1}{2}\right)^2 - K^2} \tag{2.14}$$

Substituting into expression 2.13 for ω gives

$$\omega \approx \frac{E_\gamma}{\sqrt{(I+\frac{3}{2})^2 - K^2} - \sqrt{(I-\frac{1}{2})^2 - K^2}} \tag{2.15}$$

for decays from a state of spin I+1 to one of I−1. At high spins where $I >> K$, this expression simplifies to $\omega \approx \frac{E_\gamma}{2}$.

The quasiparticle aligned angular momentum i_x, is the spin generated by the valence quasiparticles along an axis perpendicular to the axis of symmetry. It can be approximated by taking the total angular momentum and subtracting a fixed amount of spin due to the rotational motion of the core. The quasiparticle aligned angular momentum i_x is a function of rotational frequency and can be defined by

$$i_x(\omega) = I_x(\omega) - I_{ref}(\omega) \tag{2.16}$$

where I_x is the projection of the total angular momentum along the axis of rotation and can be calculated using expression 2.14 and I_{ref} is the reference angular momentum of the core, which is subtracted and is calculated in terms of Harris parameters [41], such that

$$I_{ref} = \left(\mathcal{I}_{(0)} + \mathcal{I}_{(2)}\omega^2\right)\omega \tag{2.17}$$

The Harris parameters are usually fitted to states in the band to give a constant alignment above the first band crossing.

Moments of Inertia

A rotating nucleus can be described in terms of its angular rotational frequency ω. classically, this is given as

$$\omega = \frac{dE}{dI} \tag{2.18}$$

The quantum-mechanical analogue of this is given by

$$\hbar\omega = \frac{dE(I)}{dI_x(I)} \tag{2.19}$$

Rotational energy spectra can be discussed in terms of two spin-dependent moments of inertia, which are related to the first- and second-order derivatives of the excitation energy with respect to the aligned angular momentum, I_x. The first order derivative is the *kinematic moment of inertia* [36],

$$\mathcal{I}^{(1)}(I) = I_x \left(\frac{dE}{dI_x}\right)^{-1} \hbar^2 = \hbar \frac{I_x}{\omega} \tag{2.20}$$

The kinematic moment of inertia can be related to the transition energy E_γ, through equation 2.10. For a rotational band,

$$E_\gamma = \frac{\hbar^2}{2\mathcal{I}^{(1)}} 4(I-2) \tag{2.21}$$

The second order derivative is the *dynamical moment of inertia* [36]

$$\mathcal{I}^{(2)}(I) = \left(\frac{d^2E}{dI_x^2}\right)^{-1} \hbar^2 = \hbar \frac{dI_x}{d\omega} \tag{2.22}$$

The dynamical moment of inertia can be related to the difference in transition energy of consecutive γ rays by [36]

$$\Delta E_\gamma = \frac{4\hbar^2}{\mathcal{I}^{(2)}} \tag{2.23}$$

Thus, if the dynamical moment of inertia were a constant, the transition energy difference would be the same for all values of spin. Often this is not true and $\mathcal{I}^{(2)}$ is found to increase with increasing spin.

2.3.3 Rotational Alignments

At low frequencies, the yrast band (the lowest energy configuration for a given spin) is built upon the ground state configuration. With increasing rotational frequency, the excitation of the first excited band may be lowered with respect to that of the ground-state band, until at some frequency at which it becomes energetically unfavourable. This band crossing results from the Coriolis force acting upon two valence nucleons in time-reversed orbits. The Coriolis force acts in opposite directions for each nucleon in the pair, and at the critical frequency can overcome the pairing correlations and break the pair. The phenomenon is characterized by a sudden increase in the moment of inertia, along with a decrease in rotational frequency. Thus, in a plot of the moment of inertia against the square of the rotational frequency, the moment of inertia bends back and up, hence the name backbending.

Blocking

If two quasiparticle states approach each other at a given rotational frequency, then at this point the Coriolis force is sufficient to overcome the pairing force and a band crossing occurs. If an odd quasiparticle already occupies one of the interacting levels then this quasiparticle blocks this orbital, which cannot take place in an alignment process.

2.3.4 The Shears Mechanism

The conventional concept of nuclear rotation is based on the existence of a deformed mass distribution of the nucleus. Regular rotational bands are commonly interpreted as arising from the coherent collective rotation of many nucleons about an axis perpendicular to the symmetry axis [42]. The energy levels that are formed depend on the spin I according to $E \propto I(I+1)$ (as described in section 2.3.1) and are connected by electric quadrupole ($E2$) transitions [43]. In the early 1990 s, a new type of rotational band consisting of magnetic dipole ($M1$) transitions in the nearly spherical light-Pb isotopes around A=200 [44, 45, 46, 47] were discovered. Subsequent experiments identified similar bands in other groups of nuclei, as summarized in references [48, 49] and in numerous review articles [1, 2, 50, 51].

This new type of rotational band contradicts the intuitive idea that only nuclei with deformed mass distributions show rotational-like bands. Regular bands may appear if the quantal system deviates from rotational symmetry with respect to the angular momentum vector. For the well known rotational bands of deformed nuclei, it is the charge density that deviates from the rotational symmetry. The associated quadrupole moment defines a rotational angle and generates the enhanced $E2$ radiation. In the case of bands consisting of sequences of $M1$ transitions, it is a large magnetic dipole moment with a large component perpendicular to the total nuclear angular momentum that specifies a direction. The magnetic dipole rotates around the total angular momentum axis, generating the strong $M1$ radiation. Thus quantal rotation manifests itself not only as in the familiar form of "electric rotation", but also as "magnetic rotation". However, these bands are puzzling in that their intrinsic structures have very small quadrupole deformations [52, 53].

For these nuclei, the current loops of the valence nucleons break the isotropy as illustrated in figure 2.1. It is these loops that generate the magnetic dipole vector that rotates and produces the strong $M1$ transitions. Large perpendicular magnetic dipole moments appear when high-j proton holes are coupled to high-j neutrons (or vice-versa). The high-j orbitals have toroidal density distributions, which are illustrated in figure 2.1 by the two loops. The interaction between the particles and the holes is repulsive and favours an angle of 90° at the bandhead (which can be proven by measurements of the g-factor at the bandhead [54]). Along the band, the total angular momentum is increased by gradually aligning the vectors $\mathbf{j}_\pi$ and $\mathbf{j}_\nu$. The gradual aligning of the two vectors in this way resembles the closing of the blades of a pair of sheep shears that have a spring to keep them open, and hence this process has been dubbed the "shears mechanism"

[45]. Closing the blades of the shears increases the energy because the loops are aligning. If the two blades are long it takes many steps (increments of J by $1\hbar$) until the shears are closed.

These sequences of $M1$ transitions have now been termed as "magnetic dipole" or "magnetic rotational" bands [55] and a solution of this apparent paradox has been given in the framework of the tilted axis cranking (TAC) model [3]. Figure 2.2 illustrates the generation of the $M1$ bands as predicted by the TAC model. The total angular momentum is generated almost entirely by the recoupling of the proton and neutron vectors, $\mathbf{j}_\pi$ and $\mathbf{j}_\nu$. Near the bandhead, $\mathbf{j}_\pi$ is nearly parallel to the symmetry axis, whilst $\mathbf{j}_\nu$ is approximately perpendicular to it. The total angular momentum vector $\mathbf{J}$, then lies along a tilted axis at an angle θ with respect to the symmetry axis. Higher angular momentum states are generated by aligning $\mathbf{j}_\pi$ and $\mathbf{j}_\nu$ along the direction of $\mathbf{J}$ with θ remaining approximately constant. When this happens, the perpendicular component of the magnetic moment μ_{perp} becomes shorter, and the decrease of the $B(M1)$ values with increasing angular momentum is an inevitable consequence of the shears mechanism. Only a small component of the total angular momentum $\mathbf{R}$, is from collective rotation.

Features common to magnetic rotational bands [1, 2, 50, 51] are that they consist of regular 'rotational-like' sequences of γ-rays (in the absence of band crossings) and that they display both strong $B(M1)$ transition strengths ($\sim$2$-$10 μ_N^2) and small B($E2$) values ($\sim 0.1e^2b^2$) resulting in large ($> 20(\mu_N/\text{eb})^2$) $B(M1)/B(E2)$ ratios. Measurements of the lifetimes of states in these bands can directly test the behaviour of the reduced transition strengths predicted by the shears mechanism and such measurements have confirmed the decreasing $B(M1)$ strength with increasing angular momentum in several cases in the $A{\sim}110$ mass region [4, 5, 6]. Another criterion for associating a band with the shears mechanism is the ratio of the $\mathcal{J}^{(2)}$ dynamic moment of inertia to the B($E2$) strength. this ratio is predicted to be large (>100 MeV^{-1}e^{-2}b^{-2}), an order of magnitude larger than the value for well-deformed bands [50]. This is a consequence of the angular momentum originating from the closing shears blades, as opposed to a collective core. However, in the regime of weak pairing and small deformation this ratio may still be large [24]. Therefore, the large $\mathcal{J}^{(2)}$/B($E2$) ratio should not be viewed as a sufficient condition for the shears mechanism [15].

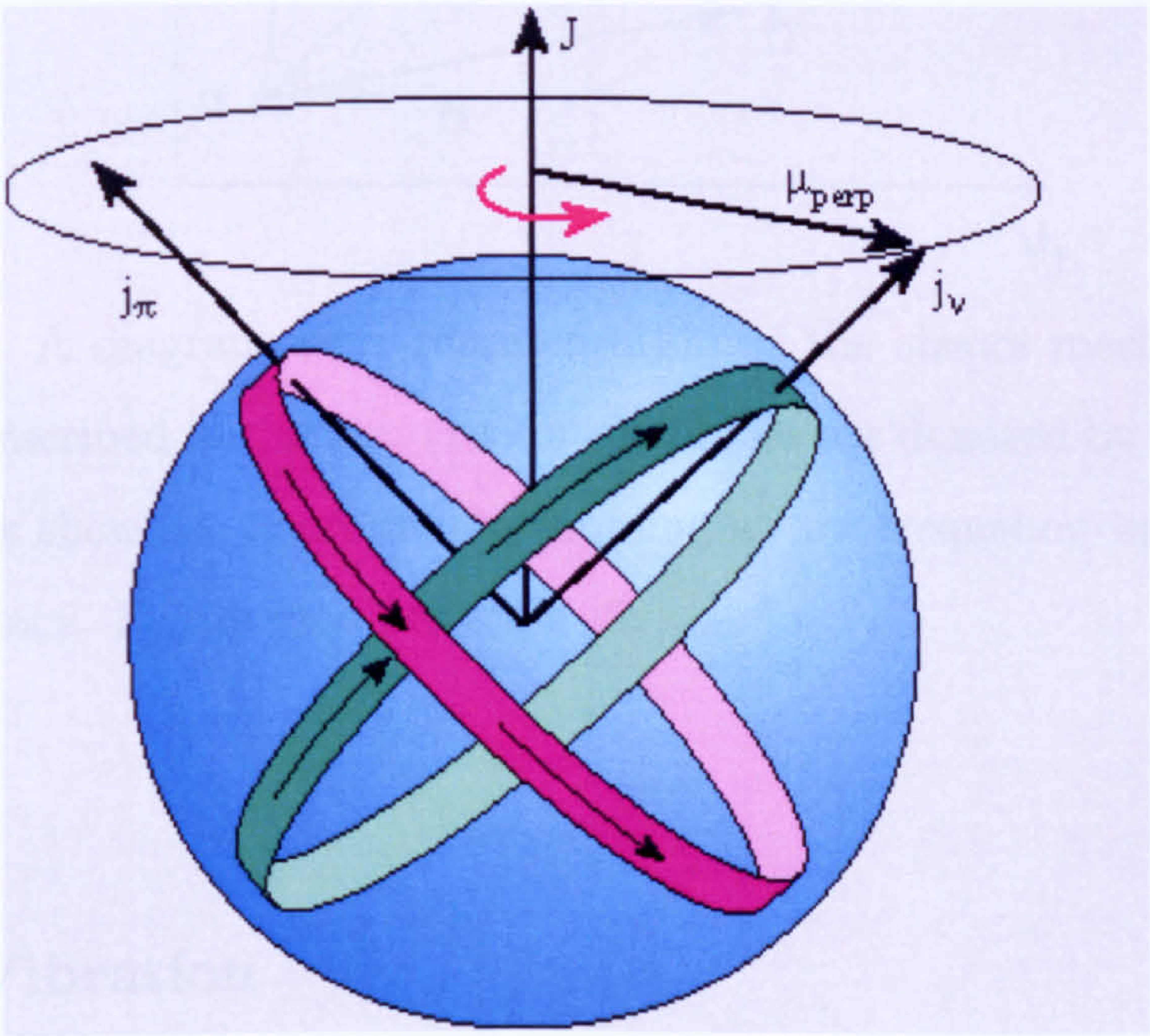

Figure 2.1: A schematic representation of the shears mechanism. The few protons and neutrons that take part in the shears mechanism form current loops embedded in the spherical mass distribution of the nucleus. These current loops enable angular momentum vectors $\mathbf{j}_\pi$ and $\mathbf{j}_\nu$ to be defined for the active protons and neutrons. The total angular momentum **J** is along the axis about which the near-spherical nucleus can rotate. The strong $M1$ radiation results from the rotation of the large magnetic dipole vector μ_{perp}, about the total spin vector **J**. Figure taken from [1]

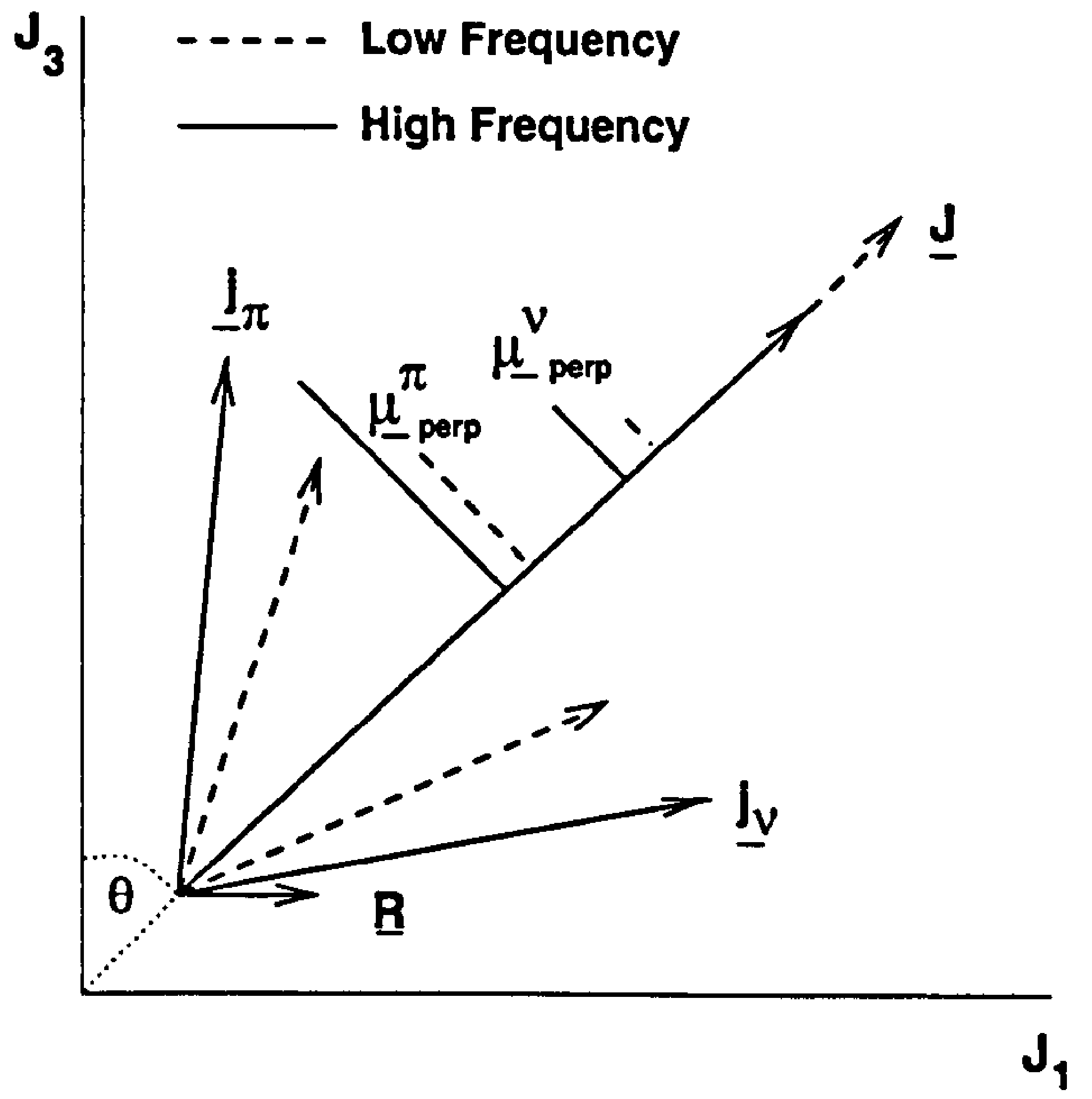

Figure 2.2: A diagrammatic representation of the shears mechanism. The labelling is described in the text (vector quantities are denoted by underbars). The solid arrows show the approximate coupling at low frequency, and the dashed at high frequency. Figure modified from [52]

2.3.5 Vibration

Another way in which nuclei can generate collective angular momentum is by vibrating around a spherical (or deformed) equilibrium shape [24]. In this case, vibrational quanta called phonons, of multipolarity λ, carry the energy. Dipole (λ=1) vibrations correspond to translations of the centre of mass of the nucleus and therefore cannot be produced by internal forces if the protons and neutrons move together. Phonons of λ=2 produce low-energy quadrupole vibrations which can take two forms. The first, β vibrations, are shape oscillations directed along the symmetry axis. A second type of quadrupole vibration produces oscillations in the γ shape parameter. Octupole vibrations are associated with λ=3 phonons, and hexadecupole vibrations with λ=4.

For quadrupole vibrations, which carry $2\hbar$, the vibrational energy need to create the first quadrupole phonon excitation relative to the ground state energy, is $\hbar\omega$. The addition of a further quadrupole phonon results in a triplet of states due to angular momentum coupling. In an even-even nucleus this results in a triplet of states consisting of 0^+, 2^+, 4^+ at roughly twice the energy of the first 2^+ state.

2.4 Vibrational to Rotational Evolution

Rotational interpretations such as the cranked shell model (CSM) [56] are the mainstream tools in the analysis of yrast states. The application of this model has been successful in interpreting much experimental data, particularly with respect to understanding the microscopical basis behind the phenomenon of backbending [58, 59], which has been explained for rotational deformed nuclei as stemming from a Coriolis-driven particle alignment [60]. In a standard CSM-type analysis, in order to compare the model predictions with experimental data, a rotational approximation is applied and an effective, spin-dependent moment of inertia is extracted. While such a prescription remains valid for well-deformed systems, its use for non-rotational (e.g. vibrational) nuclei may obscure interesting structural effects, such as the transition between vibrational and rotational collective modes as a function of nuclear spin. A new approach, named E-GOS (E-Gamma Over Spin) curves has recently been proposed [17]. This prescription invokes no structural preconceptions and allows vibrational and rotational behaviour, and the transition between the two, to be vividly highlighted.

The gamma-ray energies for a perfect harmonic vibrator are given by

$$E_\gamma(I \rightarrow I-2) = \hbar\omega \tag{2.24}$$

while, for an axially symmetric rotor,

$$E_\gamma(I \rightarrow I-2) = \frac{\hbar^2}{2J}(4I-2) \tag{2.25}$$

The ratio,

$$R = \frac{E_\gamma(I \rightarrow I-2)}{I} \tag{2.26}$$

then provides an effective way of distinguishing axially symmetric rotational and harmonic vibrational modes.

$$vibrator : R = \frac{\hbar\omega}{I} \xrightarrow{I\rightarrow\infty} 0 \tag{2.27}$$

$$rotor : R = \frac{\hbar^2}{2J}\left(4 - \frac{2}{I}\right) \xrightarrow{I\rightarrow\infty} 4\left(\frac{\hbar^2}{2J}\right) \tag{2.28}$$

For the idealized axially symmetric rotor, R increases from $3[\hbar^2\ /2J]$ for I=2, to a constant value of $4[\hbar^2/2\mathrm{J}]$ for large I while, for a pure vibrator, R decreases hyperbolically towards zero.

Figure 2.3 shows these theoretical limits plotted for two schematic nuclei: (i) a vibrator in which the first 2^+ excited state lies at an energy of 500 keV; and (ii) a rotor where this energy is 100 keV. (These values were taken to represent typical nuclear vibrator and rotor energies respectively.) Note that the curvatures of the vibrator and rotor functions are markedly different. The sharp, hyperbolic decrease in R with spin provides a clear signature of a vibrator since, by contrast, for a rotor, R actually increases at low spins. Thus plots of R=$[E_\gamma(I \rightarrow I-2)/I]$

versus I can be a simple prescription for distinguishing rotational and vibrational ranges of spin. The trajectories in such plots are called E-GOS curves.

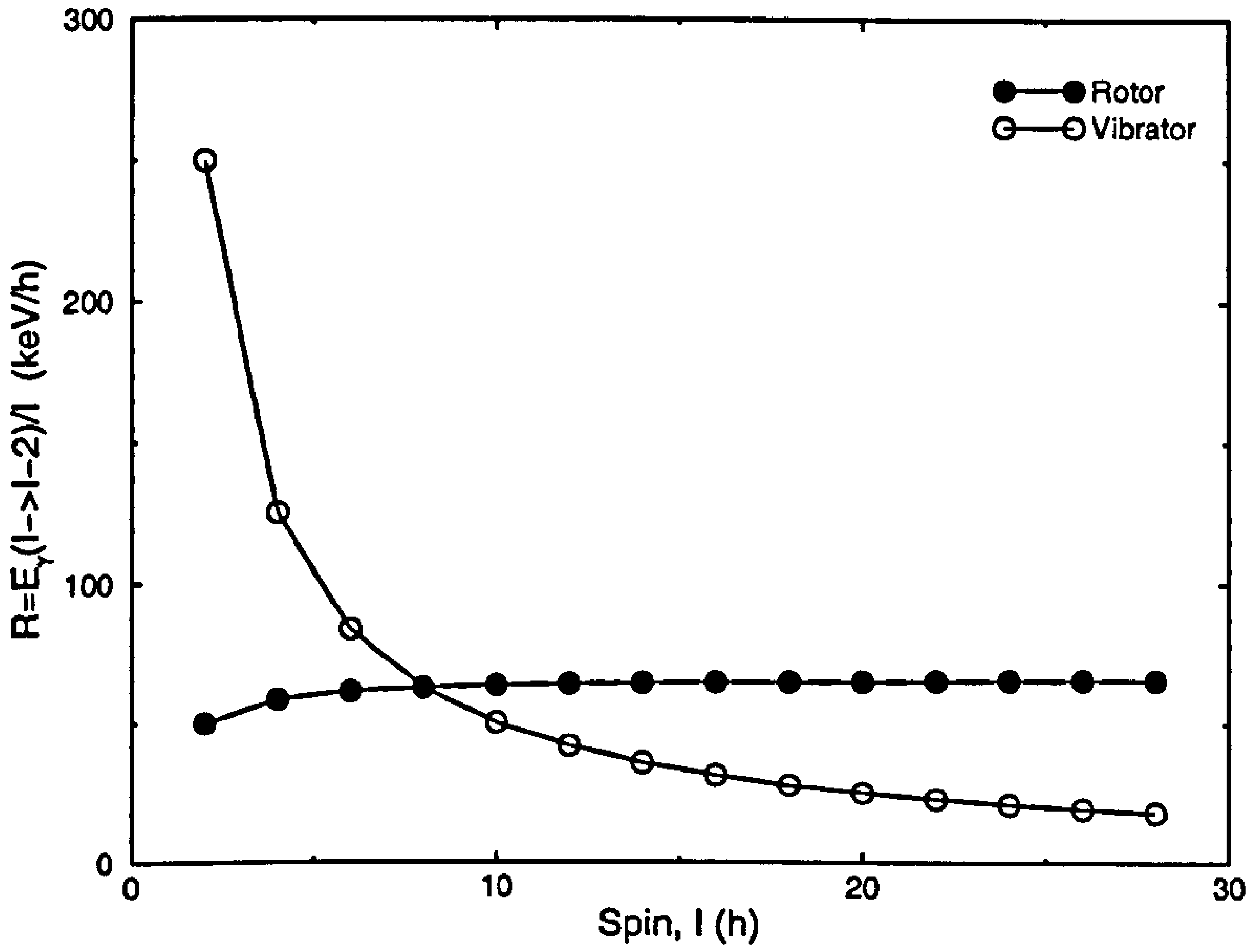

Figure 2.3: Example E-GOS curves for a perfect harmonic vibrator and an axially symmetric rotor with the first 2^+ excitations of 500 and 100 keV respectively.

2.5 Two-Particle Configurations

Practically all microscopic calculations in nuclear structure use a "residual" or "effective" two-body interaction between valence nucleons [35]. As with the energy levels of single nucleons in shell model orbits, it is only if the effects of closed shells can be neglected that the study of multi-nucleon configurations will be applicable to other than the lightest nuclei.

Since a closed shell is spherically symmetric, the interaction of a valence nucleon in the state m_j cannot depend on m, hence, the closed-shell particles have the same effect on all valence nucleons in a given j orbit. In multi-particle configurations, the effects of the closed-shell nucleons are independent of the way that the individual m_j values are coupled to the total J. Therefore, the closed shell can have no effect on the energy differences of these different J states.

In a two-particle configuration, the J values that can result from the coupling of a nucleon in orbit j_1 to a nucleon in j_2 are simply the integer values from $|j_1 - j_2|$ to $|j_1 + j_2|$ if $j_1 \neq j_2$. If the orbits are equivalent, $n_1l_1j_1 = n_2l_2j_2$ it is possible to distinguish two cases – identical and non-identical nucleons. For two identical nucleons in equivalent orbits, the allowed J states range from 0 to $2J-1$. In the non-identical case (proton-neutron), J takes on all integer values from 0 to $2j$ as there is no Pauli principle restriction on the occupation of identical m states.

2.5.1 Residual Interactions

With no residual interaction, all J states of a two-particle configuration are degenerate. In the presence of a residual interaction, the different J states are shifted in energy. A simple δ-function can be used to illustrate the effect of proton-neutron couplings. By definition, this interaction vanishes unless the particles occupy the same spatial position. It is also a short-range interaction, as is the nuclear force and at least qualitatively, a δ-function residual interaction reproduces many observed properties of nuclei. The attractive δ-function interaction can only be large when there is large spatial overlap between the orbits of the particles. For a given j_1 and j_2, the overlap for different J values depends on the orientation of the orbits in space. This concept can be treated semi-classically, by considering the angle θ between the angular momentum vectors $\mathbf{j}_1$ and $\mathbf{j}_2$, and it can be shown that the energy shift of the multiplet is approximately [35]

$$\Delta E(j^2 J) \approx \frac{-V_0 F_R}{\pi} \, tan\frac{\theta}{2} \qquad (T=1,\ J\ even) \tag{2.29}$$

where V_0 is the interaction strength between the two nucleons and F_R is a scaling factor [20]. This result expresses the shifts in different J states for a δ-interaction between two identical particles in equivalent orbits. This equation states that the energy shifts become large (and negative since the force is attractive) for $\theta{\approx}180°$, while the smallest effect occurs when $J{=}J_{max}{\approx}j+j$, since $\theta{\approx}0$.

For proton-neutron configurations, a T=1 p-n system (where T is the isospin), which cannot be distinguished from the T=1 p-p and n-n systems, consists of even J states and is described by equation 2.29 as well. However, in a T=0 p-n system (odd J states), $\Delta E_{pn}(j^2\mathrm{J})$ has a different J dependence. For the odd J, T=0 case it can be shown that

$$\Delta E(j_p j_n J)_{j_p=j_n} = \frac{-V_0 F_R}{\pi} \left(cot\frac{\theta}{2}\right)\left[1+\frac{1}{cos^2\left(\frac{\theta}{2}\right)}\right] \qquad (T=0,\ J\ odd) \tag{2.30}$$

This expression is large for both J_{min} and J_{max} and has a minimum at θ=90°. These features can be understood physically. The interaction should be small for θ=90°, since the particles are orbiting in nearly perpendicular planes and are seldom close enough to interact. For T=1, the interaction is strong when the two particles orbit in opposite directions (J=0, θ=180°). However it vanishes when they orbit in the same direction (J_{max}, θ=0°) since, then, the two particles have identical quantum numbers and the spatial wave function is required to be antisymmetric, and it must vanish if the two nucleons touch. The Pauli principle effectively introduces a short-range repulsion. The only way the particles can orbit in the same direction and yet not touch is if they circulate out of phase at opposite ends of an orbit diameter. This gives an interaction that is small for small θ, but large for large θ. The basic idea is the same for the T=0 case. Here, the particles can be treated as distinct, and for both the small and large J extremes, the orbits are nearly coplanar. There is no restriction on phasing, and contact is abundant, leading to a strong interaction for both $\theta \approx 0°$ and $\theta \approx 180°$. The effective interactions in near-magic odd-odd nuclei as discussed in more detail in reference [61].

Isospin

The proton and neutron differ in mass by only ~0.1% and because the strong nuclear force is approximately charge independent, the main difference in the way they interact is due to the much weaker electromagnetic interaction. It is therefore mathematically convenient to treat the proton and neutron as two manifestations of the same particle, the nucleon. The concept of the proton and neutron as merely two states of the same particle, leads to the concept of isospin, which is formally (but not physically) similar to intrinsic spin. In analogy with intrinsic spin, each nucleon is assigned an isospin T=1/2; protons and neutrons are differentiated by the projection of this isospin on an imaginary isospin z-axis. This projection T_z is $-1/2$ for protons and $+1/2$ for neutrons. T_z is the z-component of the total isospin T and therefore, for multi-particle systems the individual T_z values add algebraically, while the T values add vectorially. More simply

$$T_z = \frac{1}{2}(N - Z) \tag{2.31}$$

which is zero for nuclei with N=Z and ranges upwards and downwards as N and Z differ by larger amounts.

Chapter 3

Experimental Considerations

3.1 Heavy-Ion Fusion Evaporation Reactions

Heavy-ion fusion followed by nucleon evaporation has become the primary means of producing nuclei at high excitation energy and spin for spectroscopic studies with γ rays. By simple choice of beam energy and target/projectile combination, a very wide range of nuclei can be reached, in many cases with considerable selectivity. A limitation, however, is that with stable beams and projectiles, generally only near-stable and neutron-deficient products are accessible, due to the fact that the combination of a stable beam and target tend to form compound nuclei on the neutron-deficient side of the valley of stability.

The technique of fusion evaporation proceeds as follows. A beam of ionized nuclei of a specific isotope is produced by an ion source and accelerated onto a target, a thin metallic foil of another isotope. If the two nuclei collide with a sufficiently small impact parameter and an energy large enough to overcome their mutual Coulomb repulsion, then their nuclear potentials overlap and then can fuse to form a single compound nucleus. If this compound system lives as long as $\sim 10^{-20}$ seconds then it can equilibrate with respect to its energy, angular momentum and shape. The nucleus then loses all memory of the components involved in its formation process and the kinetic energy of the collision and relative angular momentum of the projectile and target are converted into excitation energy and angular momentum. The excitation energy E_x of the compound nucleus is given by [63]

$$E_x = \frac{M_T}{M_B + M_T} E_b + Q \tag{3.1}$$

where M_B and M_T are the masses of the beam and target nuclei respectively, E_b is the energy of the beam in the laboratory frame and Q is the difference in binding energy of the compound nucleus and the nuclei in the entrance channel given by $(M_B + M_T - M_{CN})c^2$.

This process usually produces compound nuclei which are highly excited and with a large amount of angular momentum. The maximum angular momentum of the compound nucleus following a reaction is given by [18]

$$l_{max}^2 = \left(\frac{2\mu R^2}{\hbar^2}\right)(E_{CM} - V_c) \tag{3.2}$$

where μ is the reduced mass of the system $(\frac{M_T M_B}{M_T + M_B})$, V_c is the Coulomb barrier ($\approx 1.44\ Z_1 Z_2$) and R is the distance of closest approach, usually given by $1.36(A_1^{1/3} + A_2^{1/3}) + 0.5$ fm [27].

On formation, the energy of the compound nucleus is above the particle emission threshold, and consequently, the decay from hot state to cold residual nucleus is initially dominated by statistical particle emission, each proton or neutron taking the order of 5 MeV and each α-particle taking the order of 10 MeV, but each taking only about $1\hbar$ of angular momentum. Linear momentum must be conserved as the evaporated nucleons and α-particles leave the compound nucleus, thus the residual nucleus must recoil, shifting it from its original trajectory. These particles are evaporated approximately isotropically in the centre of mass frame of reference, but the nucleus is moving in the lab frame in the direction of the beam, resulting in a forward focussed cone of recoils in the lab frame called the recoil cone.

By conservation of angular momentum (and neglecting the mass loss due to particle evaporation), the velocity for the recoiling nucleus v_{cm} from a heavy ion fusion reaction is given by

$$v_{cm} = \frac{M_B}{(M_B + M_T)}\sqrt{\frac{2E_B}{M_B}} \tag{3.3}$$

At high energy, the density of nuclear levels can be up to 10^{12} MeV^{-1} with level widths typically of the order eV. This results in a large degree of overlap between levels, effectively forming a continuum. After the evaporation of a number of particles, the recoiling nucleus has cooled in terms of excitation energy, but retains the high angular momentum. This is ideal for the study of the high spin states of the reaction product nuclei. Below the particle separation energies, statistical γ-ray emission dominates until, at lower excitation energy, the nature of the states changes from continuum to discrete, well defined quantum mechanical levels. The nucleus completes its decay to the ground state by γ-ray emission from these discrete states. The states which are preferentially populated in this type decay are near-yrast, meaning of lowest excitation energy for a given spin. Figure 3.1 depicts the sequence of the decay of the compound nucleus to the ground state, in terms of energy and spin. For near-stable nuclei, neutron evaporation is favoured over charged-particle evaporation due to the Coulomb barrier in the nucleus. For very neutron-deficient systems, the separation energy of the protons is increasingly less than that of the neutrons, making it energetically favourable to evaporate protons or α-particles.

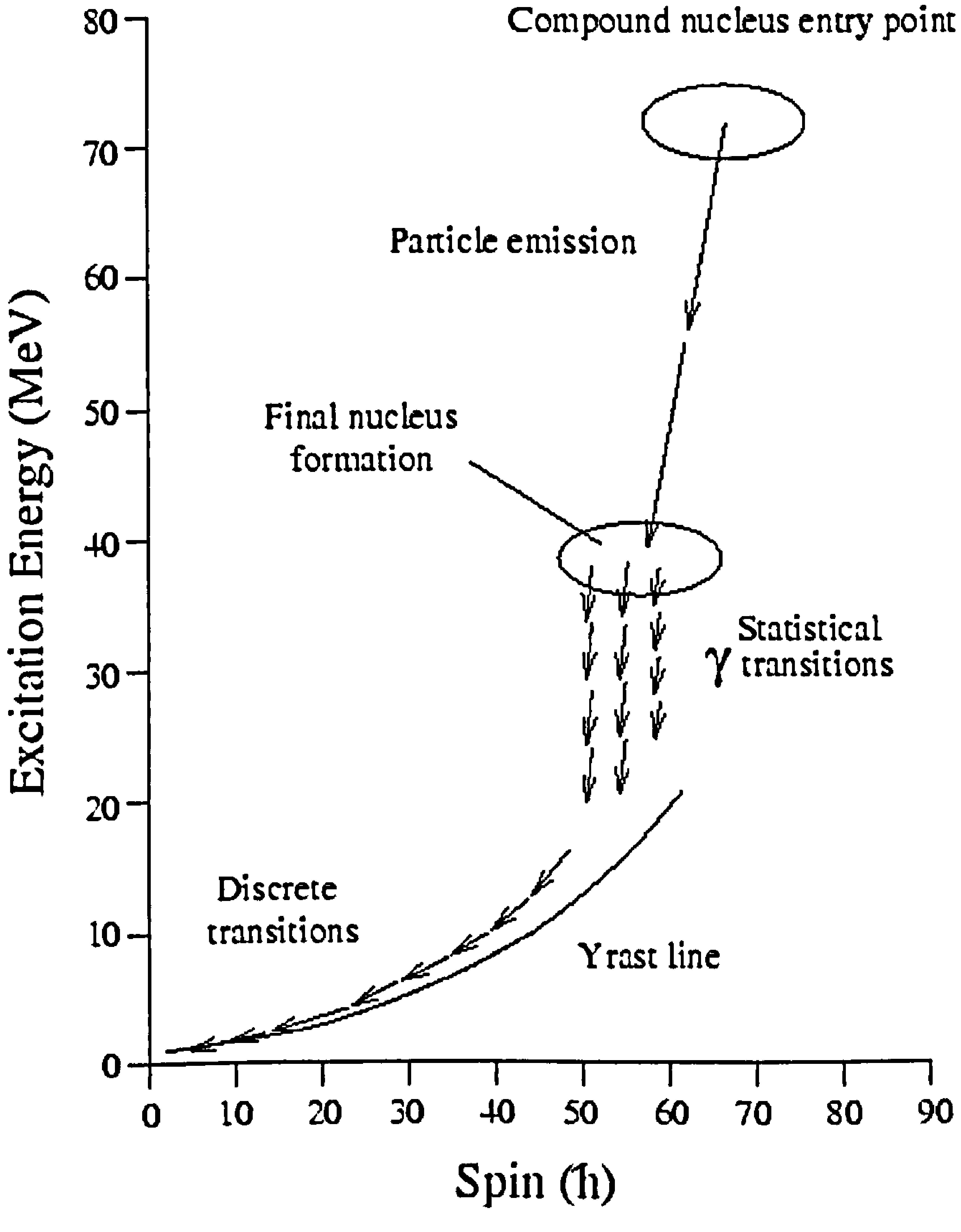

Figure 3.1: A schematic diagram of the excitation energy of compound nucleus as a function of angular momentum. Particles are first emitted, carrying away a large amount of excitation energy, but little angular momentum. When below the particle evaporation threshold, de-excitation continues to the ground state through γ-ray emission.

3.1.1 Incomplete Fusion

A limitation with stable beams and targets is that essentially only neutron deficient products are accessible. For that reason, one of the first applications of even slightly neutron-rich radioactive beams, such as ^{6}He or ^{8}He [64] will be fusion evaporation for the production of nuclei close to stability. Neutron-rich beams are in a sense already available as it is possible to use the break-up of a projectile in an incomplete fusion reaction (see reference [65] for a review of this mechanism). Fusion evaporation is a process characterized as complete fusion, in which the momentum of the relative motion is completely transferred to the compound system. However, at high energies (and small impact parameters), pre-compound emission of light particles and projectile break-up before fusion are observed. In these processes, a compound nucleus is formed with less than the full available momentum and mass. The missing momentum is carried away by emitted particles. This process is known as incomplete fusion. For example, a ^{9}Be beam incident on a heavy target exhibits products which can be interpreted as break-up of ^{9}Be with the emission of an α particle and fusion of the neutron-rich ^{5}He fragment with the target nucleus, followed by neutron evaporation from that compound nucleus (note, ^{5}He is not bound and exists only as a ^{4}He+n resonance). Due to the peripheral character of incomplete fusion reactions [66], significantly more angular momentum is transferred to the compound system compared to the complete fusion reaction.

With regard to this study, it is not clear what processes occur in a ^{7}Li-induced case although an early study [67] of residues from ^{7}Li-induced reactions on ^{208}Pb at energies up to 30 MeV showed that the dominant cross section was break-up into α particles and tritons, and subsequent studies indicated that α emission (corresponding to triton absorption) was favoured over triton emission (corresponding to α absorption) [68]. Although the measurements did not determine whether the triton fragment proceeded to fuse with the target in the case of the emission of the α particle, comparison of the measured cross sections [68] implied that this was a major proportion of the process.

In the case of the current work, if the reaction was viewed as the break-up of ^{7}Li followed by the incomplete fusion of a triton fragment, the effective energy of the triton would be given as [65]

$$E_{triton} = \frac{3}{7} \times (E_{beam} + E_s(^7Li - \alpha)) \tag{3.4}$$

where $\frac{3}{7}$ is the ratio of the masses and E_s is the separation energy of an α particle from ^{7}Li, which is approximately 8 MeV.

There is also possible evidence of the break-up of ^{7}Li into a proton and ^{6}He, due to the observation of an anisotropic distribution of emitted protons when a beam of ^{7}Li is incident on a heavy-ion target [69]. The protons are preferentially emitted in a forward direction, suggesting emission before thermal equilibration of the compound nucleus and the subsequent fusion-evaporation reaction between the ^{6}He fragment and the target.

3.2 Accelerators

In order to overcome the Coulomb barrier, ions must be accelerated into a beam of a certain energy. In this study, the only type of accelerator used was a tandem Van de Graff. In addition to an accelerator, an ion source is needed from which originates the beam of charged ions that is to be accelerated, along with a method of extracting these ions from the source and injecting them into the accelerator.

The principle of a Van de Graff accelerator [70] is that charge is continuously transferred to a terminal via a moving insulated belt. The terminal is in electrical contact with an outer shell which collects all the charge deposited by the belt. The charge that can be deposited is limited only by the insulating properties of the surrounding medium. Sulphur hexafluoride (SF_6) is used as the insulating gas, or a large constituent of the insulating gas because it is highly resistant to electrical breakdown.

The terminal voltage of a typical tandem accelerator is around 10–20 MV, and this is used to attract the negatively charged ions with a kinetic energy equal to the charge on an electron e, times the voltage on the terminal, V_T. As the ions reach the terminal, they pass through a carbon stripper foil which removes $n+1$ electrons, resulting in an ion carrying a net positive charge of $Q=+ne$. The large terminal voltage is now repulsive and the positive ions are then accelerated away from the terminal with a kinetic energy of $K=e(\mathrm{n}+1)\mathrm{V}_T$ to the end of the machine.

Tandem accelerators are commonly used in conjunction with sputter ion sources [71]. A vapour of caesium is used to ionize a solid source of the ion to be extracted (called a cone or a pill). Caesium is used as it has a very low ionization potential of 3.6 eV. These ions are then extracted with an electric field and are injected into the accelerator. This method has a yield directly comparable with other types of ion source, but unlike other sources, ions can be generated from a solid.

3.2.1 Yale ESTU Tandem

The ESTU (Extended Stretched TransUranium) tandem at the Wright Nuclear Structure Laboratory [72] is one of the largest operating electrostatic accelerators worldwide and has a maximum terminal potential of 21 MV. A high-resolution negative ion injector, mounted on a pre-acceleration platform operating up to 200 keV, can inject beams of all masses from A=1 to A=250 with a mass resolution of better than 1 in 200 and intensities of up to 20 μA.

3.3 Gamma-Ray Angular Distributions

In order to determine the spins (and thus infer the parities) of the excited states formed in a fusion evaporation reaction, one can measure the angular distribution of the γ-ray transitions. To be able to observe an anisotropic distribution, the nucleus needs to be populated in such a way which gives rise to states of aligned angular momentum with a specific orientation in space. This is achieved in a fusion evaporation reaction where the angular momentum vector $\mathbf{l} = \mathbf{r} \times \mathbf{p}$ is in a direction perpendicular to the beam direction. The effect is to align the magnetic substate population in this direction. There then will be some loss of this alignment due to particle emission and by subsequent γ-ray emission.

The general formula for the angular distribution of γ-ray angular intensity as a function of angle θ with respect to the beam direction is given by [73]

$$I(\theta) = \sum_k A_k P_k(cos\theta) \tag{3.5}$$

where $k = 2l$ and l is the highest order multipole of radiation taken away by the emitted photon. A_k is called the angular distribution coefficient which depends on the initial and final spins and the m-state distribution. P_k is a standard Lagrange polynomial. Both A_k and P_k are tabulated [74]

For pure dipole radiation

$$I(\theta) = A_0\{1 + A_2 P_2(cos\theta)\} \tag{3.6}$$

where $P_2(cos\theta) = \frac{1}{2}(3cos^2\theta - 1)$ and A_0 the 'true' intensity. For quadrupole radiation

$$I(\theta) = A_0\{1 + A_2P_2(cos\theta) + A_4P_4(cos\theta)\} \tag{3.7}$$

where $P_4(cos\theta) = \frac{1}{8}(35cos^4\theta - 30cos^2\theta + 3)$.

3.3.1 Gamma-Ray Anisotropies

By experimentally measuring the intensities of the γ-ray transitions as a function of detector angle about the beam direction, a full angular distribution can be obtained from which A_2 and A_4 can be obtained by fitting to equation 3.5. The A_k values can be used to experimentally distinguish between transitions of differing multipolarities. This technique depends on having many detectors at differing angles. However, if only a few angles are accounted for, it is still possible to distinguish between dipole and quadrupole radiation. In this case, the A_4 coefficient is set to zero. A measure of anisotropy can then be arbitrarily defined as [75]

$$A = 2\left(\frac{W(\theta_1) - W(\theta_2)}{W(\theta_1) + W(\theta_2)}\right) \tag{3.8}$$

$W(\theta)$ is the intensity of a γ-ray detected at angle θ, and this can be experimentally measured and compared either with theoretical values for dipoles and quadrupoles calculated using equations 3.6 and 3.7, or with values measured for transitions of known multipolarity.

3.3.2 DCO Ratios

With high efficiency γ-ray detector arrays, it is possible to perform measurements of Directional Correlation from Oriented states (DCO) on pairs of γ-rays detected in coincidence with one another [73, 76, 77]. In this method, the ratio of intensities is taken for a γ-ray detected at two or more different angles around the target position, provided that the γ-ray is detected in coincidence with another γ-ray of known multipolarity. This is achieved by sorting a coincidence matrix with transitions detected at θ_1 on one axis and those detected at θ_2 sorted on the other. θ is given by the geometry of the detectors in the array with respect to the beam direction; for this work, θ_1=90° and θ_2=138°. By placing γ-ray energy gates on transitions whose multipolarity had been established in previous works, a DCO ratio could be extracted using the prescription [78]

$$R_{DCO} = \frac{I(138^\circ)\ gated\ at\ 90^\circ}{I(90^\circ)\ gated\ at\ 138^\circ} \times \varepsilon \tag{3.9}$$

where I is the number of counts in a peak and ε is an efficiency multiplication factor which corrects the experimental value for the detection efficiencies of both the gate and the projected transition. This factor is given by

$$\varepsilon = \frac{\varepsilon_g(138^\circ) \times \varepsilon_p(90^\circ)}{\varepsilon_g(90^\circ) \times \varepsilon_p(138^\circ)} \tag{3.10}$$

where ε_g is the detection efficiency of the gate and ε_p is the detection efficiency of the projected transition. For example, using the YRAST Ball array as configured in this work, the geometry is such that the DCO values for known transitions were found to be R_{DCO}=1.08(4) for a quadrupole $E2$ gated by an $E2$ and R_{DCO}=0.70(4) for a pure dipole gated by an $E2$.

3.4 Gamma-Ray Interactions with Matter

The detection of photons is an indirect process involving an interaction between the photon and the detector material that results in all, or part of the energy being transferred to one or more electrons. It is only through the energy loss from these electrons that the energy of the γ ray is converted into an electrical signal. For the signal to be a good representation of the energy of the incident photon, it is desirable that the photon energy is completely converted into kinetic energy of electrons in the detecting material and that no energy escapes from the volume of the detector in the form of low-energy or backscattered photons, or in the form of secondary electrons. At the γ-ray energies of interest in this work, three basic interaction processes are dominant in converting the incident photon energy into electrons in a detector:

- *The photoelectric effect.* This process results in the total absorption of the photon and the release of an electron from an atom of the detector material. The photoelectron energy is equal to the incident photon energy minus the binding energy of the electron in the atom.

$$E_{e^-} = E_\gamma - E_{binding} \tag{3.11}$$

The vacancy left by the ejected photoelectron is filled by atomic rearrangement, producing either an Auger electron or a characteristic X-ray that is subsequently photo-electrically absorbed by a loosely bound electron. These X-rays are generally absorbed in a very short range within the detector, so the total signal corresponds to the total conversion of the original photon energy into kinetic energy of the electrons. The presence of a large mass is required to conserve momentum in the photoelectric process (i.e. the interaction must be with a bound electron). The probability of an interaction is an exponential function of the atomic number of the absorbing material. The cross-section of the interaction over the range of energies of interest and atomic number of the detector material can be approximated by [79]

$$\sigma_{pe} = k_{pe}\frac{Z^{4.5}}{E_\gamma^3} \tag{3.12}$$

where k_{pe} is a proportionality constant, σ_{pe} is the probability of a photon of energy E interacting with an electron in a material of atomic number Z. Materials with higher atomic numbers have much larger cross-sections and therefore stop a much higher proportion of photons.

Photoelectric absorption is the dominant interaction between γ rays and semiconductors below 100 keV. To detect the full energy peak, the final interaction in a full energy event must be of this type, since it is the only mechanism that does not produce secondary photons. For this type of interaction, the full energy of the γ ray is transferred to the semiconductor material, effectively around the position where the interaction takes place.

- *The Compton effect.* This process involves a photon scattering from an electron, resulting in a recoiling electron and a loss of energy of the photon. The energy of the photon after the interaction E', is dependent on the angle of scatter and is given by [80]

$$E' = \frac{E_\gamma}{1 + \frac{E_\gamma}{m_0c^2}(1 - \cos\theta)} \tag{3.13}$$

where m_0c^2 is the rest mass energy of the electron (0.511 MeV). The kinetic energy of the recoiling electron is thus the difference in energy of the incident and scattered γ ray.

If there are no further interactions then the photon scatters out of the detector and the energy deposited ranges from zero to a maximum when θ=180°. The result is incomplete energy deposition and a spectrum with a continuum of energy called the Compton background, up to the maximum value, called the Compton edge.

At higher incident photon energies, the photoelectric process becomes unlikely (see equation 3.12), but the Compton process remains relatively effective since its probability is given by [79]

$$\sigma_{cs} = k_{cs}\frac{Z}{E} \tag{3.14}$$

where k_{cs} is a proportionality constant.

The probability for a Compton scatter to occur at angle θ can be calculated from the Klein-Nishina formula for the differential cross-section per electron, correctly given as [80]

$$\frac{d_e\sigma}{d\Omega} = Zr_0^2\left(\frac{1}{1+\alpha(1-cos\theta)}\right)^2\left(\frac{1+cos^2\theta}{2}\right)\left(1+\frac{\alpha^2(1-cos\theta)^2}{(1+cos^2\theta)[1+\alpha(1-cos\theta)]}\right) \tag{3.15}$$

where α is the photon energy in units of the electron rest mass energy (α=E$_\gamma$/mc^2) and r_0 is the classical electron radius, which is equal to $\frac{e^2}{4\pi\epsilon_0 mc^2} = 2.818$ fm.

- *Pair Production.* This process is only possible when the incident photon energy is at least twice the electron rest mass energy (*i.e.* E$_\gamma$ > 1.022 MeV), so that an electron-positron pair can be created at the point of interaction of the photon. This must occur in the presence of an atom in order that momentum be conserved. The energy in excess of 1.022 MeV is transformed into the shared kinetic energy of the electron and positron. The electron and positron then quickly lose their kinetic energy by slowing down in the detecting material and when the positron comes to rest, it annihilates with an electron in the detecting material, producing two back-to-back 511 keV photons. The spectrum produced by this process contains features whose relative intensities depend on the particular geometry of the detector. A full energy peak is produced when both 511 keV annihilation photons are absorbed in the detector, a peak in the spectrum at 511 keV less than the full energy corresponds to the escape of one 511 keV photon, while a third peak at 1.022 MeV below the full energy peak corresponds to the escape of both 511 keV photons. The cross-section for pair production σ_{pp} is given by [79]

$$\sigma_{pp} = k_{pp} Z^2 ln(E) - k_{pp} z^2 ln(1.022\ MeV) = k_{pp} Z^2 ln(E) - \sigma_{ppth} \tag{3.16}$$

where k_{pp} is a proportionality constant and the second term explicitly indicates the 1.022 MeV threshold.

3.4.1 Suppression of Compton Scattered Events

The Compton continuum in γ-ray spectra from germanium detectors is generated primarily by γ rays that undergo one or more scatterings in the detector followed by escape of the scattered photon from the active volume. In contrast, the full-energy absorption events result in no escaping photons. Therefore, coincident detection of the escaping photons in a surrounding annular detector can serve as a means to reject preferentially those events that only add to the continuum, without affecting the full energy events. The rejection is carried out by passing the pulses from the germanium detector through an electronic logic coincidence gate that is closed if a coincident pulse is detected from the surrounding detector. This surrounding detector is made from a high efficiency γ-ray scintillator, usually bismuth germanate ($Bi_4Ge_3O_{12}$), often referred to as BGO [81, 82].

3.5 Germanium Detectors

In a semiconductor, there are two distinct groups of energy levels or bands known as the valence and conduction bands. The valence band consists of electrons bound to specific lattice sites, where as the conduction band represents the electrons that are free to move through the crystal. The bands are separated in energy by a band gap, the size of which determines whether the material is an insulator or a conductor. A large band gap (typically >5 eV) will classify the material as an insulator and a small band gap of approximately 1 eV will classify the material as a semiconductor.

Through interactions with the radiation, electrons can be excited from the valance band into the conduction band leaving a hole behind in the valance band and creating an electron-hole pair. Under an applied voltage, the electrons will flow towards the positive potential and the holes to the negative potential. This charge can be collected and converted to an output voltage by a pre-amplifier. The number of electron-hole pairs created, and thus the size of the output voltage, is proportional to the energy of the radiation. For temperatures greater than absolute zero, thermal energy is shared by the electrons in the crystal lattice and thus it is possible for an electron to be excited across the band gap into the conduction band. Thus for small values of a band gap (as is the case for semiconductors), there is a large probability of thermal excitation, which in a detector is a source of unwanted noise. In order to reduce the thermal noise, semiconductor detectors are operated at low temperature.

All semiconductors have a finite conductivity, and so a leakage current is observed. This current is a source of noise that can obscure small currents. The solution is to put a p-n junction in the semiconductor, that is a p-type and an n-type semiconductor in direct contact with each other. This results in a migration of charge carriers across the surface of the materials. The volume, referred to as the depletion region, is the active region where the radiation will interact, resulting in its subsequent detection. By applying a reverse bias across the p-n junction, the volume of the depletion region can be increased.

3.5.1 High-Purity Germanium Detectors

Advances in the production of crystals means that now, hyper-pure germanium (HPGe) can be used with the advantage of being able to be stored at room temperature (but still needing to be operated at liquid nitrogen temperature). As a result of the high penetration of γ rays, a relatively large depletion region is required. The thickness, d, of the depletion region is given by [80]

$$d = \sqrt{\frac{2\epsilon V}{eN}} \tag{3.17}$$

where V is the reverse bias and N is the net impurity concentration. From this equation it can be seen that a decrease in the net impurity will result in an increase in the size of the depletion region. HPGe detectors have impurity levels as low as 10^9 atoms cm^{-3}, compared with 10^{12} atoms cm^{-3} for normal semiconductors. If the remaining impurities are donor-type, then the crystal is called n-type and if they are acceptor, the crystal is called p-type.

For γ-ray spectroscopy, as large an active volume as possible is often required, so detectors are commonly constructed in a bulletised coaxial shape. Part of the central core is removed and the electrical contacts are at the centre and the outside of the crystal. In a n-type detector, the inner contact is a n$^+$ contact $\sim$ 600 μm thick, and the outer a p$^+$ contact $\sim$ 0.3μm thick. The $^+$ sign convention refers to a highly doped material. This is the usually arrangement for γ-ray spectroscopy since the thick n$^+$ contact would produce greater attenuation at the outside edge. The energy required to form an electron-hole pair in HPGe detectors is $\approx$ 3 eV. This means a large number of electron-hole pairs can be formed, and so many charge carriers are released for each γ-ray interaction. This has two consequences. Firstly, there is a relatively small statistical fluctuation in the number of charge carriers per pulse, and secondly, as a result of the large number, there is an excellent signal to noise ratio, and therefore a good energy resolution.

The other configuration of a germanium detector is a planar construction in which the germanium is fashioned into a disk with the electrical contacts on either side of the flat faces. This configuration is used in applications over an energy range from 3 to ~300 keV and is commonly known as a Low-Energy Photon Spectrometer or LEPS detector.

3.5.2 Germanium Clover Detectors

In recent years composite detectors have been developed in order to provide better photopeak efficiency and resolution in γ-ray spectroscopy. Composite detectors consist of several germanium crystals packed closely together and housed in the same cryostat. Their high granularity also allows better correction for Doppler broadening due to the reduction in the opening angle of the Ge crystals and allows for the use of add-backs in Compton scattering events. Clover detectors [83, 84] consist of four HPGe crystals configured like a four-leaf clover, each tapered at the front end allowing the detectors to be positioned closer to the reaction centre thus improving overall efficiency.

3.5.3 Add-Back

The detection of the full energy of a γ ray in a composite Ge detector made of n crystals proceeds in two ways:

- The detection in one of the n crystals called single events
- The detection in several crystals called multiple events

In the latter case the full energy of the γ ray is obtained by summing (adding-back) the energies deposited in the n crystals firing. Adding the signals corresponding to scattered events between adjacent crystals increases the efficiency with respect to the efficiency of the four individual crystals.

3.6 Gamma-Ray Coincidence Spectroscopy

In order to construct nuclear decay schemes, coincidence information between different γ-rays emitted from the same nucleus is required. To obtain these data, at least two detectors need to be used. Two γ-rays detected from the same decay cascade results in one coincident event. However, if three detectors fire, the number of coincident pair events, or doubles, rises to three. If N different γ rays are detected from one cascade there are $N(N-1)/2$ double coincidences. Therefore, in order to gain large amounts of coincident data in as short a time as possible, multi-detector arrays are required.

The coincidence data can be sorted offline into the form of a two-dimensional energy matrix or a three-dimensional energy cube and are analysed using coincidence techniques.

3.6.1 Coincidence Techniques

In each fusion evaporation event as used in the current work, there are approximately ten γ rays emitted (depending on the angular momentum transferred), but due to limited γ-ray detection efficiency, only a few of these are observed. Every time more than one is observed from each cascade (within finite time window), the energies can be written to the two axes of a γ–γ matrix. If more than two γ-rays are observed, the energies can be written to the three axes of a γ^3 cube. It is then possible to set a software gate at a particular γ-ray energy on one axis and project this gate onto the other axis in the case of a matrix, or in the case of a cube set a gate on each of the first two axes and project onto the third. Thus by gating on a particular γ ray of interest, an energy spectrum can be obtained of all the other transitions that come in coincidence with that particular γ ray.

3.7 YRAST Ball Ge Array

The YRAST Ball (Yale Rochester Array for SpecTroscopy) array [85] which is based at Yale University, USA, is currently one of the World's largest university based Ge detector arrays. The full array comprises of four rings with angles of 163° (3 positions), 135° (8 positions), 90° (9 positions), and 55° (8 positions) with respect to the beam axis. The twenty-eight detector positions can be filled with eight Compton suppressed segmented clover detectors and a selection of coaxial and LEPS detectors, giving a total photo peak efficiency of 3%.

The configuration used for the work described in this thesis was the SASSYER configuration [86]. This is a reduced version of YRAST Ball that is built surrounding the target position in front of SASSYER, the recoil separator (see figure 3.2). The YRAST Ball array frame surrounds the target position, in front of the first dipole magnet of SASSYER. The YRAST Ball array frame comprises of two detector rings and has thirteen detector positions. The first ring is at 90° to the beam direction and has nine detector positions. The second ring has four detector positions and is at 138.5° to the beam direction. With Yale's full complement of eight 150% segmented Clover detectors, the array has an efficiency of ~2.5% for 1.3 MeV γ-rays. The remaining positions can be filled from a selection of coaxial and LEPS detectors.

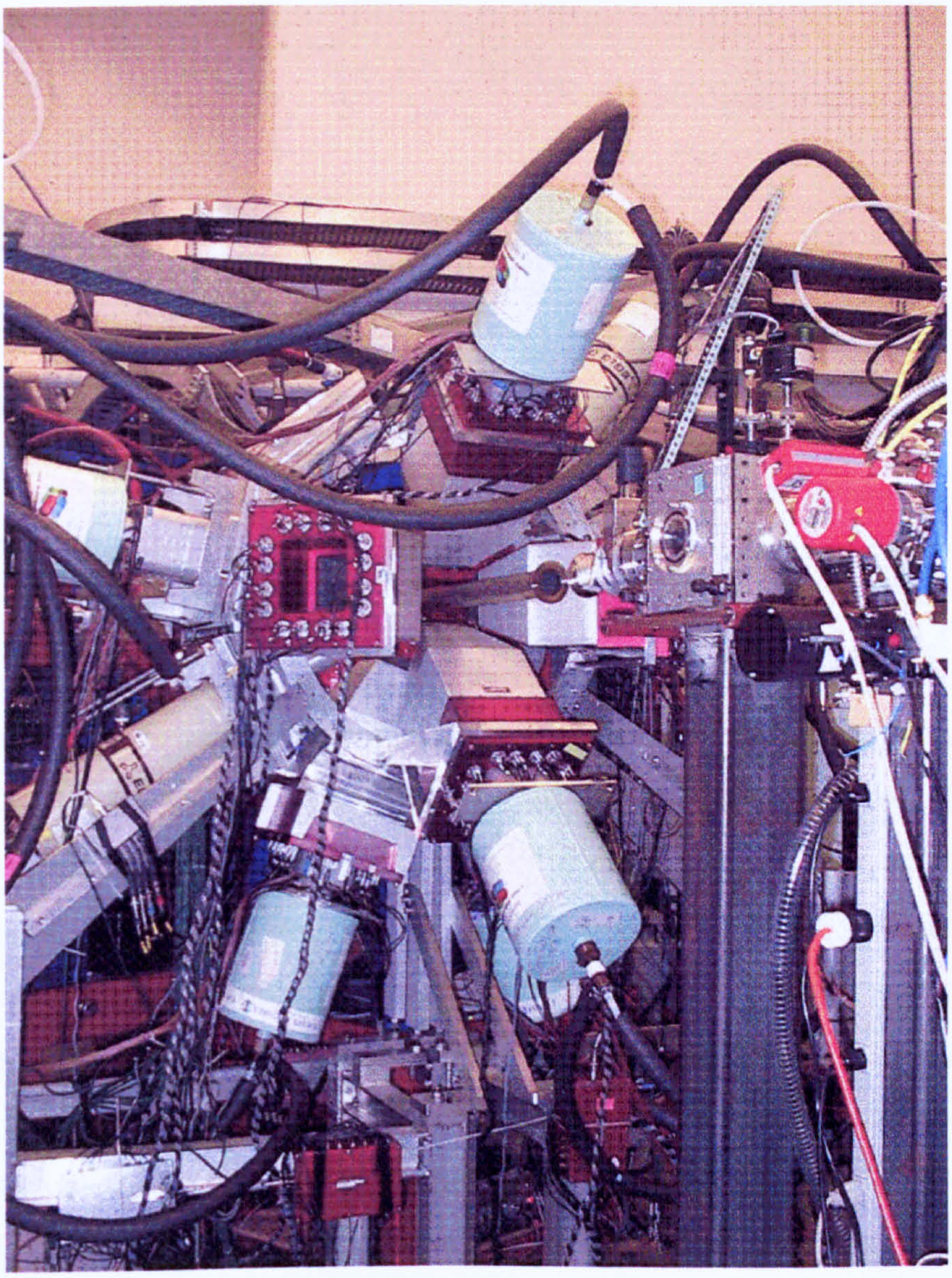

Figure 3.2: The YRAST Ball Ge array, coupled to SASSYER. See text for details.

Chapter 4

Experimental Details and Data Analysis

An experiment was performed in November 2002 at the Wright Nuclear Structure Laboratory, Yale University, using the YRAST Ball Ge array, with the intention of studying the yrast and near-yrast states of ^{112}In and ^{114}In and probing the vibrational to rotational evolution of $^{112-114}$Cd by populating these cadmium isotopes through the backbend. Due to the relatively large production cross-sections of the nuclei of interest and since the kinematics of the reaction resulted in the recoils being stopped in the target, the recoil separator SASSYER was not implemented in this particular experiment. However, SASSYER served as a beam-dump by setting the first dipole magnet to bend the beam that passes through the target without reacting, away from the Ge array and to the back of SASSYER.

A dc beam of ^{7}Li provided by the ESTU tandem impinged on an isotopically enriched (99%) metallic ^{110}Pd self-supporting foil of thickness 800 μg cm^{-2}. The reaction γ rays were detected using the YRAST Ball γ-ray array, which in this

E_{Beam}	Run Duration	$\gamma-\gamma$ Coinc. Events	l max ($\hbar$)
28 MeV	4 hrs	$1.2\text{x}10^8$	17
40 MeV	18 hrs	$4.3\text{x}10^8$	22
50 MeV	55 hrs	$12.0\text{x}10^8$	27

Table 4.1: Summary of the three ^{7}Li beam energies used in the current work.

configuration comprised of nine, four-element clover detectors, of which four were at 90° to the beam direction and the remaining five clover detectors were at 138° to the beam direction together with a single coaxial LEPS detector, also at 138°.

The acquisition master gate was set such that events where three or more γ rays were detected within 50 ns of each other were written to disk for subsequent offline analysis. Typical on-target beam currents were 10−15 electrical nanoamps for the duration of the four day experiment. This resulted in master event ($\geq\gamma^3$) rates of between 1000 and 1500 Hz.

Three different beam energies were used during the course of the experiment, 28, 40 and 50 MeV. Table 4.1 summarises the statistics obtained and calculated parameters of these three datasets. PACE [87] calculations of predicted cross-sections for the nuclei populated in this reaction are shown in figure 4.2 as a function of the beam energy.

4.1 Data Sorting and Calibration

The Ge detectors were calibrated for both energy and efficiency using standard ^{152}Eu and ^{133}Ba sources placed at the target position. A quadratic correction function was used to calibrate the clover detectors to 0.5 keV per channel and the LEPS detector to 0.125 keV per channel, giving a full-scale of 2 MeV and 500 keV respectively. A linear shift was used to align the prompt peaks of the TDCs, resulting in a timing dispersion of 0.25 nanoseconds per channel. The gain-matched data were then sorted into γ–γ coincidence matrices using the WNSL sort code, cscan [88] and γ^3 cubes using incub8r from the Radware package [89]. Both sort codes incorporated an add-back algorithm, which, if necessary, summed a further Compton scattered event to the original event within a clover detector.

4.1.1 Efficiency Calibration

Efficiency curves were created for both the full array and each of the two detector rings (90° and 138°). Figure 4.1 shows the calculated relative efficiency curve for the complete array as a function of γ-ray energy when an add-back algorithm was incorporated into the sort-code.

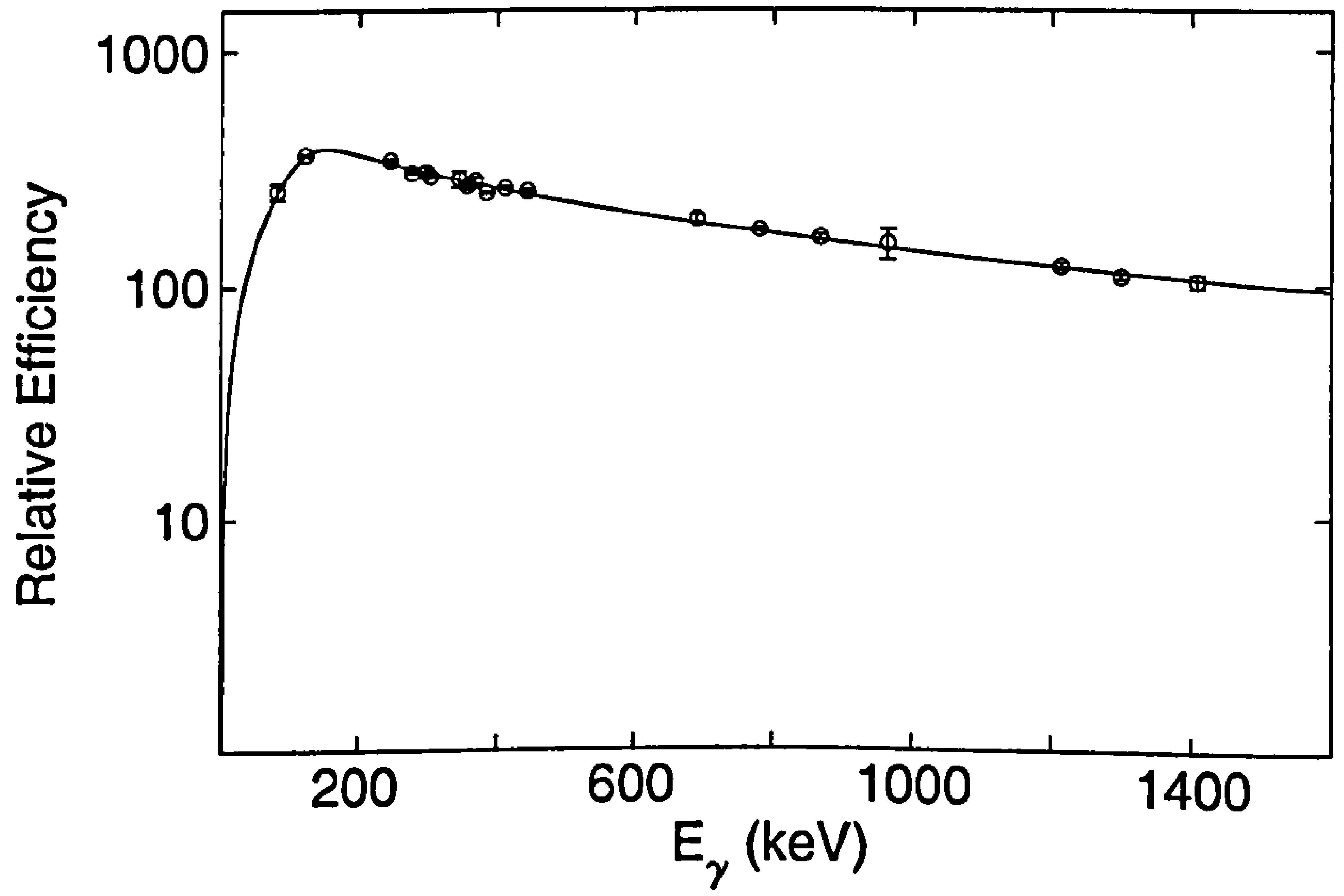

Figure 4.1: Relative efficiency curve for YRAST Ball. The experimental points correspond to ^{152}Eu and ^{133}Ba sources.

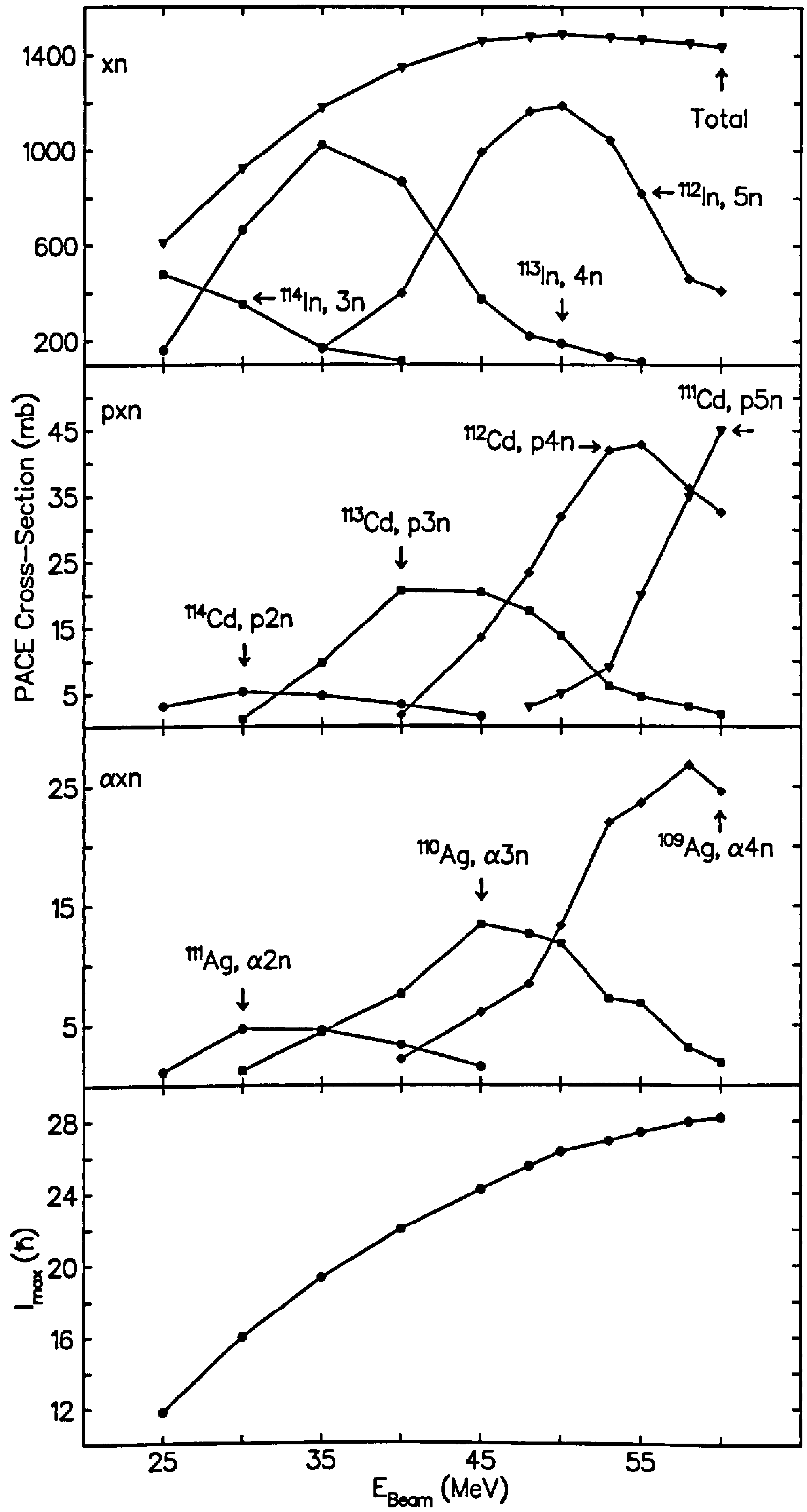

Figure 4.2: Production cross-sections for the ^{7}Li+^{110}Pd reaction as a function of beam energy, calculated using PACE [87]. The bottom figure shows the maximum angular momentum input for a ^{7}Li projectile, as a function of beam energy.

4.2 Initial Analysis

4.2.1 γ–γ and γ^3 Gating

Figure 4.3 shows the unfolded γ–γ projections from a γ–γ matrix with no TDC conditions for each of the three beam energies used. The transitions that have been reported in previous studies are labelled. Figure 4.4 shows the unfolded LEPS projection of a γ–LEPS matrix with no TDC condition for each beam energy used. The expanded region shows K_α and K_β X-ray lines of 21.1 and 23.9 keV respectively, which are associated the target material $_{46}$Pd.

Figure 4.5 shows normalised subtractions of the total projections from each other and highlights transitions associated with nuclei of mass A=112 (50–40 MeV), A=113 (40–50–28 MeV) and A=114 (28–40 MeV). Only transitions identified in previous works have been labelled. Figure 4.6 shows an excitation function, which displays the relative difference in yields of the various reactions products between the 50 and 40 MeV dataset, and the 28 and 40 MeV. It can be seen that the excitation function is consistent with the PACE calculations in that nuclei with A=112 are populated far more strongly in the 50 MeV dataset than the 40 MeV and that nuclei with A=114 are only slightly stronger in the 28 MeV than in the 40 MeV dataset.

Figure 4.7 shows the TDC sum taken from the 50 MeV dataset and displays the three regions where TDC gates were set. The late-delayed gate captured all the delayed events up to 950 ns, whilst the early-delayed gate was set to minimise the number of events associated with the 2.81 μs isomer entering the gate whilst still accepting a reasonable proportion of events associated with the 0.69 μs isomer.

By gating the matrices and cubes with transitions previously identified in other works (^{112,114}In [16], ^{113}In [15], ^{112}Cd [90], ^{113,114}Cd [91], ^{109}Ag [75], ^{110}Ag [92] and references therein), it was possible to produce spectra which identify all the detected energy transitions in a particular nucleus by their coincidence with the gating transition. By noting which transitions were present and which were absent in each gate, it was possible to build up the initial level scheme of each nucleus. Ordering of transitions in a cascade may also be inferred from such spectra because the intensity of transitions in a cascade generally increase at lower excitation energy due to side feeding from non-yrast states. Thus the intensity of transitions above a gate will tend to decrease with increasing excitation energy in the spectrum. However, transitions below a gate will usually have the same intensity (if there is no decay out of the cascade) as the feeding decay path has been defined by the gate. By measuring intensities in different gates, it is therefore possible to ascertain the ordering of the decay.

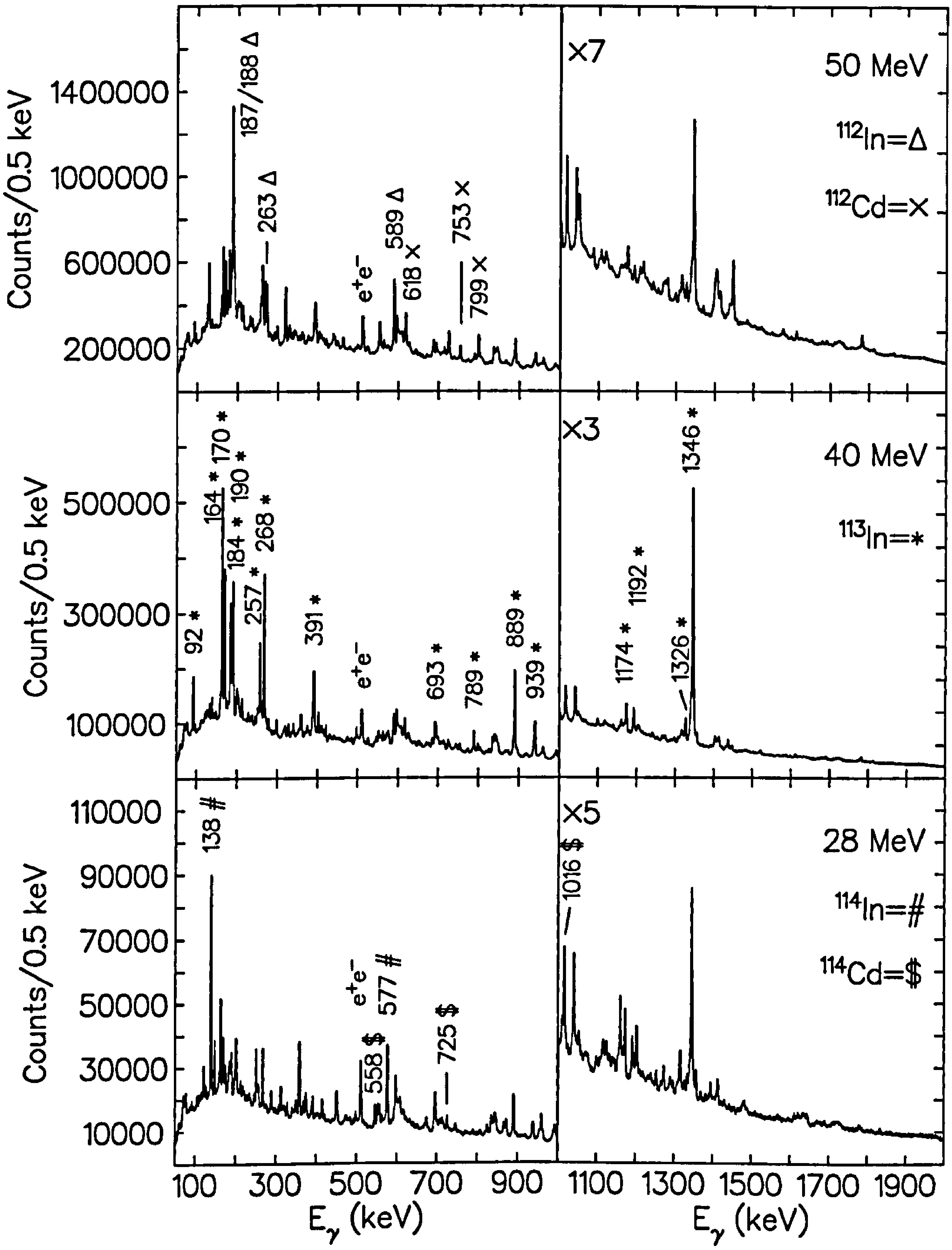

Figure 4.3: Total projections of the unfolded γ—γ coincidence matrices for each of the three beam energies used, with the labelled peaks corresponding to transitions that have been previously reported.

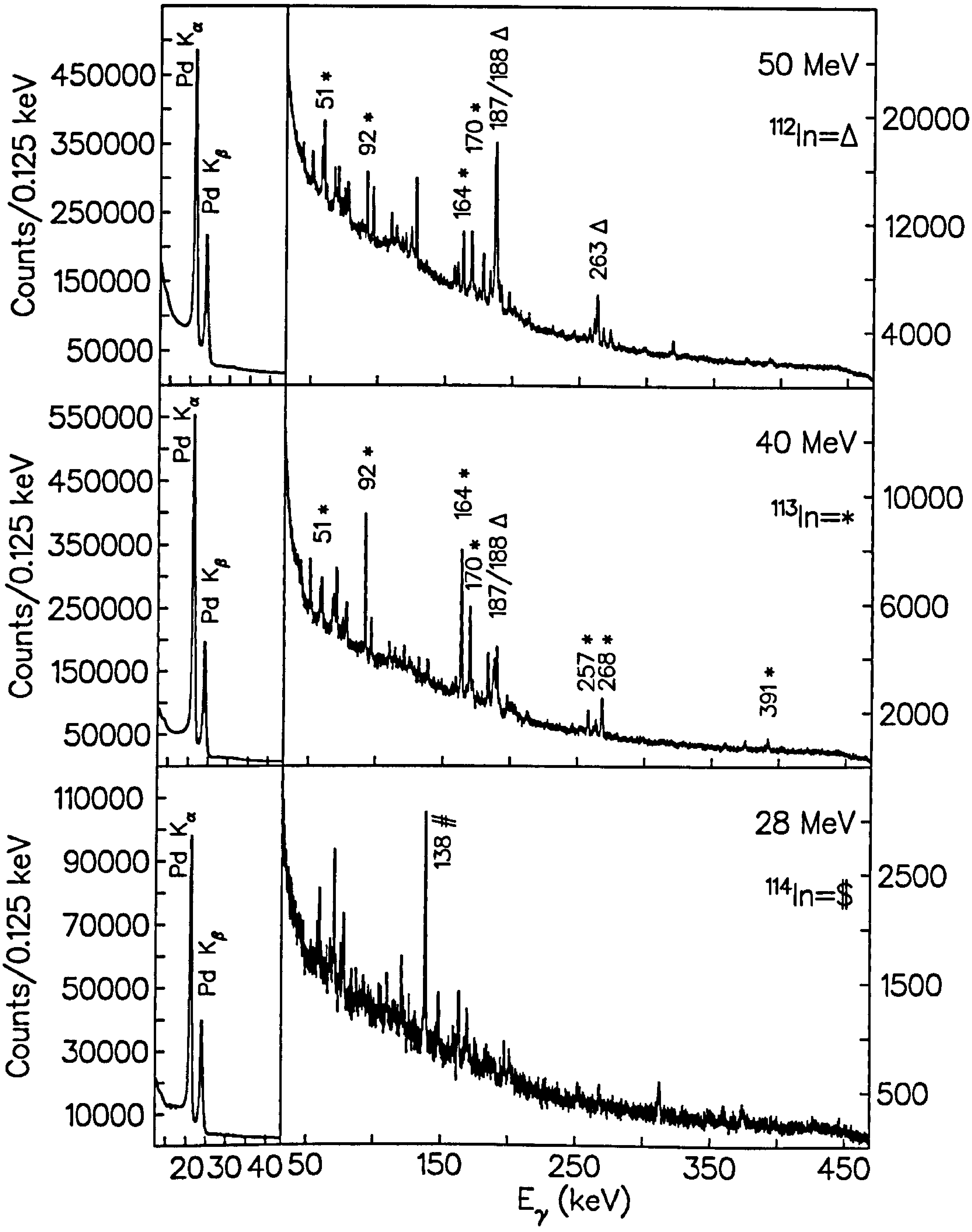

Figure 4.4: LEPS projections of the unfolded γ–LEPS coincidence matrices of the three different beam energies used, with the labelled peaks corresponding to transitions that have been previously reported.

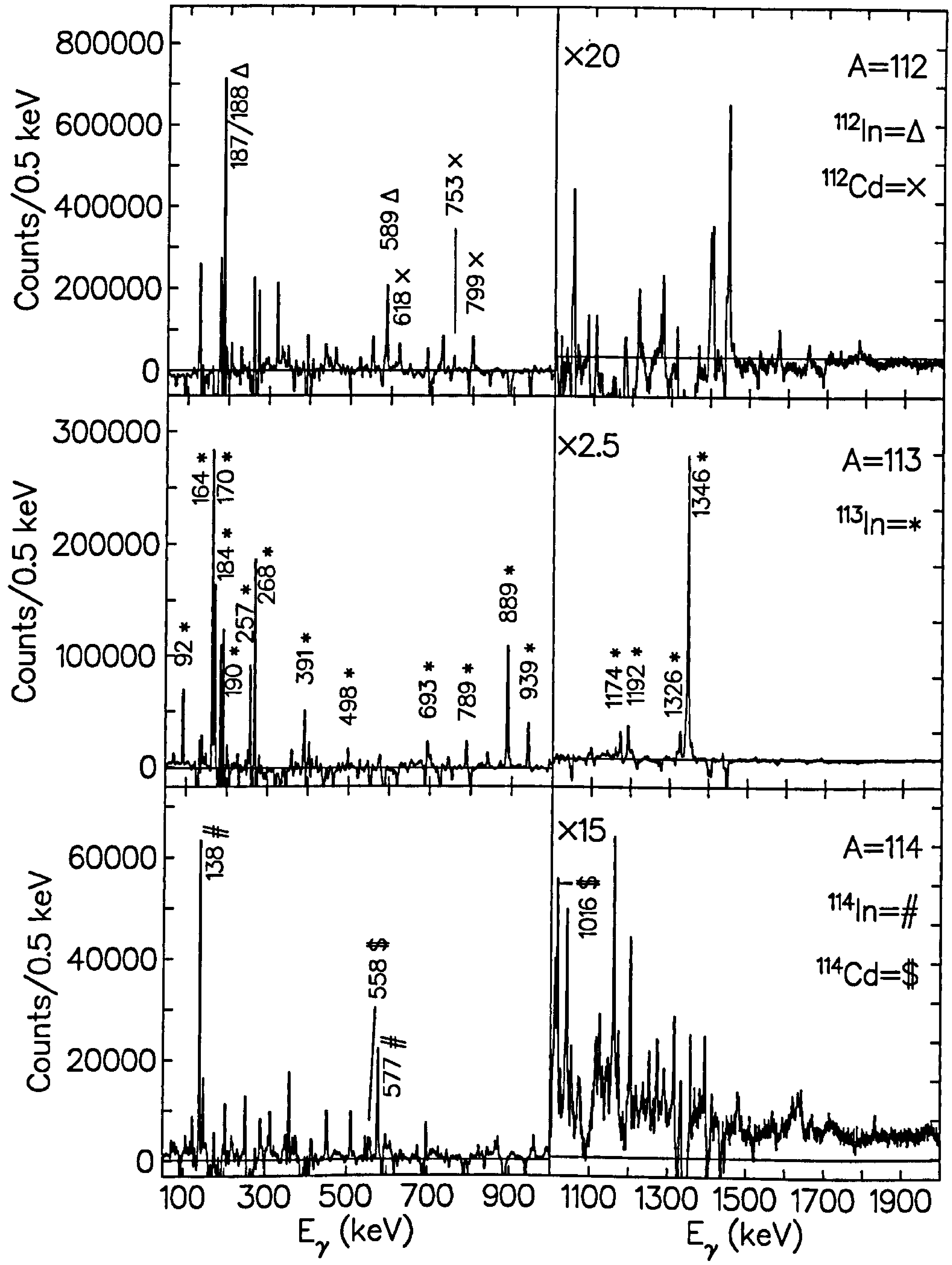

Figure 4.5: Normalised subtractions of the datasets from each other highlighting previously identified transitions by mass number A, with the labelled peaks corresponding to transitions that have been previously reported.

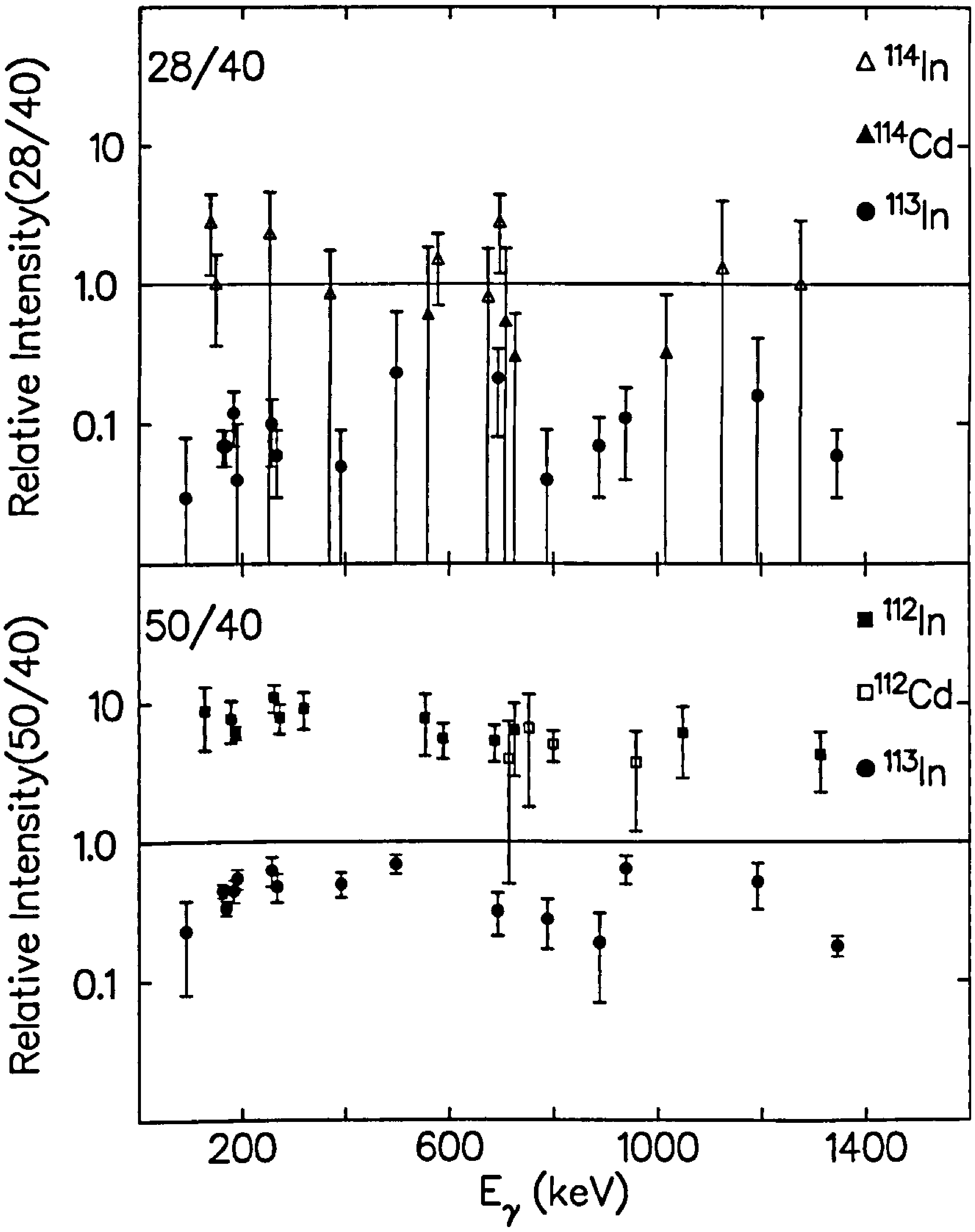

Figure 4.6: Results of excitation function analysis showing the relative difference between yields of nuclei produced in the 50 and 40 MeV datasets (bottom) and 28 and 40 MeV datasets (top).

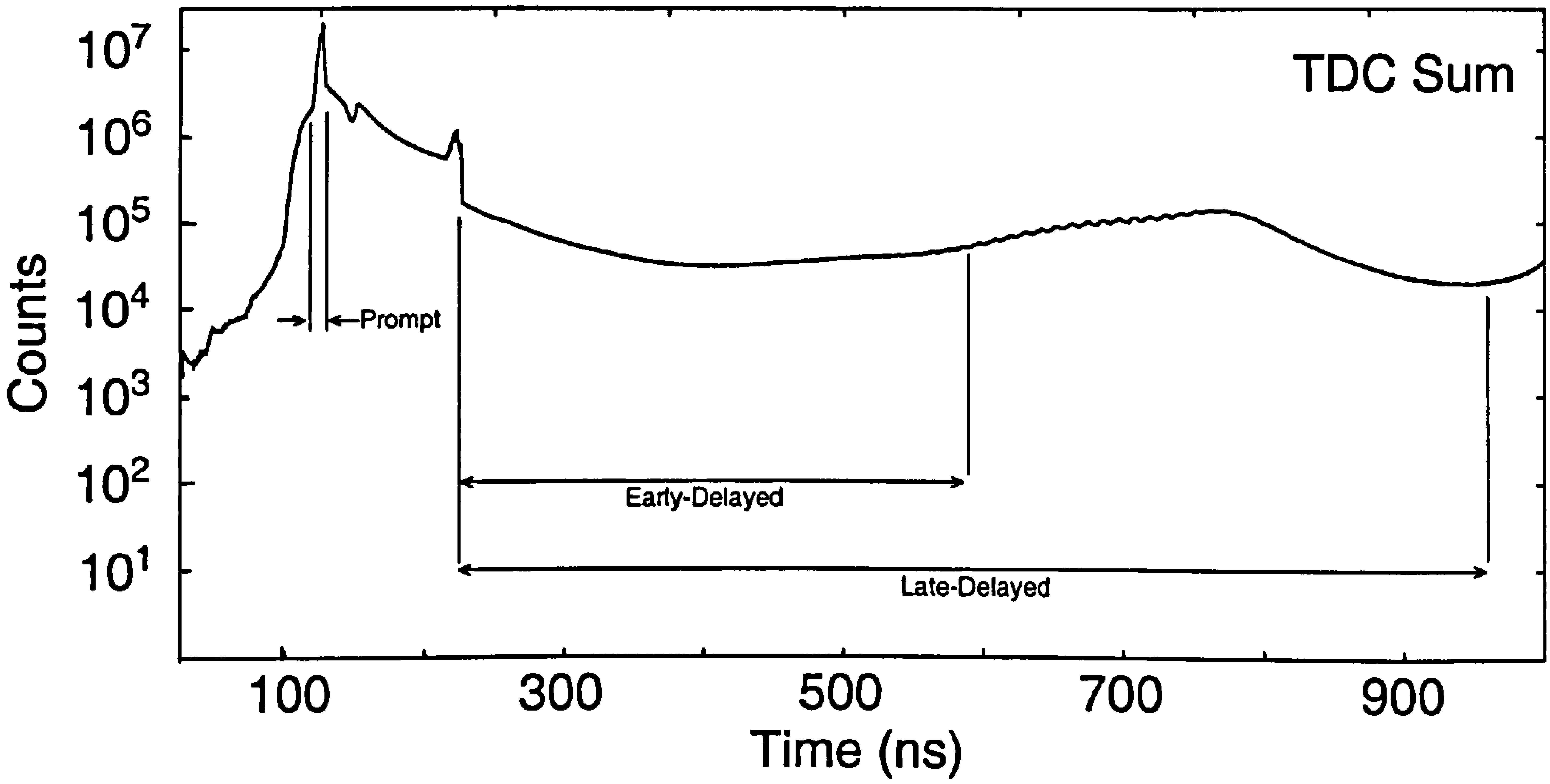

Figure 4.7: TDC Sum of the 50 MeV dataset showing the placement of the TDC gates used in this analysis. The early-delayed gate was set between 220–600 ns and the late delayed gate between 220–950 ns.

4.2.2 Spin and Parity Assignments

DCO Ratios

In order to use the DCO technique discussed in section 3.3.2, a coincidence matrix was sorted with transitions detected at 90° sorted onto one axis and transitions detected at 138° onto the other. By gating on a transition of known multipolarity, detected at one angle and projecting other transitions which are detected in coincidence, an efficiency corrected DCO ratio can be extracted using the prescription given in equation 3.9.

The difference in intensity of dipoles and quadrupoles when gated by either a ΔI=1 or ΔI=2 transition is clearly illustrated in figure 4.8. These spectra are both gated by the known 164 keV $\frac{17}{2}^- \rightarrow \frac{15}{2}^-$ ΔI=1 transition in ^{113}In [14]. The relative intensities between the ΔI=1 and ΔI=2 transitions in the two ring projections differ, the ΔI=1 transition clearly being more intense in the detectors at 90°.

DCO ratios of previously reported transitions in ^{113}In [14] were extracted and are plotted in figure 4.9. The data was taken from the 40 MeV dataset and the DCO ratios obtained serve as a guide to assigning spin and parity to the newly observed transitions in ^{112}In and ^{114}In. The gating dipoles should be chosen to be as pure as possible, being either an $E1$, or an $M1$ with minimal $E2$ admixture. Fortunately, in ^{113}In there is a single, strong 889 keV $E1$ transition from which it was possible to obtain a virtually pure dipole DCO ratio (assuming negligible $M2$ admixture). The gates used in the DCO analysis of ^{113}In are the 164 keV ΔI=1, 1346 keV ΔI=2 quadrupole, and 889 keV ΔI=1 pure dipole transition. The calculated weighted averages of the efficiency corrected DCO ratios obtained for ^{113}In are given in table 4.2. Care was taken when determining the statistics in a peak, as for higher energy transitions, a lineshape was obvious in the 138° ring due to a those nuclei which decay before they have fully stopped in the target, so they appear to have a lower energy in the 138° detectors. Clear separation is apparent between transitions of different multipolarities.

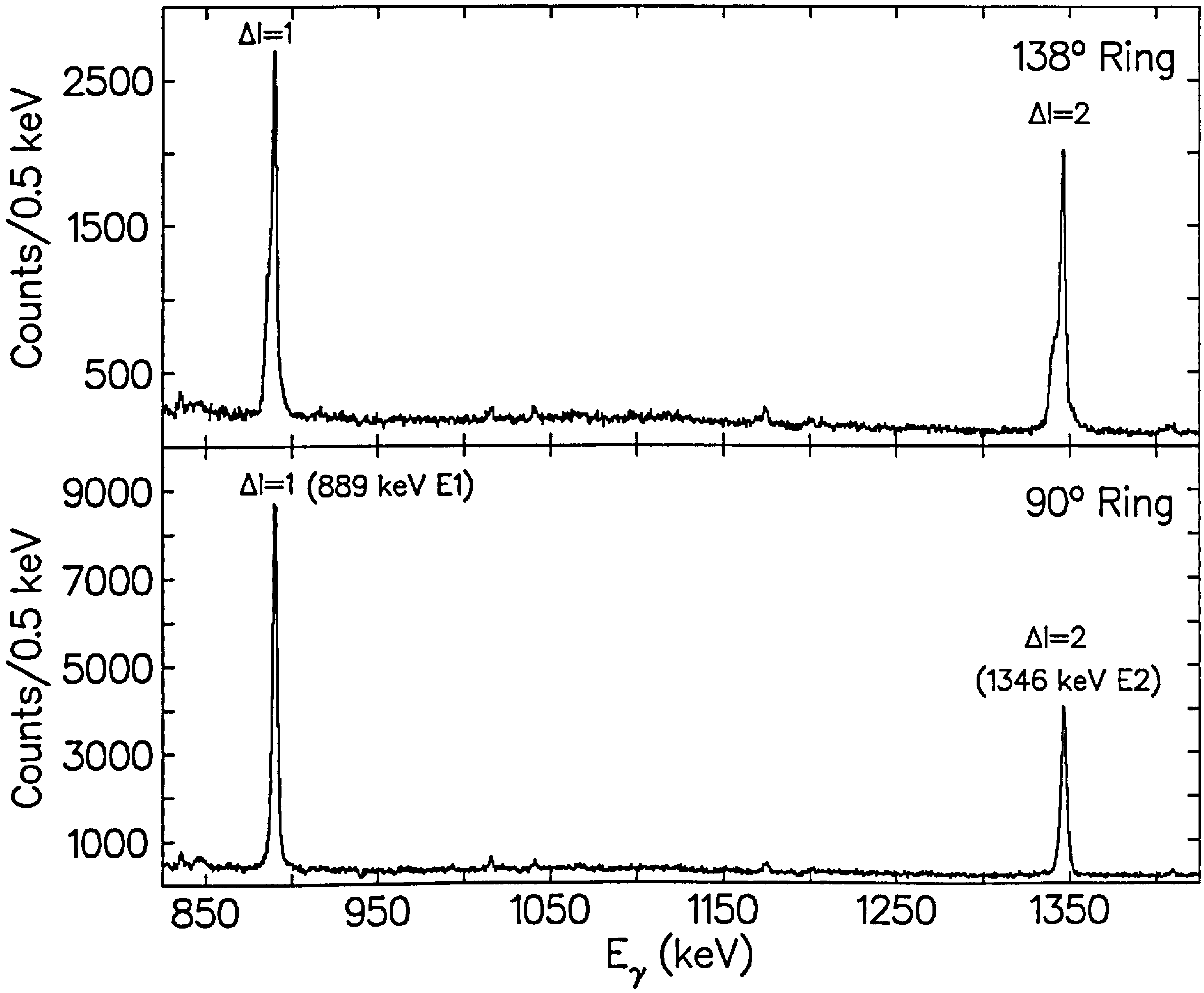

Figure 4.8: DCO gated spectra gated by the 164 keV $\frac{17}{2}^- \rightarrow \frac{15}{2}^-$ ΔI=1 transition in ^{113}In highlighting the difference between the relative intensities of ΔI=1 and ΔI=2 transitions at differing detector ring angle.

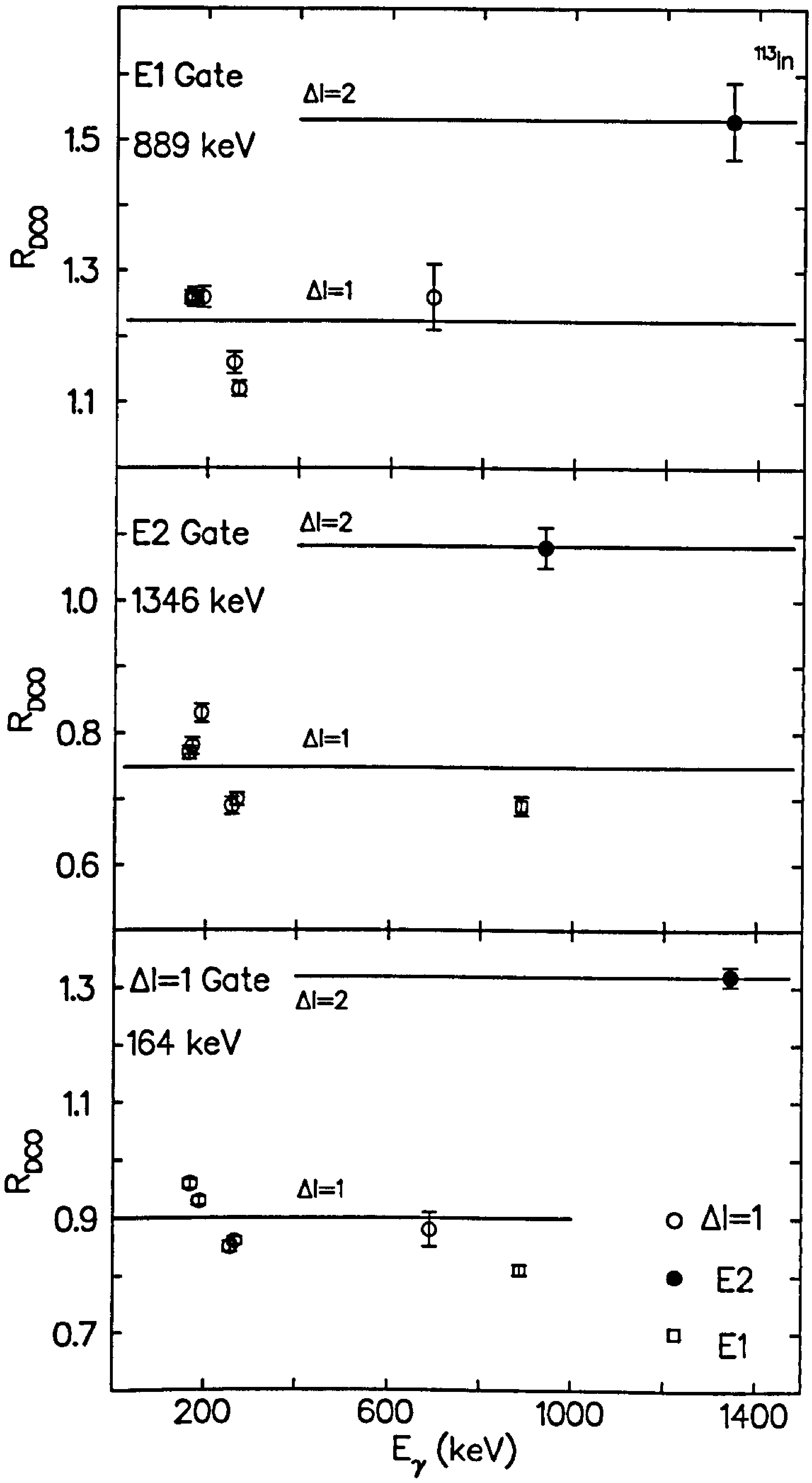

Figure 4.9: Examples of extracted efficiency corrected DCO ratio for previously reported transitions in ^{113}In [14], when gated by either the 889 keV ΔI=1 pure dipole, 1346 keV ΔI=2 quadrupole or the 164 keV ΔI=1. The horizontal lines correspond to the weighted averages for a ΔI=1 or a ΔI=2 transition.

Observed transition multipolarity	R_{DCO}, ΔI=1 $E1$ gate	R_{DCO}, ΔI=2 $E2$ gate	R_{DCO}, ΔI=1 mixed $M1/E2$ gate
ΔI=2 $E2$	1.52(8)	1.08(4)	1.32(6)
ΔI=1 $E1$	–	0.70(4)	0.81(4)
ΔI=1 mixed $M1/E2$	1.22(6)	0.75(4)	0.90(5)

Table 4.2: Extracted weighted averages of efficiency corrected DCO ratios in ^{113}In for $E1$, $E2$ and ΔI=1 transitions when gated by transitions of the same or differing multipolarity.

Anisotropies

By comparing the difference between statistics in the two efficiency corrected ring spectra for a given peak, a ratio of anisotropy can be obtained as discussed in section 3.3.1. This ratio can then be compared with values obtained for known transitions in neighbouring nuclei to determine the multipolarity of the transition.

Anisotropy values (A_2) were obtained for previously known transitions in ^{113}In [14] and are shown in figure 4.10. Clear separation is seen between ΔI=1 and ΔI=2 transitions, with the weighted average for the measured anisotropies for ΔI=2 quadrupole transitions being +0.18(10), compared to −0.11(9) obtained for ΔI=1 dipole transitions.

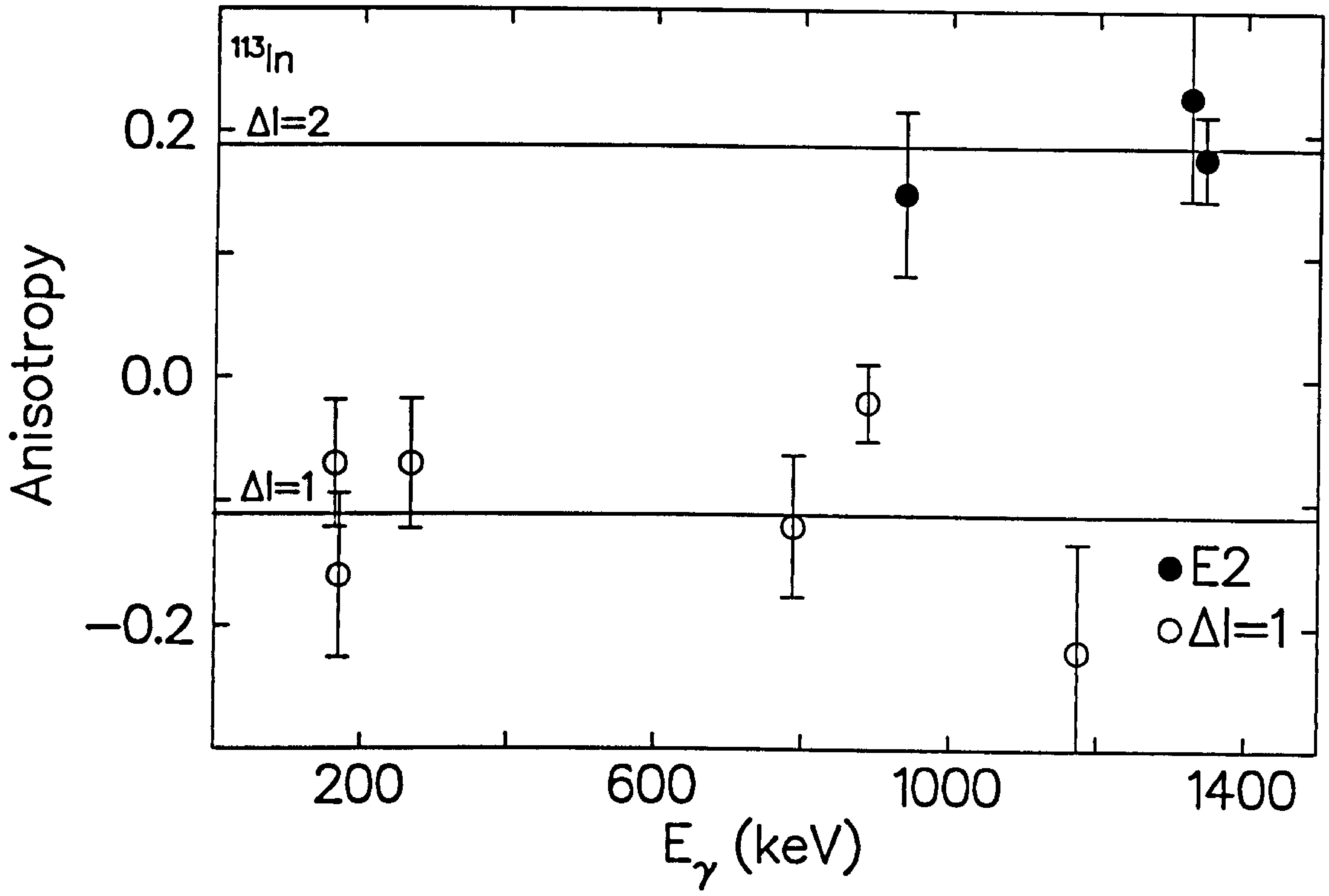

Figure 4.10: Extracted γ-ray anisotropies for known transitions in ^{113}In. The horizontal lines correspond to the weighted average of a ΔI=1 or ΔI=2 transition.

4.3 Analysis of Indium Nuclei

4.3.1 ^{112}In

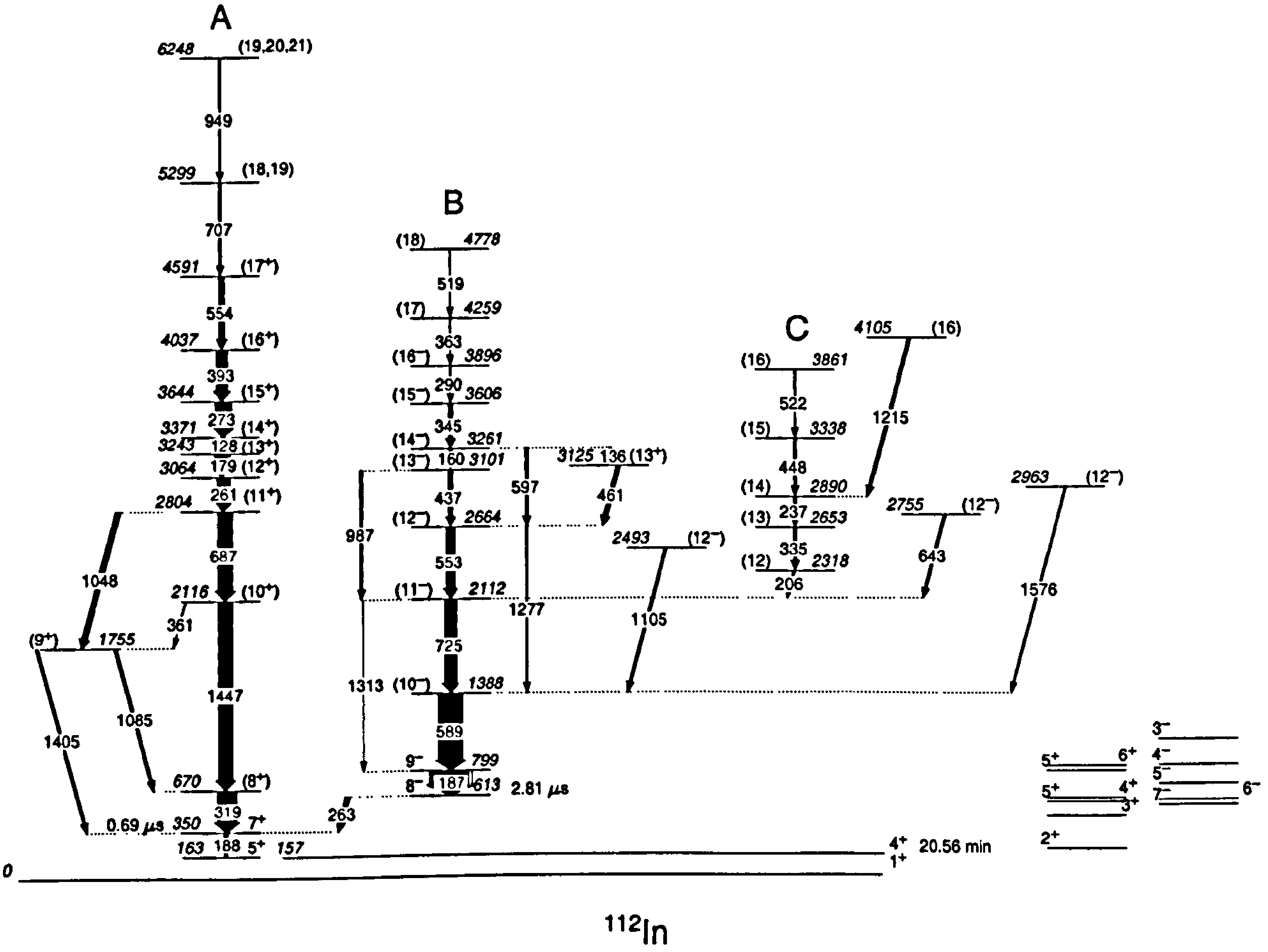

Figure 4.11: Level scheme of ^{112}In observed in this work, and to the right, the previously reported, states of known spin and parity that were unobserved in this work.

A level scheme for ^{112}In deduced from the 50 MeV dataset is shown in figure 4.11 along with the low-lying non-yrast states (of established spin and parity) that were not observed in the current work [93, 94]. The transitions associated with ^{112}In together with their intensity, spin assignment, anisotropy and efficiency corrected DCO ratio are summarized in Table 4.3.

Prior to this study, states had been observed in the nucleus ^{112}In up to an excitation energy of 1388 keV and spin (10^-) using a ^{108}Pd(^{7}Li,3n)^{112}In reaction [16]. Low-lying non-yrast states were populated by the use of ^{112}Cd(p,n)^{112}In and ^{109}Ag(α,n)^{112}In reactions [93, 94]. The two microsecond isomers were measured by the use of energy gated γ growth-decay curves using data from ^{109}Ag(α,n)^{112}In and ^{112}Cd(p,n)^{112}In reactions. The $I^\pi=8^-$ isomeric state at E_x=613 keV was subsequently assigned a lifetime of $T_{\frac{1}{2}}$=2.81 μs [95] and the $I^\pi=7^+$ isomeric state at E_x=350 keV assigned a lifetime of $T_{\frac{1}{2}}$=0.69 μs [95]. The $I^\pi=4^+$ isomeric state at E_x=157 keV was measured from a γ-decay curve to have a lifetime of $T_{\frac{1}{2}}$=20.56 mins [96]. Subsequent work studied the two isomeric states in further detail and proposed a previously unresolved doublet at the 157 keV level, corresponding to the 4^+ and 5^+ states not being resolved [97]. A changed isomer decay scheme was subsequently adopted which included the 5^+ member of the doublet at an energy of 163 keV, on account of the observation of a 6.3 keV $M1$ transition to the 157 keV state [98].

All the prompt yrast level assignments made in the previous works are in agreement with the decay scheme derived from these data. However, the non-yrast states previously identified are not observed in this work. The low-lying non-yrast states of established spin and parity [93, 94] are shown to the right of the level scheme for reference. The fact that there is no observation of these non-yrast states supports the idea of near-yrast population in heavy-ion fusion evaporation reactions and hence the assumption that when making spin assignments from DCO data, the spins increase with increasing excitation energy.

The 50 MeV in-beam γ–γ data strongly showed the two previously known prompt yrast transitions of 187 and 589 keV and the delayed 188 and 263 keV transitions in ^{112}In as previously displayed in the upper part of figure 4.3. Figure 4.12 shows γ-ray coincidence spectra from the 50 MeV γ–γ matrix (no time conditions) with gates set on these previously identified transitions (187/188, 263 and 589 keV). The labels show the energy of the newly identified coincident peaks in ^{112}In and were in agreement with the transitions identified in the normalised subtractions (figure 4.5) as being associated with A=112.

To further confirm that these newly identified transitions were associated with ^{112}In, gates were set on the γ rays of energy less than 500 keV in a γ–LEPS matrix and the sum of these gates was projected onto the LEPS axis. This LEPS sum is shown in figure 4.15 and the presence of indium X-rays can be seen. Strongly present is the 21.2 keV K_α X-ray line corresponding to $_{46}$Pd, the target material. A 24.0 keV peak is also visible, which is assigned to comprise of both the K_β of $_{46}$Pd (23.8 keV) and the K_α of $_{49}$In (24.1 keV). The energy of the K_β of $_{49}$In is labelled at 27.3 keV, but no peak is obvious in the spectrum.

To assist in the placing of these newly identified transitions within the level scheme, gates were set on the two microsecond isomers. This isomer gating was achieved by setting gates on the previously identified isomeric transitions of 263 keV ($T_{\frac{1}{2}}$=2.81 μs) and 188 keV ($T_{\frac{1}{2}}$=0.69 μs) on the delayed axis of a prompt–delayed matrix and then projecting onto the prompt axis. The "early-delayed" matrix was used in the case of the 0.69 μs isomer and the "late-delayed" matrix was used in the case of the 2.81 μs isomer. This process highlighted the prompt transitions built on the two isomeric states. The resultant spectra are shown in figure 4.13 and show two different decay paths. The spectrum of the 0.69 μs isomer was cleaned by the subtraction of a normalized part of the γ-coincidence gate set on the prompt 187 keV transition situated above both isomers in band B.

By using these two paths, in addition to the γ-ray coincident spectra gated by the previously known transitions, and transitions identified in the excitation functions, it was possible to place the transitions into two bands, Band A, built on the $I^{\pi}=7^{+}$, $T_{\frac{1}{2}}=0.69$ μs isomeric level and Band B, built on the $I^{\pi}=8^{-}$, $T_{\frac{1}{2}}=2.81$ μs isomeric level. By summing double-gated triples spectra for each band, obtained from the 50 MeV γ^3 cube, it was possible to identify further weaker transitions in each band that were not visible in the γ–γ matrices. Figure 4.14 shows the summed double-gated coincidence spectra of both band A and band B using the 50 MeV γ^3 cube. Due to lack of statistics recorded in the 28 and 40 MeV datasets, only the 50 MeV γ^3 cube was found to give any improvement over the γ–γ analysis.

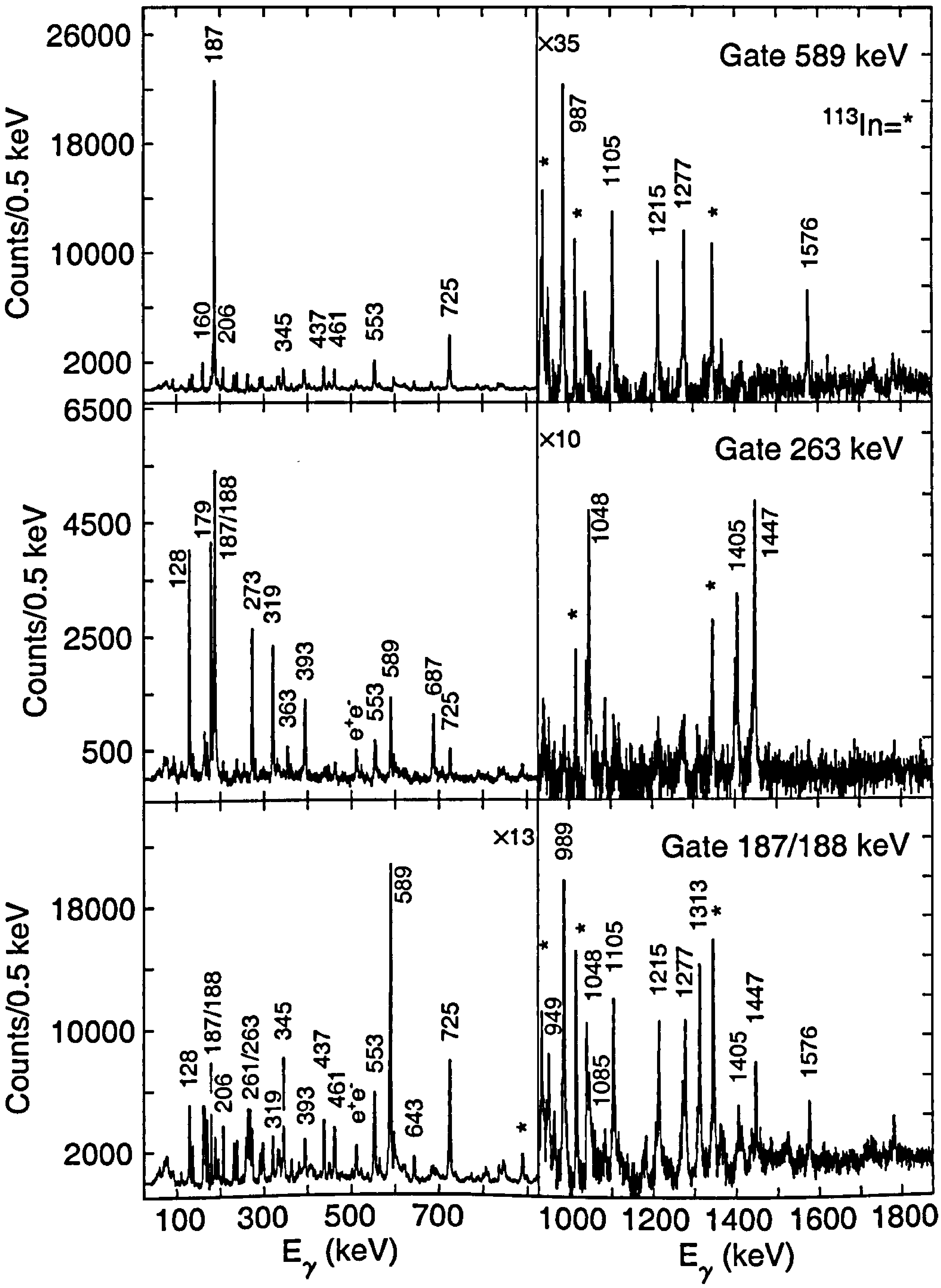

Figure 4.12: Gamma-ray coincidence spectra of ^{112}In, gated by the previously known transitions of 187/188, 263 and 589 keV. The labelled lines correspond to newly identified transitions in ^{112}In.

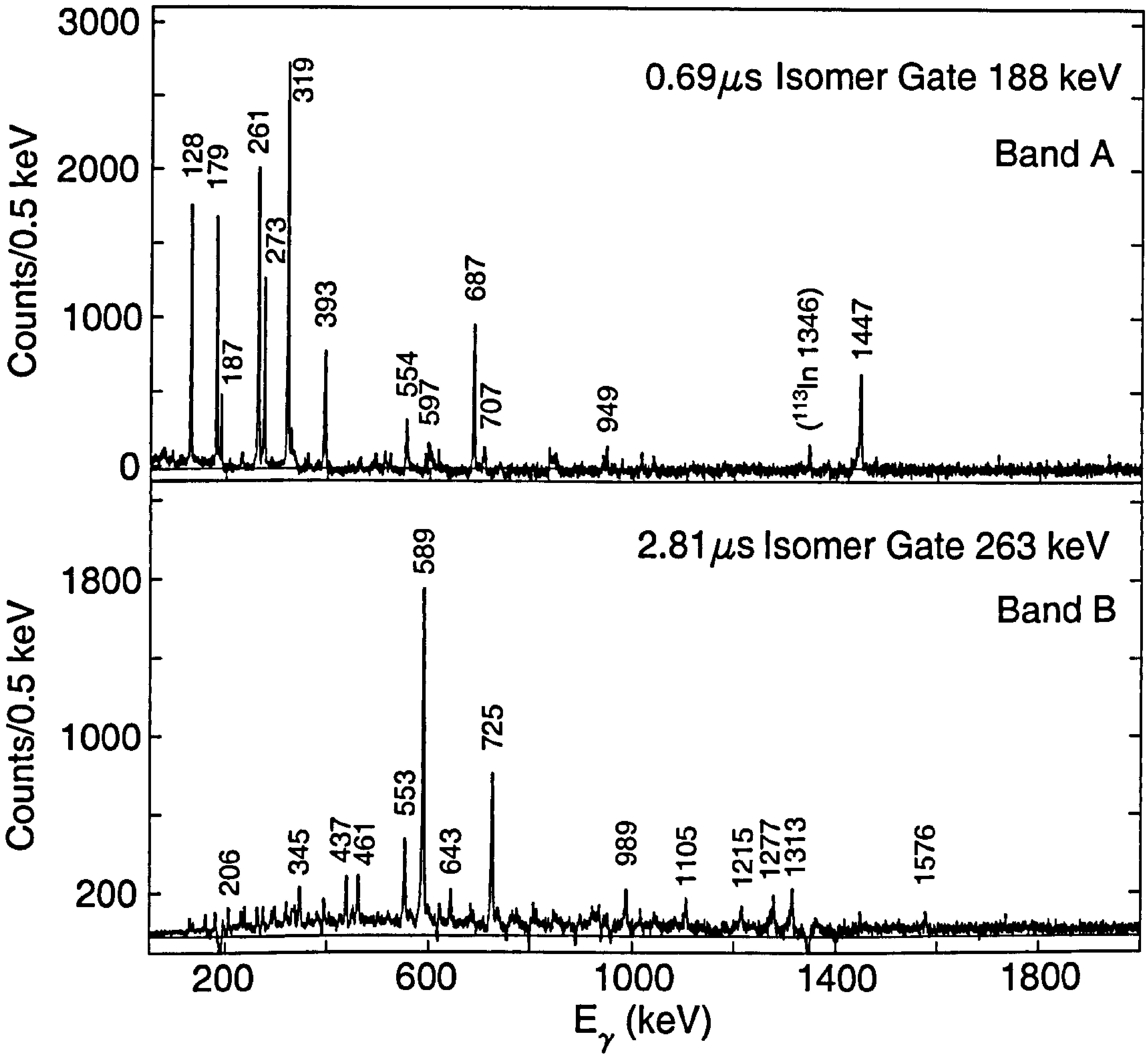

Figure 4.13: Isomer gated γ coincidence spectra highlighting the two different decay paths in ^{112}In. See text for gating conditions. The labelled lines correspond to newly identified transitions in ^{112}In.

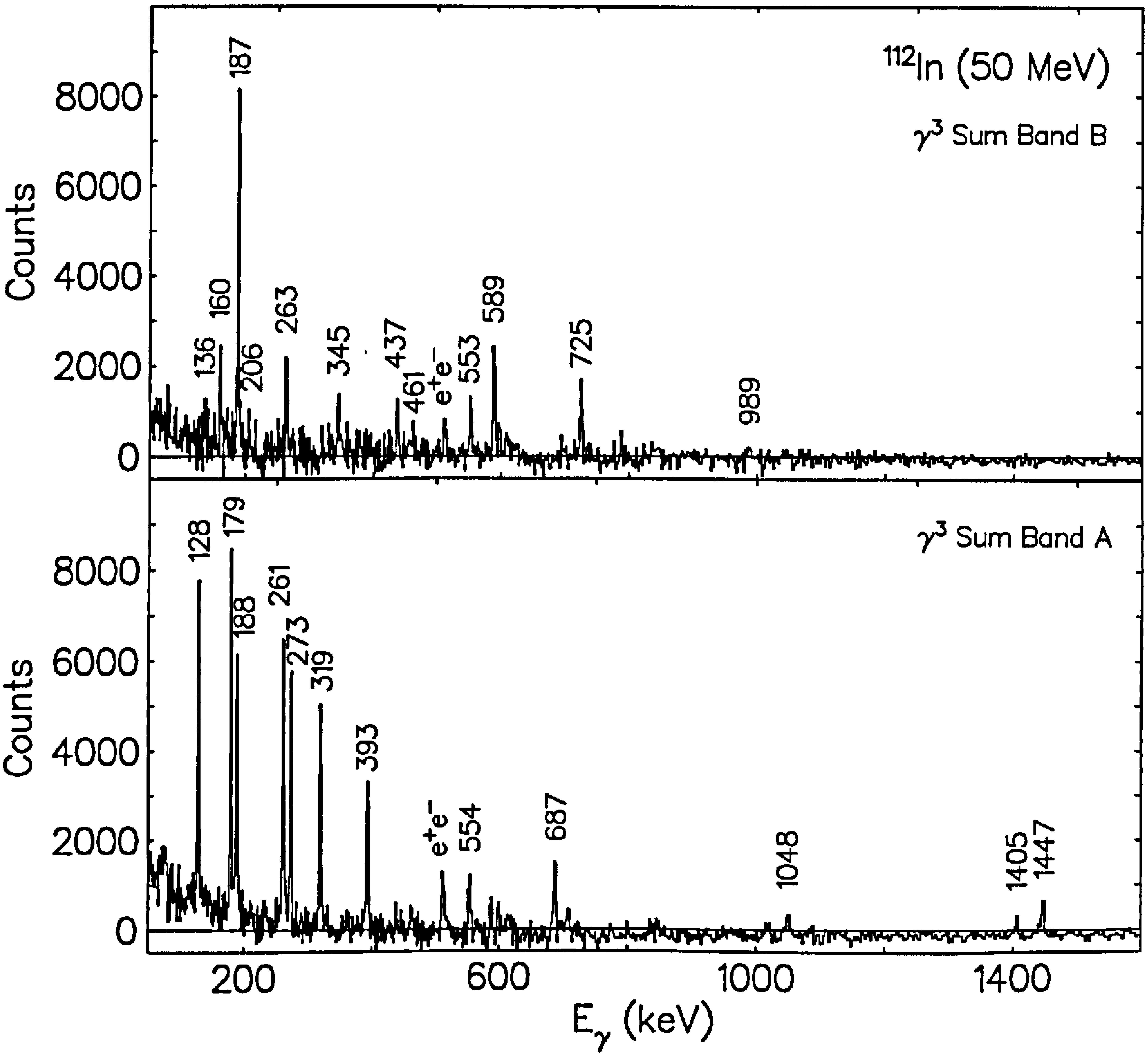

Figure 4.14: Sum of double-gated γ coincidence spectra in ^{112}In, identifying transitions in band A (bottom) and band B (top). The labelled lines correspond to newly identified transitions in ^{112}In.

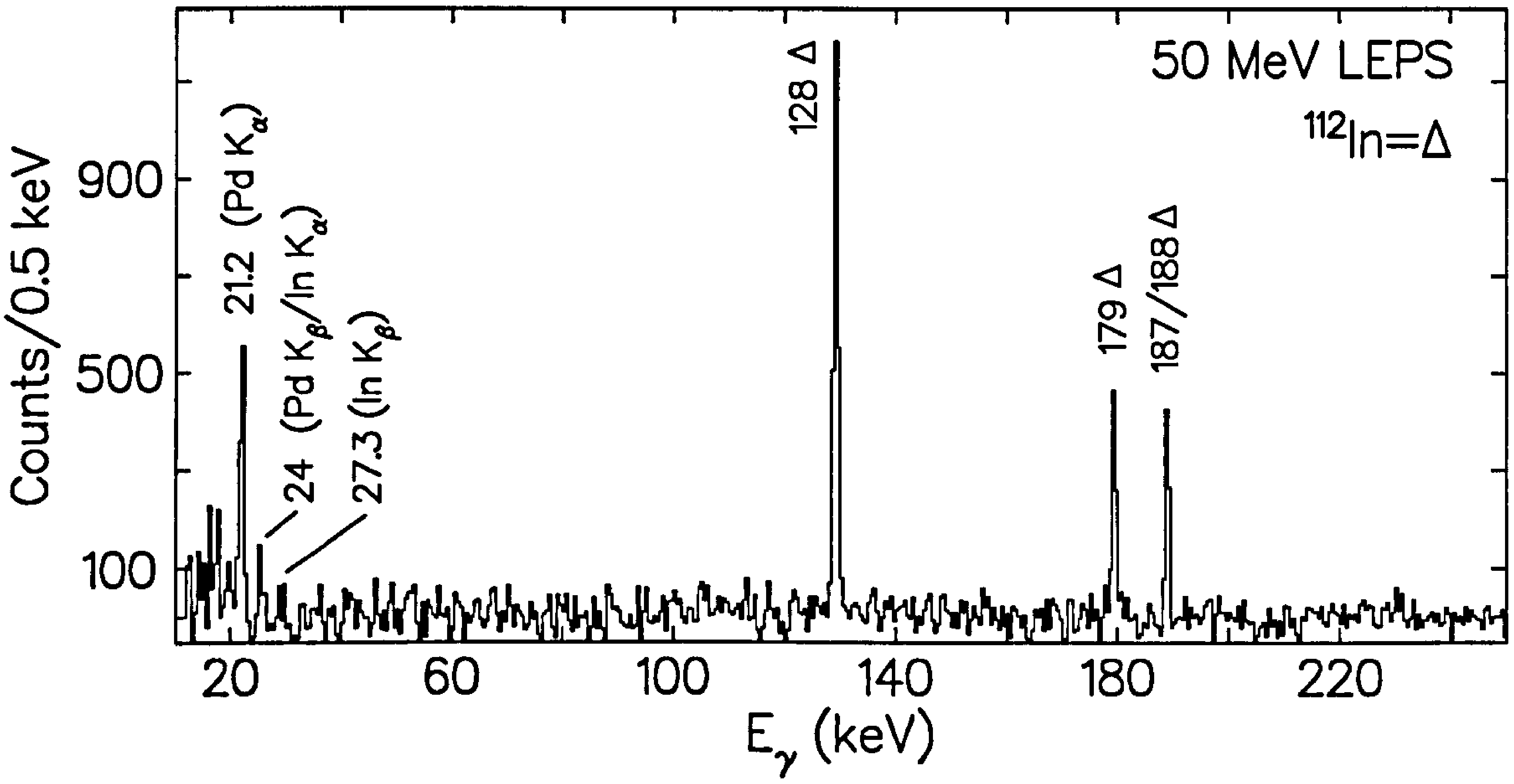

Figure 4.15: Summed LEPS coincidence spectrum gated by dipole band transitions in ^{112}In.

Band A

The sequence of γ rays labelled band A in figure 4.11 consists of a positive parity band with a $I^{\pi}=7^{+}$ bandhead at 350 keV. The multipolarity of the 188 keV transition was previously shown to be $E2$ [99], but due to its isomeric nature, it is unsuitable for use in DCO analysis. Spins and parities were assigned to levels by use of DCO ratios and anisotropic values by comparing the measured values to those obtained for transitions of established multipolarity in ^{113}In. The 319 keV transition when gated by a ΔI=1 transition had a measured DCO ratio of 1.00(8), and when gated by an $E2$, had a ratio of 0.63(6), both values indicating a ΔI=1 nature. An anisotropy measurement of −0.06(4) is in agreement with this assignment. The 1447 keV transition had a measured DCO ratio of

1.59(26) when gated by a $\Delta I=1$ transition and anisotropic value of +0.23(10), both being consistent with that of an $E2$ transition. The 687 keV and transitions built above $I^{\pi}=(11^{+})$ were consistent with being $\Delta I=1$ in nature, suggesting a cascade of dipole transitions. The members of the dipole cascade were confirmed with their coincidence with the 1405 keV transition, and the 319 keV transition was confirmed to not be a member of the dipole cascade as it was not in coincidence with the 1405 keV transition. The ordering of the 261, 179, 128 and 273 keV transitions is tentative as their intensities are similar within experimental uncertainties. No competing $E2$ crossover transitions were observed in band A, nor were any transitions linking to or from band B.

Figure 4.16 shows γ-ray coincidence gates set on the newly identified transitions of 319, 1447, 687 and 261 keV. The transitions that comprise band A can clearly be seen. The 261 and 319 keV gates display a 1048 keV transition, which from mutual coincidences, was revealed to decay from $\mathrm{I}^{\pi}=(11^{+})$ and when gated by a $\Delta I=1$, the DCO ratio was measured to be 1.85(38) strongly indicating an $E2$ nature, further confirmed by the anisotropic value of +0.19(10). The 261 keV gate also showed 1405 and 1085 keV lines, which were placed into the level scheme by further gating on the 1048, 1405 and 1085 keV transitions, as shown in figure 4.17. The 1405 keV transition had a measured DCO ratio of 1.59(33) and a anisotropy of +0.32(21), consistent with it being an $E2$ transition and decaying to the $\mathrm{I}^{\pi}=7^{+}$ level. The 1085 keV transition, on account that it was observed to be coincident with the 261 and 1048 keV transitions but not the 1405 or 1447 keV transitions, was placed decaying from the $\mathrm{I}^{\pi}=(9^{+})$ level to the $\mathrm{I}^{\pi}=(8^{+})$. The DCO ratio of the 1085 keV transition when gated by a $\Delta I=1$ is 0.92(14), consistent with its placement in the level scheme as a $\Delta I=1$ transition.

A weak 361 keV transition was observed in coincidence the 319, 1085 and

1405 keV transitions and was placed decaying from the $I^{\pi}=(10^{+})$ state to the $I^{\pi}=(9^{+})$. Due to its relative weakness, no measure could be made of its DCO ratio or anisotropy.

The 707 and 949 keV transitions were too weak to allow DCO or anisotropic analysis and thus in the current work have been assigned as $\Delta I=1$ or $\Delta I=2$. If these transitions were to be $E2$ in character, then this would enable a possible 521 keV $E1$ transition between $E_x=5299$ in band A and $E_x=4778$ in band B which would explain the yrast feeding of band B. However, this 521 keV transition could not be resolved from the 519 keV transition in band B and the 522 keV transition in band C.

Figure 4.18 shows the obtained DCO ratios of the transitions in band A and figure 4.19 shows the measured anisotropies of all transitions in ^{112}In with sufficient statistics to allow measurement.

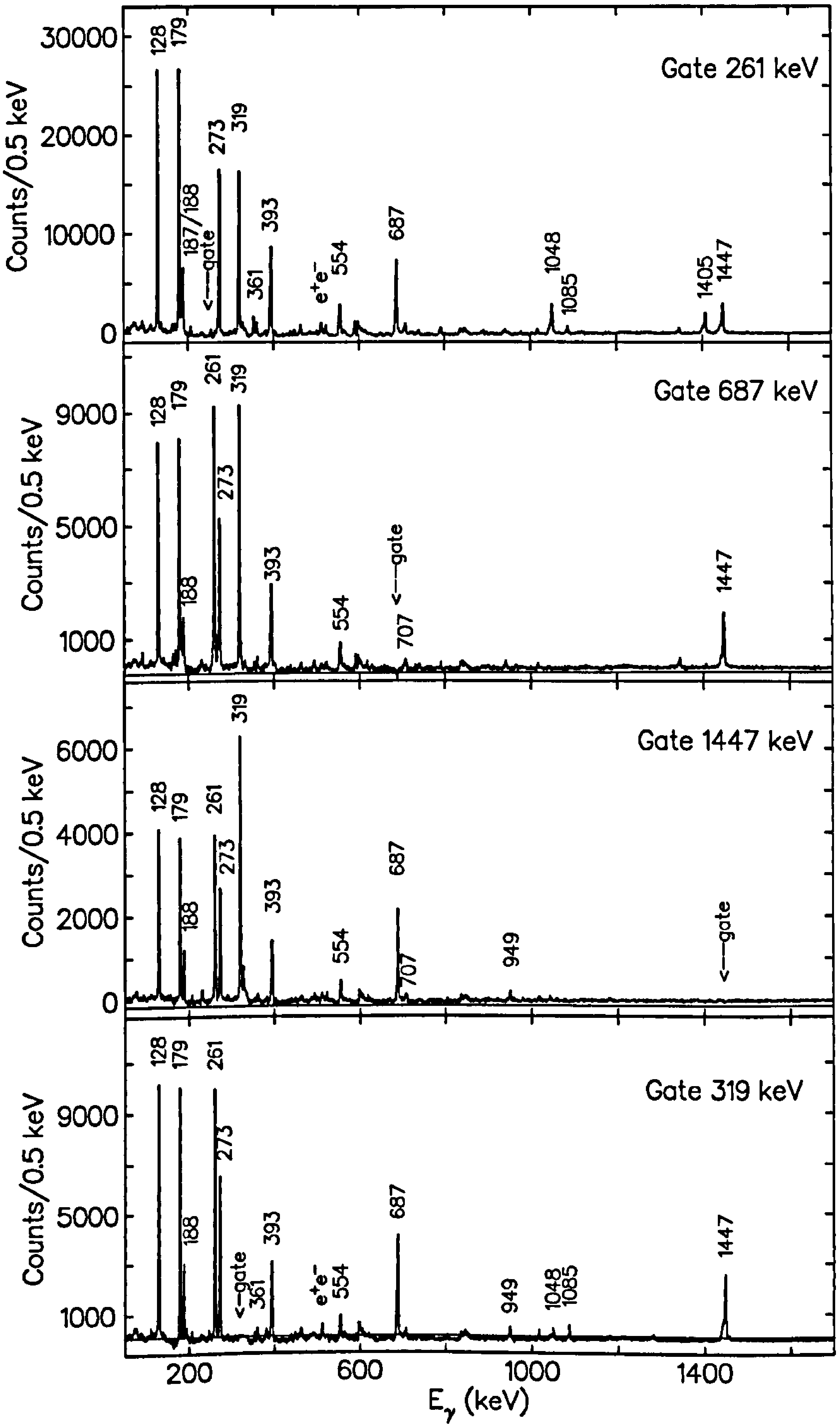

Figure 4.16: Gamma-ray coincidence spectra, gated by newly identified transitions in band A of ^{112}In.

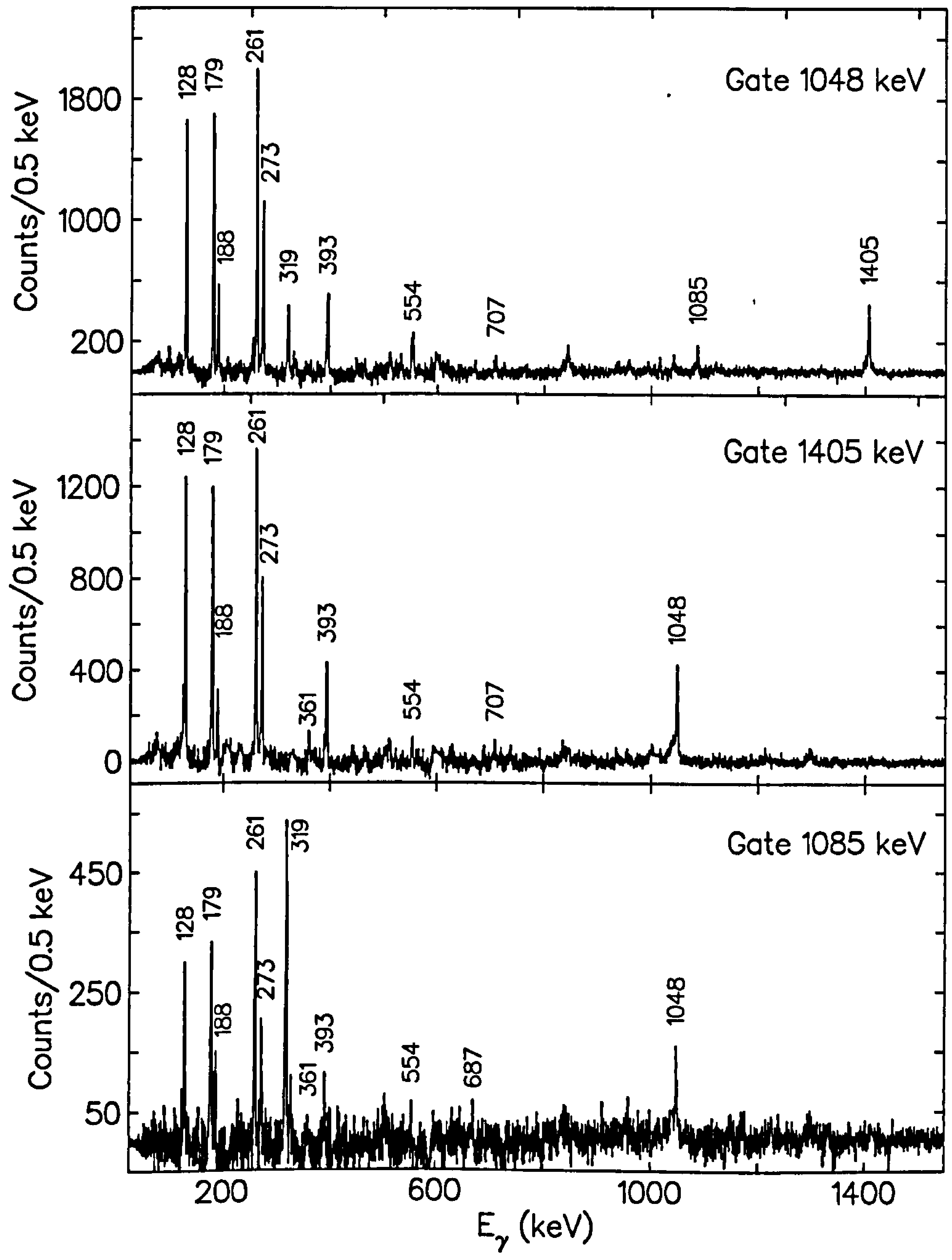

Figure 4.17: Gamma-ray coincidence spectra, gated by newly identified transitions in ^{112}In.

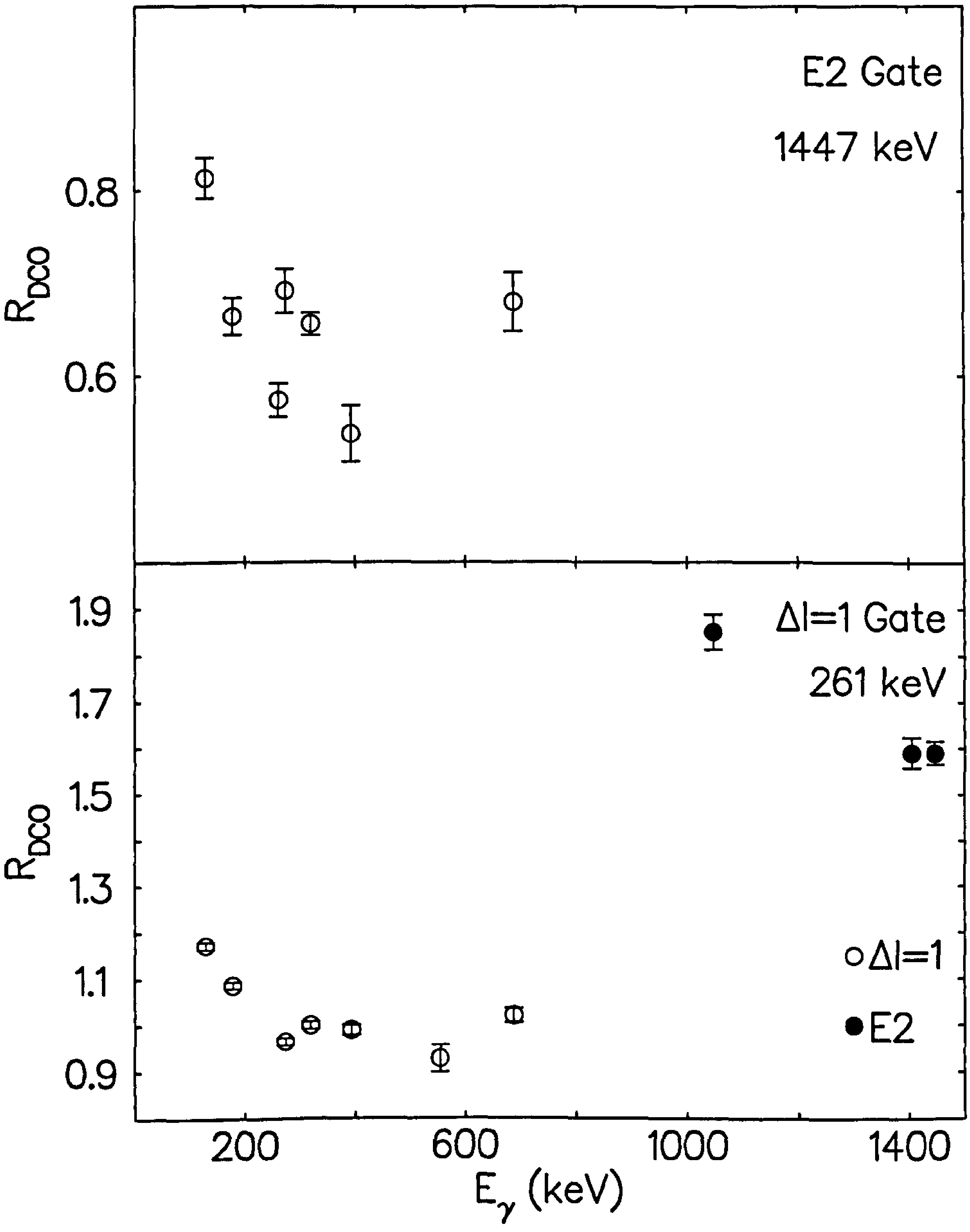

Figure 4.18: Extracted DCO ratios of transitions observed in band A of ^{112}In, gated by a ΔI=2 quadrupole and a ΔI=1 dipole.

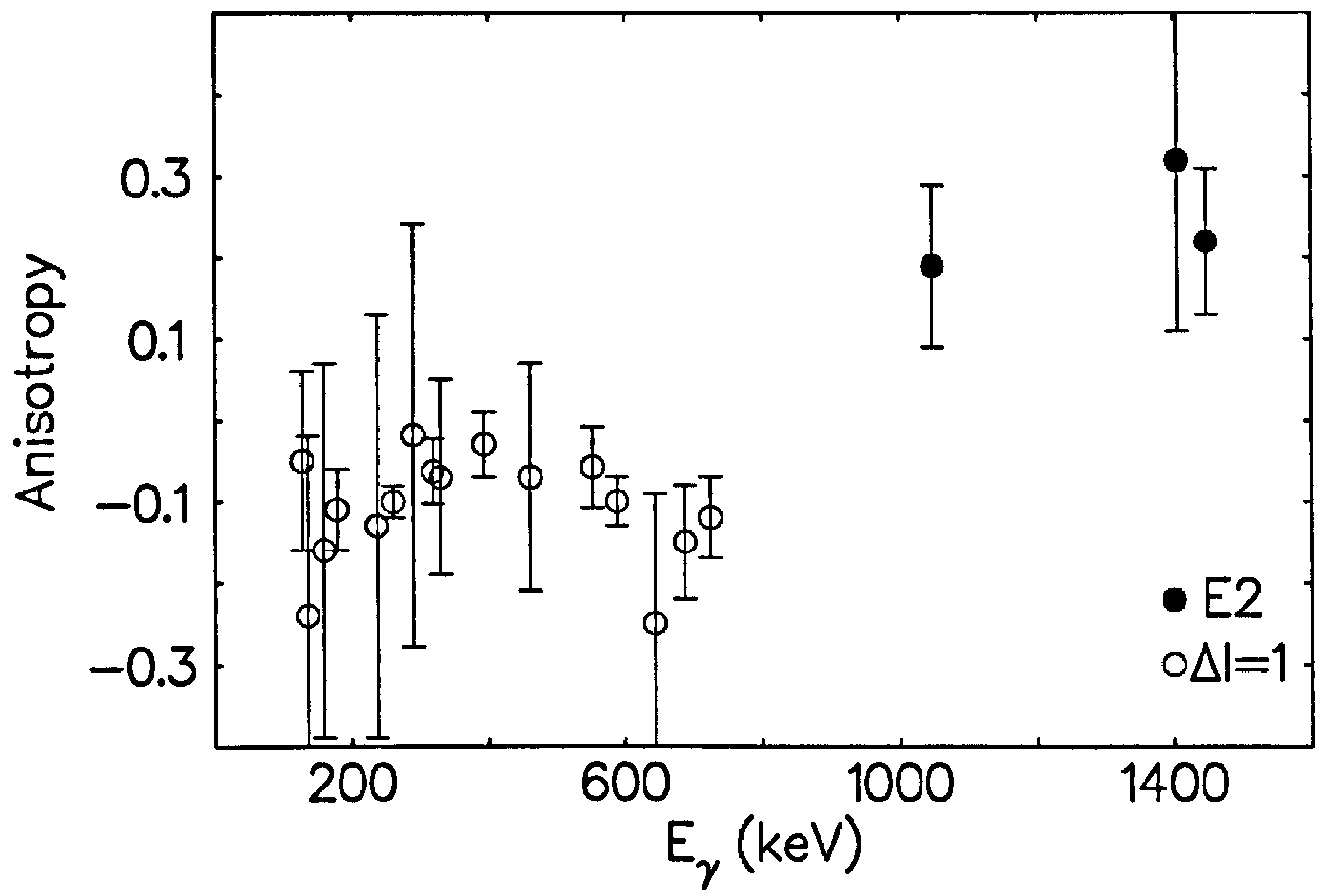

Figure 4.19: Extracted γ-ray anisotropies of transitions observed in both band A and band B of ^{112}In.

Band B

Band B is built on a $I^{\pi}=8^{-}$ bandhead at 613 keV. The 263 keV isomeric transition has previously been established to be $M2$ in character [98] and the 589 keV transition has been tentatively assigned as $M1$ [16]. Figure 4.20 shows gamma-ray coincidence gates set on the newly identified transitions of 725, 437 and 345 keV. Four crossover transitions are observed in band B which confirm the ordering of the transitions in the lower part of the band. DCO ratios and anisotropy values confirm that these crossover transitions are of $E2$ multipolarity. Further transitions were also observed feeding into band B, in particular the 461 and 136 keV γ rays. From DCO ratios, these transitions are $\Delta I=1$ in nature and have been assigned as parity changing $E1$ transitions, although other multipolarities cannot specifically be ruled out.

Three other transitions were found to feed into band B, and DCO analysis showed the 1105 and 1576 keV transitions to be $E2$ in nature and the 643 keV transition to be $\Delta I=1$ transition.

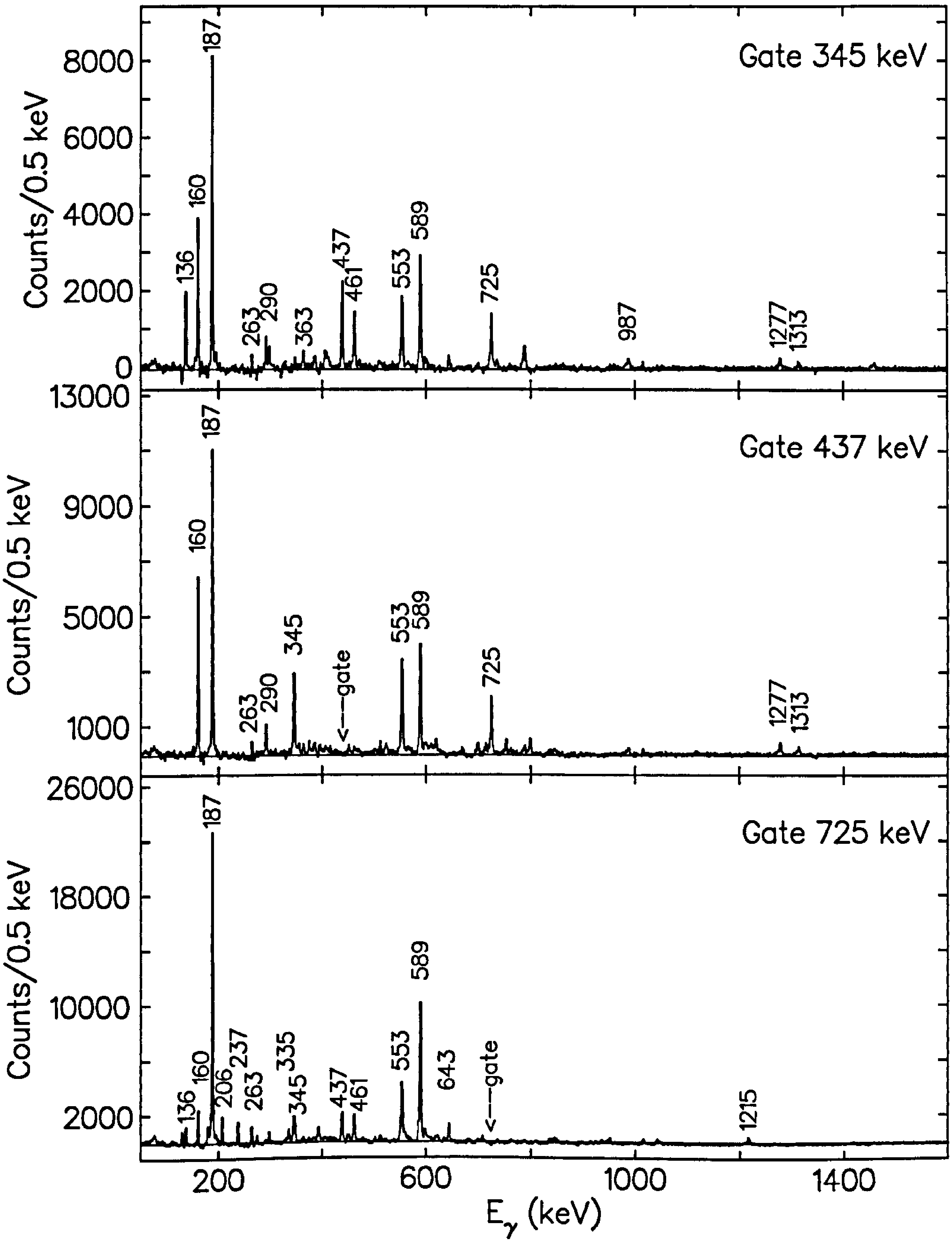

Figure 4.20: Gamma-ray coincidence spectra, gated by newly identified transitions in band B of ^{112}In.

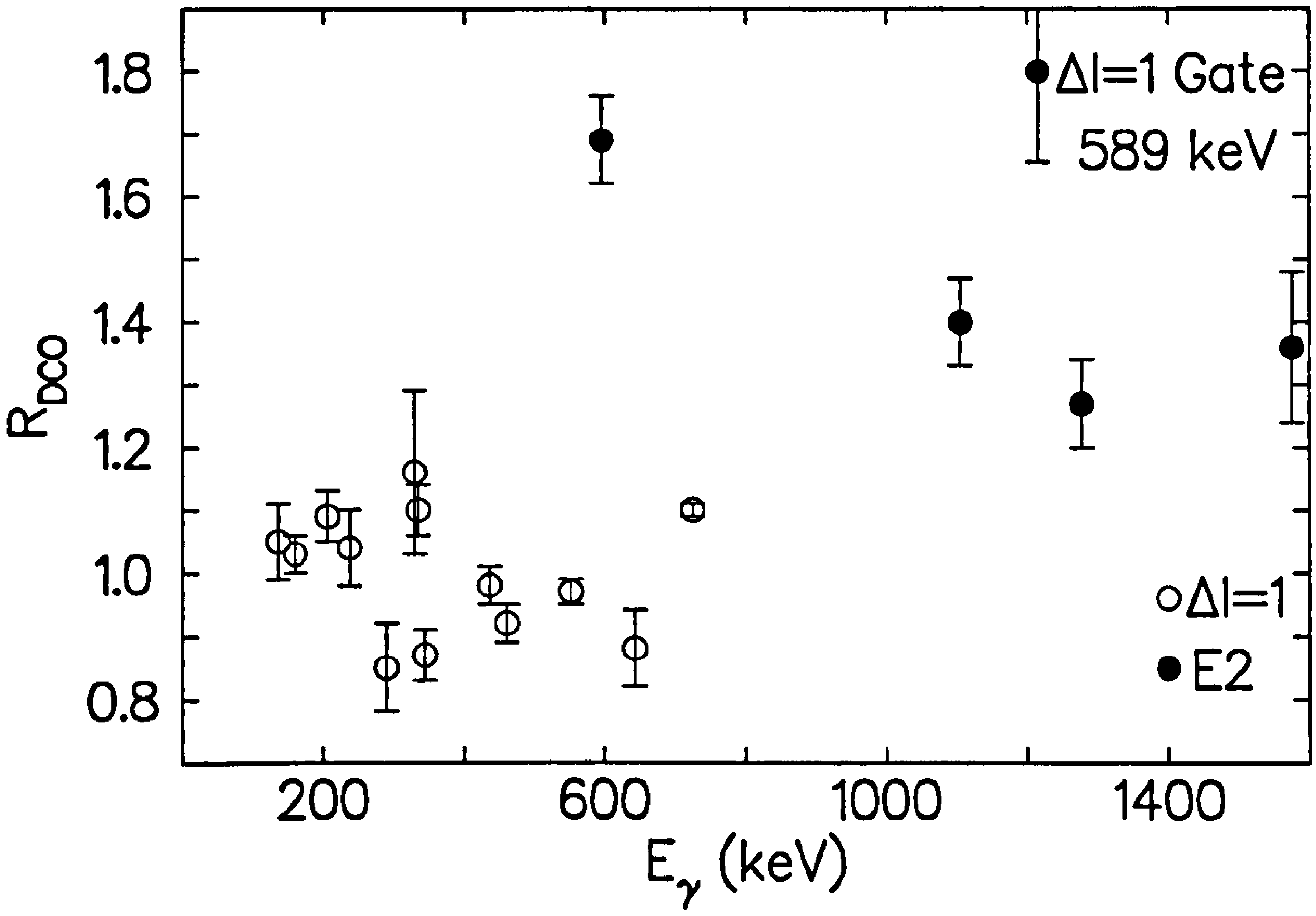

Figure 4.21: Extracted DCO ratios of transitions observed in band B of ^{112}In, gated by the 589 keV ΔI=1 transition.

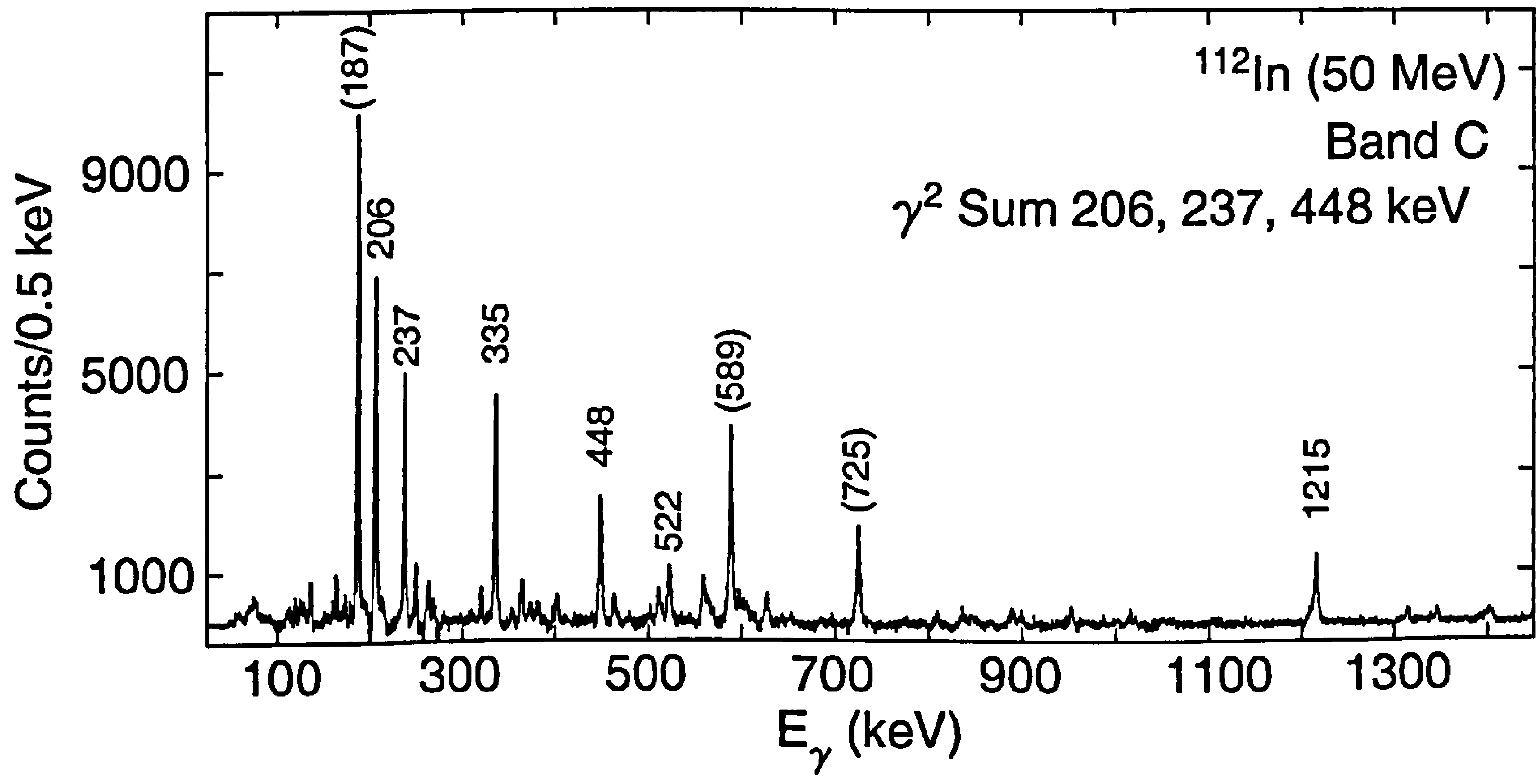

Figure 4.22: Sum of gamma-ray gated coincidence gates in band C of ^{112}In, highlighting further transitions in this band. The bracketed transitions are associated with band B

Band C

A third band of ΔI=1 transitions was identified feeding into the I^{π}=(11$^-$) level of band B at E_x=2112 keV. Figure 4.22 shows a sum of γ-ray coincidence gates set on transitions in band C. DCO analysis resulted in the 206, 335 and 448 keV lines being assigned to be ΔI=1 transitions and the 1215 keV transition that feeds into band C at E_x=2890 keV to be $E2$. No parity has been assigned to band C due to the unknown electromagnetic assignment of the 206 keV transition. However, a positive parity nature for band C is preferred (whereby the 206 keV transition is $E1$ in nature) due to the lack of an $E2$ transition between E_x=2318 and E_x=1388 keV.

Table 4.3: Gamma rays assigned to ^{112}In in the current work. The relative γ-ray intensities are normalized to 100 for the 589 keV transition. The 187.6 and 262.6 keV transitions are observed in the delayed γ spectra and thus their prompt intensities are not given. Note, the placement of the 187.6 and 262.6 keV transitions in the level scheme has been established in previous works [16, 95].

E_γ (keV)	I_γ Prompt	E_i (keV)	E_f (keV)	I_i^π	I_f^π	R_{DCO}	A_2
128.4(3)	52(6)	3371	3243	(14$^+$)	(13$^+$)	1.07(8)^1 0.71(11)^2	−0.05(11)
135.7(5)	12(5)	3261	3125	(14$^-$)	(13$^+$)	1.05(6)^3	−0.24(22)
159.7(4)	15(5)	3261	3101	(14$^-$)	(13$^-$)	1.03(3)^3	−0.16(23)
178.5(3)	57(6)	3243	3064	(13$^+$)	(12$^+$)	1.08(7)^1 0.63(10)^2	−0.11(5)
186.5(4)	153(27)	799	613	9$^-$	8$^-$		

Table 4.3 continued: Gamma rays assigned to ^{112}In in the current work

E_γ (keV)	I_γ Prompt	E_i (keV)	E_f (keV)	I_i^π	I_f^π	R_{DCO}	A_2
187.6(3)	–	350	163	7^+	5^+		
205.9(5)	9(4)	2318	2112	(12)	(11)	1.10(4)[3]	−0.07(4)
237.0(4)	10(4)	2890	2653	(14)	(13)	1.05(7)[3]	−0.13(26)
260.7(3)	63(9)	3064	2804	(12^+)	(11^+)	0.92(6)[5]	−0.10(2)
262.6(3)	–	613	350	8^-	7^+		
272.7(3)	57(7)	3644	3371	(15^+)	(14^+)	0.97(8)[1] 0.65(13)[2]	−0.06(23)
290.1(8)	5(4)	3896	3606	(16^-)	(15^-)	0.85(7)[3]	−0.02(26)
319.4(4)	84(13)	670	350	(8^+)	7^+	1.00(8)[1] 0.63(6)[2]	−0.06(4)
335.0(5)	10(5)	2653	2318	(13)	(12)	1.11(5)[3]	−0.36(23)
344.7(4)	14(7)	3606	3261	(15^-)	(14^-)	0.87(4)[3]	
361.0(17)	<2	2116	1755	(10^+)	(9^+)	0.97(11)[1]	−0.08(4)
362.8(11)	4(4)	4259	3896	(17)	(16^-)		
393.3(3)	44(8)	4037	3644	(16^+)	(15^+)	1.00(11)[1] 0.57(15)[2]	−0.03(4)
437.1(4)	18(7)	3101	2664	(13−)	(12^-)	0.98(3)[3]	
448.2(6)	7(4)	3338	2890	(15)	(14)		
461.2(5)	15(6)	3126	2664	(13^+)	(12^-)	0.92(3)[3]	−0.07(15)
519.4(29)	<2	4778	4259	(18)	(17)		
522.4(11)	5(5)	3861	3338	(16)	(15)		
552.5(4)	36(6)	2664	2112	(12^-)	(11^-)	0.98(2)[3]	−0.06(5)

Table 4.3 continued: Gamma rays assigned to ^{112}In in the current work

E_γ (keV)	I_γ Prompt	E_i (keV)	E_f (keV)	I_i^π	I_f^π	R_{DCO}	A_2
554.4(3)	26(5)	4591	4037	(17$^+$)	(16$^+$)	0.93(29)[1]	
588.5(1)	100(7)	1388	799	(10$^-$)	9$^-$	0.97(2)[4]	−0.10(3)
596.7(10)	11(8)	3261	2664	(14$^-$)	(12$^-$)	1.69(8)[3]	
643.1(10)	9(5)	2755	2112	(12$^-$)	(11$^-$)	0.89(6)[3]	−0.24(16)
687.3(4)	54(6)	2804	2166	(11$^+$)	(10$^+$)	1.02(15)[1]	−0.15(7)
						0.64(16)[2]	
707.4(8)	11(4)	5299	4591	(18,19)	(17$^+$)		
724.5(4)	49(6)	2112	1388	(11$^-$)	(10$^-$)	1.10(2) [3]	−0.11(5)
948.9(13)	6(6)	6248	5299	(19,20,21)	(18,19)		
987.4(11)	5(4)	3101	2112	(13$^-$)	(11$^-$)		
1048.2(4)	21(8)	2804	1755	(11$^+$)	(9$^+$)	1.85(38)[1]	0.19(10)
1084.5(4)	6(4)	1755	670	(9$^+$)	(8$^+$)	0.92(14)[1]	
1105.3(16)	8(6)	2493	1388	(12$^-$)	(10$^-$)	1.40(7) [3]	
1214.7(8)	11(5)	4105	2890	(16)	(14)	1.81(15)[3]	
1277.3(24)	6(5)	2664	1388	(12–)	(10$^-$)	1.27(7) [3]	
1313.0(21)	8(7)	2112	799	(11$^-$)	9$^-$		
1405.1(6)	19(11)	1755	350	(9$^+$)	7$^+$	1.59(33)[1]	0.32(21)
1446.6(6)	64(13)	2116	670	(10$^+$)	(8$^+$)	1.59(26)[1]	0.23(10)
1575.7(26)	4(4)	2963	1388	(12$^-$)	(10$^-$)	1.36(12)[3]	0.22(18)

1 = Gate set on 319 keV (ΔI=1) transition

2 = Gate set on 1447 keV ($E2$) transition

3 = Gate set on 589 keV (ΔI=1) transition

4 = Gate set on 725 keV (ΔI=1) transition

5 = Gate set on 179 keV (ΔI=1) transition

4.3.2 ^{113}In

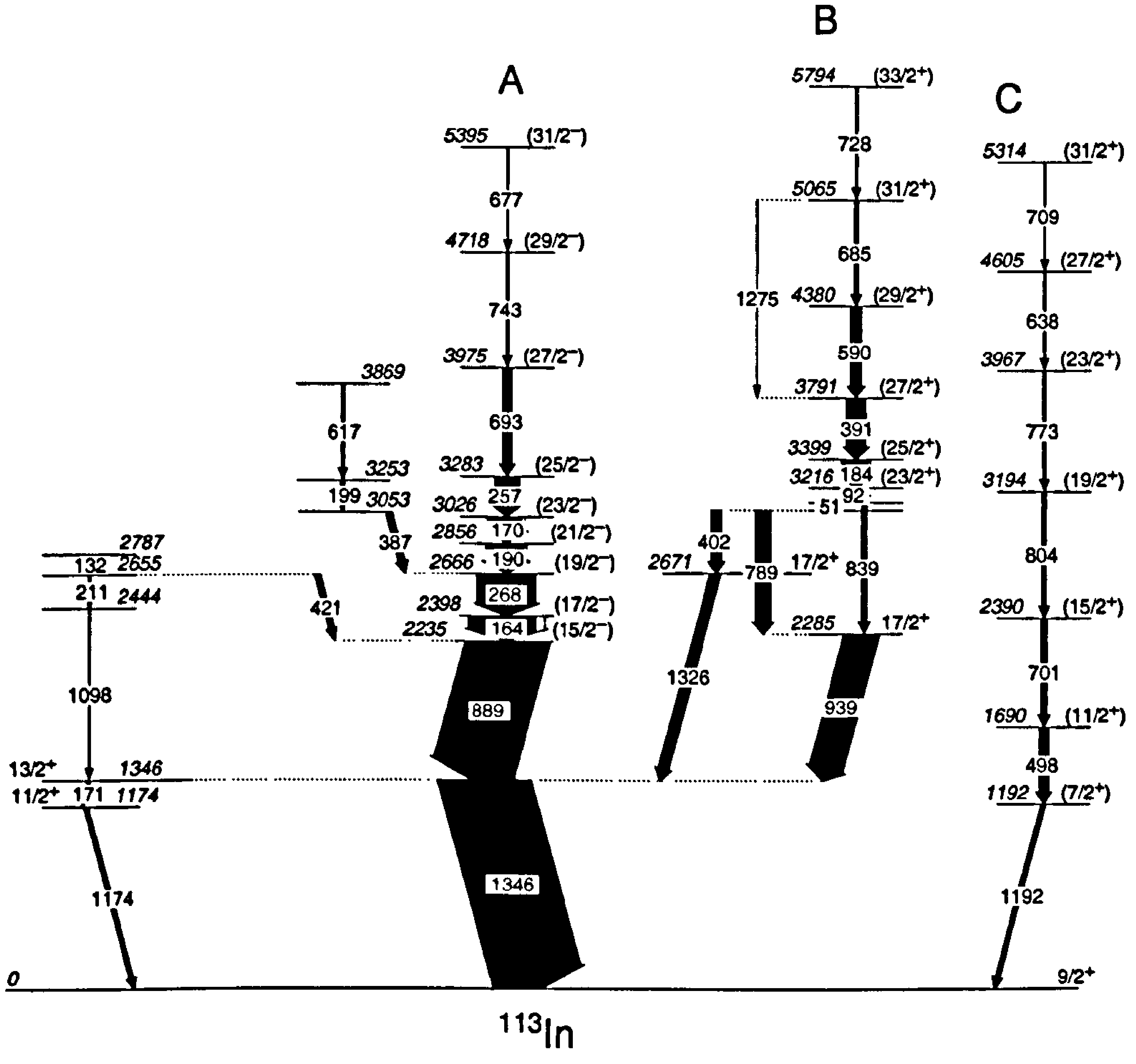

Figure 4.23: Level scheme of transitions observed in ^{113}In in the current work.

A level scheme for ^{113}In deduced from the 40 MeV dataset is shown in figure 4.23. The observed γ-rays with their intensity, spin assignment, anisotropy and efficiency corrected DCO ratio are summarized in Table 4.4. The level scheme is in agreement with the published transitions [14], which were established up to 6.2 MeV in excitation energy and to a tentative spin of (43/2$^-$) using a ^{110}Pd(^{7}Li, 4n)^{113}In reaction at a beam energy of 40 MeV amd in a ^{113}In(α,$\alpha'\gamma$)^{113}In reaction [100]. The current work observes the majority of the previously identified transitions and figure 4.24 shows the gates set on 889 and 939 keV on the 40 MeV γ–γ

matrix and the coincident transitions in ^{113}In are labelled. A sum of transitions in band C suggests a further transition of 709 keV to add to the top of this band (labelled band 7 in reference [14]) as can been seen in lower part of figure 4.25. The upper section of this figure displays the spectrum obtained by gating on the 638 keV transition, previously the highest transition in this band. The 709 keV transition is visible and is assigned as an $E2$ in accordance with the rest of the band.

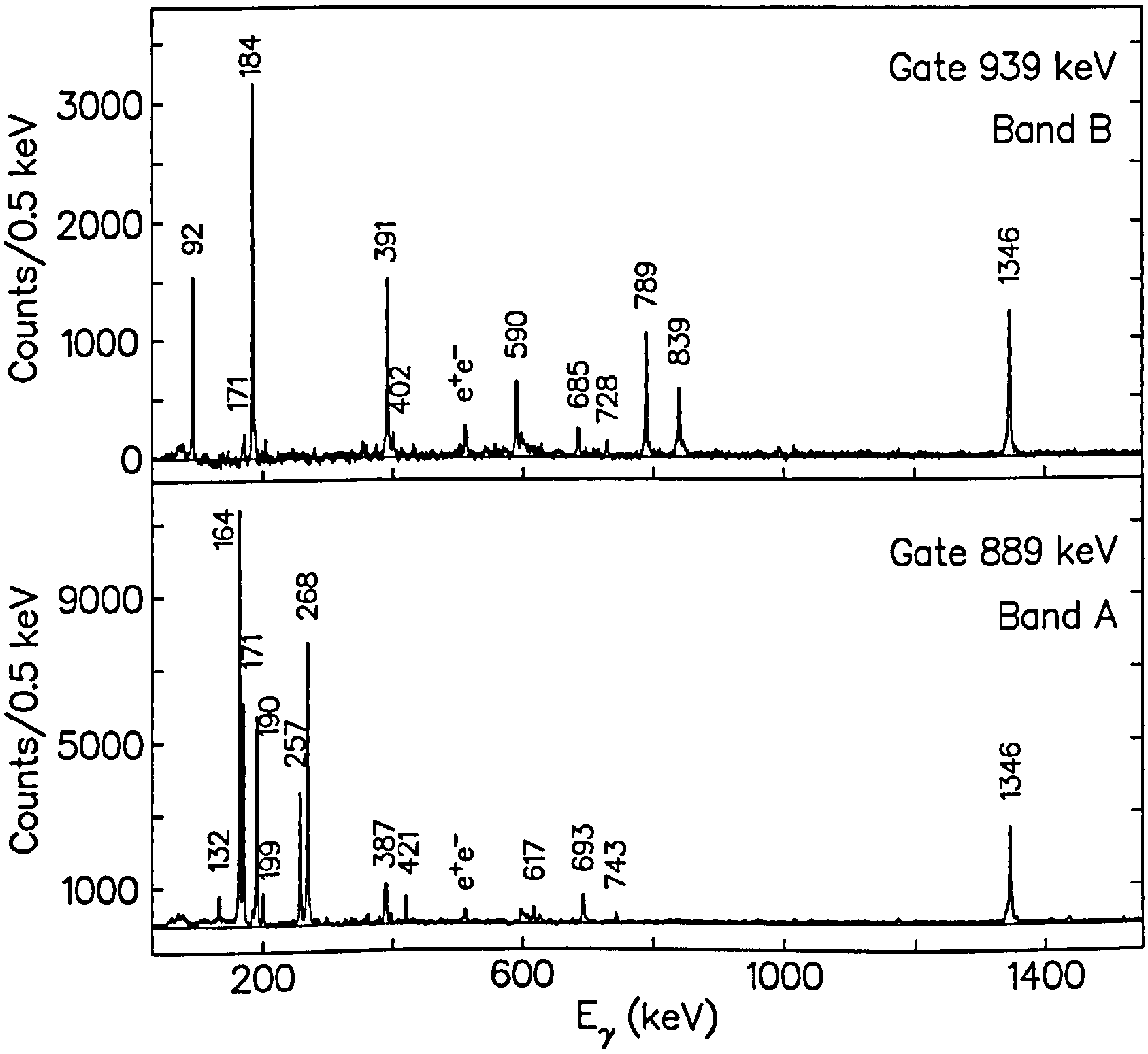

Figure 4.24: Gamma-ray coincidence spectra of ^{113}In.

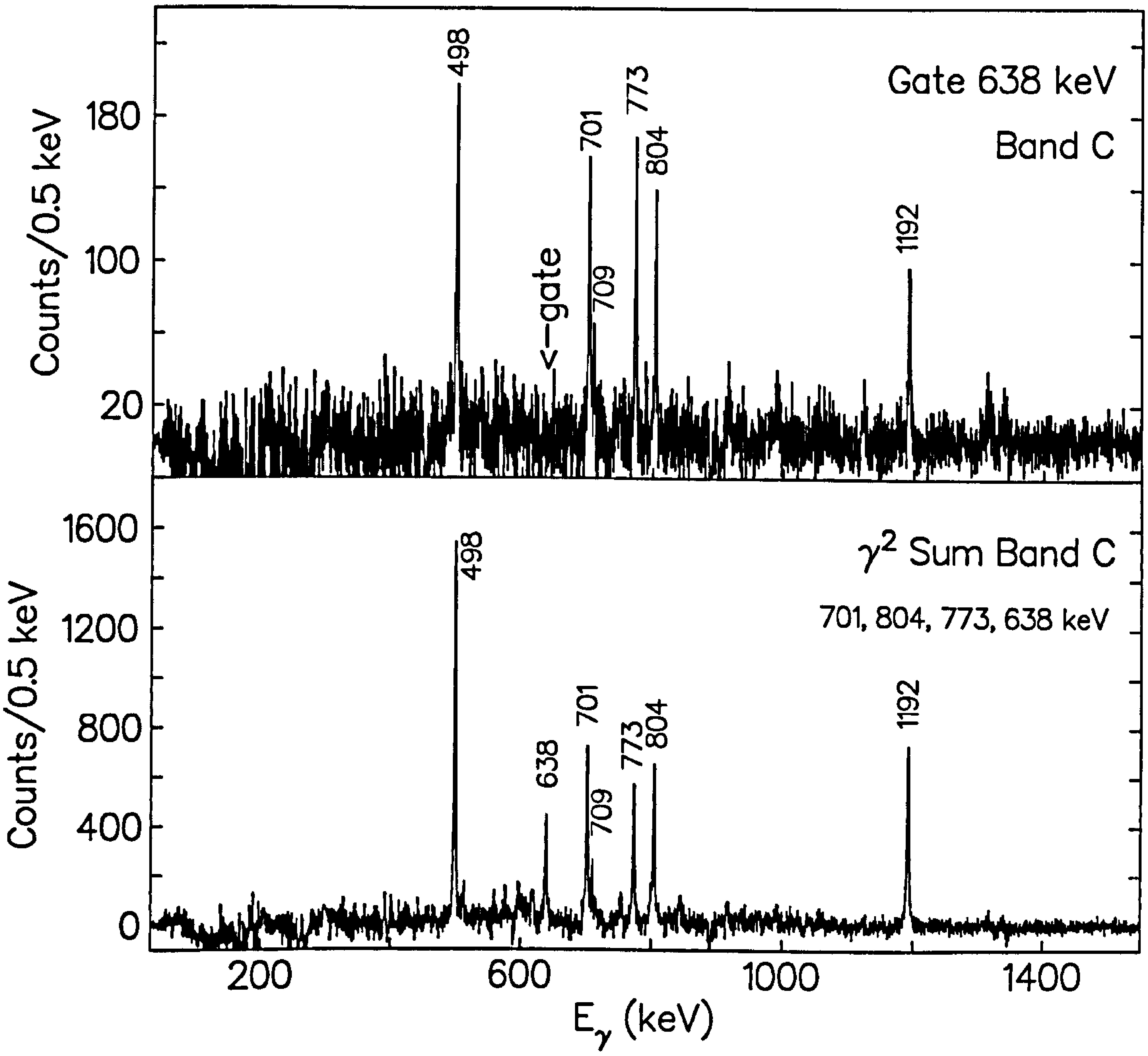

Figure 4.25: Evidence for a 709 keV ($31/2^+$)→($27/2^+$) transition in band C of ^{113}In. Top: γ-ray coincidence spectra gated by 638 keV. Bottom: Summed γ-ray coincidence spectra of band C in ^{113}In.

Table 4.4: Gamma rays assigned to ^{113}In in the current work. The relative γ-ray intensities are normalized to 100 for the 889 keV transition.

E_γ (keV)	I_γ	E_i (keV)	E_f (keV)	I_i^π	I_f^π	R_{DCO}	A_2
50.9(3)	3(3)	3124	3073	$(21/2^+)$	$(19/2^+)$		
91.8(4)	18(4)	3216	3124	$(23/2^+)$	$(21/2^+)$		
131.9(4)	6(4)	2787	2655				
163.5(3)	82(6)	2389	2235	$(17/2^-)$	$(15/2^-)$	0.77(9) [2] 1.25(10) [3]	−0.07(7)
169.6(4)	39(8)	3026	2856	$(23/2^-)$	$(21/2^-)$	0.96(8) [1] 0.78(12) [2] 1.26(15) [3]	−0.18(8)
171.3(3)	4(2)	1346	1174	$13/2^+$	$11/2^+$		
183.5(5)	31(4)	3399	3216	$(25/2^+)$	$(23/2^+)$		
189.9(4)	45(7)	2856	2666	$(21/2^-)$	$(19/2^-)$	0.93(7) [1] 0.83(14) [2] 1.26(15) [3]	
199.4(4)	5(2)	3253	3053				
211.4(7)	2(1)	2655	2444				
257.2(3)	29(2)	3283	3026	$(25/2^-)$	$(23/2^-)$	0.85(8) [2] 0.67(13) [2] 1.16(17) [3]	
267.9(4)	69(4)	2666	2235	$(19/2^-)$	$(17/2^-)$	0.86(6) [1] 0.70(10) [2] 1.12(12) [3]	−0.07(6)

Table 4.4 continued: Gamma rays assigned to ^{113}In in the current work

E_γ (keV)	I_γ	E_i (keV)	E_f (keV)	I_i^π	I_f^π	R_{DCO}	A_2
387.2(3)	9(3)	3053	2666				
391.2(5)	23(4)	3791	3399	$(27/2^+)$	$25/2^+$		
402.1(4)	13(5)	3073	2671	$19/2^+$	$(17/2^+)$		
420.9(8)	7(2)	2655	2235		$(15/2^-)$		
497.5(4)	11(3)	1690	1192	$(11/2^+)$	$(7/2^+)$		
589.7(4)	13(3)	4380	3791	$(29/2^+)$	$(27/2^+)$		
616.9(4)	4(2)	3869	3253				
638.2(11)	2(1)	4605	3967	$(27/2^+)$	$(23/2^+)$		
676.9(13)	<2	5395	4718	$(31/2^-)$	$(29/2^-)$		
685.0(17)	<1	5065	4380	$(31/2^+)$	$(29/2^+)$		
692.6(5)	11(3)	3975	3283	$(27/2^-)$	$(25/2^-)$	0.88(28) [1] 1.25(53) [3]	
700.8(5)	7(1)	2390	1690	$(15/2^+)$	$(11/2^+)$		
708.7(8)	<1	5314	4605	$(31/3^+)$	$(27/2^+)$		
728.4(6)	3(1)	5794	5065	$(33/2^+)$	$(31/2^+)$		
742.6(8)	3(1)	4718	3975	$(29/2^-)$	$(27/2^-)$		
773.0(7)	3(1)	3967	3194	$(23/2^+)$	$(19/2^+)$		
788.6(4)	18(4)	3073	2285	$(19/2^+)$	$17/2^+$		−0.12(10)
803.7(5)	5(2)	3194	2390	$(19/2^+)$	$(15/2^+)$		
839.3(7)	6(3)	3124	2285	$(21/2^+)$	$17/2^+$		

Table 4.4 continued: Gamma rays assigned to ^{113}In in the current work

E_γ (keV)	I_γ	E_i (keV)	E_f (keV)	I_i^π	I_f^π	R_{DCO}	A_2
889.1(2)	100(7)	2235	1346	$(15/2^-)$	$(13/2^+)$	0.81(8) ^{1}	−0.02(4)
						0.70(14) ^{2}	
939.1(4)	43(6)	2285	1346	$17/2^+$	$13/2^+$	1.08(31) ^{2}	0.15(3)
1097.5(12)	2(2)	2444	1346				
1173.7(6)	17(5)	1174	0	$11/2^+$	$9/2^+$		−0.22(14)
1192.0(5)	14(4)	1192	0	$(7/2^+)$	$9/2^+$		
1274.8(6)	<1	5065	3791	$(31/2^+)$	$(27/2^+)$		
1325.6(5)	13(3)	2671	1346	$17/2^+$	$13/2^+$		
1345.5(3)	115(9)	1346	0	$13/2^+$	$9/2^+$	1.32(17) ^{1}	0.24 (17)
						1.53(21) ^{3}	0.19(3)

1 = Gate set on 164 keV (ΔI=1) transition

2 = Gate set on 1346 keV ($E2$) transition

3 = Gate set on 889 keV ($E1$) transition

4.3.3 ^{114}In

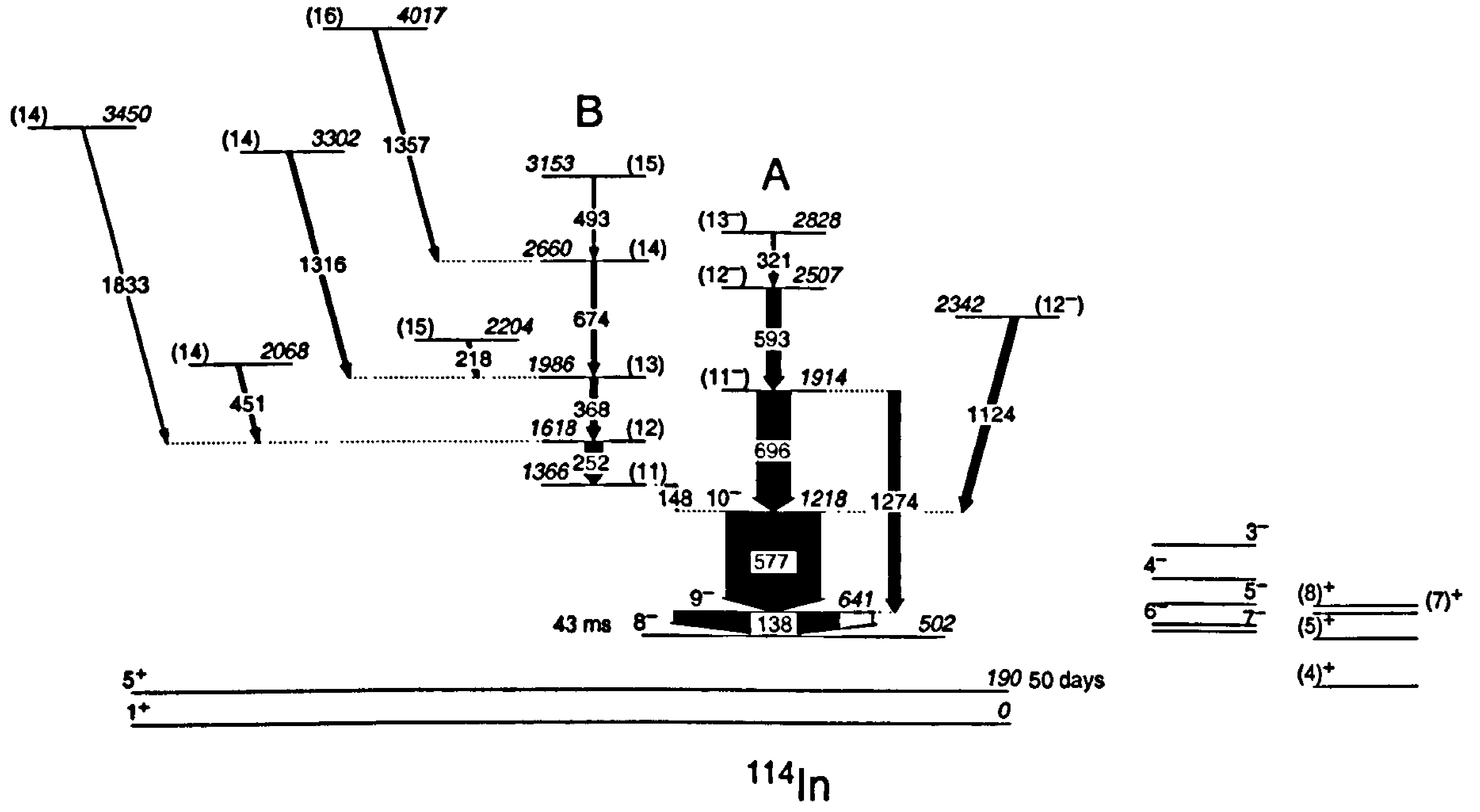

Figure 4.26: Level scheme of ^{114}In observed in the current work, and to the right, previously reported, non-yrast states that were unobserved in this work.

Figure 4.26 shows the level scheme of ^{114}In observed in the current work using the 28 MeV data. The γ rays associated with ^{114}In together with their intensity, spin assignment, anisotropy and efficiency corrected DCO ratio are summarized in Table 4.5.

Prior to this study, states had been observed in ^{114}In up to an excitation energy of 1218 keV and spin 10^- using a ^{110}Pd(^{7}Li,3n)^{114}In reaction [16] and non-yrast states had been studied by use of an (n,γ) reaction [101]. The I^π=8^- isomer in ^{114}In was assigned a lifetime of 43.1 ms from a weighted average from eight independent experiments [102] carried out between 1958 and 1968, and was again measured in 1995 by use of a cyclic activation method to be 43.24 ms [103]. The $I^{\pi}=5^{+}$ isomer was assigned its spin and parity by use of atomic beam magnetic resonance experiments [104, 105] and has a measured lifetime of 49.51 days [106]. The in-beam $\gamma-\gamma$ 28 MeV data strongly showed the previously known prompt 138 and 577 keV transitions [16] in ^{114}In as displayed in the lower part of figure 4.3. Figure 4.27 shows γ-coincidence gates on the two previously known transitions, 138 and 577 keV. The labels show the energy of the newly identified coincident peaks in ^{114}In and were in agreement with the transitions previously identified by A=114 in figure 4.5.

Figure 4.29 shows the DCO ratios obtained when gated by the 138 keV ΔI=1 transition and figure 4.30 shows the measured anisotropies of transitions in ^{114}In with sufficient statistics to allow measurement.

Band A

Band A is built on 43 ms isomeric state of $I^{\pi}=8^{-}$ at E_x=502 keV, which in turn decays via a 313 keV transition to a long-lived state at 190 keV which in turn, decays to the $I^{\pi}=1^{+}$ ground state [16]. Figure 4.31 shows γ-coincidence gates set on the first three transitions in band A. One crossover transition was identified, which confirms the ordering of the first two dipole transitions in the band. DCO analysis assigns the crossover transition as $E2$ and the members of the band ΔI=1. A 1124 keV transition is observed feeding into band A at E_x=1218 keV, and with a measured DCO ratio of 1.81(24) when gated by a $\Delta I = 1$, is assigned as an $E2$ transition.

Band B

Band B consists of a cascade of gamma rays, assigned to be ΔI=1 by DCO and anisotropic analysis. This cascade feeds into the I^{π} =(10^{-}) level of Band A via a 148 keV transition, which has measured DCO ratios of 0.98(5) and 1.04(3), which when gated by a ΔI=1 transition, suggests a ΔI=1 nature. Due to the number of states above the 148 keV transition whose parities are dependent on the correct assignment of the electromagnetic nature of the 148 keV transition, the parities of all the levels which eventually feed into band A through the 148 keV transition remain unassigned. The electromagnetic nature of this transition should be further investigated in order to reliably assign parities to the higher levels. However, a positive partity nature to band B is favoured (whereby the 148 keV transition is $E1$ in character) since there is no observation of a decay between the E_x=1366 and E_x=641 keV levels, implying a positive parity to the 1366 keV level. Figure 4.32 shows γ-ray coincidence gates set on the 368 keV transition in band B and clearly shows the other dipole transitions in this band. No crossover transitions were observed in band B, but further transitions were observed feeding into band B. The 218 keV transition with a DCO ratio of 1.43(14) was assigned as $E2$ whilst the 1316 keV transition with a DCO of 0.66(9) was assigned ΔI=1. Other transitions observed to feed into band B were assigned tentative spins and parity according to their DCO ratio. Several gamma rays that appeared to feed into band B were unable to be placed within the level scheme with any certainty. The normalised subtractions also shown that these transitions are associated with A=114. These unplaced transitions are listed at the bottom of table 4.5.

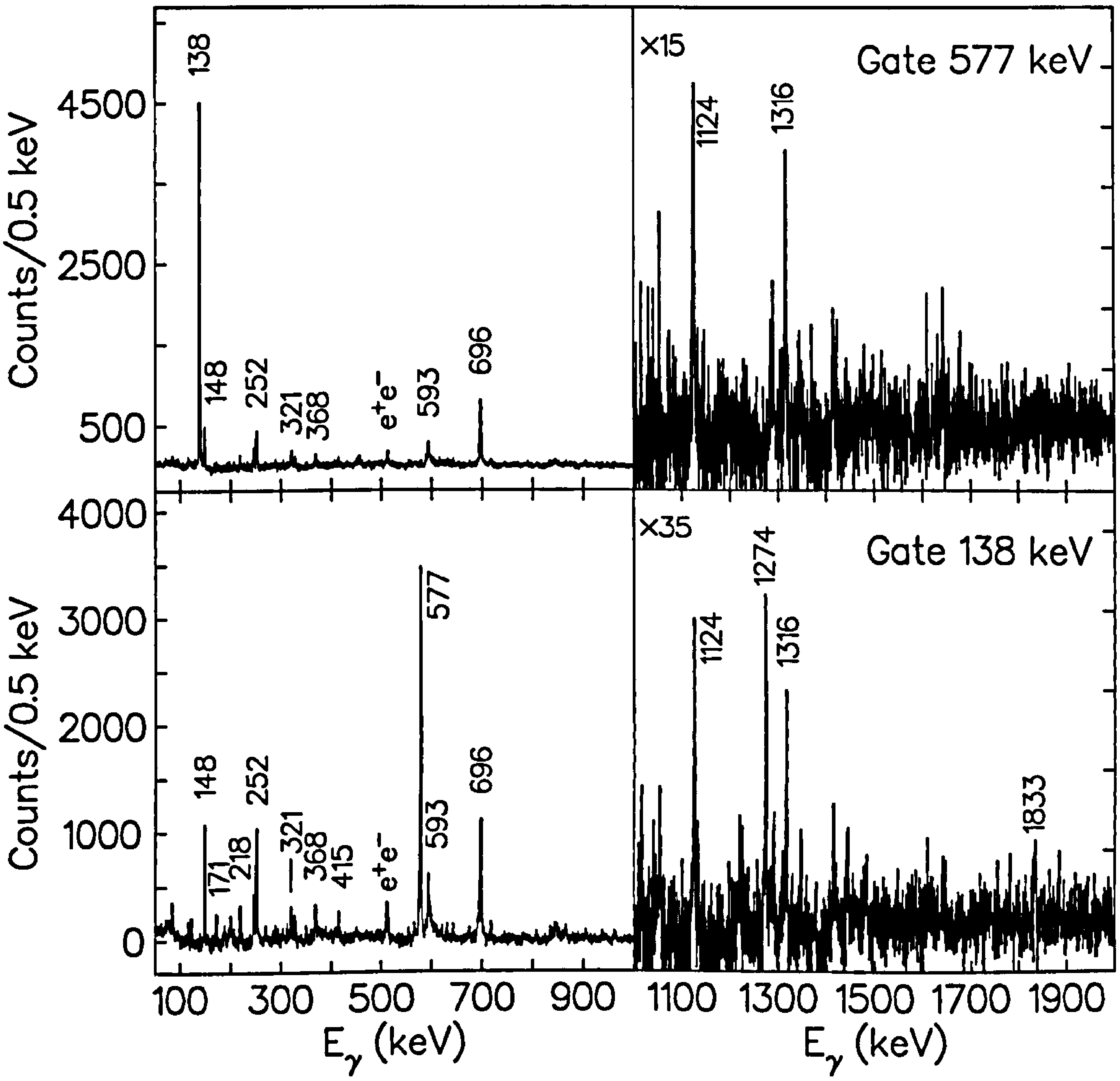

Figure 4.27: Gamma-ray coincidence spectra of ^{114}In gated by the previously reported 138 and 577 keV transitions.

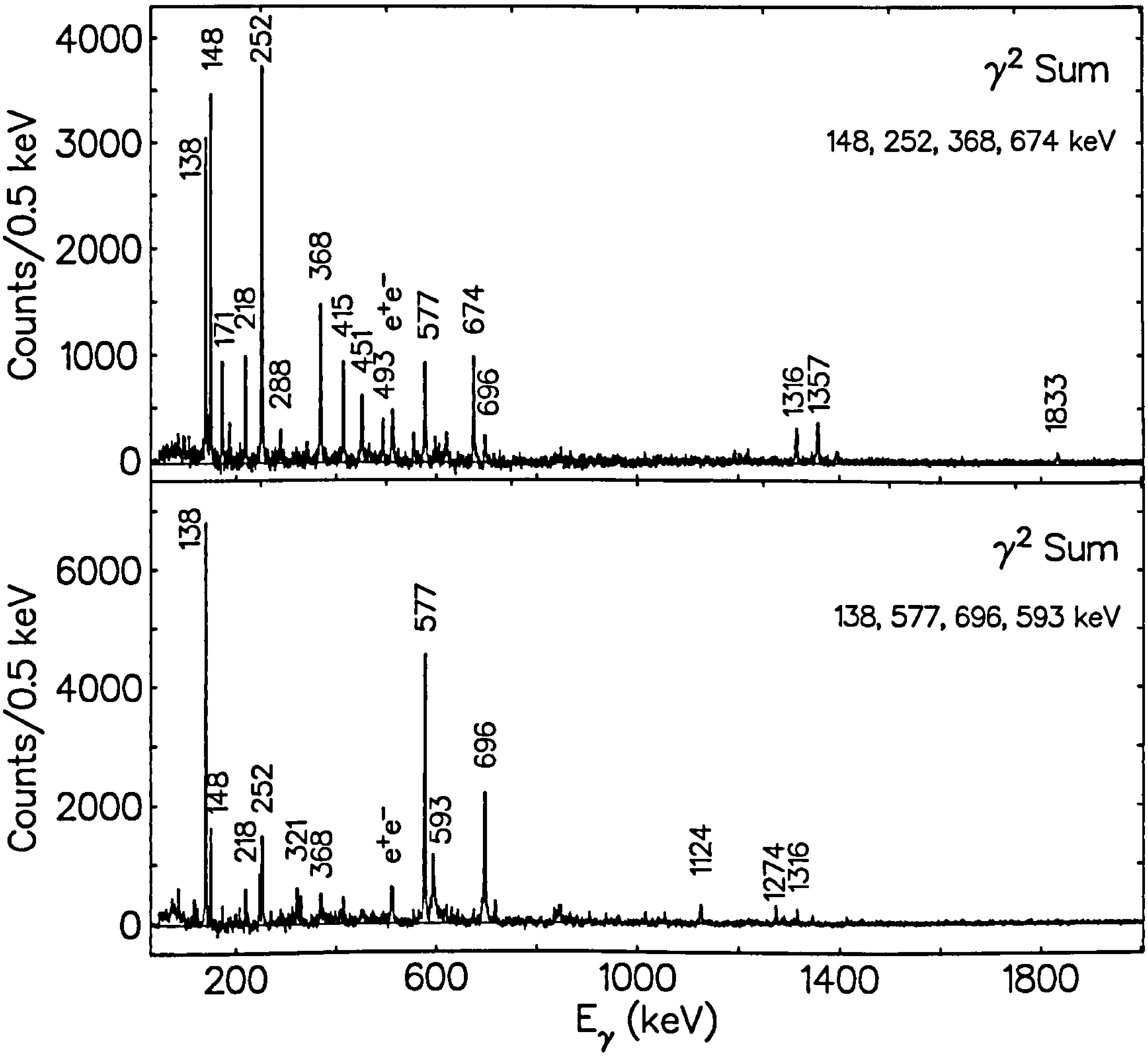

Figure 4.28: Summed γ-ray coincidence spectra of transitions in band A and band B of ^{114}In.

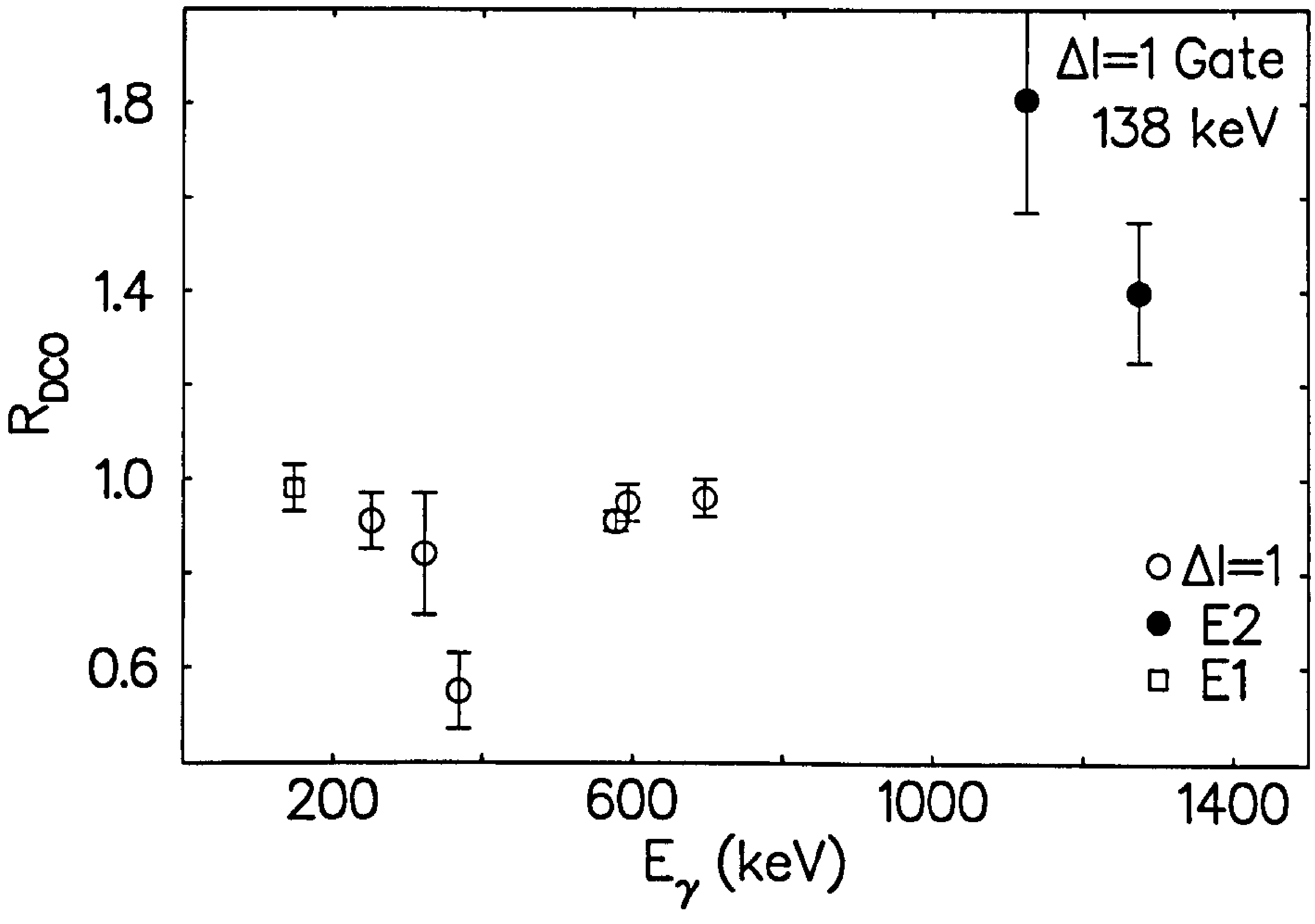

Figure 4.29: Extracted DCO ratios of transitions in ^{114}In when gated by the 138 keV ΔI=1 transition.

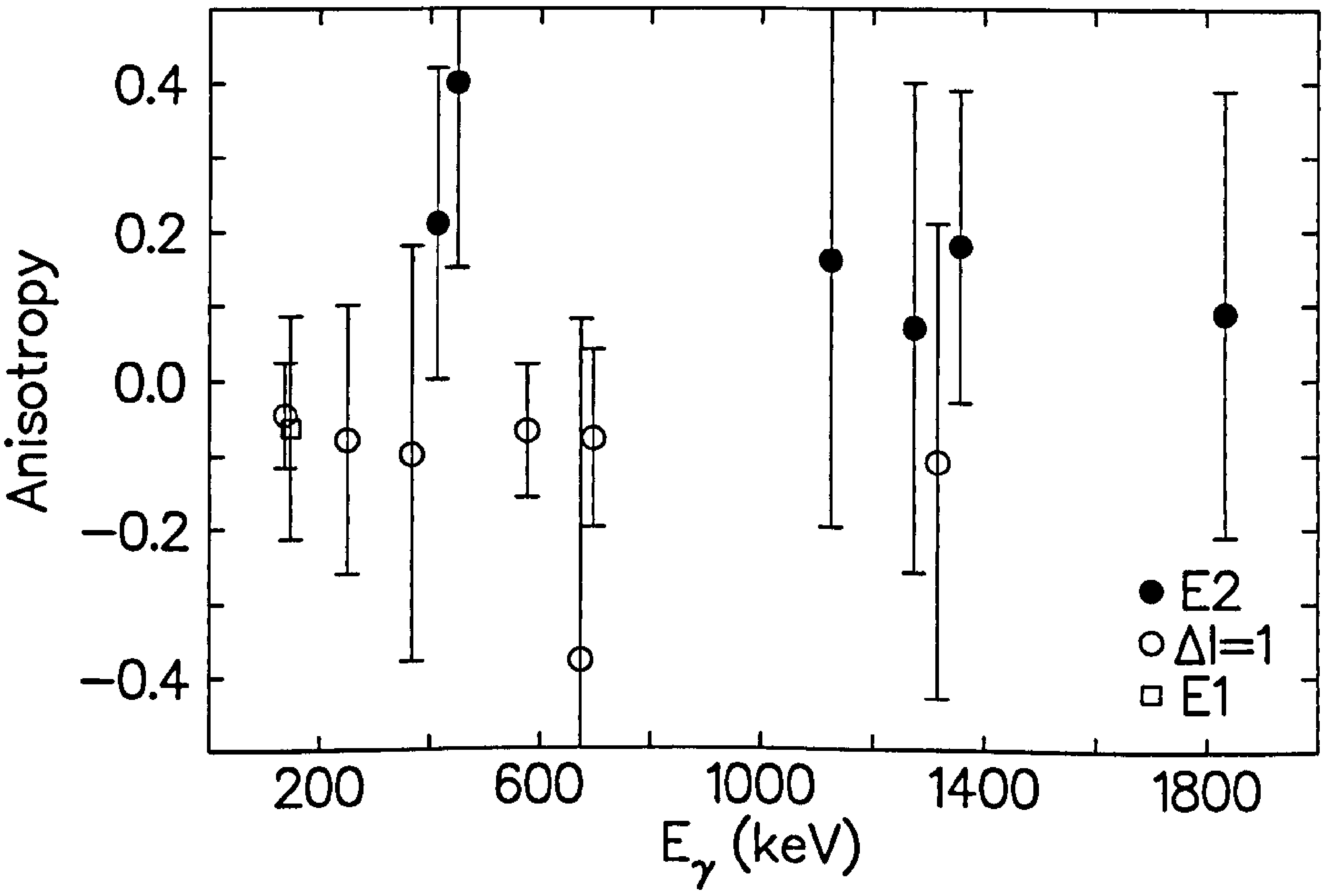

Figure 4.30: Extracted γ-ray anisotropies of transitions in ^{114}In.

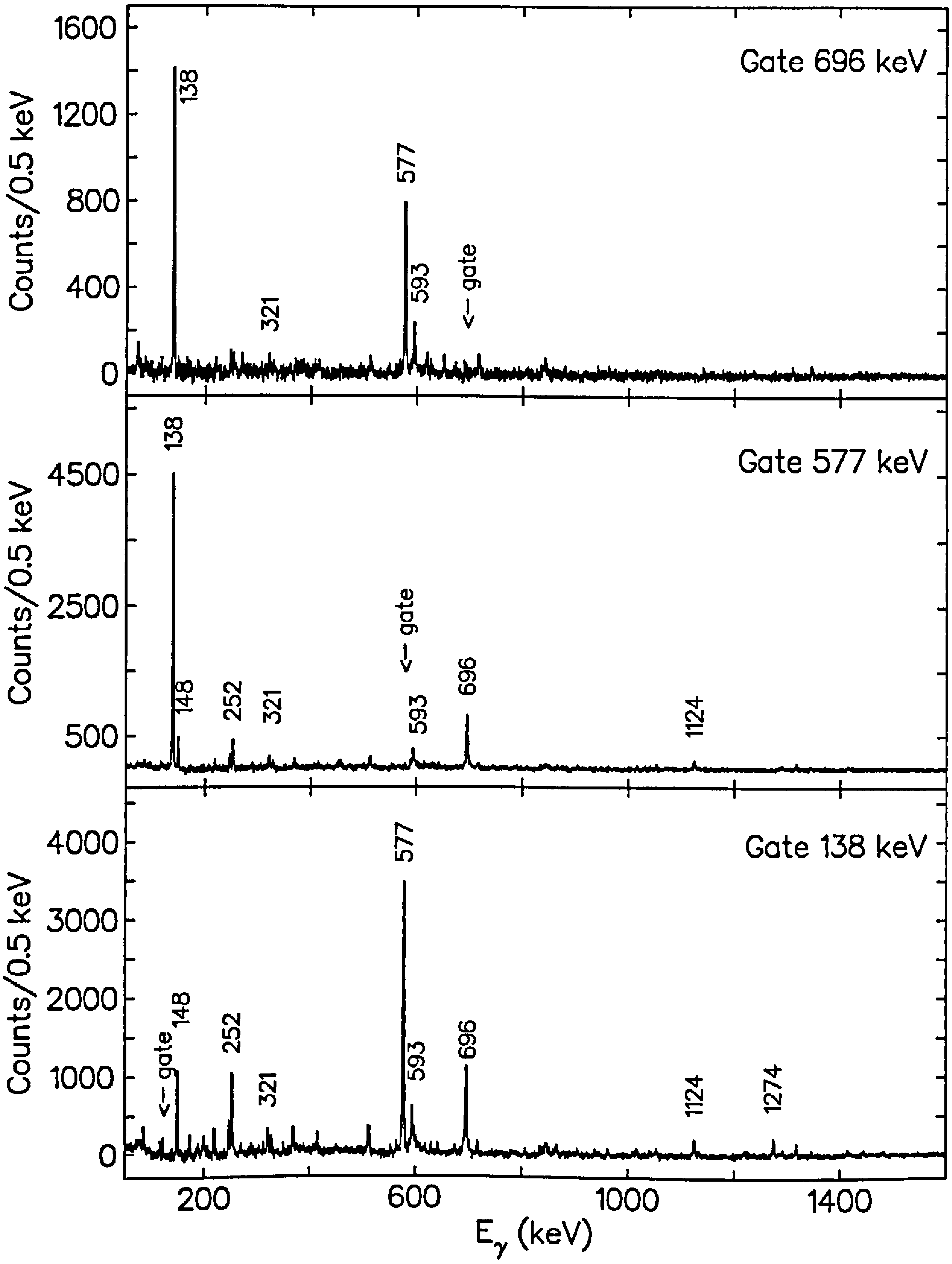

Figure 4.31: Gamma-ray coincidence spectra of band A in ^{114}In.

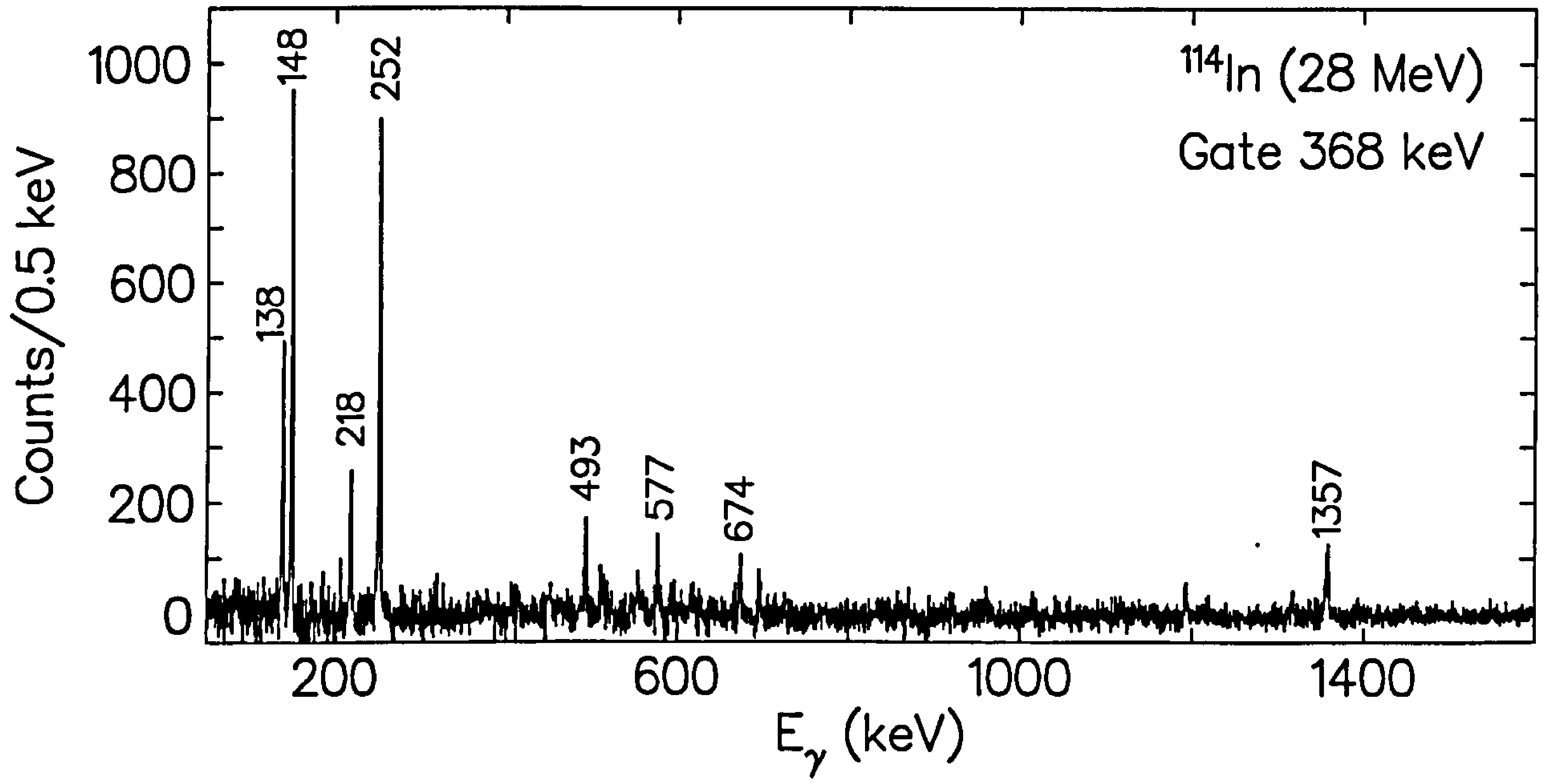

Figure 4.32: Gamma-ray coincidence spectra gated by 368 keV in band B of ^{114}In.

Table 4.5: Gamma rays assigned to ^{114}In in the current work. The relative γ-ray intensities are normalized to 100 for the 577 keV transition. Listed at the bottom of the table are the unplaced transitions.

E_γ (keV)	I_γ	E_i (keV)	E_f (keV)	I_i^π	I_f^π	R_{DCO}	A_2
138.2(3)	197(16)	641	502	9^-	8^-	1.08(4) ^{2}	−0.05(7)
148.4(3)	19(5)	1366	1218	(11)	(10^-)	0.98(5) ^{1} 1.04(3) ^{2}	−0.06(22)
217.7(4)	7(3)	2204	1986	(15)	(13)	1.43(14) ^{2}	
251.5(2)	25(7)	1618	1366	(12)	(11)	0.91(6) ^{1}	−0.09(18)
321.4(3)	4(4)	2828	2507	(13^-)	(12^-)	0.84(13) ^{1}	

Table 4.5 continued: Gamma rays assigned to ^{114}In in the current work

E_γ (keV)	I_γ	E_i (keV)	E_f (keV)	I_i^π	I_f^π	R_{DCO}	A_2
368.4(3)	11(5)	1986	1618	(13)	(12)	0.55(8)[1] 1.00(6)[2]	
450.5(4)	5(5)	2068	1618	(14)	(12)	1.57(9)	0.40(55)
492.5(2)	3(3)	3153	2660	(15)	(14)		
577.0(2)	100(8)	1218	641	10^-	9^-	0.91(2)[1]	−0.07(9)
593.1(4)	22(5)	2507	1914	(12^-)	(11^-)	0.95(4)[1]	
674.2(3)	6(4)	2660	1986	(14)	(13)	1.01(9)[2]	−0.38(46)
695.5(2)	21(4)	1914	1218	(11^-)	10^-	0.96(4)[1]	−0.08(13)
1124.1(27)	13(9)	2342	1218	(12^-)	10^-	1.81(24)[1]	
1274.4(5)	16(10)	1914	641	(11^-)	9^-	1.40(15)[1]	0.07(63)
1315.9(2)	7(5)	3302	1986	(14)	(13)	0.66(9)[2]	−0.11(12)
1357.1(2)	4(4)	4017	2660	(16)	(14)	1.34(11)	0.18(81)
1832.8(15)	<2	3450	1618	(14)	(12)		0.09(65)
171.9(7)	5(3)	Unplaced					
287.7(6)	<2	Unplaced					
414.4(7)	9(4)	Unplaced					

1 = Gate set on 138 keV (ΔI=1) transition

2 = Gate set on 252 keV (ΔI=1) transition

4.4 Analysis of Cadmium Nuclei

4.4.1 ^{112}Cd

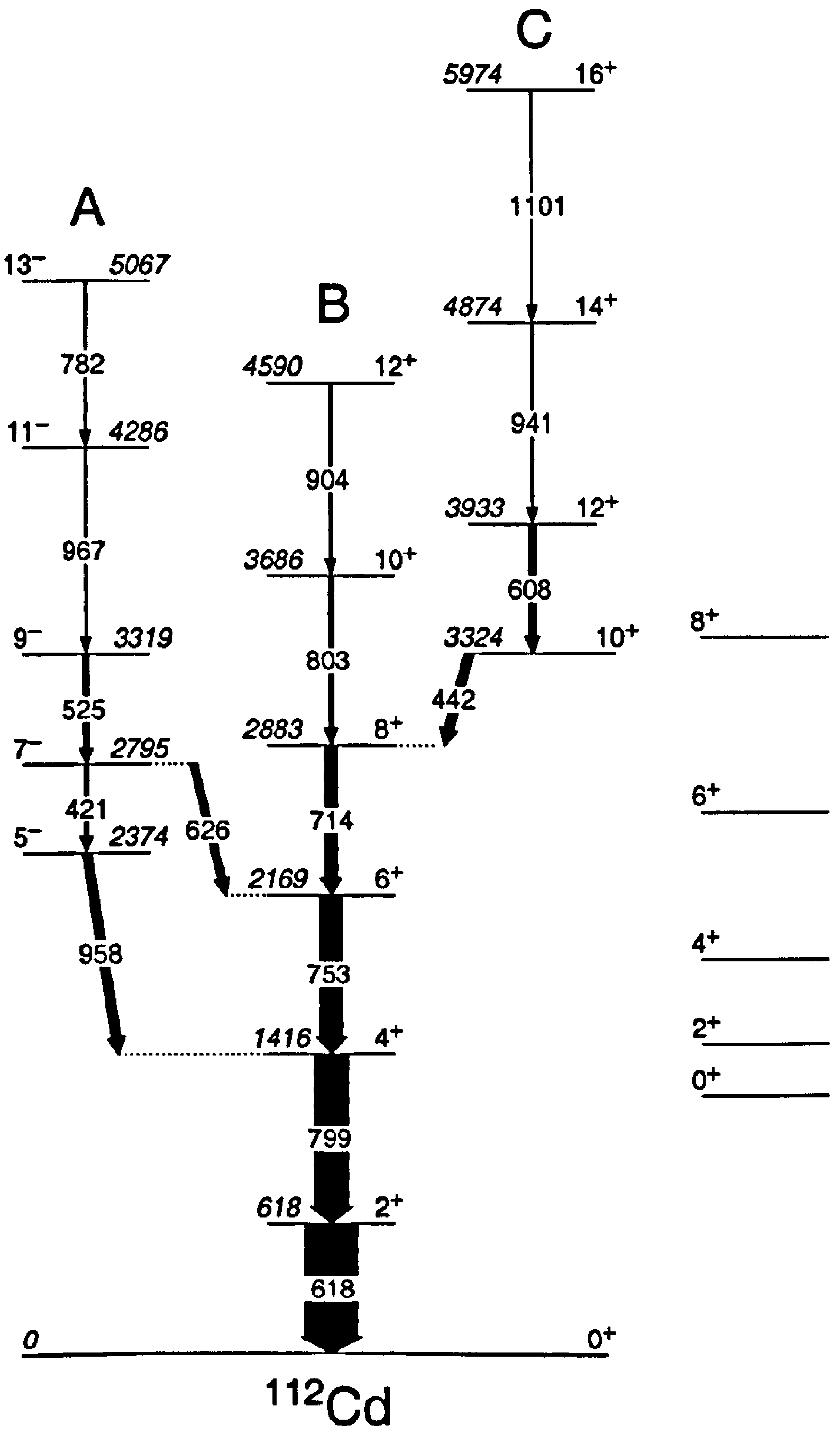

Figure 4.33: Level scheme for ^{112}Cd observed in the current work with the intruder band [90], unobserved in this work, shown to the right.

Figure 4.33 shows the level scheme of ^{112}Cd observed in the current work using the 50 MeV dataset. The transitions associated with ^{112}Cd together with their intensity, spin assignment, anisotropy and DCO ratio are summarized in Table 4.6. Prior to this study, states had been observed in ^{112}Cd up to 4874 keV, spin 14^+ using a ^{110}Pd(α, $2n$)^{112}Cd reaction [90, 107] and a $(n, n'\gamma)$ reaction [108]. The ground state band observed in the current work is in agreement with the previous works, but there was no evidence of the non-yrast intruder band as previously identified [90] or any other non-yrast states previously reported [108]. Two new transitions have been observed in this work, a 1101 keV transition on top of the previously identified 941 keV transition in band C and a 782 keV transition above the 967 keV transition in band A. These have both been assigned as $E2$ transitions in keeping with the systematics of the rest of the band. Evidence of these transitions are shown in figures 4.34 and 4.35. Figure 4.34 shows a summed gamma-ray coincidence spectrum, gated by the first three γ rays in ^{112}Cd in the 50 MeV dataset where there is evidence of the proposed new 1101 keV $16^+ \rightarrow 14^+$ and 782 keV $13^- \rightarrow 11^-$ transitions. Figure 4.35 shows a γ coincidence sum of the 525 and 967 keV transitions in band C where there is clearer evidence of a 782 keV transition.

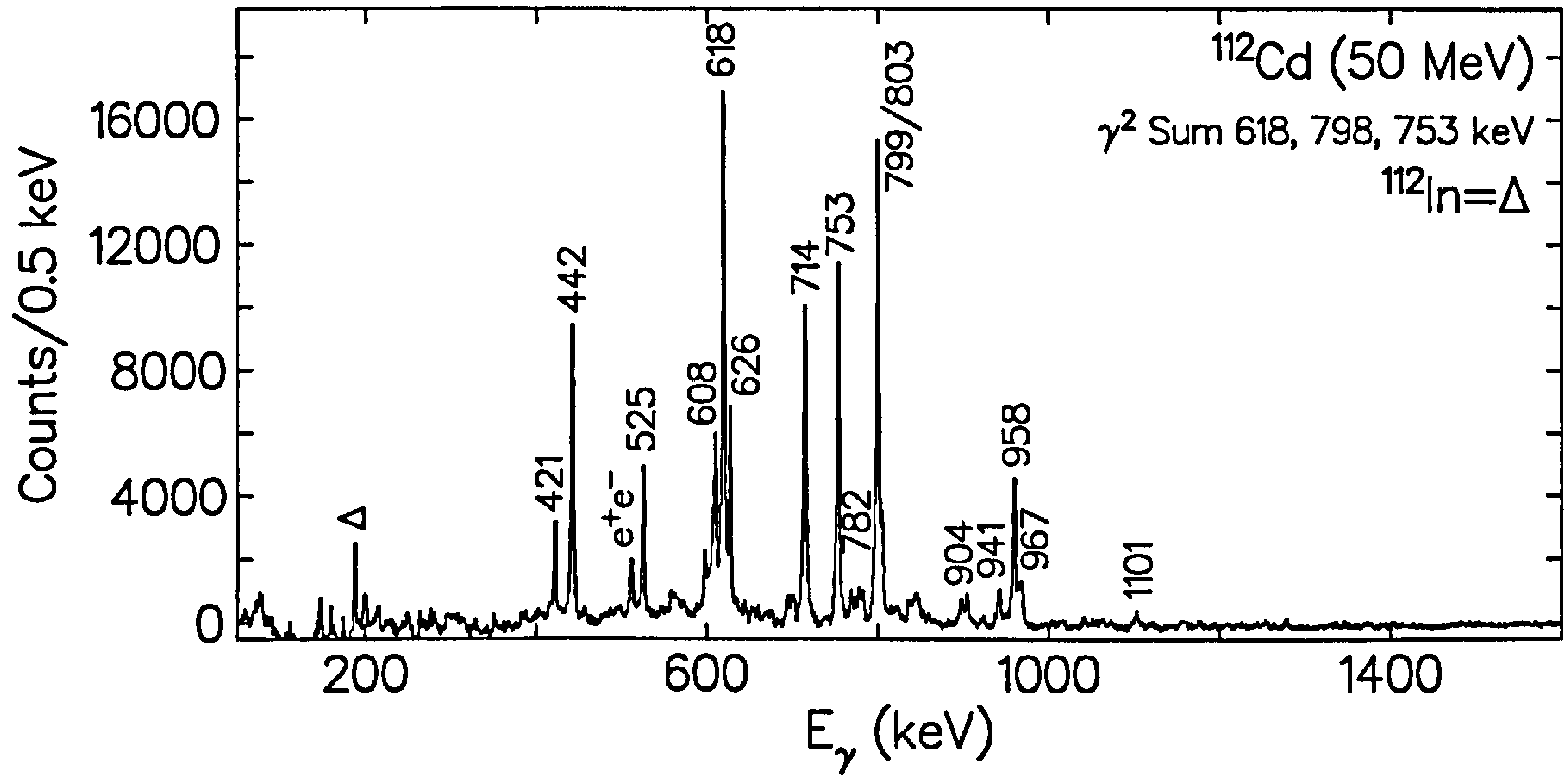

Figure 4.34: Summed γ-ray coincidence spectra of transitions in band C, showing evidence for the 1101 keV transition in ^{112}Cd.

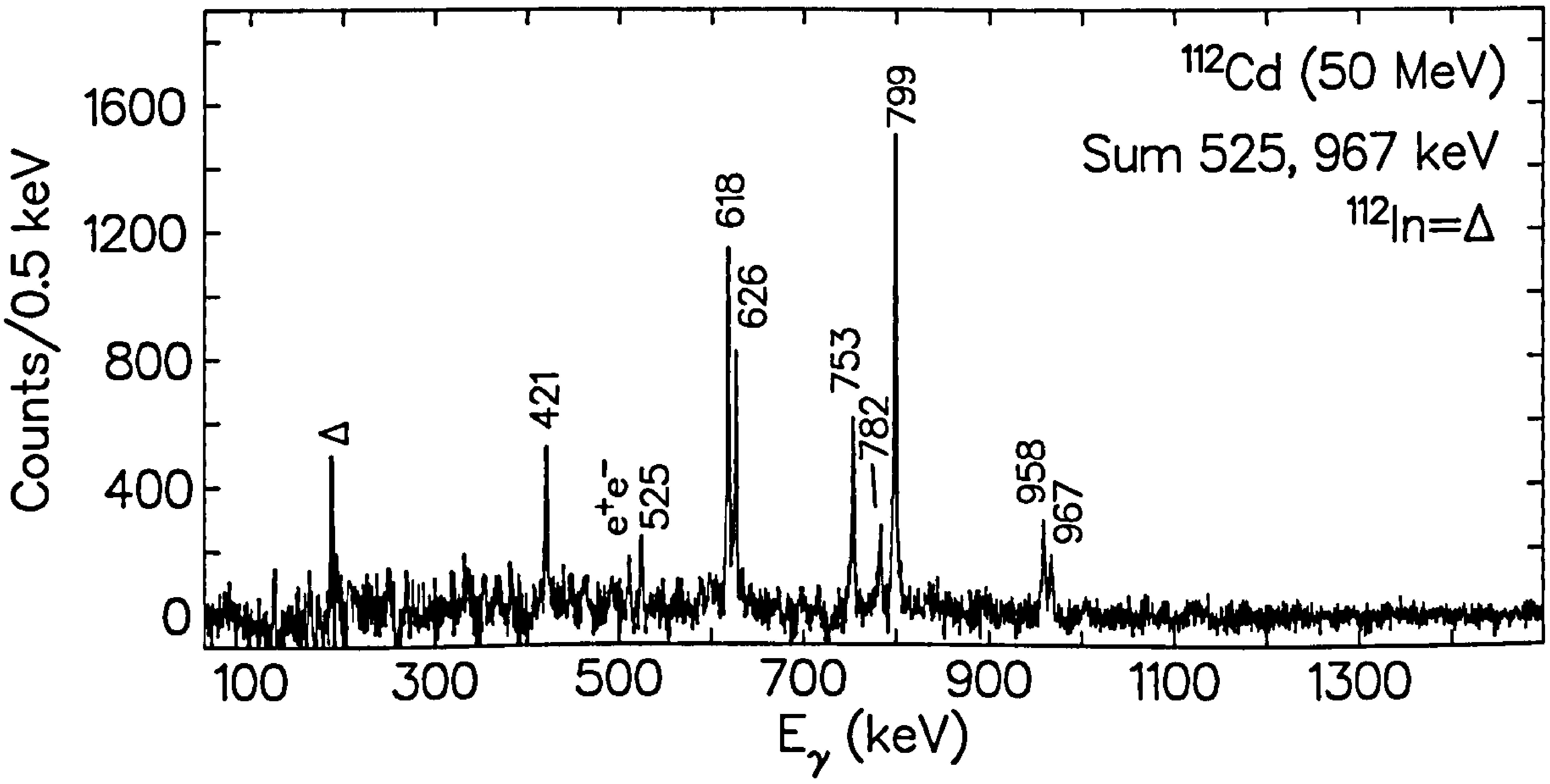

Figure 4.35: Summed γ-ray coincidence spectra in band A, showing evidence for the 782 keV transition in band ^{112}Cd.

Table 4.6: Gamma rays assigned to ^{112}Cd in the current work. The relative γ-ray intensities are normalized to 100 for the 799 keV transition.

E_γ (keV)	I_γ	E_i (keV)	E_f (keV)	I_i^π	I_f^π	R_{DCO}	A_2
420.8(3)	11(4)	2795	2374	7^-	5^-		
441.5(3)	26(4)	3324	2883	10^+	8^+	1.23(4) [1] 1.02(16)[2]	
524.5(2)	15(4)	3319	2795	9^-	7^-		
608.4(3)	19(4)	3933	3324	12^+	10^+	1.07(6) [1] 1.05(19)[2]	
617.8(2)	152(12)	618	0	2^+	0^+	1.03(10)[2]	0.12(7)
626.2(3)	23(4)	2795	2169	7^-	6^+		
713.6(4)	39(6)	2883	2169	8^+	6^+	1.01(15)[1] 1.03(17)[2]	
752.8(3)	66(6)	2169	1416	6^+	4^+	1.24(24)[1] 1.13(12)[2]	0.13(3)
781.9(3)	4(4)	5067	4286	13^-	11^-		
798.5(3)	100(9)	1416	618	4^+	2^+		0.15(5)
802.9(2)	15(4)	3686	2883	10^+	8^+		
903.6(4)	8(6)	4590	3686	12^+	10^+		
941.0(4)	6(4)	4874	3993	14^+	12^+		
958.3(5)	26(8)	2374	1416	5^-	4^+		
967.0(4)	4(4)	4286	3319	11^-	9^-		
1100.9(9)	<2	5974	4874	16^+	14^+		

1 = Gate set on 799 keV ($E2$) transition

2 = Gate set on 618 keV ($E2$) transition

4.4.2 ^{113}Cd

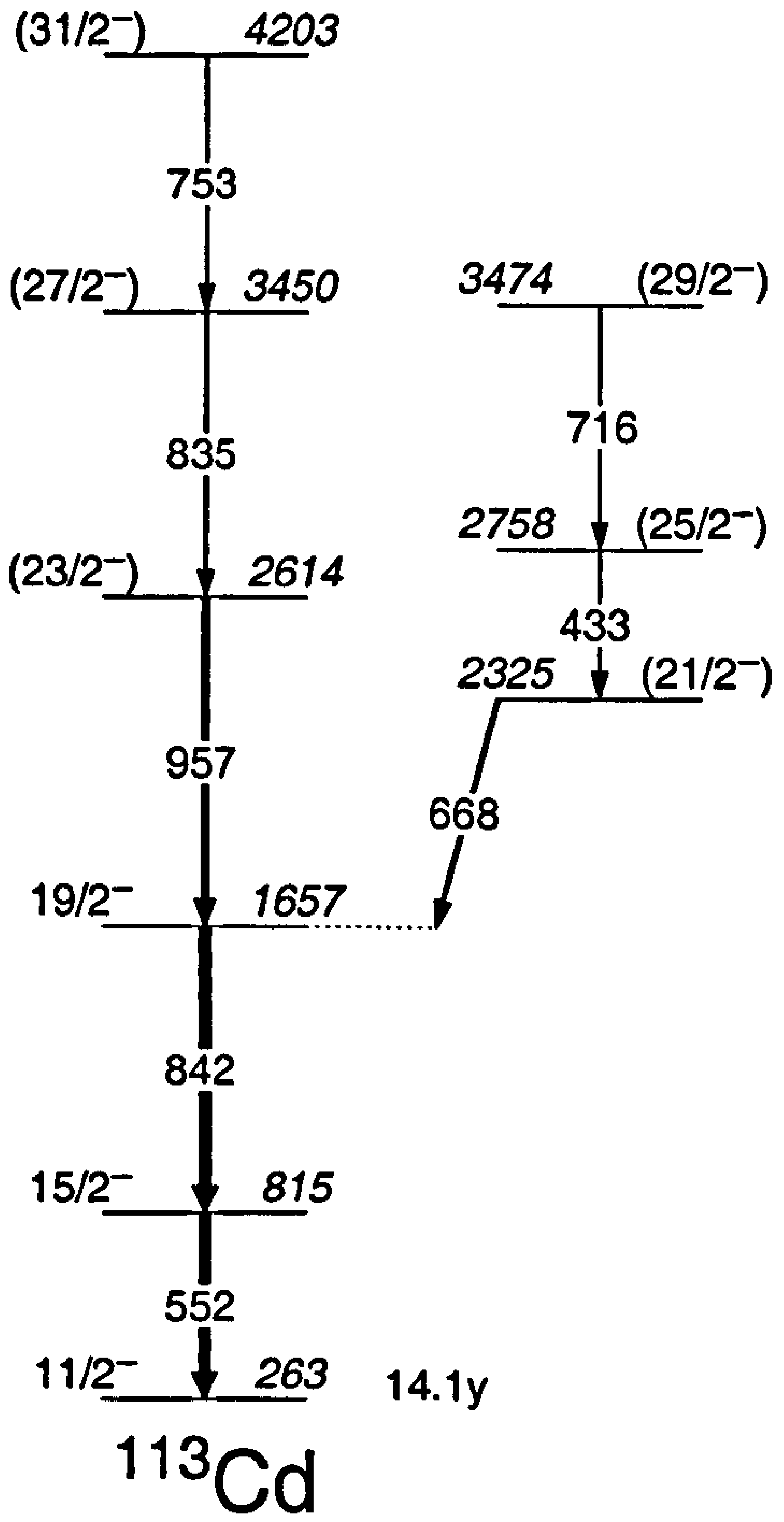

Figure 4.36: Level scheme of ^{113}Cd observed in this work.

Figure 4.36 shows the level scheme of ^{113}Cd observed in the current work using both the 40 and 50 MeV datasets. Prior to this study, states had been observed in the nucleus ^{113}Cd up to 4203 keV, spin (31/2$^-$) using fusion-fission reactions of ^{24}Mg + ^{173}Yb [109] a ^{28}Si + ^{176}Yb reaction [91] and a ^{110}Pd(α, nγ) reaction [111]. The ground state band as reported has been observed. In addition to the ground state band, the 688, 433 and 716 keV transitions were observed in this work as reported in [91]. By gating on the 552 keV transition, a spectrum contaminated by the 553 and 554 keV lines in ^{112}In (which is populated in the 40 MeV dataset) is produced. The ^{113}Cd 552 keV spectrum was cleaned by subtracting a normalised portion of the ^{112}In 552 keV gate set in the 50 MeV dataset as shown in figure 4.37. Table 4.7 lists the transitions associated with ^{113}Cd. It was not possible to extract DCO ratios or anisotropies for transitions in ^{113}Cd as the peaks did not contain sufficient statistics.

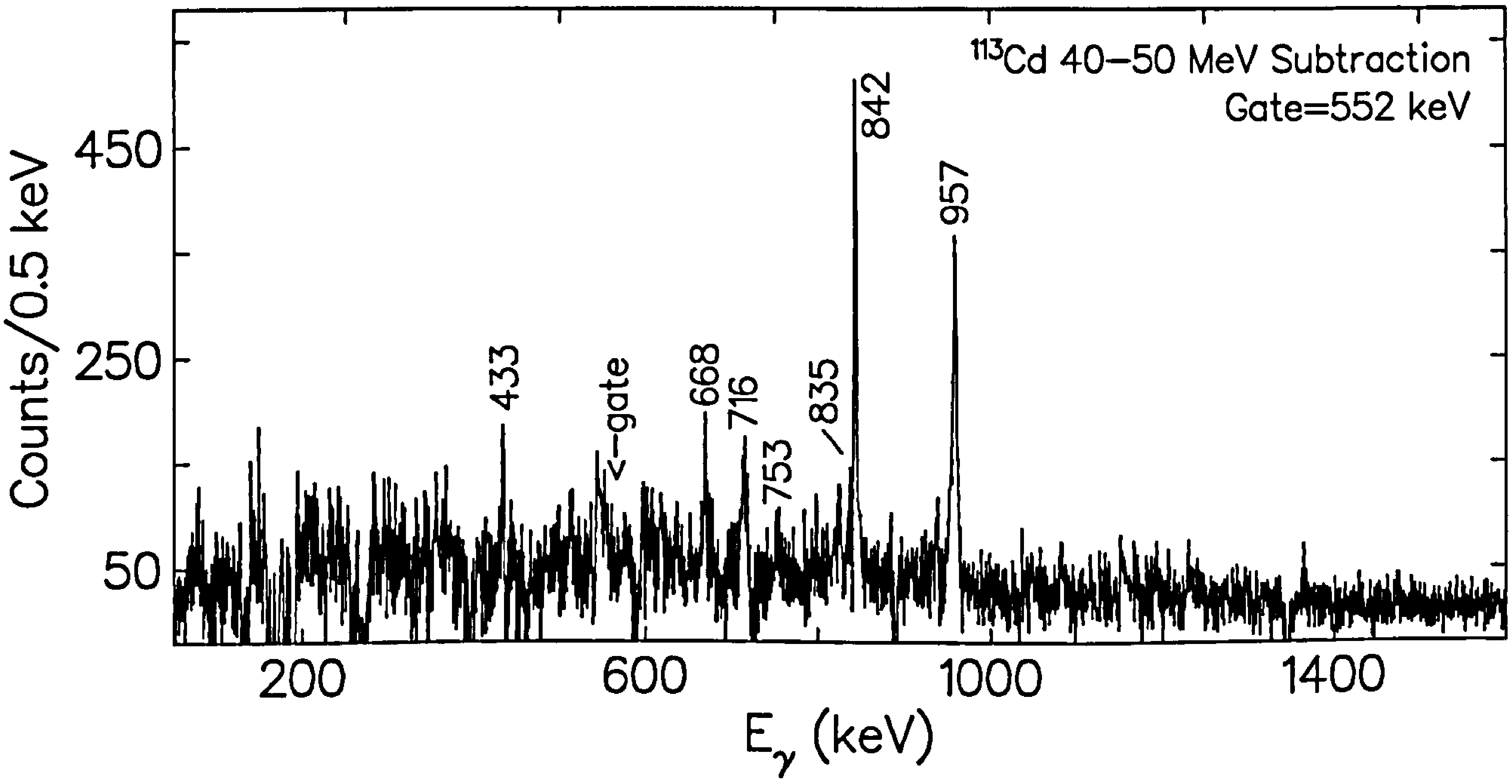

Figure 4.37: 40 MeV γ coincidence spectrum gated by 552 keV with a normalized subtraction of 552 keV in 50 MeV to highlight transitions in the $\nu(h_{11/2})$ band in ^{113}Cd.

Table 4.7: Gamma rays assigned to ^{113}Cd in the current work. The relative γ-ray intensities are normalized to 100 for the 842 keV transition.

E_γ (keV)	I_γ	E_i (keV)	E_x (keV)	I_i^π	I_f^π	R_{DCO}	A_2
433.3(3)	18(10)	2758	2325	$(25/2^-)$	$(21/2^-)$		
551.9(2)	132(11)	815	263	$15/2^-$	$11/2^-$		0.16(26)
668.2(3)	27(9)	2325	1657	$(21/2^-)$	$19/2^-$		
716.4(4)	9(5)	3474	2758	$(29/2^-)$	$(25/2^-)$		
753.1(5)	9(4)	4203	3450	$(31/2^-)$	$(27/2^-)$		
835.1(4)	18(7)	3450	2614	$(27/2^-)$	$(23/2^-)$		
842.4(3)	100(5)	1657	815	$19/2^-$	$15/2^-$		
957.4(3)	55(8)	2614	1657	$(23/2^-)$	$19/2^-$		

4.4.3 ^{114}Cd

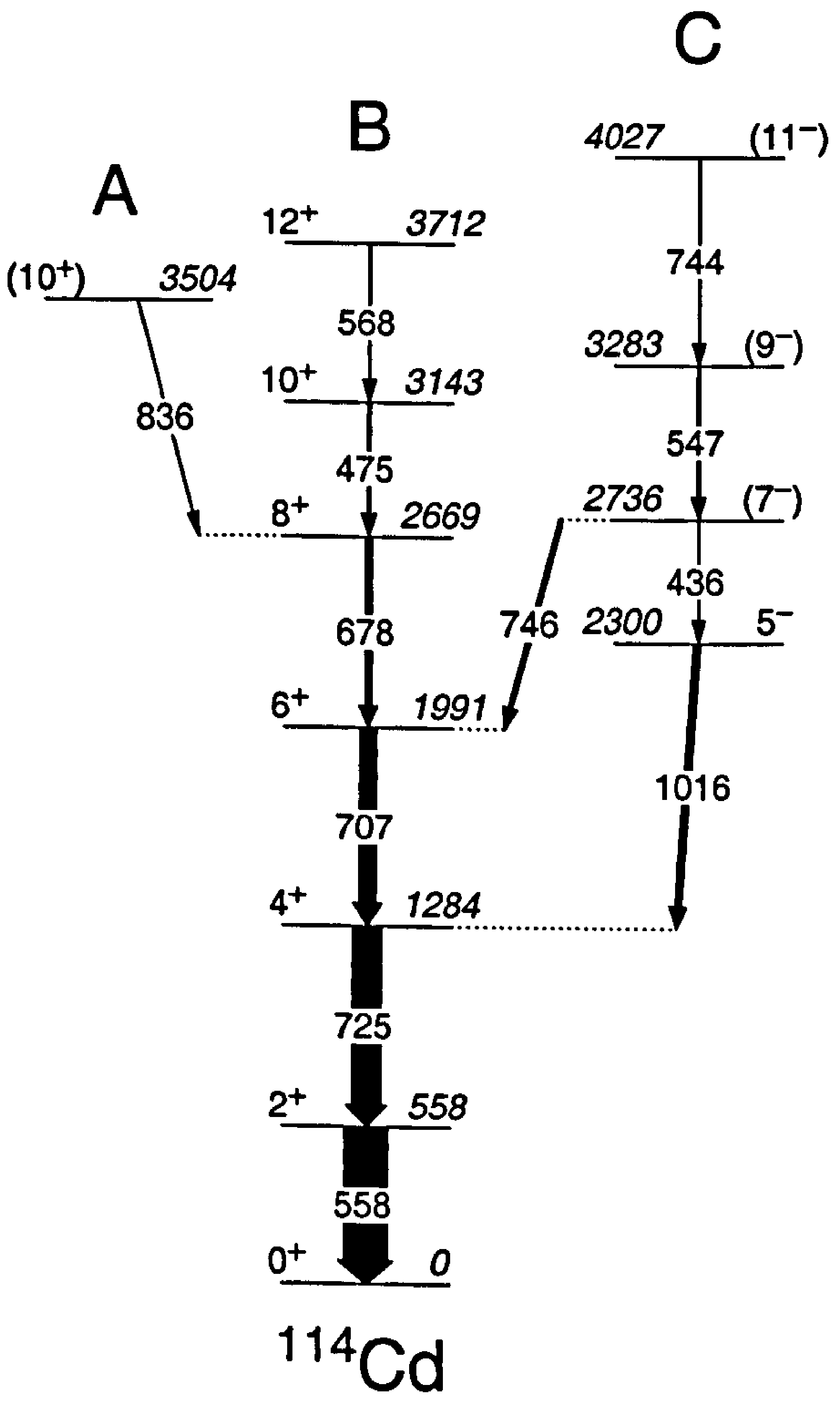

Figure 4.38: Level scheme of ^{114}Cd observed in this work.

Prior to this study, near-yrast states had been recently reported in the nucleus ^{114}Cd up to 4605 keV, spin 14^+ using a ^{28}Si + ^{176}Yb fusion-fission reaction [91] and non-yrast states were studied using a (n, n') reaction [110]. All but three of these previously identified transitions have been confirmed using data from the 28 MeV dataset. It was not possible to confirm the highest transition in each of the three bands previously identified (752 keV $12^+ \rightarrow 10^+$, 893 keV $14^+ \rightarrow 12^+$, 578 keV $13^- \rightarrow 11^-$). Figure 4.39 shows the summed γ-ray coincidence spectra of the three lowest transitions in ^{114}Cd. Table 4.8 lists the observed γ rays together with their intensity, spin assignment, anisotropy and efficiency corrected DCO ratio.

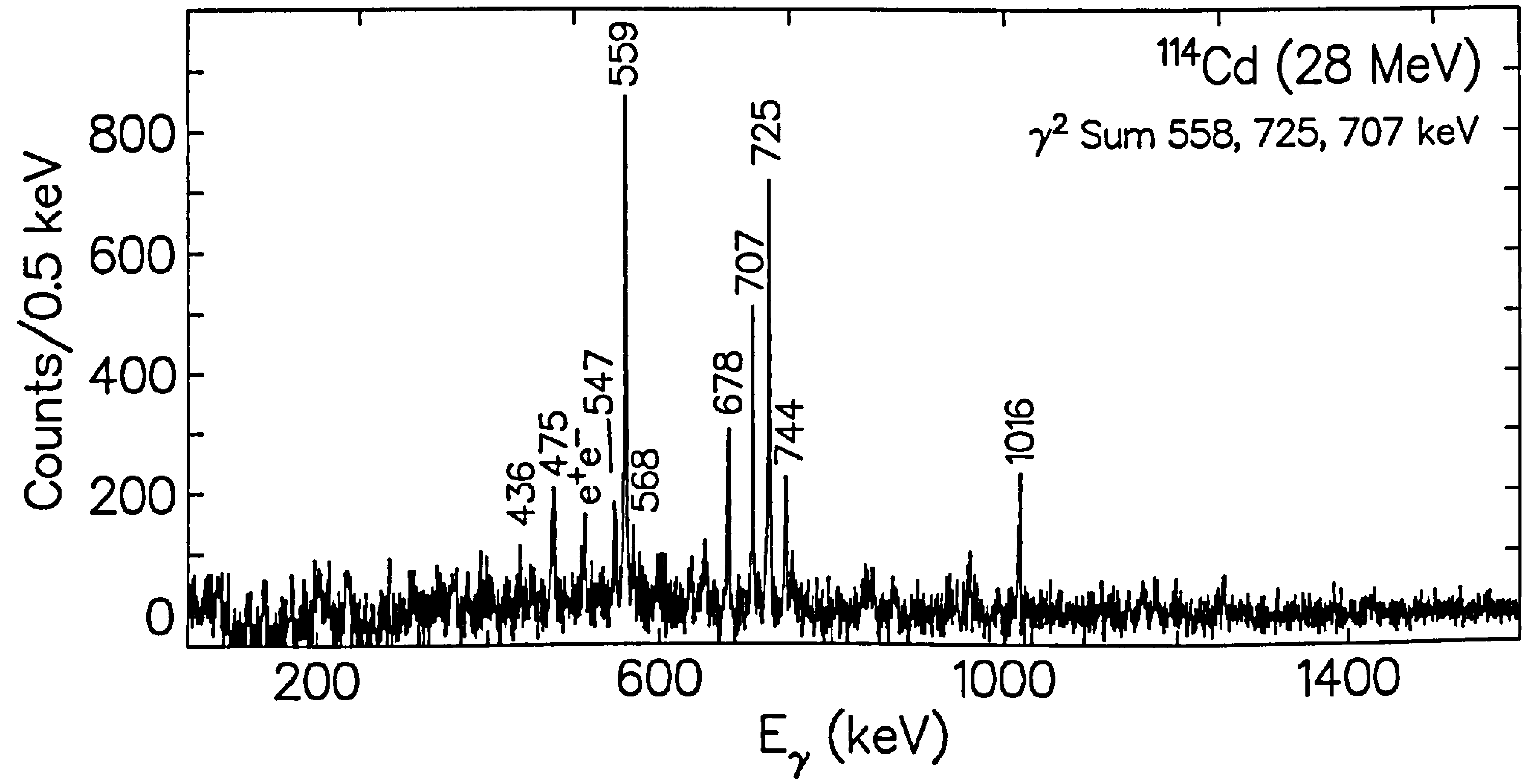

Figure 4.39: Summed γ-ray coincidence spectrum of ^{114}Cd.

Table 4.8: Gamma rays assigned to ^{114}Cd in the current work. The relative γ-ray intensities are normalized to 100 for the 725 keV transition.

E_γ (keV)	I_γ	E_i (keV)	E_f (keV)	I_i^π	I_f^π	R_{DCO}	A_2
436.2(3)	3(1)	2736	2300	(7^-)	5^-		
474.8(3)	11(1)	3143	2669	10^+	8^+		
546.9(5)	9(2)	3283	2736	(9^-)	(7^-)		
558.4(3)	152(16)	558	0	2^+	0^+		0.13(14)
						1.02(4)[2]	
568.2(2)	6(2)	3712	3143	12^+	10^+		
678.1(3)	23(2)	2699	1991	8^+	6^+	1.01(9)[1]	
						1.00(9)[2]	
706.9(3)	57(4)	1991	1284	6^+	4^+	0.98(5)[1]	0.11(17)
						1.00(4)[2]	
725.4(4)	100(6)	1284	558	4^+	2^+	0.99(7)[1]	0.13(7)
743.5(2)	3(2)	4027	3283	(11^-)	(9^-)		
745.4(3)	14(2)	2736	1991	(7^-)	6^+		
835.7(6)	3(2)	3504	2669	(10^+)	8^+		
1015.8(7)	3(3)	2300	1284	5^-	4^+	0.79(14)[1]	−0.30(12)
						0.79(6)[2]	

1 = Gate set on 558 keV ($E2$) transition

1 = Gate set on 725 keV ($E2$) transition

4.5 Analysis of Silver Nuclei

4.5.1 ^{109}Ag

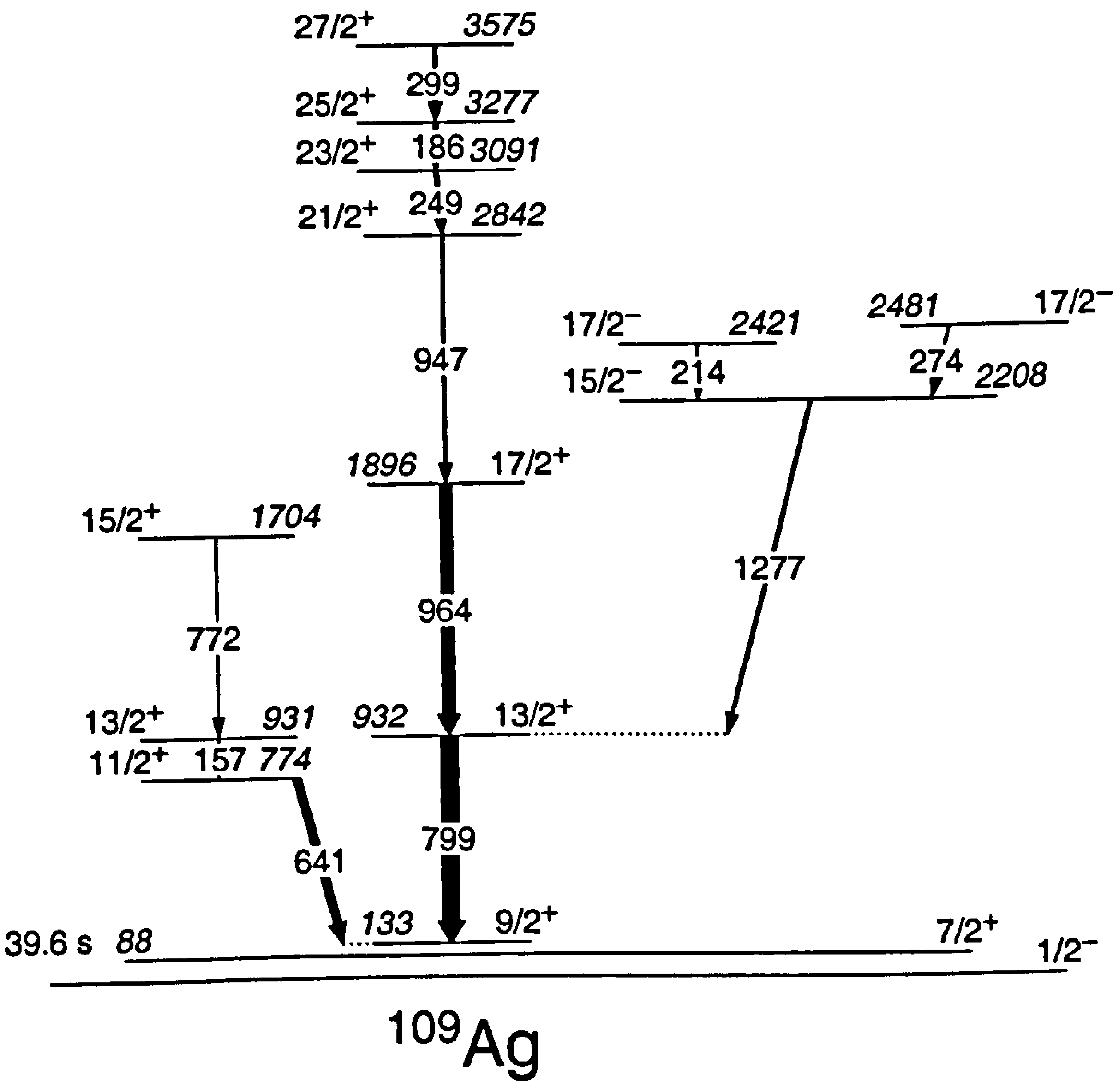

Figure 4.40: Level scheme of ^{109}Ag observed in this work.

Figure 4.40 shows the level scheme of the transitions observed in the 50 MeV dataset in ^{109}Ag. Prior to this work, states had been observed in ^{109}Ag up to an excitation energy of 5414 keV and spin (35/2$^+$) using a ^{96}Zr(^{18}O, p4n)^{109}Ag [75].

Figure 4.41 shows a γ-ray coincidence spectrum gated by the 964 keV transition, highlighting the coincident transitions observed. The 799 keV gate was not used as it displayed lines coincident with ^{112}Cd.

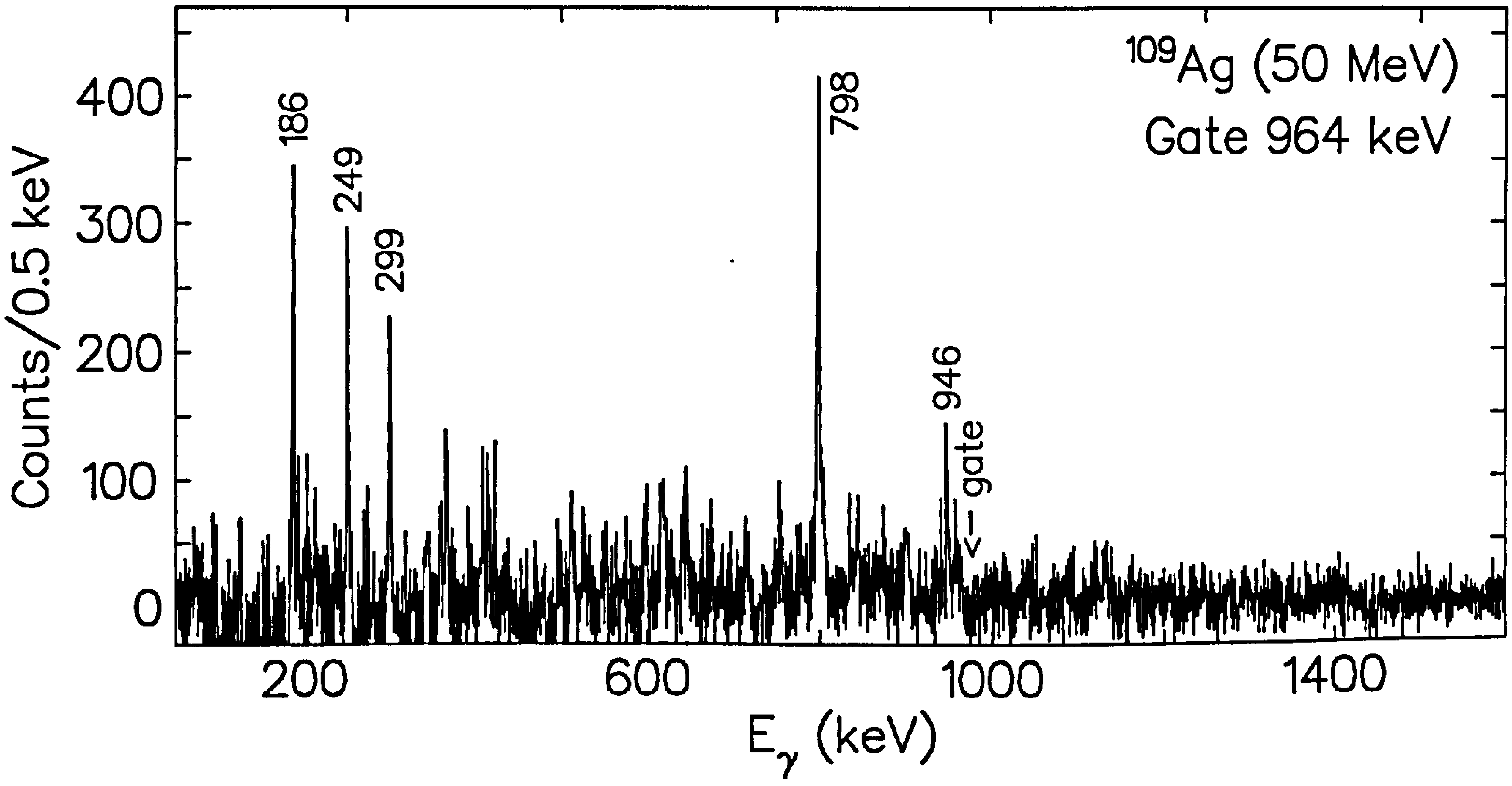

Figure 4.41: Gamma-ray coincidence spectrum gated by the 964 keV transition, highlighting the transitions observed in ^{109}Ag in the current work.

Table 4.9: Gamma rays assigned to ^{109}Ag in the current work. The relative γ-ray intensities are normalized to 100 for the 964 keV transition.

E_γ (keV)	I_γ	I_i^π (keV)	I_f^π (keV)	R_{DCO}	A_2
157.3(5)	5(3)	$13/2^+$	$11/2^+$		
186.2(3)	19(5)	$25/2^+$	$23/2^+$	0.91(4)[1]	
213.8(4)	14(5)	$17/2^-$	$15/2^-$		
249.4(5)	21(7)	$23/2^+$	$21/2^+$	0.85(5)[1]	
274.3(4)	8(4)	$17/2^-$	$15/2^-$		
299.0(3)	22(5)	$27/2^-$	$25/2^-$	0.87(6)[1]	
640.6(3)	<2	$11/2^+$	$9/2^-$		
772.3(6)	3(2)	$15/2^+$	$13/2^+$		
798.5(3)	140(8)	$13/2^+$	$9/2^+$	0.88(3)[1]	
947.4(4)	28(4)	$21/2^+$	$17/2^+$	0.89(7)[1]	
964.3(3)	100(4)	$17/2^+$	$13/2^+$		
1276.8(6)	23(4)	$15/2^+$	$13/2^+$		

1 = Gate set on 964 keV ($E2$) transition

4.5.2 ^{110}Ag

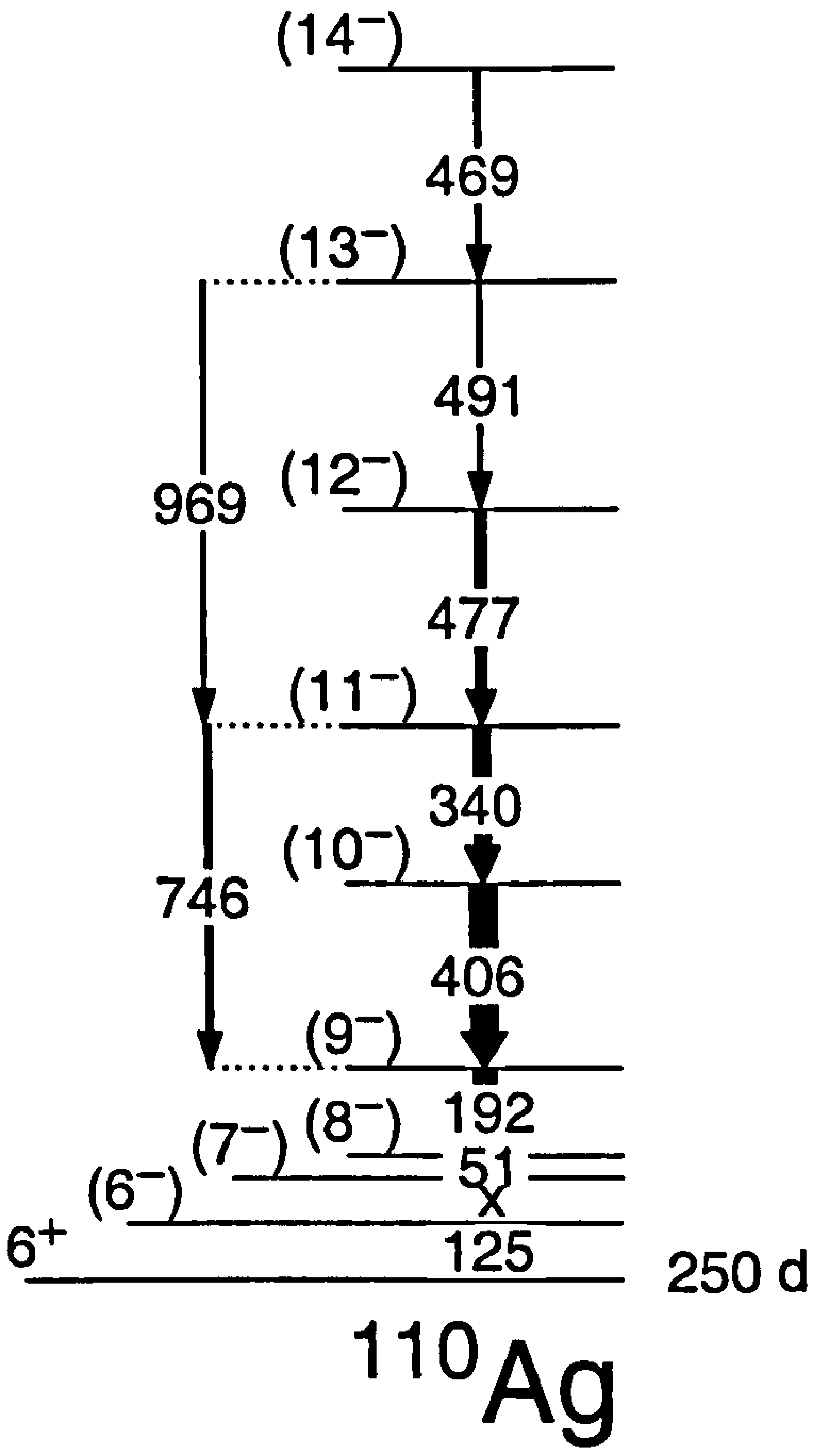

Figure 4.42: Level scheme of ^{110}Ag observed in the current work.

Figure 4.42 shows the level scheme of the transitions observed in ^{110}Ag. Prior to this work, states in ^{110}Ag had been observed up to a spin of (14$^-$) by use of a ^{28}Si+^{176}Yb fusion-fission reaction [92]. Two of the four crossover transitions have been observed in the 50 MeV dataset of this work, there was no evidence of the 816 keV (12$^-$)→(10$^-$) or 959 keV (14$^-$)→(12$^-$) γ rays as previously reported. An unobserved $M1$ gamma-ray is believed to exist between the (7$^-$) and (6$^-$)

levels [92], but there was no evidence for any transition linking these two levels in the current work. Figure 4.43 shows a gate set on the 407 keV transition, which gives a clean spectra of the other transitions associated with this nucleus.

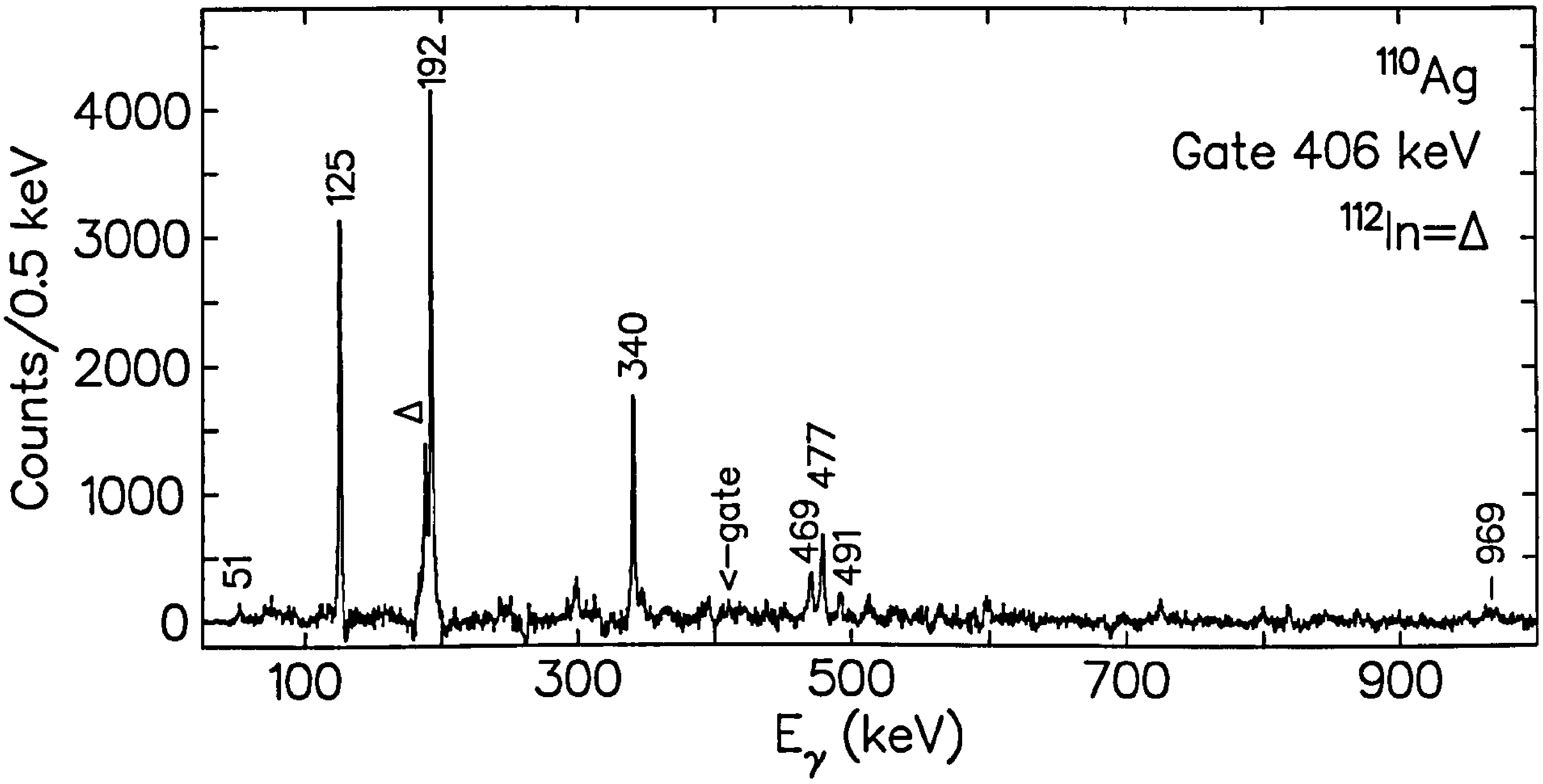

Figure 4.43: Gamma-ray coincidence spectrum gated by the 406 keV transition in ^{110}Ag.

Table 4.10: Gamma rays assigned to ^{110}Ag in the current work. The relative γ-ray intensities are normalized to 100 for the 406 keV transition.

E_γ (keV)	I_γ	I_i^π (keV)	I_f^π (keV)	R_{DCO}	A_2
51.2(5)	53(11)	(8^-)	(7^-)		
125.1(3)	112(16)	(6^-)	6^+	1.00(2) [1]	−0.05(7)
191.8(2)	80(5)	(9^-)	(8^-)	0.91(9) [1]	
339.6(4)	59(3)	(11^-)	(10^-)	0.85(5) [1]	−0.06(4)
406.3(3)	100(6)	(10^-)	(9^-)		−0.08(6)
469.1(3)	16(5)	(14^-)	(13^-)	0.93(6) [1]	
477.4(2)	40(4)	(12^-)	(11^-)	0.99(4) [1]	
491.2(3)	13(5)	(13^-)	(12^-)		
745.9(8)	14(4)	(11^-)	(9^-)		
969.1(4)	6(4)	(13^+)	(11^+)		

1 = Gate set on 406 keV (ΔI=1) transition

4.5.3 ^{111}Ag

There was no evidence of transitions associated with ^{111}Ag using γ-ray energies from [112] in either the 28 or 40 MeV datasets. This can be attributed to the fact that ^{111}Ag has the smallest production cross-section (<5 mb) of all the nuclei populated in this experiment.

4.6 Incomplete Fusion Reactions

If the reaction ^{7}Li+^{110}Pd was viewed as the break-up of ^{7}Li followed by the incomplete fusion of either a triton, an α particle or ^{6}He, as discussed in section 3.1.1, then the effective energies of the fragments can be calculated by equation 3.4. Table 4.11 shows the effective energies of the triton, α and ^{6}He fragments for the three ^{7}Li beam energies used in this experiment and figure 4.44 shows the nuclei populated by the three incomplete fusion reactions. The cross-sections (calculated by PACE) are only representative as the incomplete fusion-evaporation mechanism occurs alongside the conventional fusion-evaporation mechanism and so in practice, would be much smaller.

The α fragments with an effective energy of 26.5 and 19.5 MeV would, from figure 4.44, be expected to populate ^{112}Cd in the 40 and 28 MeV datasets respectively, if the reaction was regarded as the break-up of the ^{7}Li into an α and a triton. The 40 MeV ^{7}Li populates ^{112}Cd with a cross-section of 3 mb (see figure 4.2) and it would be expected to be present in the 40 MeV dataset, populated either by a complete or an incomplete fusion evaporation reaction mechanism. However, ^{112}Cd is not expected to be significantly populated by conventional fusion-evaporation at 28 MeV and the presence of ^{112}Cd in this dataset, as shown in figure 4.45, indicates a possible incomplete fusion mechanism taking place.

No other evidence of incomplete fusion processes can be inferred, as the remaining incomplete-fusion reaction products are populated by the conventional fusion-evaporation reaction in the same dataset *i.e.* the 25 MeV ^{3}H fragment, which is associated with the 50 MeV dataset, incident on ^{110}Pd would populate ^{110}Ag, but ^{110}Ag is also populated by ^{7}Li in the 50 MeV dataset.

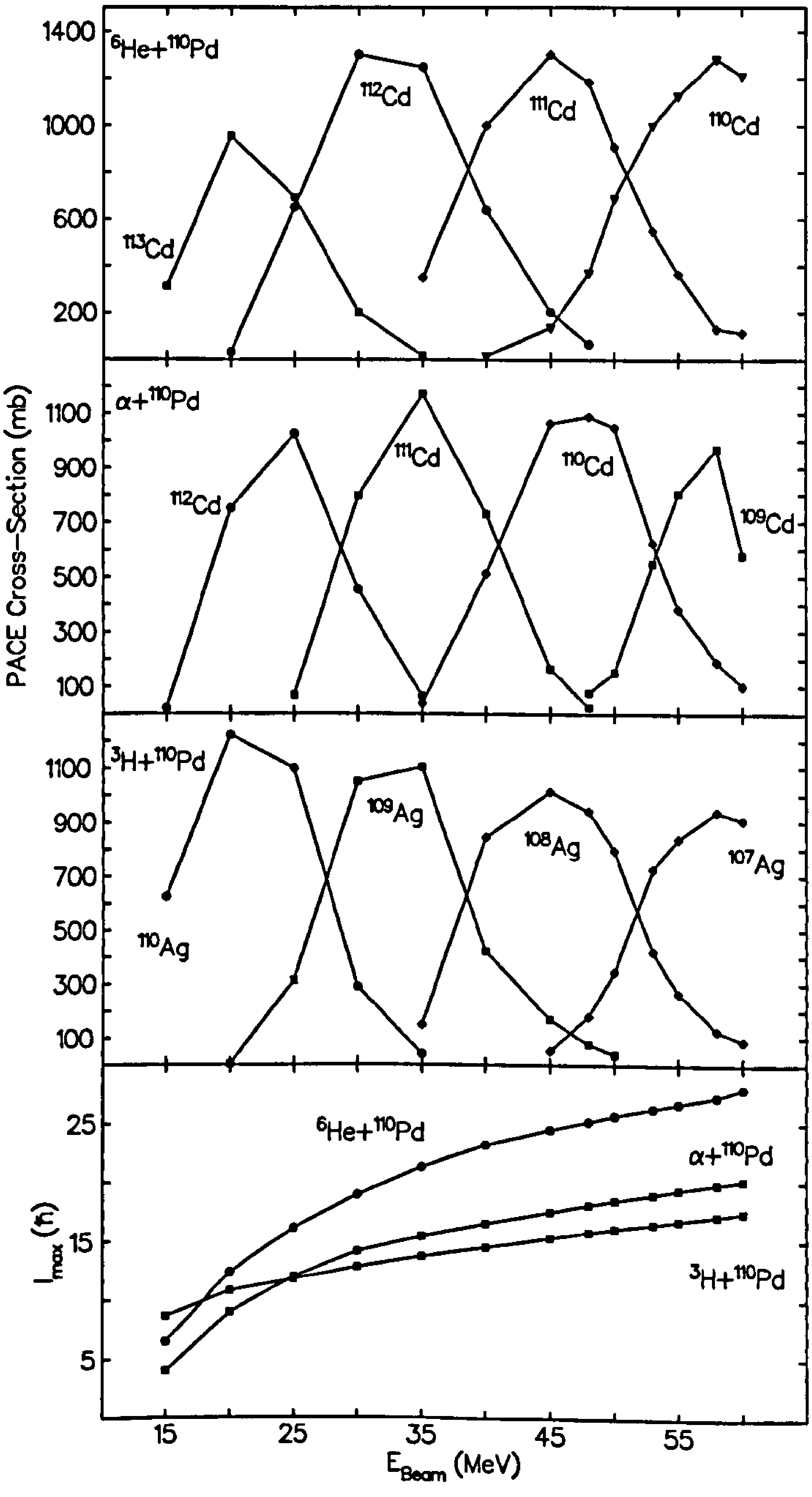

Figure 4.44: Predicted production cross-sections for the ^{3}H+^{110}Pd, α+^{110}Pd and ^{6}He+^{110}Pd reactions as a function of beam energy, calculated by PACE.

Table 4.11: Effective energies for triton, α and ^{6}He fragments in the case of incomplete fusion of a 50, 40 or 28 MeV ^{7}Li nucleus. The nuclei populated in the incomplete-fusion process are in brackets.

$E_{^7Li}$ (MeV)	$E_{^3H}$ (MeV)	E_α (MeV)	^{6}He (MeV)
50	25 (^{110}Ag)	32 (^{111}Cd)	47 (^{111}Cd)
40	20.5 (^{110}Ag)	26.5 (^{112}Cd)	38.5 (^{111}Cd)
28	15.5 (^{110}Ag)	19.5 (^{112}Cd)	26.5 (^{112}Cd)

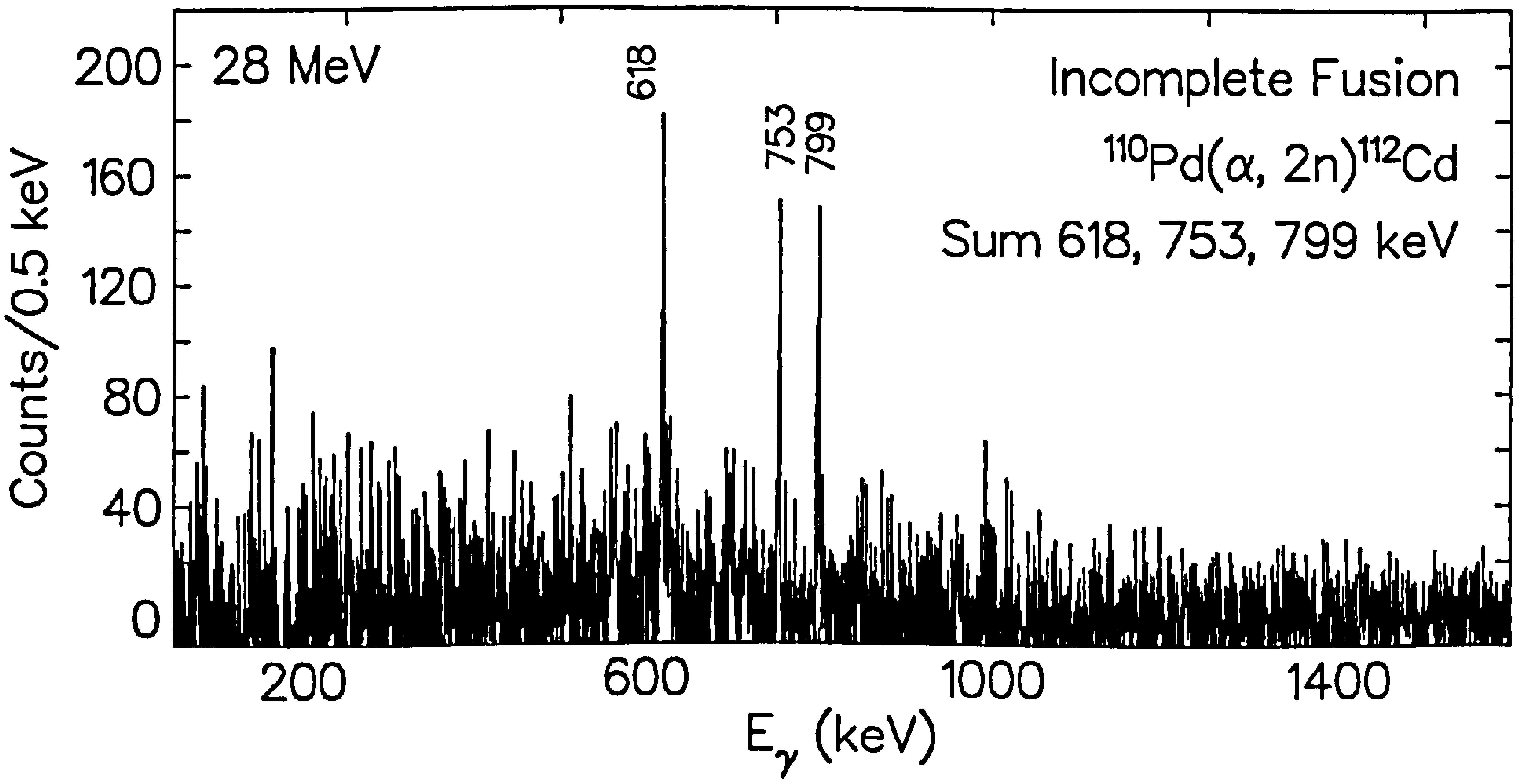

Figure 4.45: Sum of ^{112}Cd γ-ray coincidence gates displaying evidence of ^{112}Cd populated by a possible incomplete-fusion reaction mechanism in the 28 MeV dataset. The labelled lines correspond to the first three transitions in ^{112}Cd.

Chapter 5

Discussion

5.1 Indium Nuclei

Using equation 1.13, experimental $B(M1)/B(E2)$ values could be extracted for bands A and B in both ^{112}In and ^{114}In. Where the competing $E2$ crossover transitions were too weak to be observed, they were assigned an intensity of 1 thus setting a lower limit to the experimentally obtained $B(M1)/(B(E2)$ value. Intensities were used which were obtained from a 2D fit of a γ–γ matrix using escl8r [89].

Theoretical values for the $B(M1)/B(E2)$ ratios were calculated using the semi-classical geometrical model of Dönau (see section 1.2.2) for various configurations and are compared with the experimentally extracted ratios. Certain approximations and assumptions enter into these theoretical calculations, in particular relative to the K projections and individual quasiparticle alignments. The assumption that δ, the $M1/E2$ mixing ratio, was equal to zero was also made. Values for the empirical single-particle g-factors were obtained from [113] and the g-factors of multi-particle configurations were obtained using the additivity rule [114]. A quadrupole moment of Q_0= 2.0 *eb* was used [107], appropriate for $\beta_2\sim$0.12 [48].

5.1.1 ^{112}In

Band A

The low-lying positive parity states in ^{112}In have previously been assigned $\nu(g_{7/2})\otimes\pi(g_{9/2})$ or $\nu(d_{5/2})\otimes\pi(g_{9/2})$ configurations [93, 115, 116], inferred from measurements of the $I^{\pi} = 7^{+}$ quadrupole moment [117]. To keep the positive parity nature of the band, higher-spin states would require a $\nu(h_{11/2})^2$ rotation-aligned component.

The experimental alignments (see figure 5.1) were plotted using adopted Harris parameters of $\mathcal{I}^{(0)}$=3.5$\hbar^2$/MeV and $\mathcal{I}^{(1)}$=22$\hbar^4$/MeV^3 [118]. The alignment curve for the positive parity band A shows an initial alignment of 2$\hbar$ with an approximate alignment gain of 10$\hbar$ at 0.48 MeV which can be attributed to the alignment of a pair of neutrons in the $h_{11/2}$ orbital.

The experimentally obtained $B(M1)/B(E2)$ values for band A in ^{112}In are shown in table 5.1. The parameters which result in each calculated curve are listed in table 5.3. As no crossover transitions were observed in band A, the $B(M1)/B(E2)$ values given are lower limits. Band A has lower limits of $B(M1)/B(E2)$ ratio consistent with those reported in ^{108,110}In [15], ^{111}In [13] and ^{113}In [14] which report values between approximately 20 and 100 $(\mu_N/\text{eb})^2$. Figure 5.2 shows the experimentally extracted $B(M1)/B(E2)$ values with the $B(M1)/B(E2)$ values for three suggested configurations obtained using the geometrical model. Proton excitations across the Z=50 shell gap are ruled out as this would lead to occupation of the deformation driving orbitals and manifest in a rotational band of

$E2$ transitions [119]. Thus in both ^{112}In and ^{114}In it is a single $\pi(g_{9/2})$ hole that is considered to couple with various combinations of neutron configuration. It is clear that the $\nu(h_{11/2})^2$ configuration is consistent with the experimental values above spin 10.

Taking the $B(E2)$ value for the 179 keV transition, calculated by use of the geometrical model, to be approximately 0.2 $(e\cdot b)^2$ and $\mathcal{I}^{(2)}$=22.3$\hbar^2$ MeV^{-1}, calculated by use of equation 2.23, results in a $\mathcal{I}^{(2)}/B(E2)$ ratio of about 110$\hbar^2$ MeV^{-1} $(e\cdot b)^{-2}$. This ratio is typically closer to 10$\hbar^2$ MeV^{-1} $(e\cdot b)^{-2}$ in nuclei described by the collective model, as outlined in section 2.3.4. Similar calculations on the dipole transitions in this band result in values ranging between 40 and 170$\hbar^2$ MeV^{-1} $(e\cdot b)^{-2}$. Hence the shears interpretation based on the $B(M1)/B(E2)$ behaviour for band A in ^{112}In is further supported by the large $\mathcal{I}^{(2)}/B(E2)$ ratio, suggesting there is a significantly larger contribution to the angular momentum from the valence high-j particles than if the band arose solely from collective rotation. It should be noted that similar calculations carried out on bands of similar nature in ^{108}In and ^{110}In [15] result in larger $\mathcal{I}^{(2)}/B(E2)$ ratios of up to 450$\hbar^2$ MeV^{-1} $(e\cdot b)^{-2}$.

Band B

The low-lying negative parity states of band B are assigned a configuration of $\pi(g_{9/2})\otimes$ $\nu(h_{11/2})$ [93, 94, 115, 116] by measurement of the static quadrupole moment of the $I^{\pi}=8^{-}$ state [120]. The experimentally obtained $B(M1)/(B(E2)$ values for band B in ^{112}In are shown in table 5.2. As four crossover transitions were observed, four experimental $B(M1)/(B(E2)$ ratios can be extracted with their associated uncertainties, in addition to five lower limits corresponding to where crossover transitions were not observed. Figure 5.3 shows the experimentally extracted $B(M1)/B(E2)$ values plotted alongside the $B(M1)/B(E2)$ values calculated using the geometrical model for three suggested configurations. The parameters which result in each calculated curve are listed in table 5.4. It is clear that the two configurations that include the $\nu(h_{11/2})$ component are consistent with the experimental values above spin 10 and indicate a $\pi(g_{9/2})\otimes$ $\nu(h_{11/2})$ configuration as expected.

The alignment curve for the negative parity band B shows an initial alignment of $5\hbar$ with an approximate alignment gain of at least $7\hbar$ at 0.36 MeV which may indicate the alignment of a pair of neutrons in the $h_{11/2}$ orbital, although there is no evidence of the uncoupled neutron blocking this first alignment. However, it should be noted that this parameterisation is not an ideal method to investigate these irregular rotational structures.

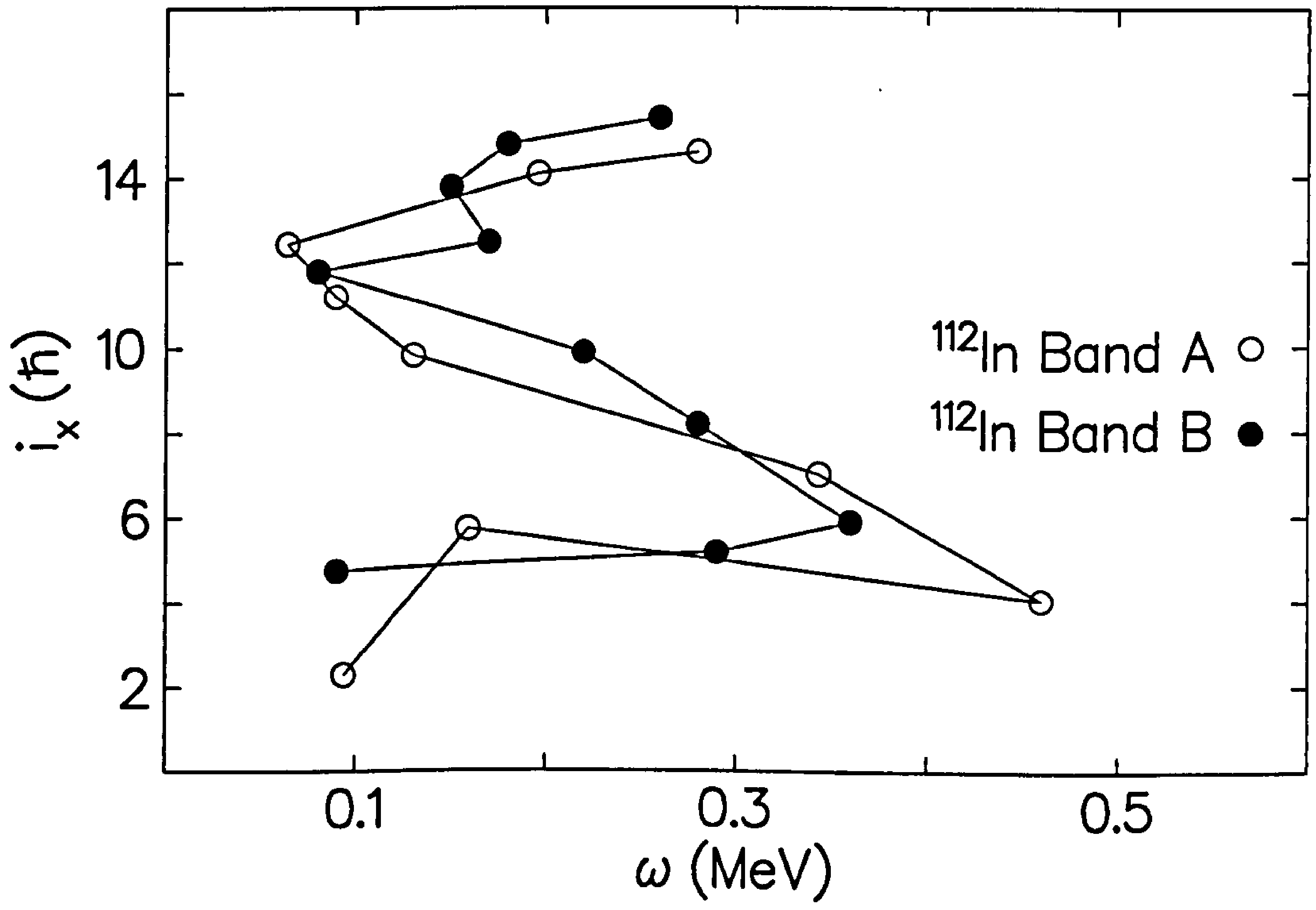

Figure 5.1: Experimental quasiparticle alignments in ^{112}In.

Table 5.1: Experimentally extracted $B(M1)/B(E2)$ ratios for band A in ^{112}In.

I_i	$E_\gamma^{\Delta I=1}$ (keV)	$E_\gamma^{\Delta I=2}$ (keV)	$\frac{I_\gamma(\Delta I=1)}{I_\gamma(\Delta I=2)}$	$\frac{B(M1)}{B(E2)}$ $(\mu_N/\mathrm{eb})^2$
12	261	(947)	40	>104
13	179	(440)	36	>51
14	128	(307)	32	>58
15	273	(401)	36	>72
16	393	(666)	28	>69
17	554	(947)	16	>50
18	708	(1262)	7	>38

Table 5.2: Experimentally extracted $B(M1)/B(E2)$ ratios for band B in ^{112}In.

I_i	$E_\gamma^{\Delta I=1}$ (keV)	$E_\gamma^{\Delta I=2}$ (keV)	$\frac{I_\gamma(\Delta I=1)}{I_\gamma(\Delta I=2)}$	$\frac{B(M1)}{B(E2)}$ $(\mu_N/\mathrm{eb})^2$
10	588	(775)	58	>56
11	724	1313	30(11)	108(54)
12	552	1277	7(3)	139(46)
13	437	989	10(4)	40(20)
14	160	597	0.7(2)	19(4)
15	345	(505)	11	>6
16	290	(635)	63	>9
17	363	(653)	2	>3

Table 5.3: Parameters used in the Dönau analysis of band A in ^{112}In.

K	Q_0(e·b)	RAL config.	$i_x^{(2)}(\hbar)$	$g^{(2)}$	DAL config.	$i_x^{(1)}(\hbar)$	$g^{(1)}$
7	2.0	$\nu[(h_{11/2})^2\otimes(g_{7/2})]$	12	−0.145	$\pi(g_{9/2})$	1	+1.27
7	2.0	$\nu(d_{5/2})$	0	−0.33	$\pi(g_{9/2})$	1	+1.27
7	2.0	$\nu(g_{7/2})$	2	+0.21	$\pi(g_{9/2})$	1	+1.27

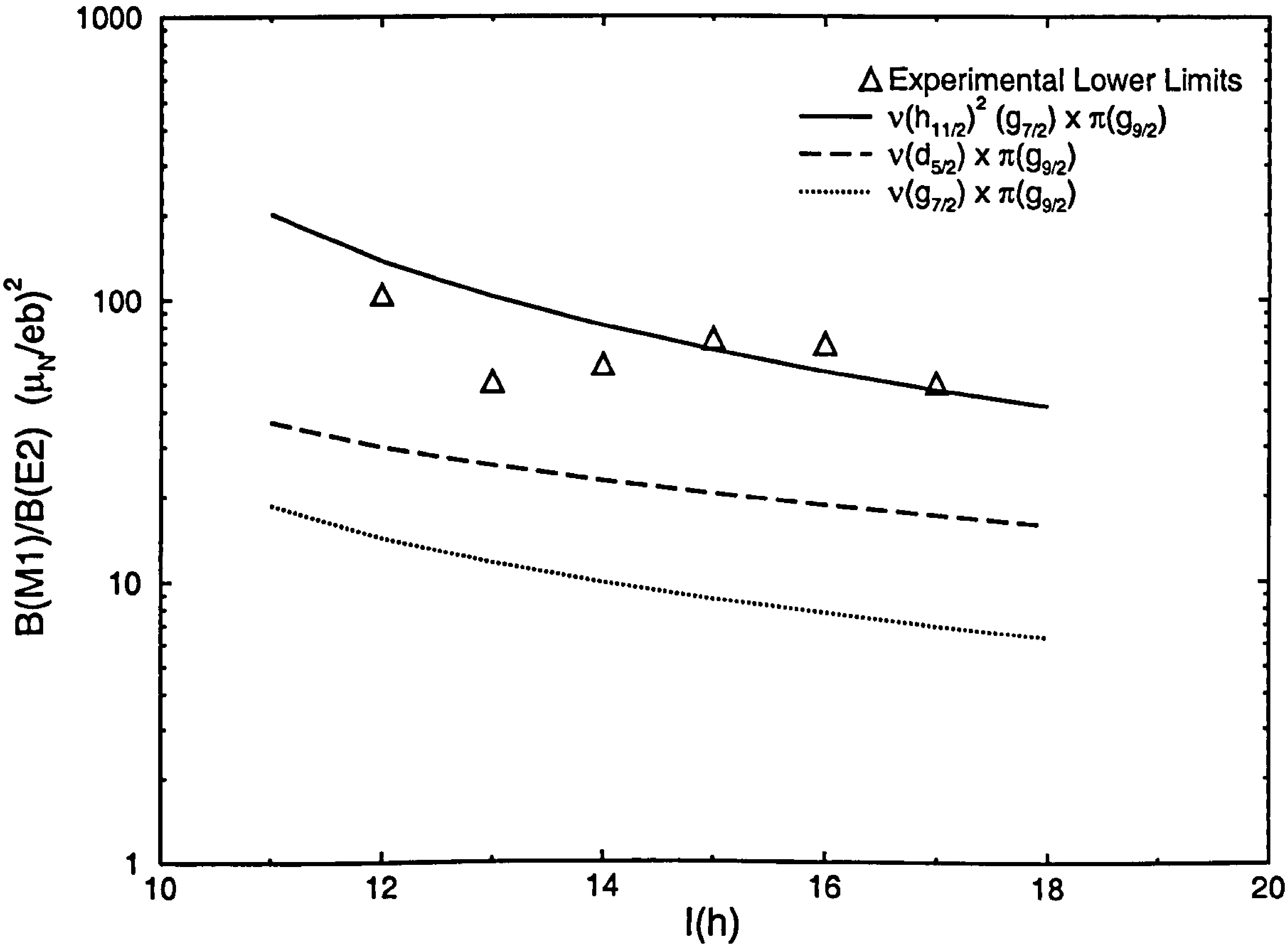

Figure 5.2: Comparison of experimental and calculated $B(M1)/B(E2)$ ratios for band A in ^{112}In.

Table 5.4: Parameters used in the Dönau analysis of band B in ^{112}In.

K	Q_0(e·b)	RAL config.	$i_x^{(2)}(\hbar)$	$g^{(2)}$	DAL config.	$i_x^{(1)}(\hbar)$	$g^{(1)}$
8	2.0	$\nu(h_{11/2})$	5	-0.21	$\pi(g_{9/2})$	1	$+1.27$
8	2.0	$\nu[(h_{11/2}) \otimes (h_{11/2})^2]$	15	-0.21	$\pi(g_{9/2})$	1	$+1.27$

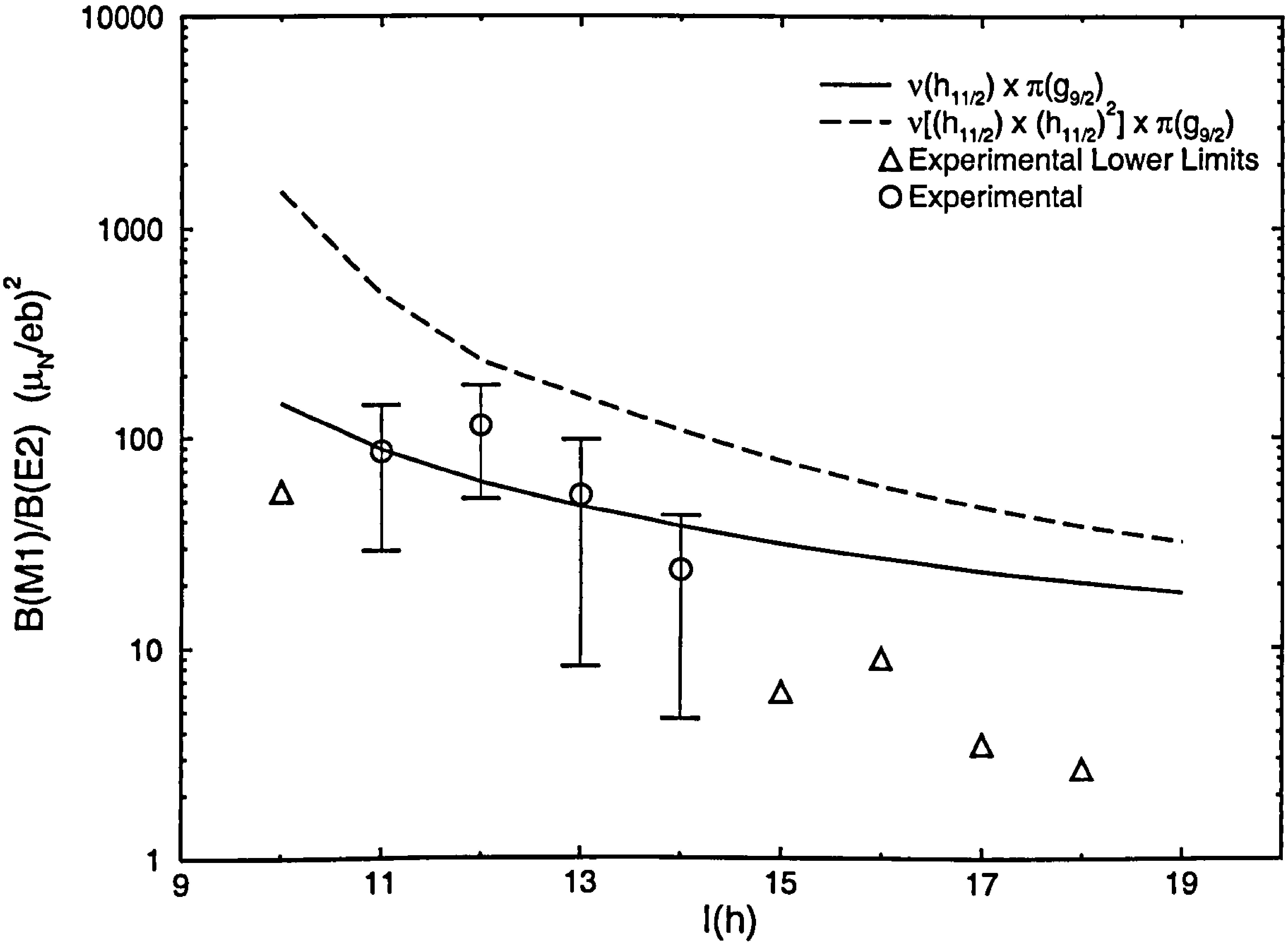

Figure 5.3: Comparison of experimental and calculated $B(M1)/B(E2)$ ratios for band B in ^{112}In.

5.1.2 ^{114}In

Band A

The low-lying negative parity bands have been assigned a configuration of $\pi(g_{9/2})\otimes\nu(h_{11/2})$ [101, 116]. The experimental alignments, plotted in figure 5.4, using the same parameters as used for ^{112}In. The alignment curve for the negative parity band A shows an initial alignment at approximately 0.35 MeV, with an approximate alignment gain of at least a further $5\hbar$, dependent of the final alignment.

The experimentally extracted $B(M1)/(B(E2)$ values for band A in ^{114}In are shown in table 5.5. The observation of one crossover transition allowed the direct measurement of one $B(M1)/(B(E2)$ value, in addition to three lower limits. The values are consistent with those expected for a shears band, but with only one direct measurement, further data points are required to make a more reliable interpretation of this band. Figure 5.5 shows the experimentally extracted $B(M1)/B(E2)$ values with the $B(M1)/B(E2)$ values for three suggested configurations obtained using the geometrical model and the parameters used in this analysis are listed in table 5.7. Proton excitations across the Z=50 shell were ruled out as previously outlined. Thus in the negative parity band A, it is a single $\pi(g_{9/2})$ hole that is considered to couple with various combinations of neutron configuration. The $\nu(h_{11/2})$ configuration appears to be consistent with the experimental values above spin 10.

Calculations of the $\mathcal{I}^{(2)}/B(E2)$ ratios range between 25 and $50\hbar^2$ MeV^{-1} $(e\cdot b)^2$, lower than ratios obtained in ^{112}In, but still larger than would be expected if the band arose solely from collective rotation.

Band B

The experimentally obtained $B(M1)/B(E2)$ values for band B in ^{114}In are shown in table 5.6. No crossover transitions were observed, so the values given are lower limits. Figure 5.6 shows the experimentally derived $B(M1)/B(E2)$ values with the $B(M1)/B(E2)$ values for three suggested configurations obtained using the geometrical model and the parameters used in this analysis are listed in table 5.8. The low-lying positive parity bands have been assigned a configuration of $\pi(g_{9/2})\otimes$ $\nu(g_{7/2})$ or $\pi(g_{9/2})\otimes$ $\nu(d_{5/2})$ [101, 116], and a measurement of the magnetic moment of the ground state suggest the same configurations [121]. The current calculations suggest that if band B is of positive parity (whereby the 148 keV transition is of $E1$ character), it is consistent with being based on the $\pi(g_{9/2})\otimes$ $\nu(g_{7/2})$ configuration. However, due to the unknown multipolarity of the 148 keV transition, band B could also be of negative parity (whereby the 148 keV transition is $M1$) and the calculated values for the negative parity $\pi(g_{9/2})\otimes$ $\nu(h_{11/2})$ configuration are shown to be not significantly different from that of the positive parity $\nu(g_{7/2})$ based configuration. Therefore, the assigning of band B to that of unknown parity appears to be valid at this time.

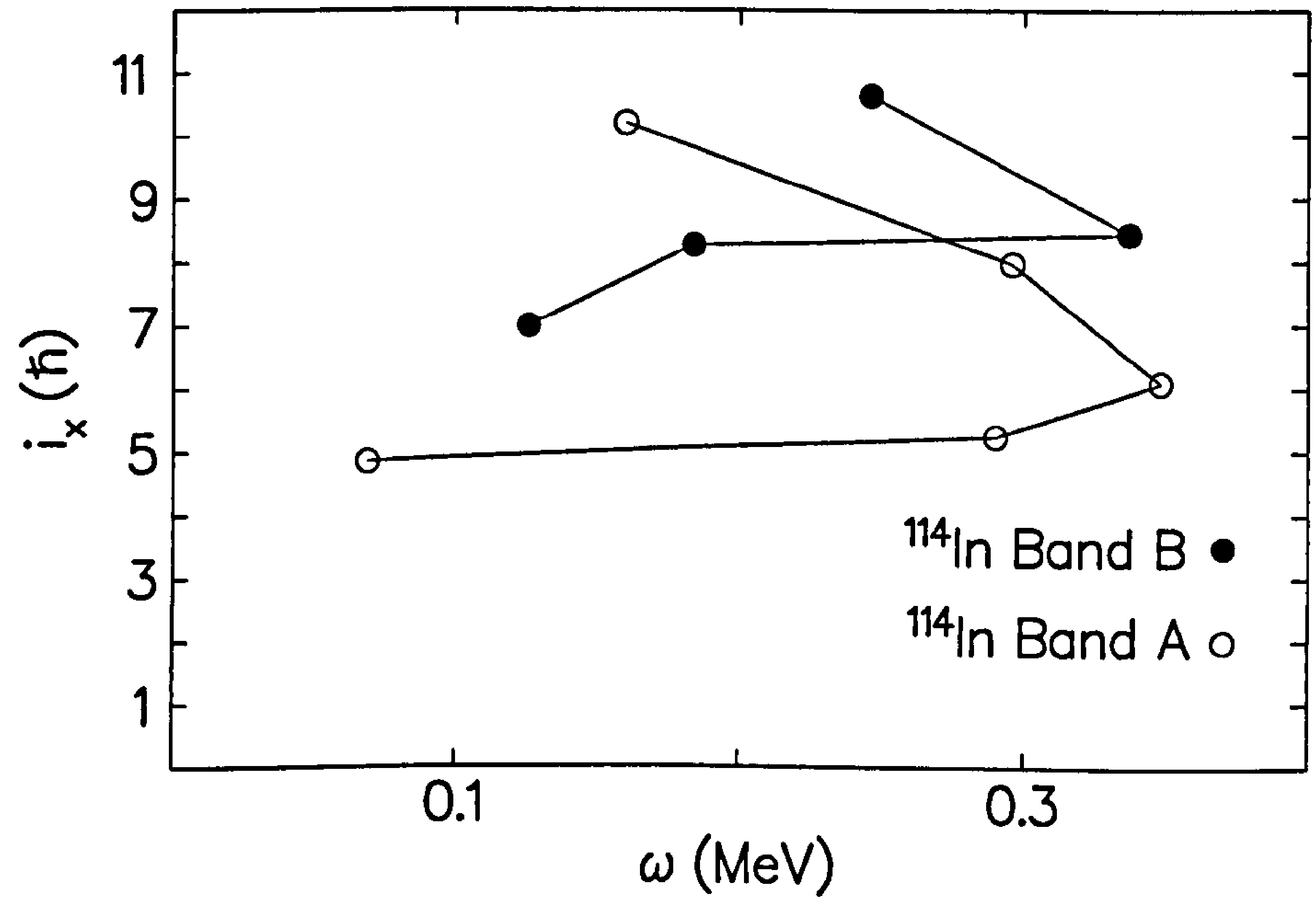

Figure 5.4: Experimental quasiparticle alignments in ^{114}In

Table 5.5: Experimentally obtained $B(M1)/B(E2)$ ratios for band A in ^{114}In.

I_i	$E_\gamma^{\Delta I=1}$ (keV)	$E_\gamma^{\Delta I=2}$ (keV)	$\frac{I_\gamma(\Delta I=1)}{I_\gamma(\Delta I=2)}$	$\frac{B(M1)}{B(E2)}$ $(\mu_N/\text{eb})^2$
10	577	(715)	57	>37
11	696	1275	5(3)	21(17)
12	593	(1289)	2	>47
13	321	(914)	1	>13

Table 5.6: Experimentally extracted $B(M1)/B(E2)$ ratios for band B in ^{114}In.

I_i	$E_\gamma^{\Delta I=1}$ (keV)	$E_\gamma^{\Delta I=2}$ (keV)	$\frac{I_\gamma(\Delta I=1)}{I_\gamma(\Delta I=2)}$	$\frac{B(M1)}{B(E2)}$ $(\mu_N/\text{eb})^2$
12	368	(620)	3	>6
13	674	(1042)	2	>8
14	493	(1166)	1	>12

Table 5.7: Parameters used in the Dönau analysis of band A in ^{114}In.

K	Q_0(e·b)	RAL config.	$i_x^{(2)}(\hbar)$	$g^{(2)}$	DAL config.	$i_x^{(1)}(\hbar)$	$g^{(1)}$
8	2.0	$\nu(h_{11/2})$	5	-0.21	$\pi(g_{9/2})$	1	$+1.27$
8	2.0	$\nu[(h_{11/2}) \otimes (h_{11/2})^2]$	15	-0.21	$\pi(g_{9/2})$	1	$+1.27$

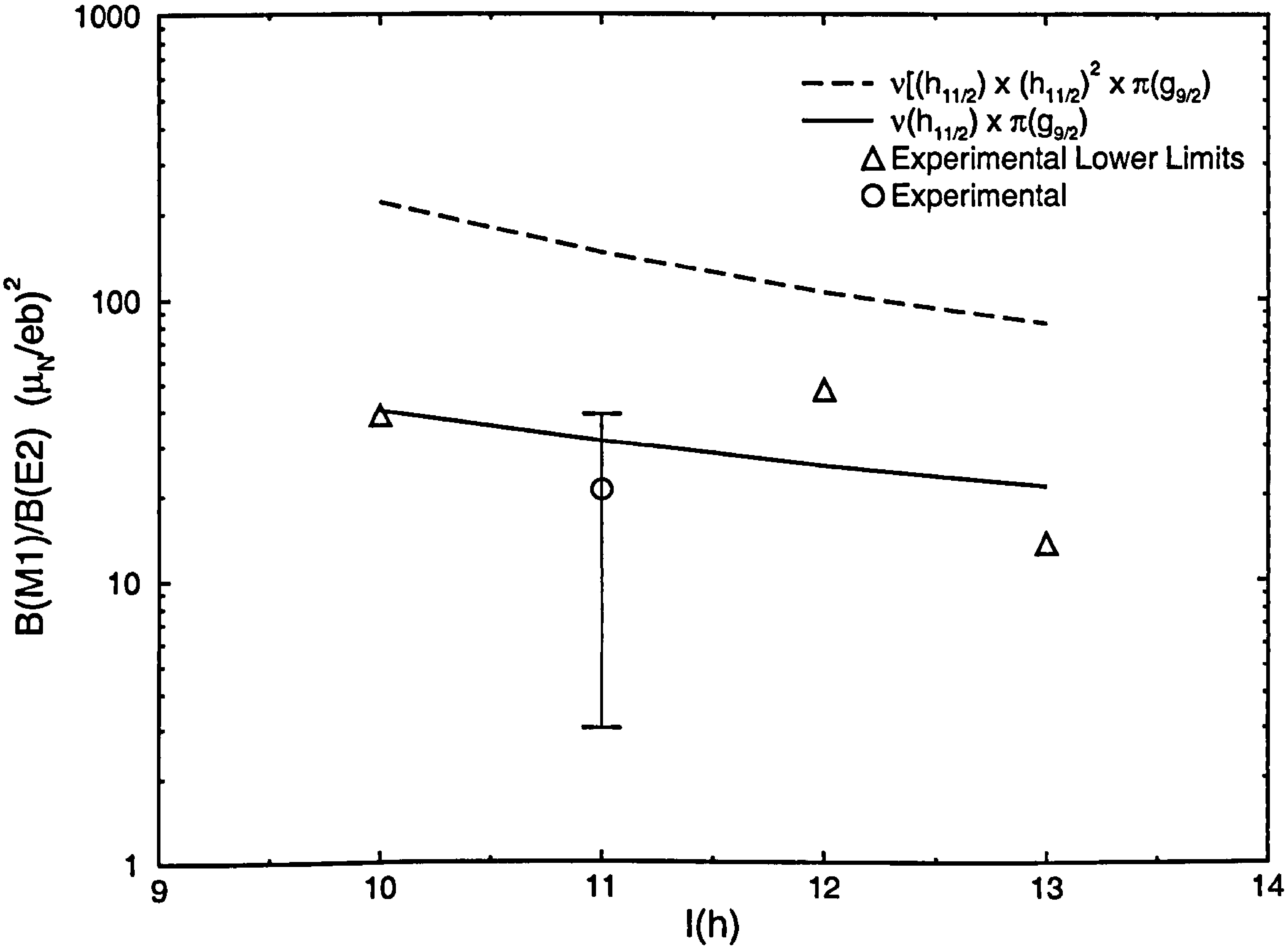

Figure 5.5: Comparison of experimental and calculated $B(M1)/B(E2)$ ratios for band A in ^{114}In.

Table 5.8: Parameters used in the Dönau analysis of band B in ^{114}In.

K	Q_0(e·b)	RAL config.	$i_x^{(2)}(\hbar)$	$g^{(2)}$	DAL config.	$i_x^{(1)}(\hbar)$	$g^{(1)}$
10	2.0	$\nu(d_{5/2})$	0	−0.33	$\pi(g_{9/2})$	1	+1.27
10	2.0	$\nu(h_{11/2})$	5	−0.21	$\pi(g_{9/2})$	1	+1.27
10	2.0	$\nu(g_{7/2})$	2	+0.21	$\pi(g_{9/2})$	1	+1.27

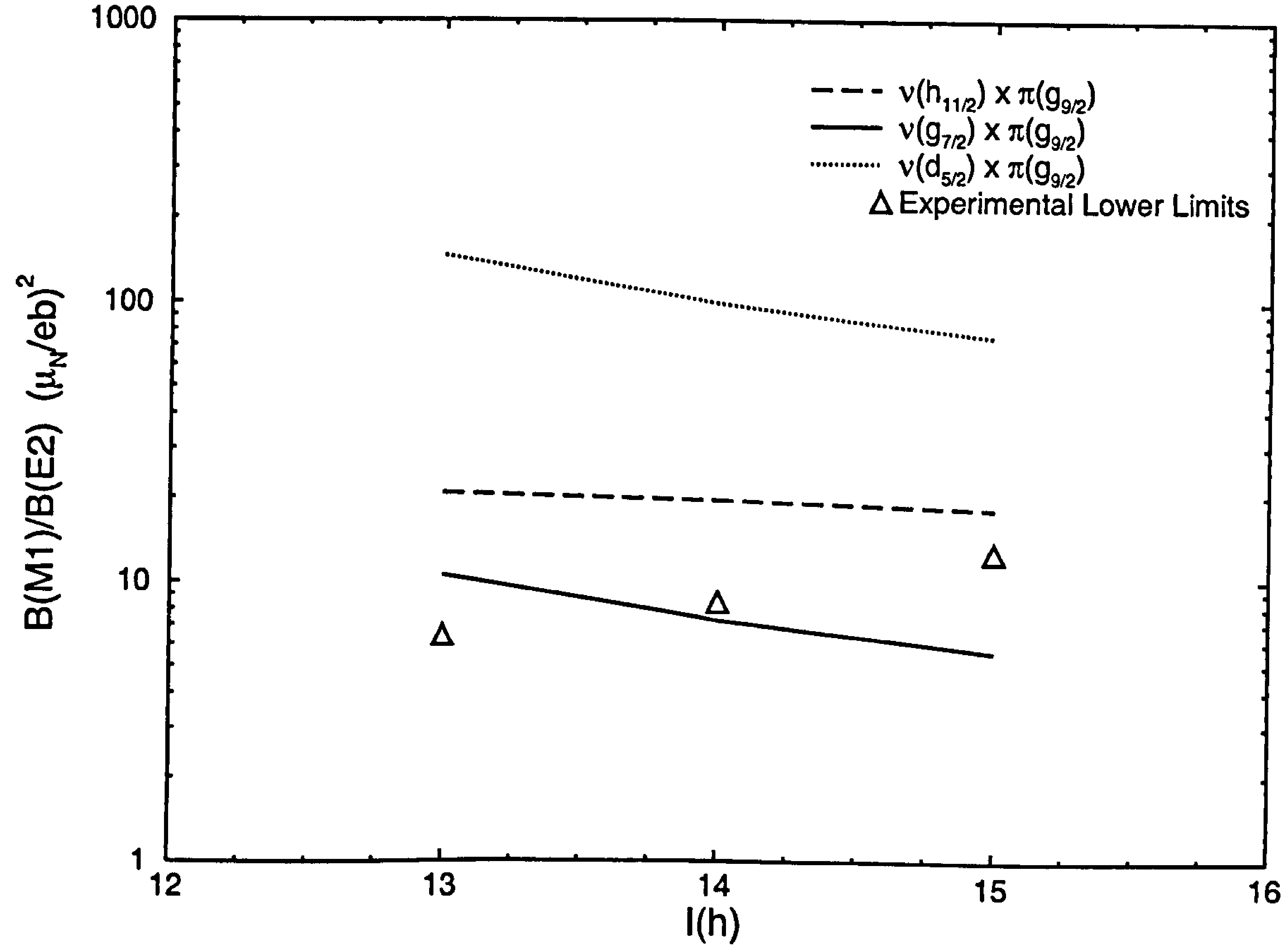

Figure 5.6: Comparison of experimental and calculated $B(M1)/B(E2)$ ratios for band B in ^{114}In.

5.2 Cadmium Nuclei

The comparison of experimental alignment properties from different Cd isotopes allows the identification of chief orbitals responsible for the structural changes frequently observed in this mass region. Figure 5.7 shows the experimental alignments for the yrast bands in $^{112-114}$Cd. Harris parameters of $\mathcal{I}^{(0)}$=3.5$\hbar^2$/MeV and $\mathcal{I}^{(1)}$=22$\hbar^4$/MeV^3 were adopted to give a relatively constant alignment above the first crossing [118]. For the even-N Cd-isotopes ^{112}Cd and ^{114}Cd, the initial alignment is zero and the curves exhibit a backbend at $\sim$ 0.38 MeV and a gain in alignment of about 10 $\hbar$, which can be attributed to the alignment of two neutrons in the $h_{11/2}$ orbital. This behaviour is consistent with that of ^{110}Cd [91] as shown in the top part of figure 5.7. A theoretical interpretation of such experimental data is provided by the TRS calculations. An advantage of the TRS calculations is that it allows the proton and neutron contributions to the total aligned angular momentum to be decomposed separately, such that the experimental data on a specific nucleus can be analysed with respect to the changes in both proton and neutron configurations. In figure 5.8, the TRS calculations predict that the total aligned angular momentum is almost entirely comprised of the neutron contribution, with an gain in alignment of 10$\hbar$ at approximately 0.3 MeV, which is in agreement of the experimentally extracted alignments.

The E-GOS curves plotted for ^{112}Cd and ^{114}Cd, as shown in figure 5.9, initially follow near hyperbolic loci associated with harmonic quadrupole vibrational structures. With the addition of the further data point obtained in this work, ^{112}Cd appears to exhibit a phase change from a vibrator to a constant R-value, suggestive of a rotational structure. This phase change from the vibrational to rotational nuclear collectivity at a spin of $\sim$10$-$12$\hbar$ is often interpreted as the crossing of a vibrational ground state structure with an aligned $(\nu h_{11/2})^2_{10^+}$ structure [122].

Concerning the odd-N isotope, ^{113}Cd, the initial alignment is about $5\hbar$. The crossing frequency is higher (~0.45 MeV) due to the uncoupled $h_{11/2}$ neutron blocking the alignment of the second neutron ("BC") $h_{11/2}$ pair. The final alignment is uncertain because the continuation of the bands after the alignment is not clearly established. However, from the existing data it is possible to deduce a frequency for the backbending of ~0.4 MeV. This increase in alignment of at least $8\hbar$ is most likely associated with the breaking of the "BC" $h_{11/2}$ neutron pair in this mass region. The TRS calculations (see figure 5.8) are in good agreement with the experimentally extracted alignments, again showing the total aligned angular momentum is almost entirely comprised of the neutron component, with a neutron alignment occurring at ~0.4 MeV and a gain in alignment of approximately $8\hbar$.

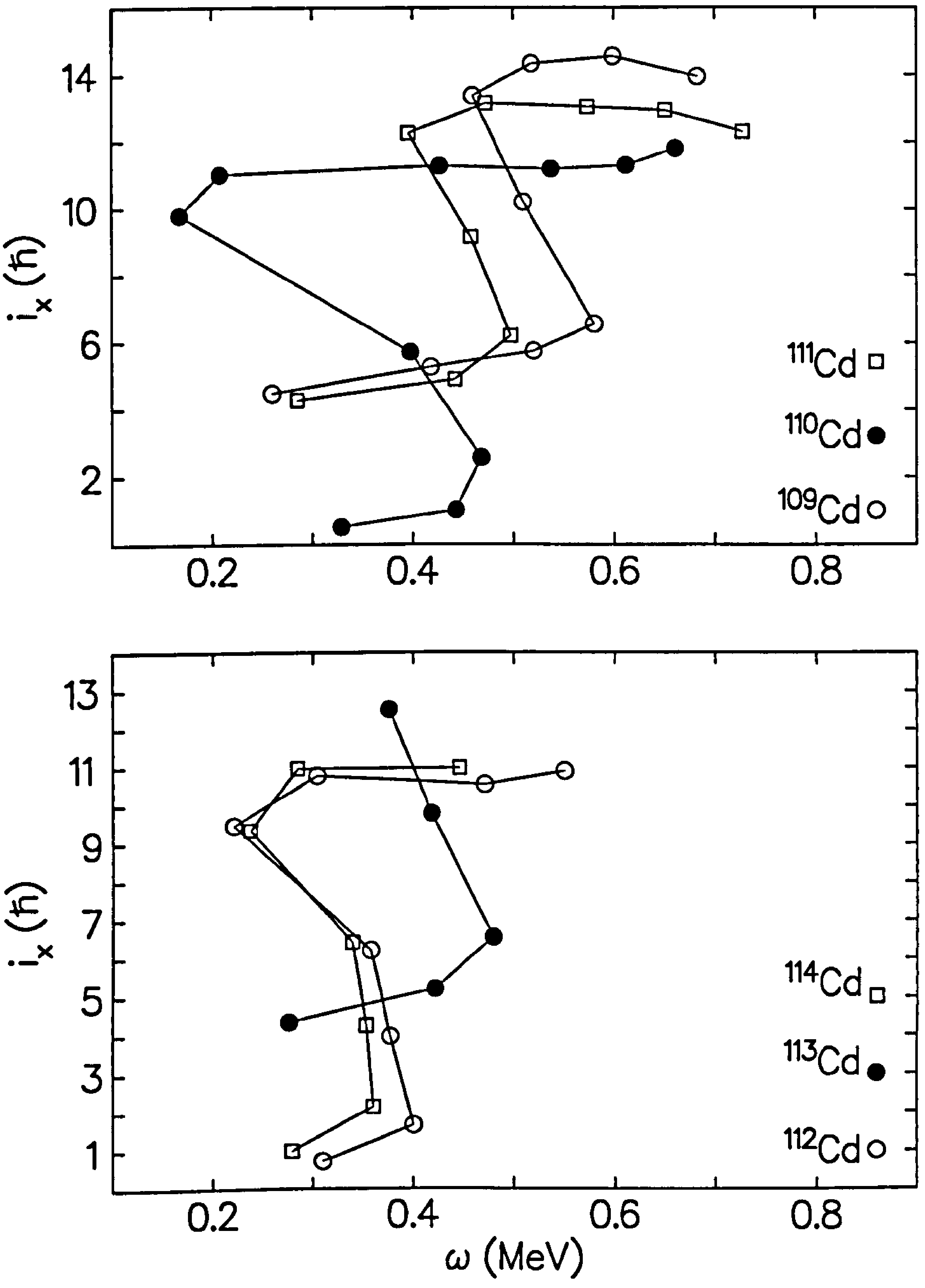

Figure 5.7: Bottom: Experimental quasiparticle alignments for the yrast bands in ^{112,113,114}Cd. Top: Quasiparticle alignments for the yrast bands in ^{109,110,110}Cd taken from Ref. [118]. Harris parameters of $\mathcal{I}^{(0)}=3.5\hbar^2/\mathrm{MeV}$ and $\mathcal{I}^{(1)}=22\hbar^4/\mathrm{MeV}^3$ were used in all cases.

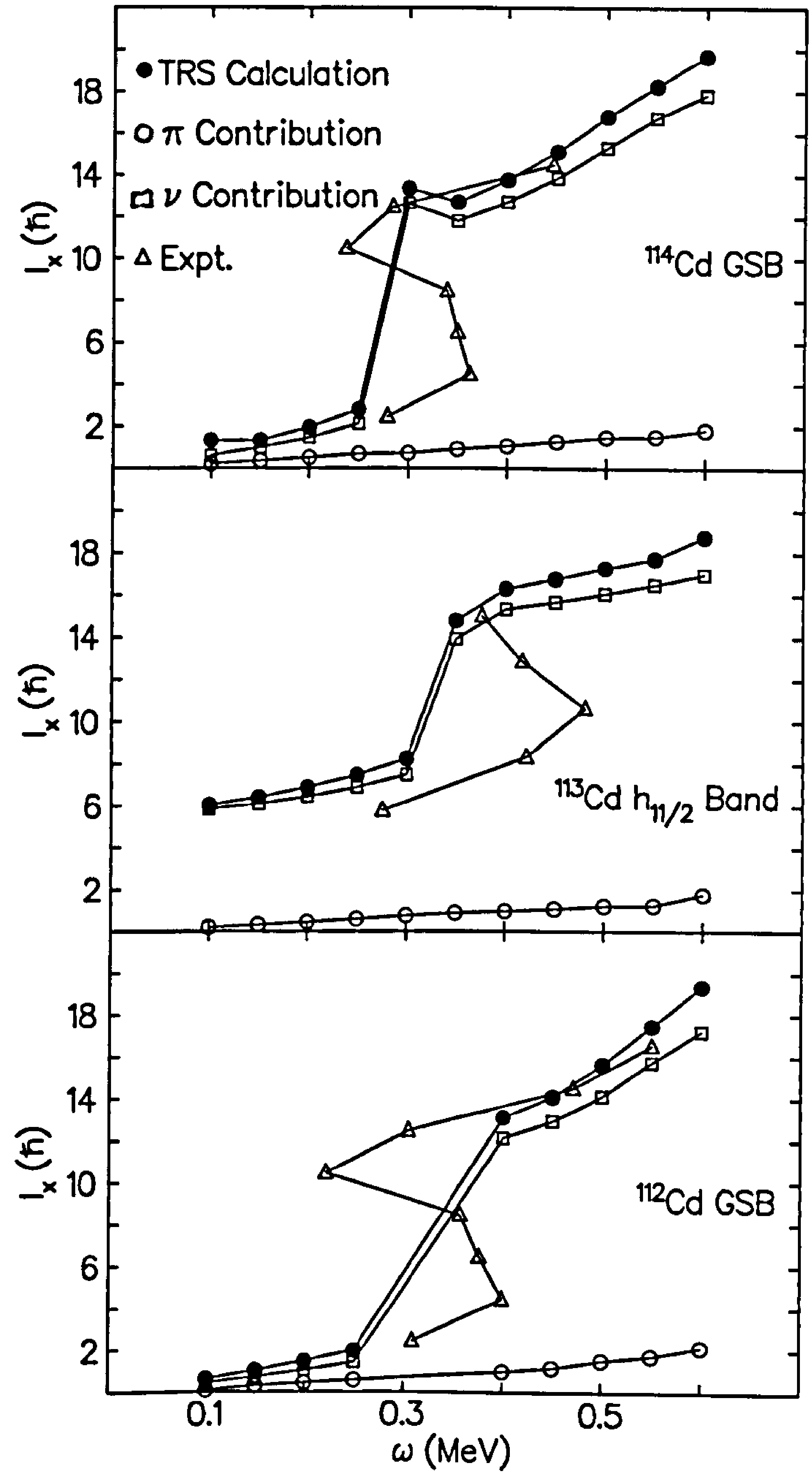

Figure 5.8: Comparison of results from TRS calculations for the ground state bands in ^{112}Cd and ^{114}Cd and the $h_{11/2}$ band in ^{113}Cd with experimentally deduced values. The calculated total aligned angular momentum (I_x is shown by the filled circles. The proton and neutron contributions to I_x are shown by the open circles and squares respectively. The open triangles represent the experimentally extracted I_x.

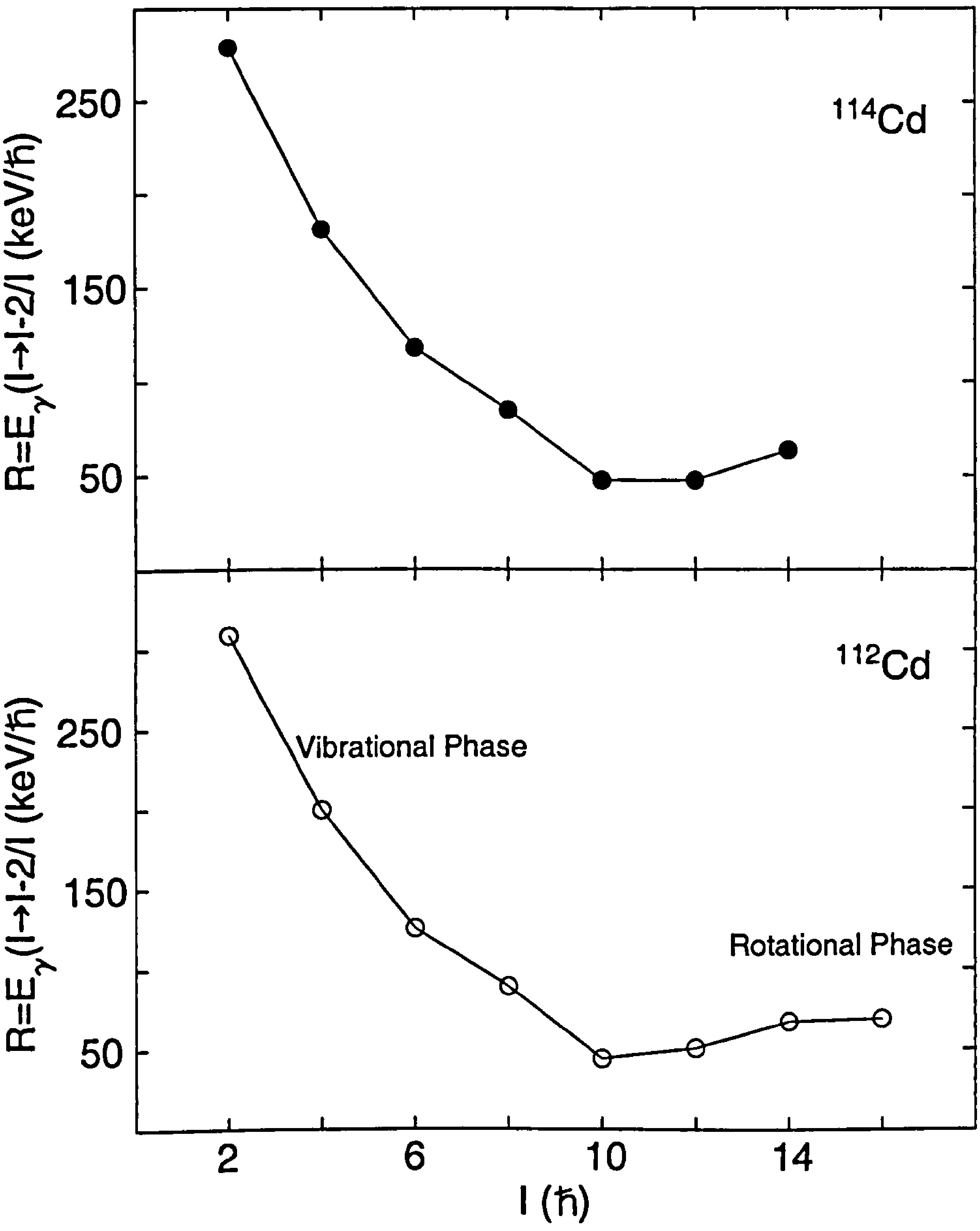

Figure 5.9: E-GOS curves for ^{112}Cd and ^{114}Cd displaying a transition from a vibrational phase to a rotational phase.

Chapter 6

Conclusions

This thesis is the result of the analysis of an experiment which has led to the observation of numerous previously unreported states in ^{112}In and ^{114}In which have been assigned tentative spin and parity on the basis of DCO ratios and anisotropic analysis. Experimentally extracted B($M1$)/B($E2$) ratios have values that are consistent with those believed to be indicative of the shears mechanism as well as consistent with those of neighbouring nuclei in the $A{\sim}110$ mass region. Simple $\mathcal{I}^{(2)}/B(E2)$ ratios are shown to be larger than those expected for rotational bands based on collective rotation of the nucleus, further adding to the case for the presence of a shears mechanism. Comparison of the experimental B($M1$)/B($E2$) values with various calculated configurations of neutron quasiparticle indicate configurations based on rotationally aligned neutrons and deformation aligned protons, consistent with configurations assigned in previous works.

The present work also studied the experimental and theoretical alignments of $^{112-114}$Cd which were found to be consistent with neighbouring Cd isotones. The experiment also populated two previously unreported states in ^{112}Cd, and a single unreported state in ^{113}In.

In Appendix A of this thesis, the commissioning of a recoil separator is reported, with the successful use of mono-crystalline solar cells as focal plane recoil detectors. The first commissioning experiments are described, with the effect of various master-gate requirements on the quality of data investigated, in addition to simple measurements of the transmission efficiency of the device.

6.1 Future Work

Definitive evidence for shears bands only exists in the light lead and tin/cadmium regions. New regions need to be investigated where different orbitals are active and to try and establish the general character of the mechanism. In the known regions there are also interesting issues relating to the boundaries associated with the transition from shears mechanism to either fully collective or non-collective dipole structures. Lifetime measurements will be important for these studies, since they enable matrix elements to be deduced for the transitions between states.

The shears picture suggests that other types of shears bands should exist in near-spherical nuclei. For example, both blades of the shears could be formed from the same type of particle, i.e. two-proton (or neutron) blades. Here, angular momentum is generated by the simultaneous closing of the two shears blades with one of the principal axes, along which lies a fixed vector contribution from the neutrons (or protons). Such a combination could not give rise to a large magnetic dipole moment because the individual moments from each combination of one proton and one neutron will be equal and opposite. A regular sequence of energy levels should, however, still be formed from the closing shears, but the decay will now occur by weak electric quadrupole transitions, since the mean field will once again have both rotational and reflection symmetry and the cranking axis coincides with the principal axis. This has been termed "anti-magnetic" rotation, by analogy with anti-ferromagnetism [50]. One of the best regions to look for this effect in nuclei is the light Cd isotopes where this mechanism was first reported in ^{109}Cd [15], ^{110}Cd [50] and more recently in ^{106}Cd [123].

With regard to the current work, lifetime measurements using a recoil distance method to extract more accurate $B(M1)/B(E2)$ ratios in ^{112}In and ^{114}In are planned in 2004 which will allow further investigation into the nature of the dipole bands. Further experiments are required to observe ^{113}Cd through the backbend to provide further data on the vibrational-to-rotational evolution of nuclei in the $A{\sim}110$ mass region.

Appendix A

The Commissioning of SASSYER

A.1 Introduction

SASSYER (Small Angle Separator System at Yale for Evaporation Residues) is a gas filled magnetic separator, which was previously situated at the Lawrence Berkeley Laboratory, where it was known as SASSY (Small Angle Separating System) [124]. In May 2000, SASSY was relocated to the Wright Nuclear Structure Laboratory at Yale University, where it was refurbished and installed. This appendix details the commissioning process that took place throughout 2002.

A.2 Recoil Separators

Recoil separators for heavy-ion-induced fusion products have become primary tools for studying production and decay properties of heavy elements [124, 125, 126]. In these devices, reaction products recoiling out of a thin target are separated in-flight from the accelerator beam using electric and/or magnetic fields.

When a beam of heavy ions impinge on a thin target with an energy sufficiently high enough to overcome the Coulomb barrier between the nuclei in the beam and in the target, nuclear reactions take place and new nuclei that are formed in these reactions recoil out of the target. These "recoils" can be collected and spatially sorted with the use of a recoil separator. The environment of spatially separated recoils provided by recoil separators enable highly sensitive, highly selective experiments that allow the study of weakly produced nuclei very far from stability [127]. To date, these devices have been used to study nuclei with production cross-sections as small as 1 nb [128].

As SASSYER has so far only been used primarily to study products of fusion-evaporation reactions, the discussion here is limited to this context. Thus a recoil here is the residual heavy ion that remains after the compound nucleus de-excites. This residual heavy ion exits the target because of the kinetic energy transferred to it from the beam particle. Due to the loss or pickup of electrons as they travel through the remainder of the target, recoils emerge with a distribution of atomic charge states, Q. Recoils also leave the target at an angle that is dependent not only on the impact parameter of the collision that produces it but also on the number, type and direction of the particles evaporated in the reaction. This angle is also a function of the target thickness and the depth that the recoil is formed in the target due to multiple scattering within the target. The energy with which a recoil leaves the target is dependent on the number and direction of the particles that are evaporated in the reaction; it is also a function of the depth within the target at which the recoil is formed.

To spatially separate recoils of interest, a recoil separator is designed to perform two important tasks. The primary function of a recoil separator is to separate the recoils leaving the target according to their mass-to-charge ratio, M/Q. The location where this spatial dispersion of recoils into groups by M/Q is realized is called the focal plane. This dispersion generally allows the identification of recoils within a group by mass. Ambiguities can arise, however, because recoils with different mass and charge states can have the same M/Q. These ambiguities in general are not a significant problem since only a limited range of masses and charges are populated within a given reaction.

The other primary function of a recoil separator is the rejection of scattered beam particles. The use of thin targets to ensure that the reaction products are able to recoil out of the target means that the recoils are completely dominated by the beam particles that pass through the target without reacting. The recoils from fusion-evaporation reactions are centred around the initial beam direction of 0°. In order to maximise recoil collection efficiency, recoil separators must be capable of operating at 0°, the direction in which all of the unreacted beam particles enter. As they are separated from the recoils, these beam particles can scatter off surfaces within the separator with a range of energies and trajectories and can even create new reaction products that can then pass through the device. Even if a tiny fraction of these scattered beam events has the right kinematic and charge characteristics, enough will be transmitted to the focal plane to flood and possibly damage the detectors situated there. The high sensitivity required for observing exotic nuclei at the focal plane depends very much on the level of beam rejection; if the detectors at the focal plane are swamped with beam events, the rare, "good" events will be lost because of dead time and a high background.

A.2.1 Gas Filled Separators

The performance and design of recoil separators is governed by two aspects, namely the need for maximum possible transmission of the reaction products through the separator, and high mass resolution. In practice, a compromise between the two is taken. For instance, the Fragment Mass Analyser at the Argonne National Laboratory [129] and the HRIBF recoil mass separator at Oak Ridge [130] are devices with excellent mass resolution (typically one part in 300), but suffer from low transmission efficiencies. These devices are classed as mass separators, and generally use a magnetic dipole between two electric dipoles to select a particular M/Q ratio of a recoiling reaction product and then further tuning can select a particular mass number to enter the focal plane. The poor efficiency in separators of this type, which operate with the field region in a vacuum, is mainly due to the fact that only two or three charge states can be collected, whilst the recoiling nuclei have a wide distribution of charge states due to passing through windows and the remainder of the target.

In order to overcome this problem, the field region can be filled with a dilute gas such as helium, an idea proposed by Cohen and Fulmer [131], and further improved by Armbruster et al. [132], Karnaukhov et al. [133], and Ghiorso et al. [134]. The effect of filling the field region with gas is shown schematically in figure A.1. In the gas filled region, multiple scattering of the recoiling ions in the dilute gas means that they will follow a trajectory through the separator corresponding to that of q_{ave}, the average charge state of the ions exiting the target, provided that the mean free path of the recoils between these charge exchanging collisions is small compared to the flight distance through the separator. The acceptance of essentially all charge states thus leads to much higher transmission, however, mass selectivity is lost as all reaction products will be tuned to the focal plane together. The trajectory of the primary beam is usually sufficiently different from that of the recoiling nuclei, giving beam suppression factors of the order of 10^{-10}–10^{-15}.

The first recoil separator of this type to be constructed was SASSY [134] at the Lawrence Berkeley National Laboratory. Other gas filled separators include RITU at the University of Jyväskylä [135] and the JINR device at Dubna, Russia [136]. The performance of gas-filled recoil separators can be described to first order by the formula for magnetic rigidity [124]

$$B\rho = \frac{mv}{q_{ave}} = \frac{mv}{[(v/v_0)\,eZ^{1/3}]} = \frac{0.0227A}{Z^{1/3}}Tm \qquad \text{(A.1)}$$

where A, Z and v are the mass number, proton number and velocity of the recoiling ion respectively, and v_0 (=2.19×10^6 ms^{-1}) is the Bohr velocity. The product Bρ is defined as the magnetic rigidity, where B is the magnetic field strength and ρ is the radius of curvature. The magnetic rigidity is a characteristic of a particle with a certain mass, charge and velocity. The average charge state q_{ave} of an ion moving in a dilute gas can be obtained from the Thomas-Fermi model of the atom [137] and expressed as

$$q_{ave} = (v/v_0)eZ^{1/3} \qquad \text{(A.2)}$$

It can be seen that q_{ave} is proportional to the velocity of the ions, thus charge and velocity focussing is achieved and the device acts as a M/Q separator. An accurate estimation of q_{ave} requires knowledge of charge exchange cross-sections, which are generally unknown. Therefore q_{ave} is estimated from empirical results. Oganessian et al. [138] proposed that

$$q_{ave} = (1.8\times10^{-7})vZ^{1/3} + 1.65 \quad for \quad vZ^{1/3} < 2\times10^{7} \qquad \text{(A.3)}$$

$$q_{ave} = (3.3\times10^{-7})vZ^{1/3} - 1.18 \quad for \quad vZ^{1/3} > 2\times10^{7} \qquad \text{(A.4)}$$

for heavy ions of element Z in 1 torr of He gas. Extensive studies of average charge states in He have been made, especially in Berkeley using SASSY [124] and in Dubna [138]. A combination of these data suggest that

$$q_{ave} = Z(1 - 1.04e(^{(4.15\times10^{-7})vZ^{-2/3}}) \tag{A.5}$$

At Berkeley, the SASSY group used equation 1.5 for recoil velocities $v > 8.3\times10^6$ ms^{-1}. For slower velocities, the larger calculated q_{ave} of either equation 1.3 or 1.5 was used. At Yale, the same formalism was used for SASSYER.

The presence of a gas induces a significantly lower average charge state than the most probable charge state in vacuum. For example, the ~24 MeV ^{150}Dy recoils from the ^{122}Sn(^{32}S,4n) commissioning experiment (see section A.6.2) have a calculated [139] most probable charge state of 16$^+$ in vacuum. In 1 torr of He gas, these recoils are calculated to have an average charge state of only 6.5$^+$, whilst the beam particles remain almost fully stripped. When the dipole field is set to bend the recoils along the central axis of the gas-filled separator, unreacted beam particles will have a significantly lower rigidity and therefore smaller bending radius. The unreacted beam can then be collected in a beam dump on the low-ρ side of the first dipole, thus separating the unreacted beam from the recoils. The first dipole magnet is then usually followed by a quadrupole magnet, which focuses the recoils into the focal plane. Additional dipole and quadrupole magnets may be used to further bend or focus the recoils.

Instruments of this kind provide short separation times of the order 1 μs and higher efficiency than typically obtained in vacuum operated recoil mass separators. To achieve the sensitivity needed to study nuclides with production cross-sections below 1 nb, the mass resolving power of the separator is sacrificed. The mass resolution for these devices is typically around 1 in 10.

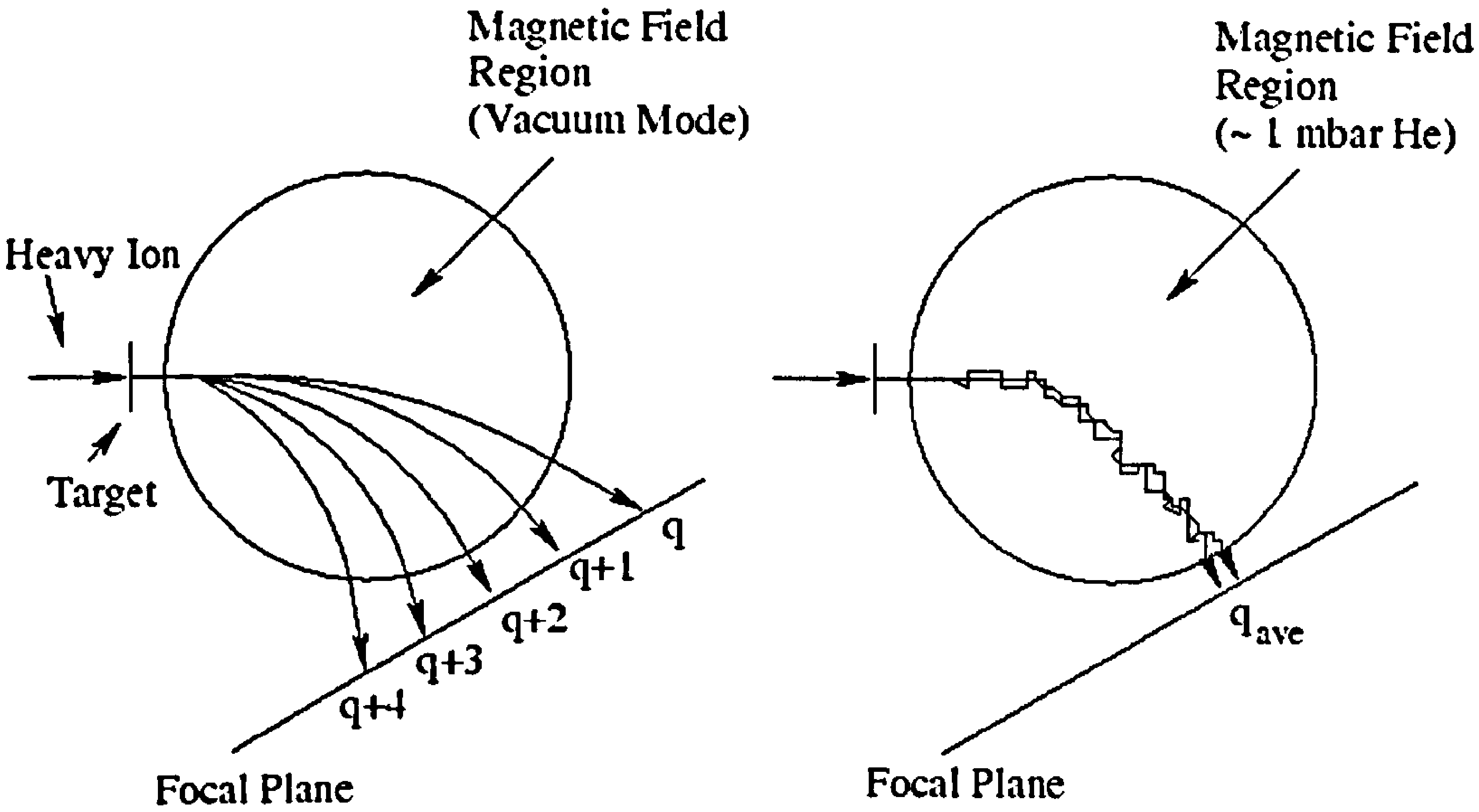

Figure A.1: A schematic illustration of the trajectories followed by heavy ions in a magnetic field region: Left, in a vacuum, right in a dilute gas. In the gas-filled magnetic region, the discrete trajectories corresponding to the different charge states coalesce around a trajectory defined by the mean charge state of the ion in the gas.

A.3 Auxiliary Detectors

A critical detector system used with a recoil mass separator is a position sensitive detector set-up at the focal plane which detects the presence of a recoil that has passed through the device to the focal plane and also records its arrival time. These detectors are commonly either a gas-filled multi-wire proportional counter, an ionization chamber, a moving tape collector and/or a double-sided silicon strip detector (DSSSD). At Yale, an array of standard solar-cells was found to be a affordable and effective alternative to a DSSSD, as described in section

A.5.1. Germanium detectors to measure the energies of γ rays can be placed surrounding the target position to detect prompt radiation emitted when the nuclei are produced, and also at the focal plane to study the γ-emission from nuclei that have isomeric states that have half-lives comparable to the time-of-flight through the separator.

A.4 Modes of Operation

For nuclear structure experiments, a recoil tagging method is commonly used in conjunction with a recoil separator. In this technique, prompt γ-rays, emitted directly following heavy-ion fusion evaporation reactions are detected in the Ge array surrounding the target position. Reaction recoils are subsequently separated by the separator and implant into the solar-cell array at the focal plane. By delaying the signals from the Ge detectors so that they coincide with signals arising from recoils implanting in the solar-cells, it is possible to correlate the prompt γ-rays to the events which produced the recoil nuclei of interest.

Other techniques include isomer decay tagging [140] and recoil decay tagging [127]. By use of isomer decay tagging, it is possible to study the γ-emission from nuclei within a mass group that have microsecond isomers. These isomers live long enough to survive the flight time through the separator (typically 1-2 μs) and their γ-decay is observed at the focal plane by use of Ge detectors. A clean spectrum of the isomeric decay is obtained by recording the γ rays occurring within a time window after the arrival of the recoil at the focal plane. In recoil decay tagging, prompt γ transitions observed at the target are correlated with a separated recoil and a known proton or alpha decay from the implanted recoil. This arrangement makes it possible to correlate prompt γ rays observed at the target with the known proton or α-emission from an exotic nucleus, thus enabling an in-beam study of the nucleus.

A.5 SASSYER

SASSYER consists of three magnets, two vertically-focussing dipoles either side of a horizontally-focussing quadrupole, comprising a total length of 2.4 m. A picture showing a side-view of SASSYER is shown in figure A.2 and a schematic diagram is shown in figure A.3. The γ-ray array, YRAST Ball [85], was placed around the target position in front of the first dipole magnet as described in section 3.7.

SASSYER has an angular acceptance of ~5 msr and a maximum Bρ value of 2.2 Tm. The separator volume is filled with helium, typically at a pressure of 1 torr. A 50 μg cm^{-2} carbon window is situated 1 m upstream of the target and contains the helium within SASSYER. The beam dump is a lead-lined aluminium box situated on the low-ρ side of the first dipole magnet.

A.5.1 Focal Plane Detectors

For the commissioning program, an array of low capacitance, mono crystalline solar-cells [141] were placed at the focal plane, within the focal plane chamber, as shown in figure A.4, to act as a charged particle and recoil detector. The focal plane chamber is an aluminium box measuring 45×30×30 cm and is situated 80 cm behind the last dipole magnet. Each solar cell measured 1 cm^2 and a 3 × 10 array was constructed. This array of solar-cells was tested with a ^{228}Th 5 MeV α-source under vacuum in a duplicate focal plane chamber. The solar cells were found to provide a FWHM resolution of ~90 keV and with the application of a bias voltage of 50 V a FWHM of ~50 keV was obtained. It was decided that the unbiased resolution of ~90 keV was sufficient for the commissioning program and the solar-cells were left unbiased.

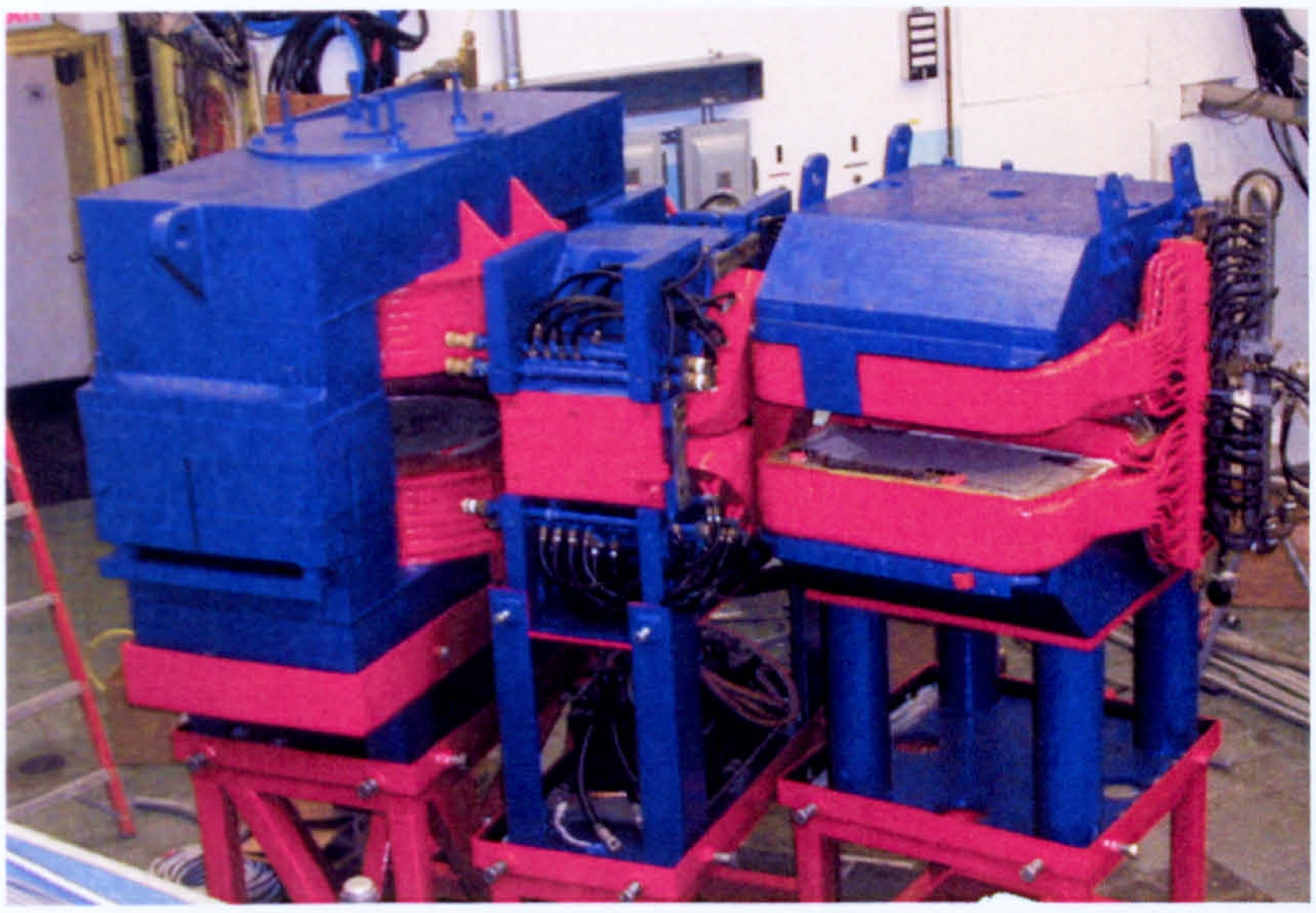

Figure A.2: A side view of SASSYER showing the three magnets, a dipole magnet either side of the central quadrupole magnet. The beamline enters the separator from the right.

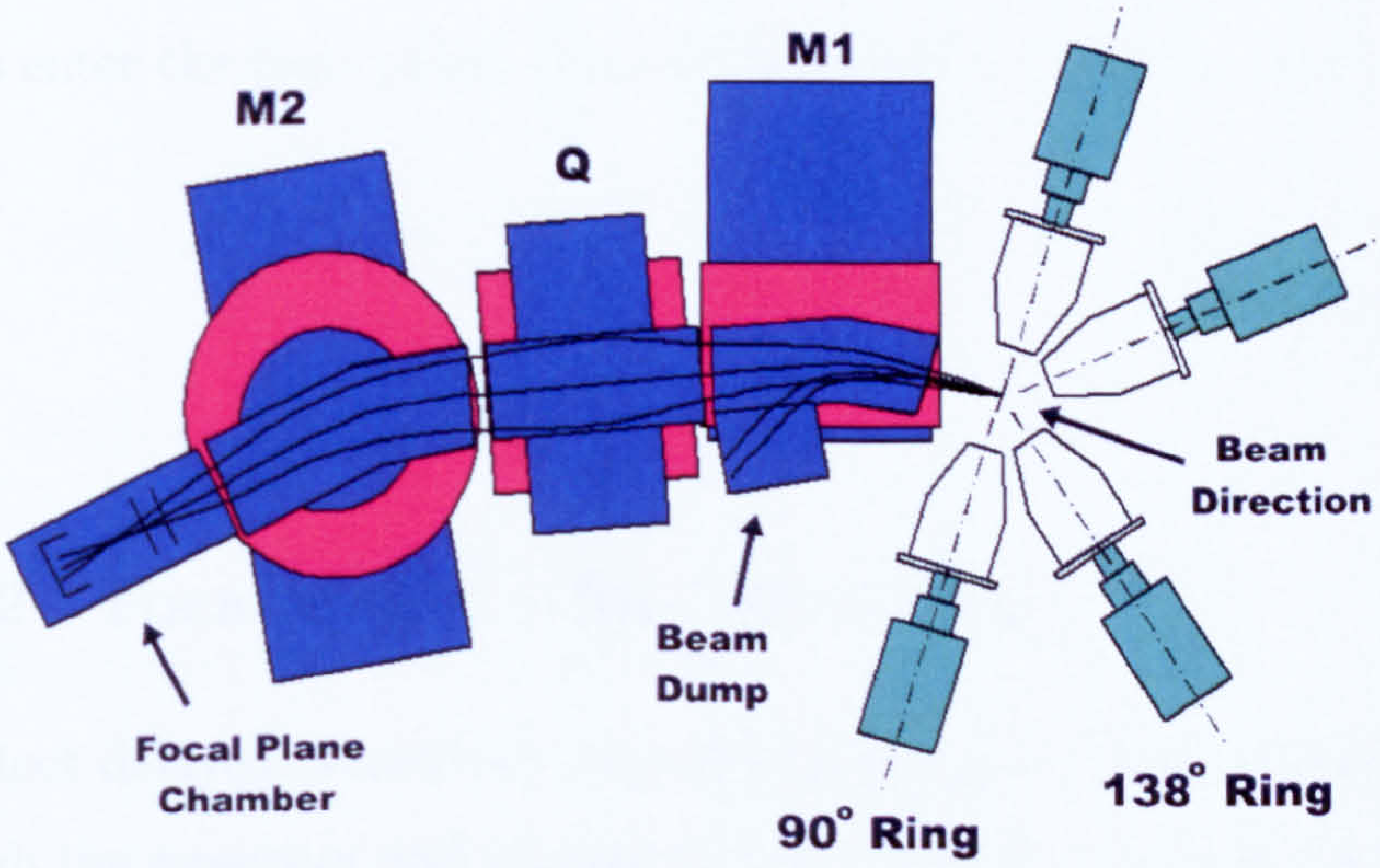

Figure A.3: A schematic diagram showing SASSYER coupled to YRAST Ball which comprises of two rings of detectors at 90° and 138° to the beam direction.

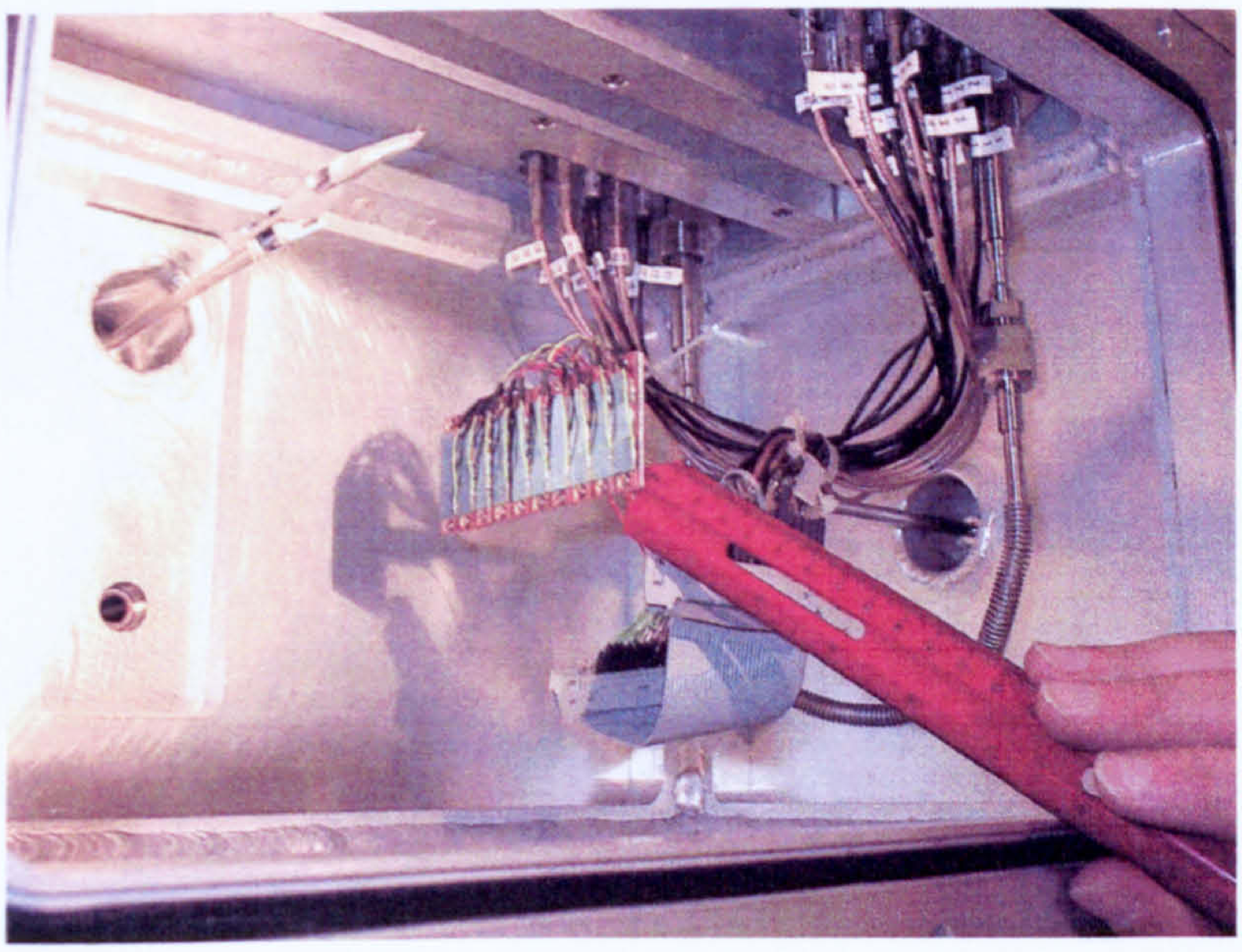

Figure A.4: The 3 × 10 array of solar cells within the focal plane chamber. The recoils enter the focal plane chamber from the left of the picture.

A.5.2 Focal Plane γ-Ray Detection

To detect delayed transitions depopulating from microsecond isomers that pass through the separator and implant in the solar cells, a single coaxial detector was placed facing the focal plane chamber for the initial commissioning. Windows were created in the thick focal plane chamber walls by machining the aluminium down to a thickness of 5 mm. Subsequent experiments [142] ran with four coaxial detectors surrounding the focal plane chamber, as shown in figure A.5.

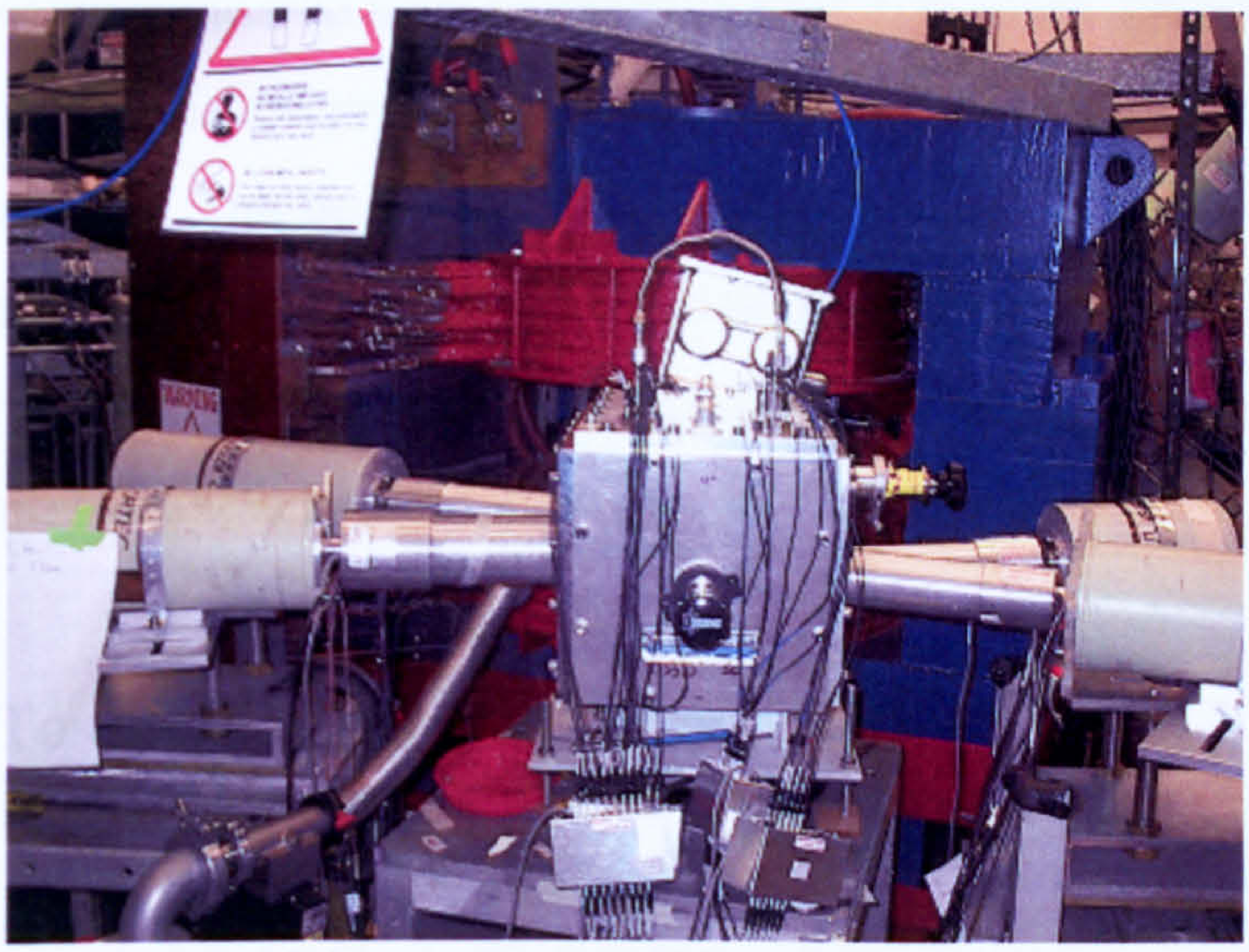

Figure A.5: View from the rear of SASSYER showing four coaxial detectors surrounding the focal plane chamber, acting as delayed γ-ray detectors.

A.6 The Commissioning Program

A.6.1 Tests with Beam

Light ($A \leq 50$) low energy stable beams were used to further test, calibrate and align the magnet system. There are several advantages offered by low intensity beams for calibration purposes compared to other types of ion. One advantage is that the beam energy is narrowly defined, and its value is known precisely. Another advantage is that the use of a stripping foil can lead to widely separated calibration points: a low rigidity point from a charge state at the upper end of the charge state distribution and a high rigidity point from a charge state from the lower end of the charge state distribution. A disadvantage of using low intensity beams compared to α-particles is that it is more difficult to ensure that the beam position is set properly to enter at and follow along the central axis of the spectrometer. The beam was tuned visually using the glow produced when the ions strike a "phosphor", a thin slab of chromium doped alumina placed at the focal plane. In order to avoid creating dead spots in the phosphor too rapidly, the beam intensity was kept to a minimum.

A.6.2 Tests with Recoils

The first "beam-on-target" run used a 500 μg cm^{-2} ^{122}Sn target and a ^{46}Ti beam at an energy of 195 MeV. A PACE [87] calculation suggested that the most populated channel to be ^{164}Hf (4n) with a cross-section of 180 mb, 66% of the total cross-section. ^{161}Yb was also populated through the α4n channel with a cross-section of 20 mb and allows the transmission efficiency of the 4n channel to be compared with the α4n (see section A.6.3). For this particular run, only two clover detectors were mounted in the target-position array frame. Data were recorded using a variety of master gates at a beam intensity of ~ 4 enA. Figure A.6 shows data recorded using either a γ-singles, a γ—γ, or a γ-recoil master gate requirement. The recoil gate requirement was satisfied when at least one solar-cell at the focal plane fires. Even with relatively short run times and only two clover detectors, a large number of statistics were collected. The γ-singles spectrum is dominated by the 511 keV (positron annihilation) line, and two higher energy lines, 1173 and 1332 keV following the β-decay of ^{60}Co contamination in the iron of the separators magnets. The use of a γ—γ master gate significantly reduces the ^{60}Co contamination and increases the detail of the nuclear structure. When using a γ-recoil master gate, the spectrum shows a further increase in detail, with strong lines corresponding to transitions in ^{164}Hf and ^{161}Yb [143] seen due to a greatly reduced background and contaminant content.

The next test run used the same ^{122}Sn target, but with a 140 MeV ^{32}S beam and a full complement of eight clovers detectors in the array. PACE calculations showed that the two strongest channels to be ^{149}Dy (220 mb) and ^{146}Gd (110 mb). However, both ^{149}Dy [144] and ^{146}Gd [145] have reported isomers with significant lifetimes. Due to the presence of these isomers, only ^{150}Dy with a cross-section of 45 mb is seen in the prompt spectra with significant intensity [146]. Figure A.7 shows how the addition of a recoil requirement to the singles master-gate greatly improves the detail of the structure that can be seen. The γ-singles run used a beam current of 3 enA for a duration of 60 mins. The γ-recoil run used a beam of 27 enA for a duration of 135 mins, and in the offline sorting, had a gate set on the recoil "hump".

Figure A.8 shows the output from one of the unbiased solar-cell ADCs during this experiment. Clearly separated are the recoil "hump", characteristic of recoils with a spread in energy, the scattered beam to the right and the α-particles to the left. The α-particles have been assigned to the 4.18 MeV and 4.351 MeV α-decay of ^{150}Dy [143] which implanted in the solar cells. In this particular run, there is evidence of a small amount scattered beam.

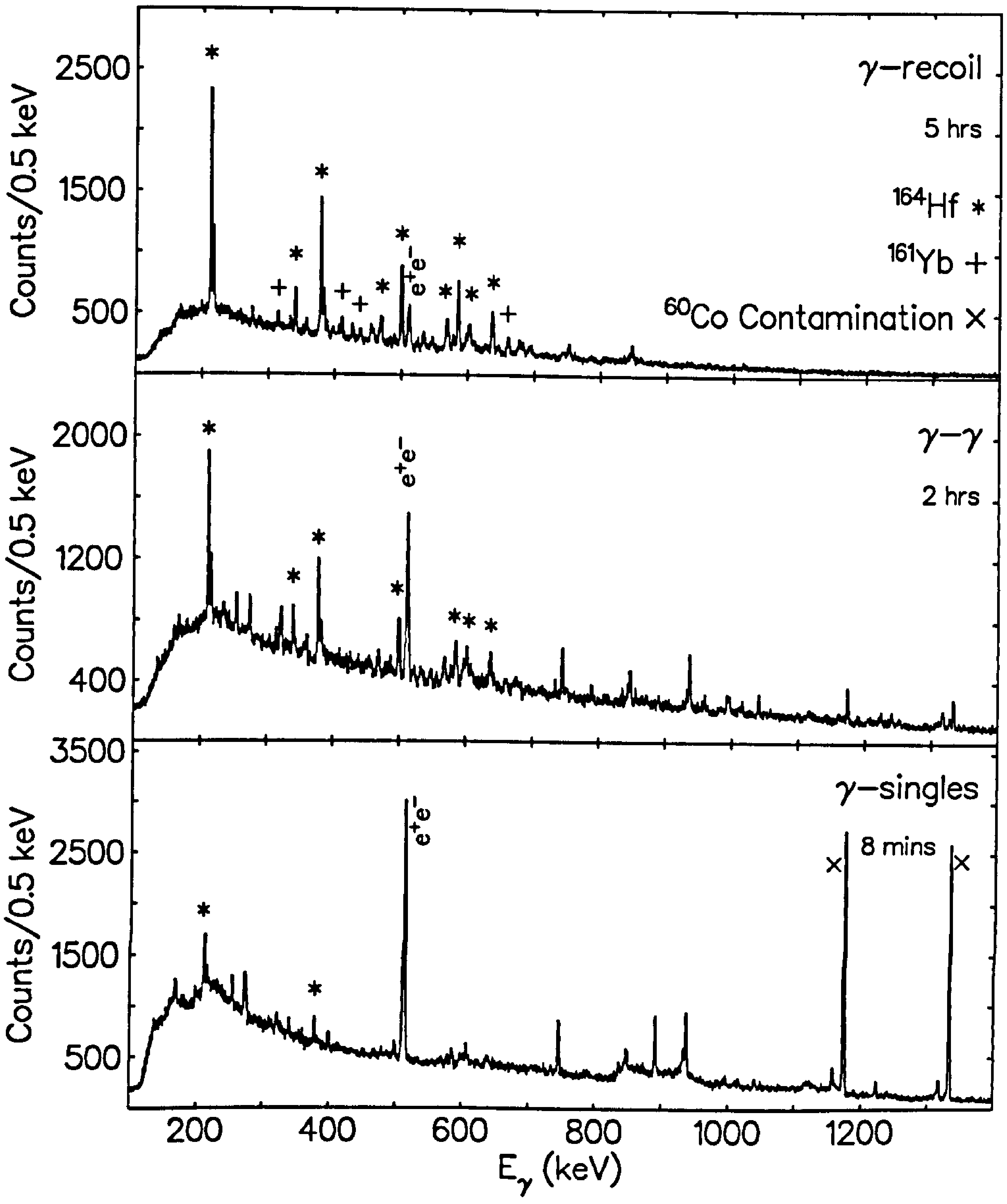

Figure A.6: Total projections obtained from the ^{46}Ti+^{122}Sn (E_B=195 MeV) commissioning run using different master-gate requirements. The γ-singles gate (lower) is dominated by ^{60}Co contamination and positron annihilation. The γ–γ gate (middle) reduces the contamination and allows numerous transitions to be assigned to ^{164}Hf. The γ-recoil gate (top) further reduces the contamination and enhances the ^{164}Hf transitions and allows the observation of ^{161}Yb from the weaker α4n channel.

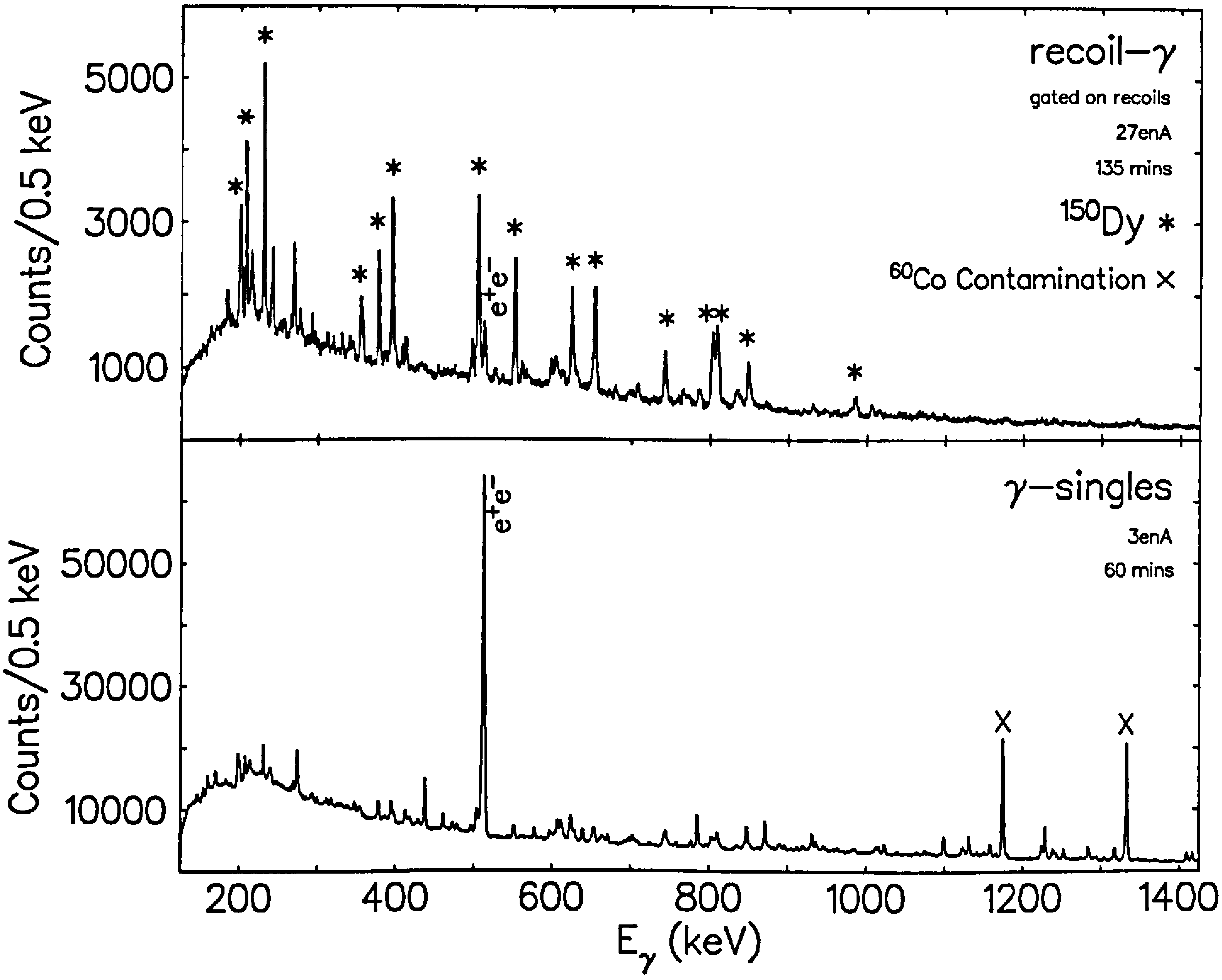

Figure A.7: Total projections obtained from the ^{32}S+^{122}Sn (E_B=140 MeV) commissioning run using different master-gate requirements. The γ-singles spectrum is dominated by ^{60}Co contamination, but is significantly reduced with the addition of a recoil requirement to the master gate. In this run, a gate was also set on the recoil hump in the solar cell output in the subsequent offline sort.

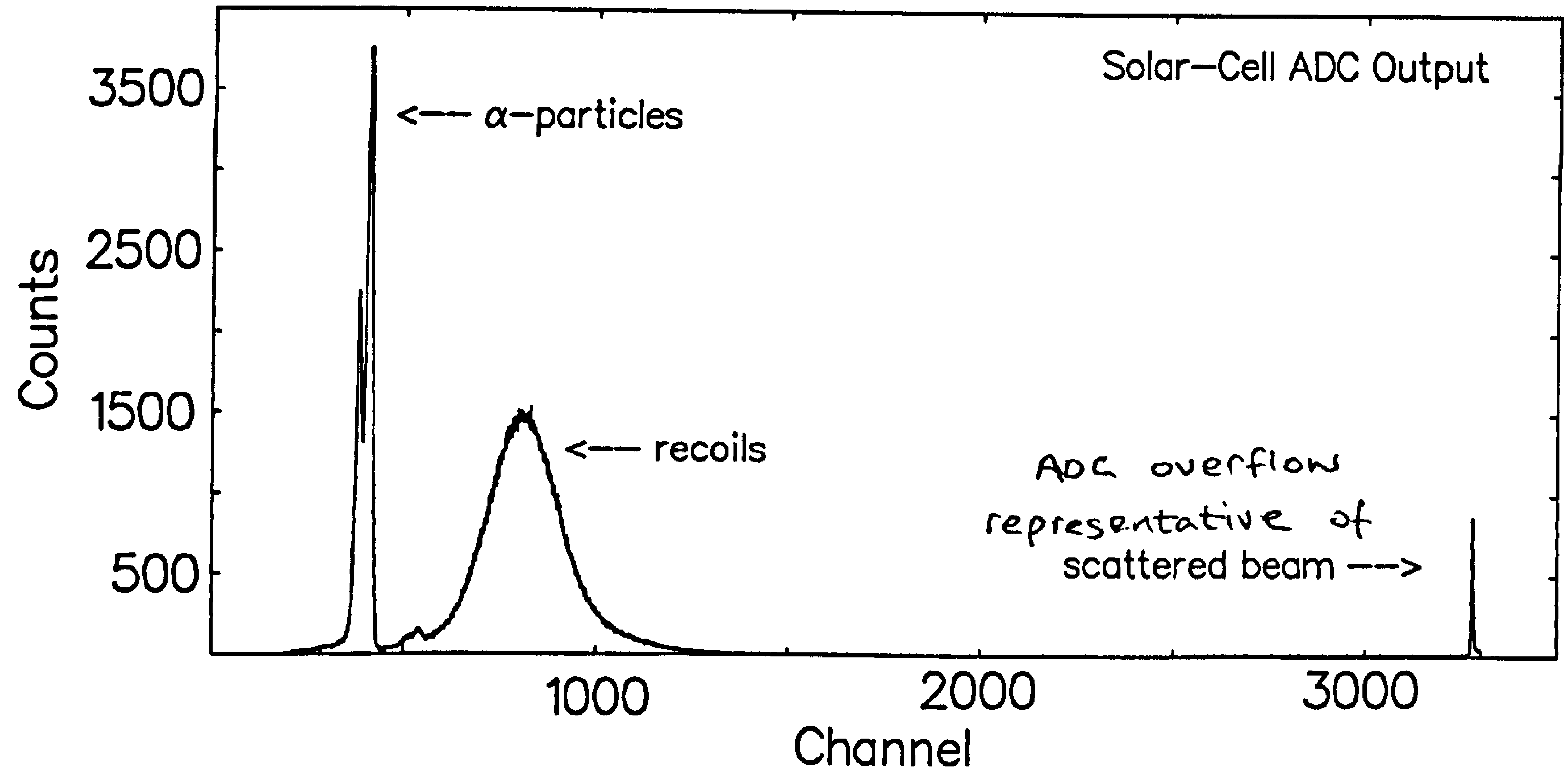

Figure A.8: Energy spectrum of implanted particles in a single solar cell for the reaction ^{122}Sn(^{32}S, 4n)^{150}Dy.

A.6.3 The Performance of SASSYER

It was also possible to measure the transmission efficiency of SASSYER by comparing the number of counts observed in a specific peak in the γ—γ data recorded at the target position to the number of count in the same peak in the γ-γ-recoil data. Using data from the ^{122}Sn(^{32}S,4n)^{150}Dy channel, the transmission efficiency was calculated to be 15±1%. From the ^{122}Sn(^{46}Ti,4n)^{164}Hf reaction and the ^{122}Sn(^{46}Ti, α3n)^{161}Yb channel, the calculated transmission efficiencies were 14±1% and 10±2% respectively. The transmission efficiency varies with the reaction and reaction channel. The recoil momentum from the isotropic emission of an α-particle clearly reduces the transmission of the α3n channel compared to the 4n. Figure A.9 shows these calculations and all the parameters relating to the performance of SASSYER throughout the various commissioning runs are tabulated in table A.6.3. However, recoil transmission depends on too many factors external to the separators design, such as reaction kinematics, reaction channel and target thickness. Transmission efficiency is therefore not a good way to describe the devices performance, and only makes sense to use this parameter in the context of a specific reaction channel from a specific reaction.

Channel	(E_{beam}) MeV	Target Thickness (μg cm^{-2})	Efficiency (%)
^{122}Sn(^{46}Ti,4n)^{164}Hf	195	500	14±1
^{122}Sn(^{46}Ti α3n)^{161}Yb	195	500	10±2
^{122}Sn(^{32}S,4n)^{150}Dy	150	500	15±1

Table A.1: Summary of SASSYER parameters measured during the commissioning process.

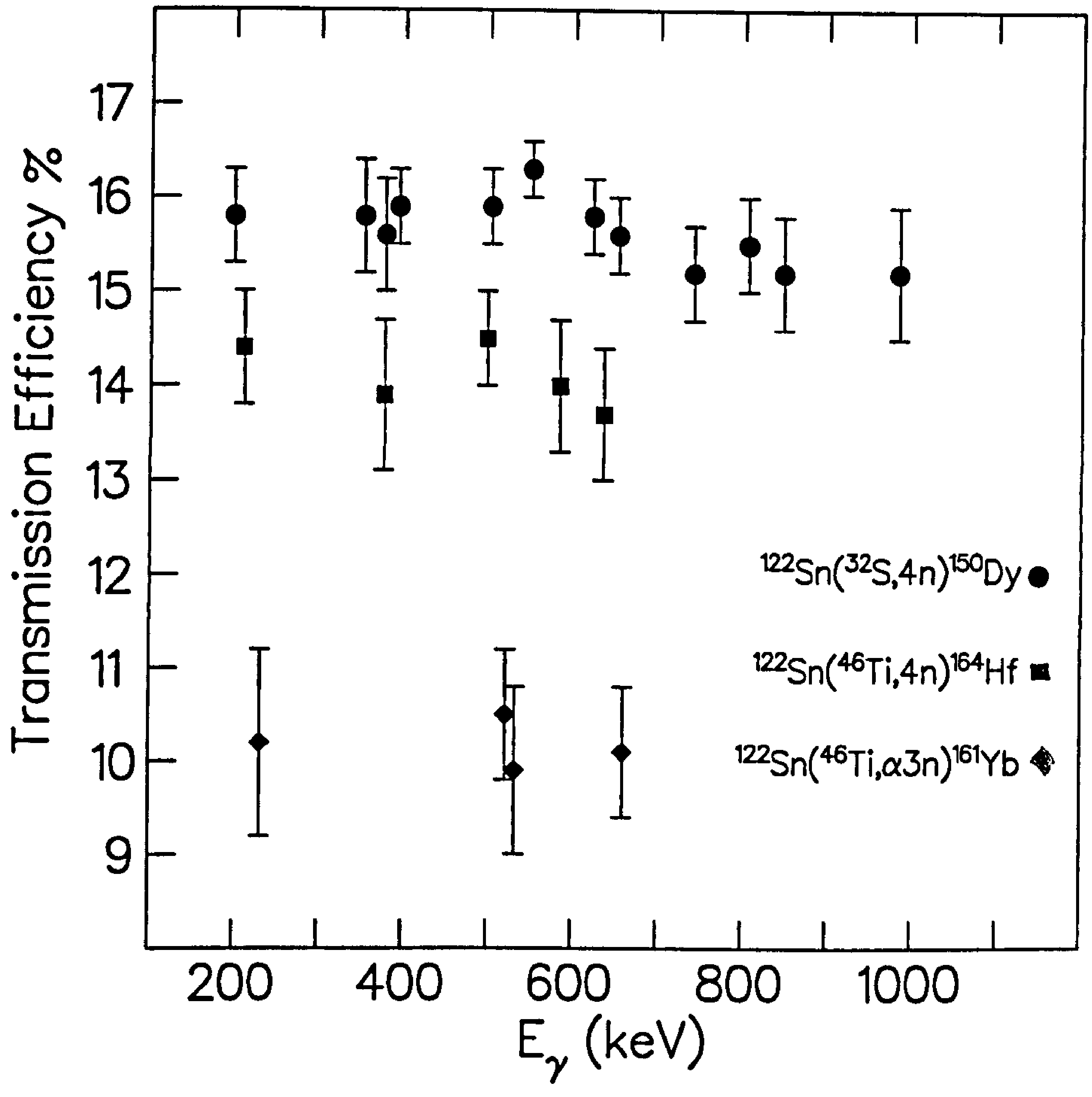

Figure A.9: SASSYER transmission as a function of energy and reaction channel for the commissioning runs.

A.7 First Physics Study

The first significant physics study focussed on the structure of ^{203}Rn and used a beam of ^{32}S at an energy of 165 MeV incident on a target of ^{176}Yb (500 μg cm^{-2}). This was also the first time a delayed γ detector was implemented at the focal plane. This consisted of a single coaxial detector placed to one side of the focal plane chamber, facing the solar cell detectors. A PACE calculation gave the production cross-section of ^{203}Rn to be 1 mb out of a total cross-section of 310 mb. This nucleus had previously been studied at Yale by Newman et al [149] using the full YRAST Ball array without any other additional devices and a ^{174}Yb(^{34}S, 5n)^{203}Rn reaction at 167 MeV. By comparing the data from the two experiments, it is possible to see the fission suppression capabilities that SASSYER provides.

The target position was surrounded by the Ge detector array, which consisted of four detectors at 90° and three at 138°. Recoiling reaction products were subsequently separated in SASSYER. Due to the high rigidity of the Rn recoils ($B\rho$ =1.9 Tm), only ~0.7 torr He gas was used in the magnet chamber.

Figure A.10 shows, the total γ–γ projection from Newman et al using YRAST Ball. The strongest transition is the $17/2^+ \rightarrow 13/2^+$ in ^{203}Rn which occurs at 498 keV. This transition is dominated by a large fission background and Coulomb excitation of the target and can barely been seen in the spectrum.

Using SASSYER with a γ–γ-recoil master gate, it was possible to significantly reduce the fission background, and numerous peaks become clear, all corresponding to transitions in ^{202,203}Rn. Figure A.10 shows the total γ–γ projection from the SASSYER experiment and the identified Rn transitions are labelled. Figure A.11 shows the spectrum obtained from the delayed γ detector. This coaxial detector did not have any recoil requirement and was not integrated into the master gate in any way in this particular experiment, and is thus a spectrum of activity of the implanted ions in the solar cells. Several nuclei are identifiable. Lines from ^{203}At are present in the delayed spectrum due to electron capture ($T_{\frac{1}{2}}$=18 s) by the implanted ^{203}Rn nuclei as are lines from ^{202}Rn from electron capture by ^{202}Fr ($T_{\frac{1}{2}}$=0.34 s). Several lines corresponding to ^{200}Po (populated with a cross section of 2 mb) are also seen in the delayed spectrum, from the decay out of a 61 ns isomeric state [143]. A single transition (238 keV) from the $T_{\frac{1}{2}}$=4.1 m isomer in ^{199}Po is observed, which is populated via α-decay of ^{203}Rn and also in the reaction with a cross-section of 1 mb.

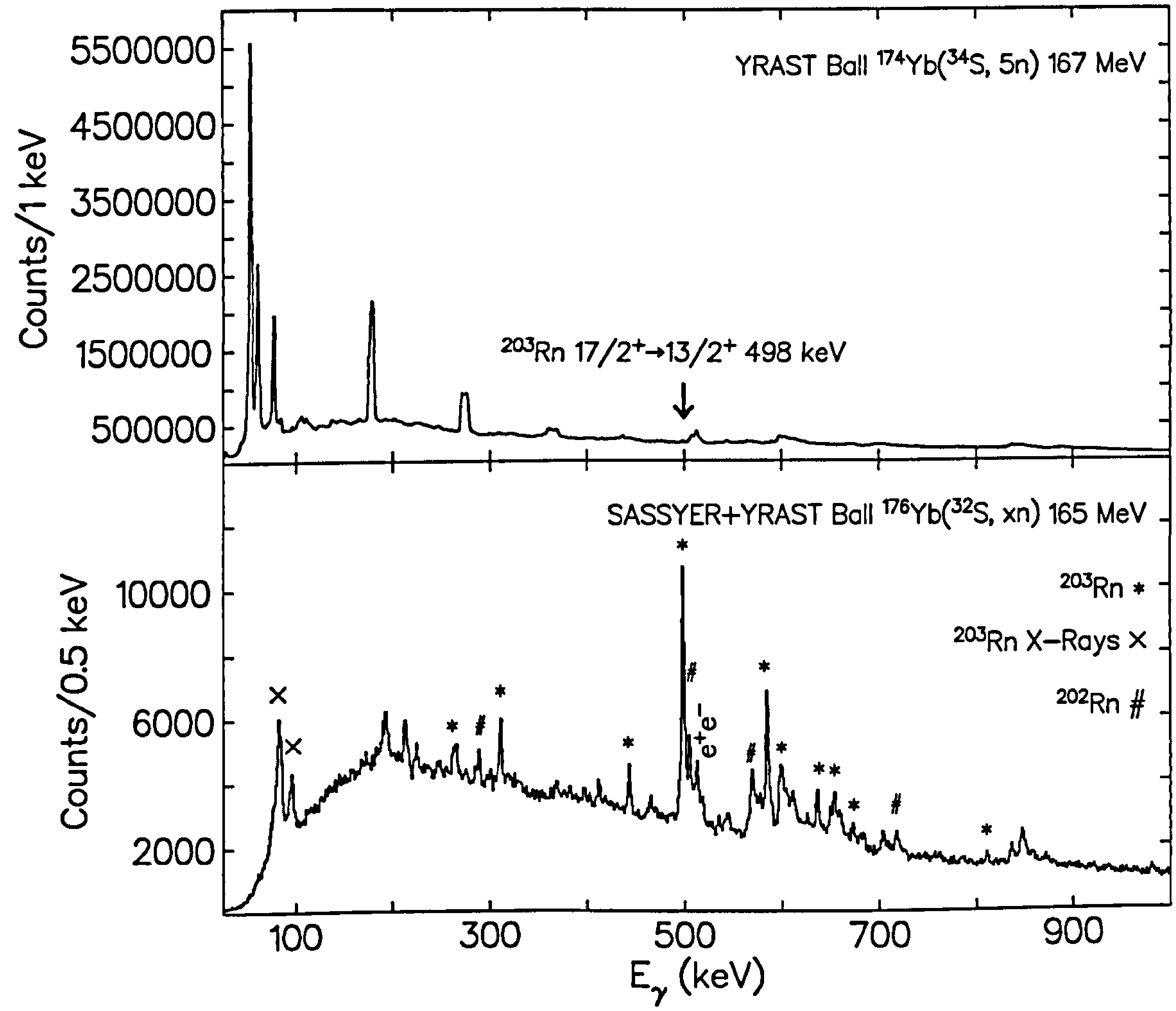

Figure A.10: Top: Total projection from the earlier ^{176}Yb(^{34}S, 5n)^{203}Rn experiment using YRAST Ball only The spectrum is dominated by Coulex of the Yb target. The most intense transition in ^{203}Rn (498 keV) is highlighted. Bottom: Total projection when using SASSYER in conjunction with SASSYER and a γ-γ-recoil master gate. Identified transitions from ^{202,203}Rn are highlighted.

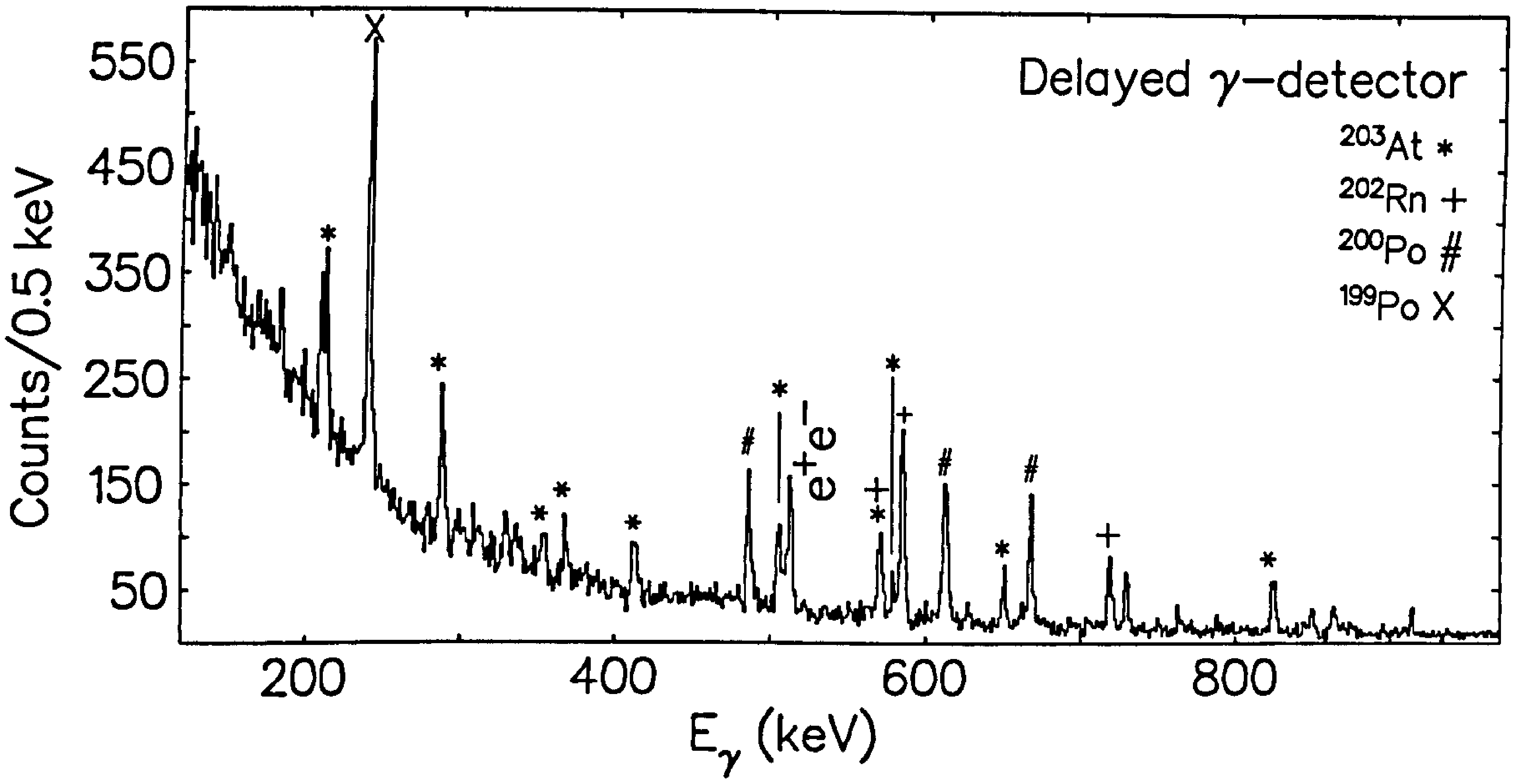

Figure A.11: Delayed γ spectrum from the ^{32}S+^{176}Yb reaction.

A.8 Conclusions

The commissioning program has been successful, and SASSYER is fully operational and in regular use. The delayed γ-detector array has been increased to six coaxial detectors, and experiments can now be run with various delayed γ and/or recoil master gates. Results have already been presented at international conferences [150] and the current experimental program is the study neutron-deficient Ra nuclei [142]. Future planned improvements to SASSYER include the replacement of the solar cells with a double-sided silicon strip detector, which will allow recoil decay tagging experiments to be performed. Lifetime measurements using a recoil distance Doppler shift technique are also to be performed using a plunger in conjunction with SASSYER, a technique similiar to that reported in reference [151].

Bibliography

[1] R.M. Clark and B. Wadsworth, *Physics World*, July 1998, 25

[2] R.M. Clark and A.O. Macchiavelli, *Ann. Rev. Nucl. Part. Sci.* **50** (2000) 1

[3] S. Frauendorf, *Nucl. Phys.* **A557** (1993) 259

[4] N.S. Kelsall et al. *Phys. Rev.* **C61** (2000) 011301(R)

[5] C. Chiara et al. *Phys. Rev.* **C61** (2000) 034318

[6] R.M Clark et al. *Phys. Rev. Lett.* **82** (1999) 3220

[7] A. Gaeda et al. *Phys. Rev.* **C55** (1997) R1

[8] D.G Jenkins et al. *Phys. Lett.* **B428** (1998) 23

[9] R. Wadsworth et al. *Phys. Scripta* **T88** (200) 49

[10] D.G Jenkins et al. *Phys. Rev.* **C58** (1998) 2703

[11] G.J. Lane et al. *Phys. Rev.* **C58** (1998) 127

[12] P. Vaska et al. *Bull. Am. Phys. Soc.* **40** (1995) 1006

[13] P. Vaska et al. *Phys. Rev.* **C57** (1998) 1634

[14] R.S. Chakrawarthy and R.G. Pollay, *Phys. Rev.* **C55** (1997) 154

[15] C. Chiara et al. *Phys. Rev.* **C64** (2001) 054314

[16] M. Eibert et al. *J. Phys.* **G2** (1976) L203

[17] P.H. Regan et al. *Phys. Rev. Lett* **90** (2003) 152502

[18] H. Ejiri and M.J.A de Voigt, *Gamma-ray and Electron Spectroscopy in Nuclear Physics*, Oxford University Press, New York (1989)

[19] E. Paul et al. *J. Phys.* **G17** (1991) 605

[20] A. de Shalit and H. Feshback, *Theoretical Nuclear Physics Vol. I: Nuclear Structure*, John Wiley and Sons, New York (1974)

[21] J.M. Blatt and V.F. Weisskopf, *Theoretical Nuclear Physics*, John Wiley and Sons, New York (1974)

[22] J. Kantele, *Heavy Ions and Nuclear Structure, Vol 5, Nuclear Science Research Conferences Series B*, ed. B.Sikora and Z. Wilhemi, Harwood, 391 (1984)

[23] P.M. Endt, *Atom. Nucl. Data Tables* **23** (1979) 547

[24] A. Bohr and B.R. Mottelson, *Nuclear Structure Vol. 2*, Benjamin (1975)

[25] F. Dönau, *Nucl. Phys.* **A471** (1987) 469

[26] N.A. Dyson, *X-Rays in Atomic and Nuclear Physics*, Longman (1973)

[27] K.S. Krane, *Introductory Nuclear Physics*, John Wiley and Sons, New York (1988)

[28] E. Recknagel, *Nuclear Spectroscopy and Reactions, Part C, ed. J. Cerny,* Academic Press (1974)

[29] J.M. Reid, *The Atomic Nucleus*, Manchester University Press (1986)

[30] A. de Shalit and I. Talmi, *Nuclear Shell Theory*, Academic Press, New York (1963)

[31] M.G. Mayer, *Phys. Rev.* **75** (1949) 1969

[32] R.D. Woods and D.S. Saxon, *Phys. Rev.* **95** (1954) 577

[33] W. Greiner, *Nuclear Models*, Springer-Verlag Berlin and Heidelberg, New York (1996)

[34] S.G. Nilsson, *Dan. Mat. Phys. Medd.* **29**, No. 16 (1955)

[35] R.F. Casten, *Nuclear Structure from a Simple Perspective*, Oxford Science Publications (2000)

[36] R.M. Diamond and F.S. Stephens, *Ann. Rev. Nucl. Part. Sci.* **30** (1980) 85

[37] J. Bardeen, C.N. Cooper and J.R. Schreifer, *Phys. Rev.* **108** (1957) 1175

[38] C.J. Gallagher and S.A. Moszkowski, *Phys. Rev.* **111** (1958) 1282

[39] D.R. Inglis, *Phys. Rev.* **96** (1954) 1059

[40] R. Bengtsson and S. Frauendorf, *Nucl. Phys.* **A327** (1979) 139

[41] G.I. Harris et al. *Phys. Rev.* **139** (1965) 1113

[42] A. Bohr, *Mat. Fys. Medd. K. Dan. Vidensk. Selsk.* **26** (1952)

[43] A. Bohr and B.R. Mottelson, *Phys. Rev.* **90** (1953) 717

[44] R.M. Clark et al. *Nucl. Phys.* **A562** (1993) 121

[45] G. Baldsiefen et al. *Nucl. Phys.* **A574** (1994) 521

[46] M. Neffgen et al. *Nucl. Phys.* **A595** (1995) 499

[47] R.M. Clark et al. *Phys. Rev. Lett.* **78** (1997) 1868

[48] Amita, A.K. Jain and B. Singh, *At. Data Nucl. Data Tables* **74** (2000) 283

[49] Amita, A.K. Jain and B. Singh, *Nuclear Science Reference Database at NNDC, Brookhaven*

[50] S. Frauendorf, *Rev. Mod. Phys.* **73** (2001) 463

[51] R. Wadsworth and P.J. Nolan, *Rep. Prog. Phys.* **65** (2002) 1079

[52] D.G. Jenkins et al. *Phys. Rev. Lett.*, **83** (1999) 500

[53] R.M. Clark et al. *Phys. Rev. Lett.* **82** (1999) 3220

[54] S. Chmel et al. *Phys. Rev. Lett.* **79** (1997) 2002

[55] S. Frauendorf, *Proc. Conf. on Phys. from Large Gamma-Ray Detector Arrays, Berkeley, 1994 (Report No. LBL-35687, Vol 2,* p52)

[56] R. Bengtsson, S. Frauendorf and F.R. May, *At. Data Nucl. Data Tables* **35** (1986) 15

[57] B.R. Mottelson and J.G. Valatin, *Phys. Rev. Lett.* **5** (1960) 511

[58] J. Simpson et al. *Phys. Rev. Lett.* **53** (1984) 141

[59] R.V.F. Janssens et al. *Phys. Lett.* **B106** (1991) 167

[60] F.S. Stephens and R.S. Simon, *Nucl. Phys.* **A183** (1972) 257

[61] J.P. Schiffer, *Annals of Phys.* **66** (1971) 798

[62] D. Kleppner and R.J. Kolenkow, *Introduction to Mechanics*, McGraw-Hill Education (1973)

[63] D.A. Bromley, *Treatise on Heavy-Ion Science*, Plenum Press, New York (1984)

[64] Z. Podolyák et al, *Nucl. Inst. Meth.* **A511** (2003) 354

[65] G.D. Dracoulis et al. *J. Phys.* **G23** (1997) 1191

[66] J. Wilczyński et al. *Nucl. Phys.* **A373** (1982) 109

[67] O. Hausser et al. *Phys. Lett.* **38B** (1972) 75

[68] H. Freiesleben et al. *Phys. Rev.* **10** (1974) 245

[69] K. Spohr, *unpublished*

[70] J.D. Lawson and M. Tigner, *Ann. Rev. Nucl. Part. Sci.* **34** (1984) 99

[71] R. Middleton, *Nucl. Instr. Meth.* **122** (1974) 35

[72] H. Hyder et al. *Nucl. Inst. Meth.* **A328** (1993) 126

[73] K.S. Krane, R.M. Steffen and R.M. Wheeler, *Nucl. Data Tables* **11** (1973) 351

[74] E. Der Mateosian and A.W. Sunyar, *Atom. Nucl. Data Tables* **13** (1974) 407

[75] K. Pohl et al. *Phys. Rev.* **C53** (1996) 2682

[76] A. Krämer-Flecken et al. *Nucl. Inst. Meth.* **A275** (1989) 333

[77] C. Bargholtz and P.E. Tegnér, *Nucl. Inst. Meth.* **A256** (1987) 513

[78] S.M. Vincent et al. *Phys. Rev.* **C60**, (1999) 064308

[79] K. Debertin and R.G. Helmer, *Gamma and X-Ray Spectrometry with Semiconductor Detectors*, North-Holland, Amsterdam (1988)

[80] G.F. Knoll, *Radiation Detection and Measurement*, John Wiley and Sons (2000)

[81] P.J. Nolan, *Nucl. Inst. Meth.* **A236** (1985) 95

[82] J.F. Sharpey-Schafer and J. Simpson, *Prog. Part. Nucl. Phys.* **21** (1988) 293

[83] G. Duchene, *Nucl. Instr. Meth.* **A432** (1999) 90

[84] S.L. Shepherd et al. *Nucl. Instr. Meth.* **A434** (1999) 373

[85] C.W Beausang et al. *Nucl. Inst. Meth.* **A452** (2000) 431

[86] J.J. Ressler et al. *Nucl. Inst. Meth.* **B204** (2003) 141

[87] F. Pühlofer, *Nucl. Phys.* **A280** (1977) 267 and A. Gavron, *Phys. Rev.* **C21** (1980) 230

[88] M.A. Caprio and J.J. Ressler, *cscan sorting package and site specific routines, WNSL, Yale University, unpublished*

[89] D.C. Radford, *Nucl. Inst. Meth.* **A361** (1995) 297

[90] M. Délèze et al. *Nucl. Phys.* **A551** (1993) 269

[91] N.Buforn et al. *Eur. Phys. J.* **A7** (2000) 347

[92] M.-G. Porquet et al. *Eur. Phys. J.* **A15** (2002) 463

[93] T. Kibédi et al. *Phys. Rev.* **C37** (1988) 2391

[94] M. Adachi et al. *Z. Phys.* **A295** (1980) 251

[95] M. Ionescu-Bujor et al. *Nucl. Phys.* **A272** (1976) 1

[96] T.B Ryves et al. *J. Phys.* **G9** (1983) 1549

[97] L.E. Samuleson et al. *Bull. Am. Phys. Soc.* **23** (1978) 962

[98] M. Ionescu-Bujor et al. *Z. Phys.* **A336** (1989) 291

[99] W.D. Fromm et al. *Z. Phys.* **262** (1973) 59

[100] W.K. Tuttle et al. *Phys. Rev.* **C13** (1976) 1036

[101] D. Rabenstein and D. Harrach, *Nucl. Phys.* **A242** (1975) 189

[102] J. Blachot, *Nucl. Data Sheets* **97** (2002)

[103] B. Antonot et al. *Nucl. Instr. Meth.* **B99** (1995) 513

[104] L.S. Goodman and S. Wexler, *Phys. Rev.* **108** (1957) 1524

[105] G.H. Fuller and V.W. Cohen, *Nucl. Data Sheets* **A5** (1969) 433

[106] Y.V. Melikov et al. *Nucl. Phys.* **A180** (1972) 241

[107] D. Frenne and E. Jacobs, *Nucl. Data Sheets* **79** (1996)

[108] P.E. Garrett et al. *Phys. Rev.* **C64** (2001) 024316

[109] N. Fotiades et al. *Phys. Rev.* **C61** (2000) 064326

[110] J. Jolie et al. *Phys. Rev.* **C42** (1990) 2034

[111] N. Warr et al. *Nucl. Phys.* **A620** (1997) 127

[112] S. Zehbib et al. *Phys. Rev.* **C36** (1987) 939

[113] T. Lönnroth et al. *Z. Phys.* **A317** (1984) 215

[114] R.J. Blin-Stoyle, *Rev. Mod. Phys.* **28** (1956) 75

[115] J. Van Maldeghem et al. *Phys. Rev.* **C32** (1985) 1067

[116] T. Fényes et al. *Fizika* **22** (1990) 273

[117] M. Ionescu-Bujor et al. *Hyperfine Ints.* **77** (1993) 111

[118] P.H. Regan et al. *Phys. Rev.* **C49** (1994) 1885

[119] S. Frauendorf and J. Reif, *Nucl. Phys.* **A621** (1997) 736

[120] M. Ionescu-Bujor et al. *Phys. Lett.* **64B** (1976) 36

[121] C. Nuytten et al. *Phys. Rev.* **C26** (1982) 1701

[122] P.H. Regan et al. *Phys. Rev.* **C55** (1997) 2305

[123] A.J. Simons et al. *Phys. Rev. Lett.* **91** (2003) 162501

[124] A. Ghiorso et al. *Nucl. Inst. Meth.* **A269** (1988) 192

[125] G. Munzenberg et al. *Nucl. Inst. Meth.* **161** (1979) 65

[126] A.V. Yeremin et al. *Nucl. Inst. Meth.* **A274** (1989) 528

[127] R. -D. Herzberg et al. *Phys. Rev.* **C65** (2001) 014303

[128] M. Leino et al. *Nucl. Inst. Meth.* **B126** (1997) 320

[129] C. Davids et al. *Nucl. Inst. Meth.* **B40/41** (1989) 1224

[130] C. Gross et al. *Nucl. Inst. Meth.* **A450** (2000) 12

[131] B.L. Cohen and C.B. Fulmer, *Nucl. Phys.* **6** (1958) 547

[132] P. Armbruster, *Nukleonika* **3** (1961) 188

[133] V.A. Karnaukhov et al. *JINR P13-4454, Dubna* (1969)

[134] A. Ghiorso et al. *Phys. Rev.* **C51** (1995) R2293

[135] M. Leino et al. *Nucl. Inst. Meth.* **B99** (1995) 653

[136] Y. Oganessian et al. *Proc. of Fourth Int. Conf. on Dynamical Aspects of Nuclear Fission*, World Scientific, Singapore (2000) 334

[137] E.H. Leib, *Rev. Mod. Phys.* **53** (1981) 603

[138] Y. Oganessian et al. *Z. Phys.* **D21** (1991) S357

[139] Sassy Setup, *Fortran code, Lawrence Berkeley Laboratory, unpublished*

[140] D.M. Cullen et al. *Phys. Rev.* **66** (2002) 034308

[141] Silicon Sensors Inc. *305 County YZ, P.O. Box 330, Dodgeville, WI 53533.* (www.siliconsensors.com)

[142] J.J. Ressler, *submitted to Phys. Rev. C*

[143] R.B. Firestone and V.S Shirley, *Table of Isotopes*, John Wiley and Sons (1996)

[144] A.M. Stefanini et al. *Nucl. Phys.* **A258** (1976) 34

[145] R. Broda et al. *Z. Phys.* **A285** (1978) 423

[146] M. Piiparinen et al. *Phys. Scripta* **17** (1978) 103

[147] V. Ninov et al. *Nucl. Inst. Meth.* **A357** (1995) 486

[148] T. Enqvist et al. *Nucl. Inst. Meth.* **B126** (1997) 344

[149] H. Newman et al. *Phys. Rev.* **C64** (2001) 027304

[150] J.J. Ressler et al. *AIP Conf. Proc.* **638** (2002) 125

[151] A. Dewald et al. *Phys. Rev.* **C68** (2003) 034314

Appendix B

List of Publications

1. *Dipole bands in* $^{112,114}In$

   S.D.Langdown, P.H. Regan, C.W. Beausang, J.J. Ressler, H. Amro, A. Bruce, M. Burns, M.A, Caprio, R. Chapman, E.A. McCutchan, D.A. Meyer, J. Ollier, M. Sciacchitano, M. Taylor, A.D. Yamamoto and N.V. Zamfir

   in preparation for submission to Phys. Rev. C

2. *Multi-quasiparticle states in* ^{184}W *via multi-nucleon transfer*

   C. Wheldon, J.J. Valiente-Dobón, P.H. Regan, C.J. Pearson, C.Y. Wu, J.F. Smith, A.O. Macchiavelli, D. Cline, R.S. Chakrawarthy, R. Chapman, M. Cromaz, P. Fallon, S.J. Freeman, A. Görgen, W. Gelletly, A. Hayes, H. Hua, S.D.Langdown, I.Y. Lee, X. Liang, Zs. Podolyák, R. Teng, D. Ward, D.D. Warner and A.D. Yamamoto

   in press, Eur. Phys. J. A (2004)

3. *Low spin states in* ^{162}Yb *and first order phase/shape transitions*

   E.A. McCutchan, N.V. Zamfir, M.A. Caprio, R.F. Casten, H. Amro, C.W.

Beausang, D.S. Brenner, A.A. Hecht, C. Hutter, **S.D.Langdown**, D.A Meyer, P.H. Regan, J.J. Ressler and A.D. Yamamoto
in press, Phys. Rev. C (2004)

4. *Production of Exotic Nuclear Isomers in Multi-Nucleon Transfer Reactions*
   P.H. Regan, J.J. Valiente-Dobón, C. Wheldon, C.Y. Wu, J.F. Smith, A.O. Macchiavelli, D. Cline, R.S. Chakrawarthy, R. Chapman, M. Cromaz, P. Fallon, S.J. Freeman, A. Görgen, W. Gelletly, A. Hayes, H. Hua, **S.D.Langdown**, I.Y. Lee, X. Liang, Zs. Podolyák, R. Teng, D. Ward, D.D. Warner and A.D. Yamamoto
   in press, Laser Phys. (2004)

5. *High-spin states populated in deep-inelastic reactions*
   S. Mohammadi, Zs. Podolyák, G. de Angelis, M. Axiotis, D. Bazzacco, P.G. Bizzeti, F. Brandolini, R. Broda, D. Bucurescu, E. Farnea, W. Gelletly, A. Gadea, M. Ionescu-Bujor, A. Iordachescu, Th. Kröll, **S.D.Langdown**, S. Lunardi, N. Marginean, T. Martinez, N.H. Medina, B. Quintana, P.H. Regan, B. Rubio, C.A. Ur, J.J. Valiente-Dobón, P.M. Walker and Y.H. Zhang
   in press, Brazilian J. Phys. (2004)

6. *Study of ^{136}Ba via deep inelastic collisions: identification of the $(\nu h_{\frac{11}{2}})^{-2}_{10^{+}}$ isomer*
   J.J. Valiente-Dobón, P.H. Regan, C. Wheldon, C.Y. Wu, N. Yoshinaga, K. Higashiyama, J.F. Smith, D. Cline, R.S. Chakrawarthy, R. Chapman, M. Cromaz, P. Fallon, S.J. Freeman, A. Görgen, W. Gelletly, A. Hayes, H.

Hua, **S.D.Langdown**, I.Y. Lee, X. Liang, A.O. Macchiavelli, C.J. Pearson, Zs. Podolyák, R. Teng, D. Ward, D.D. Warner and A.D. Yamamoto
Accepted for publication in Phys. Rev. C (2004)

7. *Low-lying structure of* ^{210}Ra *and* ^{209}Ra
   J.J. Ressler, C.W. Beausang, H. Ai, H. Amro, M.A. Caprio, R.F. Casten, A.A. Hecht, **S.D.Langdown**, E.A. McCutchan, D.A Meyer, P.H. Regan, M.J.S Sciacchitano, A.D. Yamamoto and N.V. Zamfir
   submitted to Phys. Rev. C (2004)

8. *Studies Around A≈100 using Binary reactions*
   P.H. Regan, A.D. Yamamoto, C.Y. Wu, A.O. Macchiavelli, D. Cline, J.F. Smith, S.J. Freeman, J.J. Valiente-Dobón, R.S. Chakrawarthy, M. Cromaz, P. Fallon, A. Hayes, H. Hua, **S.D.Langdown**, I.Y. Lee, C.J. Pearson, Zs. Podolyák, R. Teng and C. Wheldon
   To be published in AIP Conference Proceedings (2004)

9. *Structure of neutron-rich nuclei from deep-inelastic reactions*
   Zs. Podolyák, S. Mohammadi, G. de Angelis, Y.H. Zhang, M. Axiotis, D. Bazzacco, P.G. Bizzeti, F. Brandolini, R. Broda, D. Bucurescu, E. Farnea, W. Gelletly, A. Gadea, M. Ionescu-Bujor, A. Iordachescu, Th. Kröll, **S.D.Langdown**, S. Lunardi, N. Marginean, T. Martinez, N.H. Medina, B. Quintana, P.H. Regan, B. Rubio, C.A. Ur, J.J. Valiente-Dobón and P.M. Walker
   To be published in Int. J. Mod. Phys. E (2004)

10. *Binary-Reaction Spectroscopy of* ^{99,100}*Mo: Intruder Alignment Systematics in N=57 and N=58 Isotones*
    P.H. Regan, A.D. Yamamoto, F.R. Xu, C.Y. Wu, A.O. Macchiavelli, D. Cline, J.F. Smith, S.J. Freeman, J.J. Valiente-Dobón, K. Andgren, R.S. Chakrawarthy, M. Cromaz, P. Fallon, W. Gelletly, A. Hayes, H. Hua, **S.D.Langdown**, I.Y. Lee, C.J. Pearson, Zs. Podolyák, R. Teng and C. Wheldon
    Phys. Rev. C 68 (2003) 044313

11. *Signature for Vibrational to Rotational Evolution Along the Yrast Line*
    P.H. Regan, C.W. Beausang, N.V. Zamfir, R.F. Casten, Jing-ye Zhang, A.D. Yamamoto, M.A. Caprio, G. Gürdal, A.A. Hecht, C. Hutter, R. Krücken, **S.D.Langdown**, D.A Meyer and J.J. Ressler
    Phys. Rev. Lett. 90 (2003) 152502

12. *The Highs And Lows Of The A=100 Region: Vibration-To-Rotation Evolution In Mo And Ru Isotopes*
    P.H. Regan, A.D. Yamamoto, C.W. Beausang, N.V. Zamfir, R.F. Casten, Jing-ye Zhang, M.A.Caprio, G. Gürdal, A.A. Hecht, C. Hutter, R. Krücken, **S.D.Langdown**, D. Meyer and J.J. Ressler
    Proc. Frontiers of Nuclear Structure, Berkeley, California, P. Fallon and R. Clark, Eds; AIP Conf. Proc. 656 (2003) 422

13. *High-j proton and neutron alignments in* γ*-soft* ^{101}*Ru*

A.D. Yamamoto, P.H. Regan, C.W. Beausang, F.R. Xu, M.A. Caprio, R.F. Casten, G. Gürdal, A.A. Hecht, C. Hutter, R. Krücken, **S.D.Langdown**, D.A Meyer, J.J. Ressler and N.V. Zamfir
Phys. Rev. C66 (2002) 024302

14. *In-Beam Thin Target Fragmentation of* ^{197}Au
P.H. Regan, **S.D.Langdown**, K. Gladnishki, S.M. Mullins, Zs.Podolyak, M. Benatar, P. Kwinana, E. Gueorguieva, P. Kwinana, J.J. Lawrie, G.K.Mabala, S. Mukherjee, R.T.Newman, C.J. Pearson, J.F. Sharpey-Schafer, F.D. Smit, S.M. Vincent and A.D. Yamamoto
AIP Conf. Proc. 638 (2002) 43